Magnetoelectric and Multiferroic Properties of Some Perovskite Oxides and Other Materials

A Thesis
Submitted for the Degree of
Doctor of Philosophy

by

Chandan De

Chemistry and Physics of Materials Unit
Jawaharlal Nehru Centre for Advanced Scientific Research
(A Deemed University)
Bangalore - 560064

June 2018

Dedicated to my parents

DECLARATION

I hereby declare that the matter embodied in the thesis entitled **“Magnetoelectric and Multiferroic Properties of Some Perovskite Oxides and Other Materials”** is the result of investigations carried out by me at the Chemistry and Physics of Materials Unit, Jawaharlal Nehru Centre for Advanced Scientific Research, Bangalore, India under the supervision of Prof. A. Sundaresan and it has not been submitted elsewhere for the award of any degree or diploma.

In keeping with the general practice in reporting the scientific observations, due acknowledgements have been made whenever the work described is based on the findings of other investigators. Any omission that might have occurred due to oversight or error in judgement is regretted.

Bangalore
25/06/2018

Chandan De

CERTIFICATE

I hereby certify that the matter embodied in this thesis entitled **“Magnetoelectric and Multiferroic Properties of Some Perovskite Oxides and Other Materials”** has been carried out by Mr. Chandan De at the Chemistry and Physics of Materials Unit, Jawaharlal Nehru Centre for Advanced Scientific Research, Bangalore, India under my supervision and it has not been submitted elsewhere for the award of any degree or diploma.

Prof. A. Sundaresan
(Research Supervisor)

ACKNOWLEDGMENTS

I express my deepest gratitude to my research supervisor Prof. A. Sundaresan for providing me an opportunity to work under his guidance and introducing me to the field of materials science. I thank him for his invaluable guidance, immense support and constant encouragement throughout my research career. I am very much grateful to him for the many opportunities of collaborations he has provided me. These experiences have greatly enhanced my education as well as my research experience. I am grateful to him for giving me enough freedom for carrying out research work. His enthusiasm and passion for science will be an everlasting inspiration for me.

I would like thank Prof. C. N. R. Rao, FRS for providing me various experimental facilities and for being a constant source of inspiration. I am also grateful to him for creating such a vibrant research atmosphere in the institution to carry out the research work.

I would like to thank past and present chairmen of our unit Prof. N. Chandrabhas, Prof. S. Balasubramanian and Prof. G. U. Kulkarni, for allowing me to utilize the various facilities in the unit. I am thankful to the Int. PhD. co-ordinators (Prof. S. Balasubramanian and Prof. T. K. Maji) for their help and support during M. S. I acknowledge Sheikh Saqr Laboratory at JNCASR for providing various experimental facilities.

I would like to thank all the faculties of CPMU and NCU, Prof. S. Balasubramanian, Prof. A. Sundaresen, Prof. M. Ewaramoorthy, Prof. G. U. Kulkarni, Prof. K. S. Narayan, Prof. N. Chandrabhas, Prof. T. K. Maji, Prof. S. M. Shivaprasad, Dr. R. Ganapathy, Dr. R. Dutta, Prof. Swapan K. Pati, Prof. Umesh V. Wagmare, Prof. S. Narasimhan, Prof. H. Ila, Dr. S. Rajaram and Dr. S. Peter for their useful and informative course work.

It is a great pleasure to thank my collaborators. My sincere thanks are due to Dr. Surjeet Singh and Mr. Rabindranath Bag from IISER, Pune for accommodating me there and helping as well as guiding me to grow the single crystal sample. I would like to thank Prof. Maxim Mostovoy from University of Groningen, Netherlands and Dr. N. V. Ter-Oganessian from Southern Federal University for theoretical studies. I am also thankful to Prof. K. H. Kim and Dr. T. H. Kim from Seoul National University for PUND measurements. I am thankful to Prof. Pascal Manuel and Dr. Fabio Orlandi from RAL, UK and Prof. J. Rodríguez-Carvajal, Dr. Maria Teresa and Dr. Oscar from ILL for neutron diffraction study. I am thankful to my thesis supervisor Prof. A. Sundaresan and Dr. Ángel M. Arévalo-López and Prof. J. Paul Attfield from University of Edinburgh, UK for high-pressure synthesis and Dr. A. K. Nayak and Dr. Michael Nicklas for the high field magnetic measurements.

I thank Mr. Srinath from whom I have learnt many technical things related to various instruments, Mr. Anil, Mr. A. Srinivas, Mr. Srinivasa, Mr. Vasu, Ms. Selvi and Mr. Mahesh for their technical assistance in various experiments.

I would like to acknowledge JNCASR for the fellowship and SERB for financial support for attending the conference.

My special thanks to all of my past and present lab mates, Dr. Vengadesh, Dr. Pranab, Dr. Madhu, Dr. Nitesh, Dr. Rana, Dr. Somnath, Dr. Sundarayya, Dr. Rambabu, Dr. Chandraiah, Dr. Shivani, Mr. Bharath, Mr. Abhijit, Mr. Premakumar, Mr. Ravi, Ms. Pavitra, Mr. Amit, Ms. Swarnamayee and Ms. Sanchayita for their various helps and useful discussion during my research work and maintaining a friendly atmosphere in lab. It was always pleasure working with them.

I thank Academics, Administration staff, Library, Complab, Hostel, Dhanvantari, Gym instructor for providing and maintaining various facilities.

I thank all my Int. PhD batch mates Anirban, Ankush, Arkamita, Chandan Mishra, Rajashekhar, Ram, Koshik and Sisir for their company.

I thank all my friends at JNCASR, specially Arpan, Abhijit, Avijit, Jiarul, Saikat, Sanjay, Sisir, Somnath and Subhajit and at IISc, Tirthankar, Pradip and Shyamashis for their company in various academic and nonacademic activities.

Finally, I want to thank my family. My wife Priyanka has been supportive of me with her various helps and patience. I would like to thank my parents, late grandfather, my grandmother, my brother and all of my family relatives specially my father-in-law, mother-in-law and my uncles and my school teachers for their love, support, guidance and motivating me towards research over many years that has made me who I am today.

Preface

The aim of the thesis is to study magnetoelectric and multiferroic properties of materials towards understanding the structure-property relationship. The thesis presents a detailed study on magnetic, magnetoelectric and multiferroic properties on some simple perovskites, double perovskites, spinels and other materials with various frustrated non-collinear and collinear magnetic state. The present investigations were undertaken on some polycrystalline materials, made at ambient pressure as well as high pressure and high temperature conditions and some single crystalline materials, grown by floating zone technique.

Chapter 1 gives an introduction to magnetoelectric and multiferroic properties. A classification and various mechanisms of multiferroicity, mainly different type of magnetism induced ferroelectricity, have been discussed. The symmetry aspects of magnetoelectrics and multiferroics are briefly introduced. The challenges of determining multiferroic behavior in the materials are also discussed.

Chapter 2 describes various synthetic procedures of the samples studied in the thesis. It also describes the details of experimental set up and the basic operation principles used for various structural characterizations and physical properties investigation.

Chapter 3 demonstrates a new method of determination of an intrinsic ferroelectric polarization in the multiferroic materials. A clear signature of electric polarization that is distinct from trapped charges related behavior has been demonstrated by using a new technique called DC-bias current through investigating a prototype spin induced multiferroic $TbMnO_3$. An interesting interplay between the ferroelectric polarization and the thermally stimulated charge carrier related internal electric field is also presented.

Chapter 4 deals with the investigation of magnetoelectric behavior in mixed rare-earth manganites $Eu_{0.5}Dy_{0.5}MnO_3$ and $Gd_{0.5}Dy_{0.5}MnO_3$. An unusual existence of polarization along both *a* and *c*-direction is observed, which is due to Mn-cycloidal plane lying in (102) plane. Most interestingly, the polarization at low temperature is suppressed by the short-range ordering of rare-earth ions, which drives the cycloidal spin structure to a pseudo-helix. Applied magnetic fields induce long range ferromagnetic ordering of rare-earth ions and thus the cycloidal polarization is recovered. An intriguing memory effect of ferroelectric polarization is studied in this multiferroic material.

Chapter 5 deals with investigation of multiferroic properties in polar structure of double perovskites, $\mathrm{Na}R\mathrm{MWO}_6$ (M = Mn, R = La, Nd, Tb, Y; M = Co, R = La, Nd, Ho; M = Fe, R = La) exhibiting simultaneous ordering of A-site cations (Na and R-ions) in layered arrangement and B-site cations (M and W) in rock salt fashion. It is found that the oxides with large R-ions do not exhibit electric polarization whereas the compounds with lower size R-ions show non-switchable polarization at the magnetic ordering temperatures.

Chapter 6 presents two distinct new multiferroic materials. First part demonstrates a high pressure stabilized polar phase of $\mathrm{BiFe}_{1-x}\mathrm{Al}_x\mathrm{O}_3$ (x= 0.2, 0.3, 0.4 and 0.5) compounds. The most interesting outcome in this study was finding the ordered arrangement of Fe and Al atoms with equal charges in the $\mathrm{Bi}_2\mathrm{FeAlO}_6$ compounds, which crystallizes in a lower symmetry of $R3$ instead $R3c$ found in all other compositions including the end members. The second part deals with the discovery of a new spin induced multiferroicity in monoclinic phase of $\mathrm{MnSb}_2\mathrm{S}_4$ prepared under ambient pressure. Most interestingly, applied magnetic field strongly enhances the electric polarization, which confirms the magnetoelectric nature of this compound. A *p-d* hybridization mechanism has been attributed to the multiferroic behavior. Besides, in the high pressure orthorhombic (*Pnam*) polymorph of $\mathrm{MnSb}_2\mathrm{S}_4$, a multiferroic behavior at the magnetic transition was also found in addition to a structural transition occurring well above the magnetic ordering.

Chapter 7 addresses the magnetoelectric effect in single crystal of frustrated magnetic spinel $\mathrm{CoAl}_2\mathrm{O}_4$ with less anti-site disorder of Co^{2+} and Al^{3+} ions. This chapter evidences the magnetoelectric effect in $\mathrm{CoAl}_2\mathrm{O}_4$ at certain directions under certain magnetic field directions. Comparing the value of experimental polarization ratio ($P_{1\text{-}10}$) to the theoretical one obtained by symmetry analysis, the magnetic easy axis has been proposed to be along [111] and thus confirms the long range magnetic ordering.

Publications

1. "Non-switchable polarization and magnetoelectric coupling in the high-pressure synthesized doubly ordered perovskites $NaYMnWO_6$ and $NaHoCoWO_6$", **Chandan De** and A. Sundaresan, *Phys. Rev. B,* **97**, 214418, (2018)
2. "Magnetic compensation-induced sign reversal of exchange bias in a multi-glass perovskite $SmFeO_3$", **Chandan De**, Ajaya K. Nayak, Michael Nicklas, and A. Sundaresan, *Appl. Phys. Lett.*, **111**, 182403 (2017)
3. "Possible coexistence of cycloidal phases, magnetic field reversal of polarization, and memory effect in multiferroic $R_{0.5}Dy_{0.5}MnO_3$ (R = Eu and Gd)", **Chandan De** and A. Sundaresan, *Appl. Phys. Lett.*, **107**, 052902 (2015)
4. "Effect of internal electric field on ferroelectric polarization in multiferroic $TbMnO_3$", **Chandan De**, Somnath Ghara and A. Sundaresan, *Solid State Commun.*, **205**, 61 (2015)
5. "The absence of ferroelectric polarization in layered and rock-salt ordered $NaLnMnWO_6$ (Ln = La, Nd, Tb) perovskites", **Chandan De**, T. H. Kim, K. H. Kim, and A. Sundaresan, *Phys. Chem. Chem. Phys.*, **16**, 5407 (2014)
6. "Spin-driven ferroelectricity and large magnetoelectric effect in $MnSb_2S_4$", **Chandan De** and A. Sundaresan, under review, (2018)
7. "Rare-earth induced rotation of cycloidal spin and helical ground state in $Gd_{0.5}Dy_{0.5}MnO_3$", **Chandan De**, R. Bag, S. Singh, F. Orlandi, P. Manuel, M. Mostovoy and A. Sundaresan, to be communicated (2018)
8. "Origin of memory effect in multiferroic $Gd_{0.5}$Dy0.5MnO3", **Chandan De** and A. Sundaresan, to be communicated, (2018)
9. "Isovalent cation ordering in the high-pressure and high-temperature synthesized polar rhombohedral perovskite Bi_2FeAlO_6" **Chandan De**, Ángel M. Arévalo-López, J. Paul Attfield and A. Sundaresan, to be communicated, (2018)

10. “Magnetic easy axis of frustrated spinel $CoAl_2O_4$”, **Chandan De**, N. V. Ter-Oganessian and A. Sundaresan, under preparation, (2018)
11. “Spin-driven ferroelectricity and structural change in high pressure orthorhombic polymorph of $MnSb_2S_4$”, **Chandan De** and A. Sundaresan, under preparation, (2018)

Miscellaneous Publications

12. “Critical Comparison of $FAPbX_3$ and $MAPbX_3$ (X= Br and Cl): How Do They Differ?”, Sharada Govinda, Bhushan P Kore, Diptikanta Swain, Akmal Hossain, **Chandan De**, Tayur N Guru Row, DD Sarma, *J. Phys. Chem. C*, DOI: 10.1021/acs.jpcc.8b00602 (2018)
13. “New rare earth hafnium oxynitride perovskites with photocatalytic activity in water oxidation and reduction”, Ashley Phillip Black, Hajime Suzuki, Masanobu Higashi, Carlos Frontera, Clemens Ritter, **Chandan De**, Sundaresan Athinarayanan, Ryu Abe, Amparo Fuertes, *Chem. Commun.*, **54**, 1525 (2018)
14. “Is $CH_3NH_3PbI_3$ Polar”, G Sharada, Pratibha Mahale, Bhushan P Kore, Somdutta Mukherjee, Mysore S Pavan, **Chandan De**, Somnath Ghara, A Sundaresan, Anshu Pandey, Tayur N Guru Row, DD Sarma, *J. Phys. Chem. Lett.*, **7**, 2412 (2016)
15. “Ti-rich double perovskites $LnCu_{3-y}Ti_{2-x}Mn_{2+x+y}O_{12}$: ferrimagnetism and magnetoresistance up to room temperature”, Md Motin Seikh, V Caignaert, A Sundaresan, **Chandan De**, B Raveau, *J. Mater. Chem. C*, **2**, 6061 (2014)

Contents

1 Introduction to magnetoelectrics and multiferroics

Summary 1
- 1.1 Introduction 3
- 1.2 Magnetoelectric effect and multiferroicity 3
- 1.3 Symmetry criteria of magnetoelectrics and multiferroics 6
- 1.4 Origin of multiferroic properties 8
  - 1.4.1 Independent origin (Type-I multiferroic) 8
    - 1.4.1.1 Lone pair effect 9
    - 1.4.1.2 Geometric frustration 10
    - 1.4.1.3 Incorporation of magnetic ordering in a ferroelectric material 11
    - 1.4.1.4 Heterostructures of ferroelectric and magnetic layer 12
  - 1.4.2 Magnetism induced ferroelectric (Type-II multiferroic) 12
    - 1.4.2.1 Symmetric exchange interaction 12
    - 1.4.2.2 Spin-current or inverse DM interaction mechanism 14
      - 1.4.2.2.1 Phase diagram of *R*MnO$_3$ 16
    - 1.4.2.3 *p*–*d* hybridization 18
- 1.5 Difficulties of finding intrinsic multiferroics 20
- 1.6 Scope of the thesis 21

References 22

2 Experimental techniques

Summary 25
- 2.1 Introduction 27
- 2.2 Sample Preparation 27

2.2.1 Powder sample 27

2.2.2 High-pressure solid-state reaction 28

2.2.3 Single crystal growth 30

2.2.3.1 Preparation of Ceramic Rods 30

2.2.3.2 Optical Float-Zone Method 31

2.3 Sample Characterization 32

2.3.1 Powder X-ray and Neutron Diffraction 32

2.3.2 Rietveld Refinement 34

2.4 Physical Property Measurements 36

2.4.1 Magnetization measurements 36

2.4.1.1 dc magnetization 36

2.4.1.2 ac susceptibility 39

2.4.2 Heat Capacity 41

2.4.3 Dielectric property 42

2.4.4 $P(E)$ hysteresis loop 43

2.4.5 Piezoelectric loop measurement 45

2.4.6 Pyroelectric current measurement 46

2.5 Fabrication of tube furnace 47

References 49

3 Thermally stimulated free charge carriers and intrinsic ferroelectric polarization in multiferroic materials: A study on $TbMnO_3$

Summary 51

3.1 Introduction 53

3.2 Experiments 54

3.3 Results and discussion 55

3.3.1 Magnetization and heat capacity and dielectric property........................55

3.3.2 Pyrocurrent and DC-bias current..56

3.3.3 Internal field due to TSFC carriers..60

3.3.4 Schematic of ferroelectric dipoles and TSFC carrier.............................64

3.4. Conclusion..66

References..67

4 Part-I Effect of rare-earth on multiferroic properties of $\mathbf{R_{0.5}Dy_{0.5}MnO_3}$ ($\mathbf{R}$ = Eu and Gd)

Summary...69

4.1 Introduction...71

4.2 Experiments..73

4.3 Results and discussions...74

4.3.1 Results on polycrystalline EDMO and GDMO......................................74

4.3.2 Results on single crystal $Gd_{0.5}Dy_{0.5}MnO_3$...80

4.3.2.1 Crystal Laue pattern and images...80

4.3.2.2 Magnetic phase transitions...80

4.3.2.2 Temperature-dependent spontaneous electric polarization..............82

4.3.2.3 Effect of magnetic field ($H||a$) on the polarization (P_a and P_c).......83

4.3.2.4 Effect of magnetic field ($H||b$) on the polarization (P_a and P_c).......84

4.3.2.5 Neutron diffraction results in polycrystalline $^{160}Gd_{0.5}Dy_{0.5}MnO_3$...86

Paramagnetic state:..86

Spin density wave state:...87

Cycloidal state:..89

Pseudo-helix state:...90

4.3.2.6 Electric polarization in the *p*-helix phase...96

4.3.3 Discussion on various polar states 97

4.4 Conclusions 99

4 Part-II Multiferroic memory effect

Summary 101

4.5 Introduction to the memory effect 102

4.6 Results and discussion 103

4.6.1 Observation of memory effect 103

4.6.2 Dielectric relaxation 107

4.6.3 Origin of memory effect 109

4.7 Conclusions 113

References 114

5 Magnetic and dielectric properties of the layered and rock-salt ordered Na*R*MWO$_6$ (*R* = La, Nd, Tb, Y and Ho; M = Mn, Fe and Co) double perovskites

Summary 117

5.1 Introduction 119

5.1.1 Hybrid improper ferroelectricity in perovskites 120

5.2 Experiments 123

5.3 Results and discussion: Na*R*MWO$_6$ (for M = Mn, *R* = La, Nd and Tb; M = Co, *R* = La and Nd; M = Fe, *R* = La) synthesized under ambient pressure 125

5.3.1 Structural details of Na*R*MnWO6 (*R* = La, Nd and Tb) 125

5.3.2 Magnetic properties 131

5.3.3 Polarization 135

5.3.4 Magnetodielectric effect at low temperature 138

5.3.5 Dielectric property near room temperature 142

5.4 Results on high pressure synthesized NaYMnWO$_6$ and NaHoCoWO$_6$ 146

5.4.1 Crystal Structure 146
5.4.2 Magnetic properties 148
5.4.3 Dielectric properties 151
5.4.4 Low temperature dielectric and pyroelectric properties 153
5.5 Conclusion 157
References 158

6 Part-I Multiferroicity in high-pressure synthesized isovalent cation ordered Bi_2FeAlO_6

Summary 163
6.1 Introduction 165
6.1.1 Experimental details 166
6.1.2 Results and discussions 167
6.1.2.1 Structure 167
6.1.2.2 Magnetic properties 170
6.1.2.3 Dielectric property 171
6.1.2.4 Ferroelectric and piezoelectric properties 173
6.1.3 Conclusions 175

6 Part-II Spin driven multiferroicity in ambient pressure and high-pressure phase of $MnSb_2S_4$

Summary 176
6.2A Monoclinic $MnSb_2S_4$ 177
6.2A.1 Experimental details 178
6.2A.2 Results and discussions 179
6.2A.2.1 Structure 179
6.2A.2.2 Magnetization and heat capacity 180

6.2A.2.3 Dielectric property..182

6.2A.2.4 Ferroelectric polarization 183

6.2B High pressure orthorhombic phase of $MnSb_2S_4$.......................................186

6.2B.1 Experimental details 186

6.2B.2 Results and discussions 187

6.2B.2.1 Structure..187

6.2B.2.2 Magnetic properties 188

6.2B.2.3 Dielectric property..190

6.2B.2.4 Ferroelectric polarization..191

6.2B.3 Conclusions 193

References 194

7 Magnetoelectric effect in frustrated spinel $CoAl_2O_4$

Summary 197

7.1 Introduction 199

7.2 Experiments..201

7.3 Results and discussions 202

7.3.1 Structural data 202

7.3.2 Magnetization and heat capacity 204

7.3.3 Magnetodielectric effect..207

7.3.4 Magnetoelectric effect...209

7.3.5 Neutron Laue Diffraction..211

7.3.6 Easy axis determination from electric polarization...................................213

7.4 Conclusion..214

References 215

Summary of the thesis…………………………………………………………217

List of abbreviations…....………………………………………………………218

Chapter 1

Introduction to magnetoelectrics and multiferroics

Summary

This chapter presents an introduction to magnetoelectric effect and multiferroics which includes the history, definition, importance and their applications. The classification and the various mechanisms of multiferroicity mainly different types of magnetism induced ferroelectric behaviors are discussed. The symmetry aspects of magnetoelectrics and multiferroics are briefly introduced. The challenges of determining multiferroic behavior in the materials are also addressed. Finally, the scope of the thesis is provided.

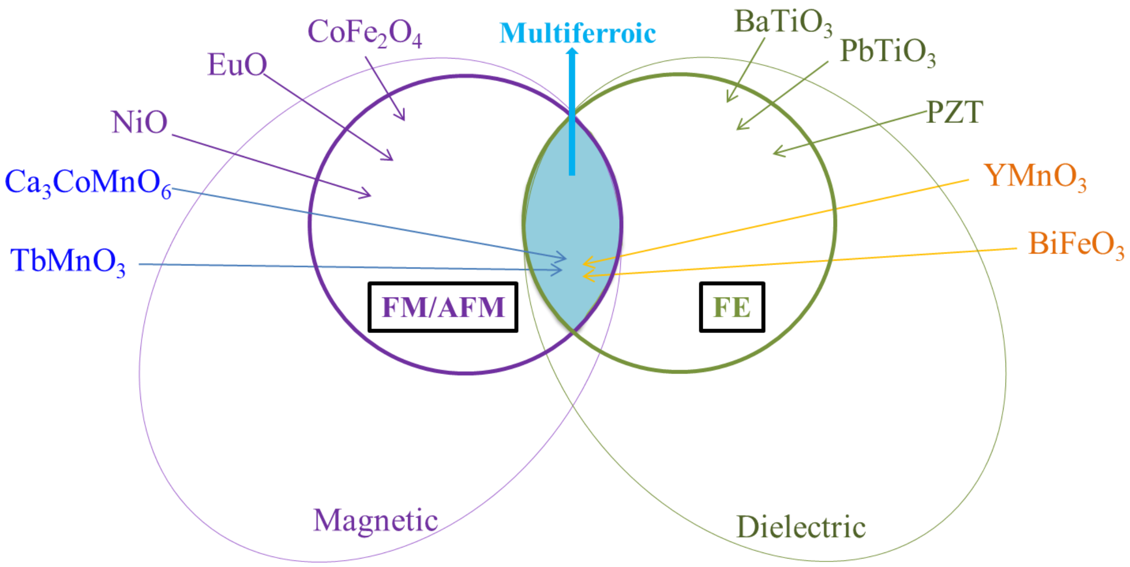

1.1 Introduction

Magnetic and ferroelectric materials are in the heart of the modern science and technology. Magnetic materials with switchable spontaneous magnetization (*M*) driven by an external magnetic field (*H*) have been widely used in data-storage industries such as magnetic random-access memories (MRAMs). The sensors and actuators in the electronic devices greatly depend on ferroelectric materials with spontaneous polarization reversible upon an external electric field (*E*). The coupled strain and polarization in the ferroelectric materials allow elastic energy to be converted into electric energy or vice versa. Another major application of ferroelectric material is ferroelectric random-access memories (FeRAMs) which is non-volatile and has high-speed memory access, superior feature to the semiconductor flash memories. Towards device miniaturization, combining more than one functionality in a single component is highly desirable. For this reason, it is a natural tendency that combining magnetic and ferroelectric properties in a single unit can generate the new generation memory devices, smart sensors and actuators. The coexistence of more than one ferroic ordering in a single device can in fact provide a synergistic effect which can create even new functionality. The magnetoelectric (ME) or the multiferroic are such properties which can generate a signal on one parameter by varying the another parameter or may facilitate two parameter independently in a single material. The multiferroic devices can offer the spintronics effect much more efficiently such as it can write the magnetic states using electric field which can overcome the high energy consumption in writing the data in memory devices. Although ferroelectricity and magnetism are well understood scientifically and well characterized technologically, the multiferroics underwent a number of challenges in both fundamental physics point of view as well as technological usage. Therefore, study of multiferroic materials have been a major focus in condensed matter physics and materials science since its discovery. A more detailed overview of magnetoelectrics and multiferroics are given below.

1.2 Magnetoelectric effect and multiferroicity

Magnetoelectric effect is a materials property where an induction of magnetization (*M*) occurs by an electric field (*E*) and electric polarization (*P*) by a magnetic field (*H*). Although the dynamic relations between *E* and *H* are well understood by Maxwell's equations, but those between *P* and *M* are highly nontrivial. The coupling between *P* and *M* is mediated by the electrons in the crystal. The journey of magnetoelectric effect started a century ago and it has progressed through the contributions of many famous scientists (figure 1.1). In 1894, Pierre Curie first predicted the possibility of an intrinsic magnetoelectric effect in some crystals by considering the crystalline symmetry [1].

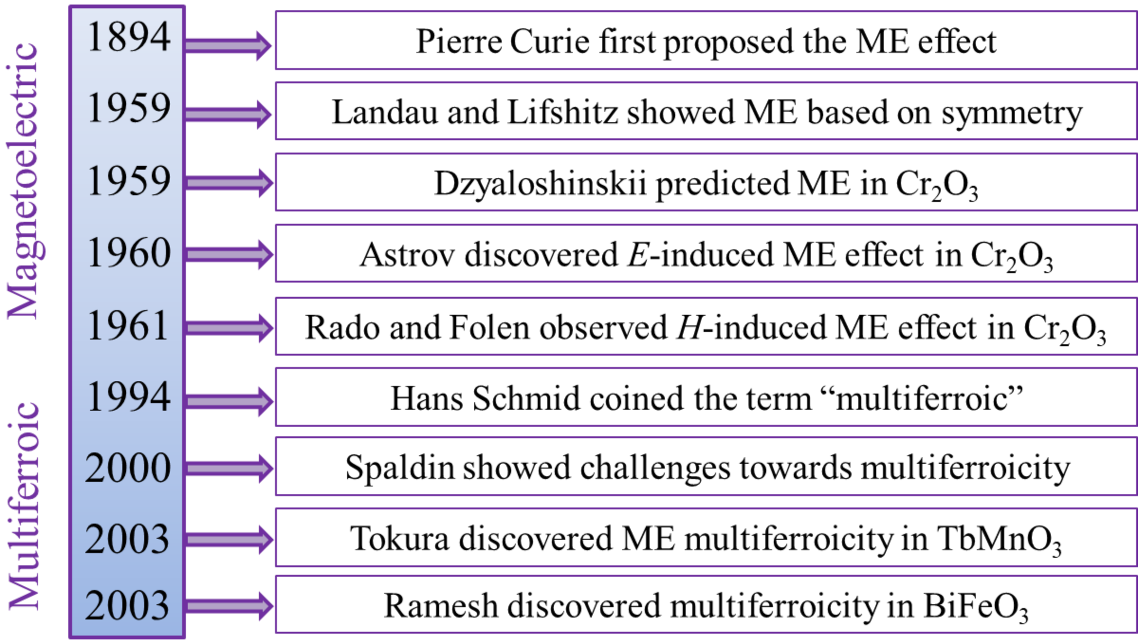

Figure 1.1 History and progress of magnetoelectric and multiferroics.

But the work on magnetoelectrics began after a long period of time with the advancement of theory in condensed matter physics. Landau and Lifshitz worked on the theoretical aspects of magnetoelectric effects and remarked in one of the famous books on theoretical physics in 1959 [2] which reads *"Let us point out two more phenomena, which, in principle, could exist. One is piezomagnetism, which consists of linear coupling between a magnetic field in a solid and a deformation (analogous to piezoelectricity). The other is a linear coupling between magnetic and electric fields in a media, which would cause, for example, a magnetization proportional to an electric field. Both these phenomena could exist for certain classes of magnetocrystalline symmetry. We will not however discuss these phenomena in more detail because it seems that till present, presumably, they have not been observed in any substance."* Very soon after this publication, Dzyaloshinskii predicted that the well-known antiferromagnet Cr_2O_3 should exhibit the linear magnetoelectric effect based on its crystal symmetry [3]. The symmetry aspect of magnetoelectric and multiferroic effect is described in the following section of this chapter. In another year, this effect was indeed observed experimentally in Cr_2O_3 by Astrov by measuring magnetization under electric field [4]. Within two years it was further confirmed by Rado and Folen in 1961 by measuring electric polarization under magnetic field and the magnetoelectric coupling coefficient was reported to be 4.13 ps/m [5]. According to the Landau theory, the free energy can be expressed in the following way for a magnetoelectric system,

$$F(E,H) = F_0 - P_i^S E_i - M_i^S H_i - \frac{1}{2}\varepsilon_0\varepsilon_{ij}E_iE_j - \frac{1}{2}\mu_0\mu_{ij}H_iH_j - \alpha_{ij}E_iH_j - \frac{1}{2}\beta_{ijk}E_iH_jH_k - \frac{1}{2}\gamma_{ijk}H_iE_jE_k - \cdots,$$

where F_0 is the ground state free energy. ε_0 and μ_0 are the dielectric and magnetic susceptibilities of vacuum. Subscripts (i , j, k) refer to the three components of a variable in spatial coordinates. μ_{ij} and ε_{ij} are the second-order tensors of magnetic and dielectric susceptibilities. E_i and H_i are the components of the electric field E and magnetic field H, respectively, P_i^s and M_i^s are the components of spontaneous polarization P_s and magnetization M_s. The polarization and magnetization can be determined from above equation as follows,

$$P_i(E,H) = -\frac{\partial F}{\partial E_i} = P_i^s + \epsilon_0\epsilon_{ij}E_j + \alpha_{ij}H_j + \frac{1}{2}\beta_{ijk}H_jH_k + \gamma_{ijk}H_iE_j + \cdots,$$

$$M_i(E,H) = -\frac{\partial F}{\partial H_i} = M_i^s + \mu_0\mu_{ij}H_j + \alpha_{ij}E_j + \frac{1}{2}\beta_{ijk}H_jE_i + \gamma_{ijk}E_jE_k + \cdots,$$

From these equations, we see that the magnetodielectric effect is mainly depends on the coefficient α_{ij} which is related to the dielectric and magnetic response in the following way $\alpha_{ij} < \chi_e\chi_m$, where χ_e and χ_m are the electric and magnetic susceptibilities. Therefore we can see that a large magnetoelectric coefficient can be observed at the ordering temperatures where χ_e and χ_m diverges. However, in general it is small in single-phase specimen for the practical purpose. One way to enhance the magnetoelectric effect in compounds is to make large dielectric and magnetic susceptibilities. It is well known that ferroic materials (ferroelectric or ferromagnetic) have the largest dielectric or magnetic susceptibility, respectively. Therefore the materials combining ferroelectrics with ferromagnetism would be prime candidates for large magnetoelectric effect. In this way the term “multiferroic” was proposed by H. Schmid in 1994, where two or more primary ferroic order parameters i.e ferroelectricity, ferromagnetism and ferroelasticity coexists [6]. A schematic diagram containing various types of ferroic materials is given in the beginning of this chapter. Since there is not much satisfactory progress in obtaining ferroelastic and ferromagnetic materials, the term multiferroic in general represents the coexistence of (anti)ferroelectric and (anti)ferromagnetic. Throughout the thesis we will be discussing only ferroelectric and (anti)ferromagnetic properties.

1.3 Symmetry criteria of magnetoelectrics and multiferroics

The symmetry criteria to be fulfilled for the ferroelectric materials, is the breaking of spatial inversion. Electric polarization which is a polar vector ($q\vec{r}$, where $\vec{r}$ is the distance between the charges, $\mp q$) changes its sign under special inversion symmetry whereas under time reversal symmetry, it is invariant. Therefore the overall polarization in a macroscopic specimen remains finite when there is a breaking of spatial inversion symmetry. On the other hand the time reversal symmetry should be broken for any magnetically ordered materials. The following equations show the symmetry operation for electric polarization and magnetization under spatial and time reversal symmetry.

$$\vec{P}_I' = I\vec{P} = -\vec{P}; \quad \vec{P}_T' = T\vec{P} = \vec{P}$$

According to the Neumann's principle, "*the symmetry of any physical property of a crystal must include the symmetry elements of the point group of the crystal*" meaning that any physical property of a crystal would remain invariant under the symmetry element present in the crystal. Therefore, to have a spontaneous polarization, there must be broken spatial inversion symmetry. It is for this reason we observe ferroelectricity or piezoelectricity only in the ten non-centrosymmetric (polar) space group out of total 32 space group [7]. Using the Neumann's principle, the electric polarization direction can be determined. For example, in the case of orthorhombic crystal system with a polar point group *mm*2, the polarization direction would be along the z-direction. The polarization along *x* and *y*-direction would be reversed under the two-fold rotation. The detailed polarization directions for the other crystal systems can be found in the book [7].

On the other hand, magnetization or the magnetic field is an axial vector which is odd with respect to the time reversal, but even with the spatial inversion, shown in the following expressions.

$$\vec{M}'_I = I\vec{M} = \vec{M}; \qquad \vec{M}'_T = T\vec{M} = -\vec{M}$$

We can understand these rules considering magnetic moment as a current carrying loop $M \sim \vec{r} \times \vec{J}$ where $\vec{J} = e\, d\vec{r}/dt$. Figure 1.2 indicates that the magnetization changes its sign under time reversal and remains invariant under spatial inversion. Thus, in ferromagnetic or antiferromagnetic materials, spontaneous magnetization appears by breaking time-reversal symmetry.

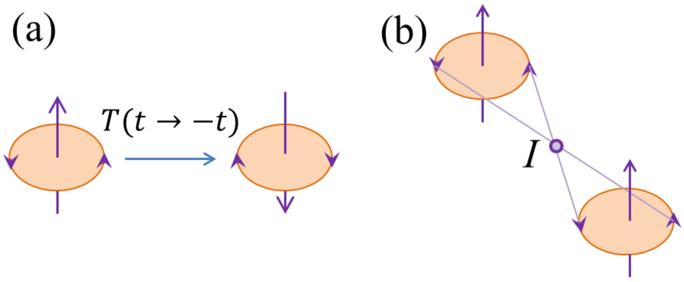

Figure 1.2(a) time reversal operation and (b) spatial inversion operation on magnetic moment.

For magnetoelectric as well, the symmetry considerations play a crucial role. In this case, both time reversal (*T*) and spatial inversion (*I*) symmetry should be broken. For the multiferroics where the polarization exists without application of magnetic field, apart from the breaking of *T* and *I*, the product of *T I* (time reversal followed by inversion) also should be broken. Thus by looking at the symmetries, we can understand whether a material with a given magnetic structure would be a real multiferroic or only a magnetoelectric. For example, in Cr_2O_3, both the *T* and *I* is broken [8]. However, the simultaneous inversion and time reversal returns the state to the original one. Thus Cr_2O_3 is only a magnetoelectric with magnetic point group $(\bar{3}'m')$. Very recently, the magnetoelectric effect is found in another binary oxide Co_3O_4 with spinel structure where *A*-site magnetic ions break both time and special inversion symmetry below the antiferromagnetic ordering at ~32 K [9]. Based on this mechanism, we have found magnetoelectric effect in a spinel $CoAl_2O_4$ which has been investigated in chapter 7. On the other hand in Ca_3CoMnO_6 with alternation of ions with different charges, e.g. (+) and (−) and with the magnetic structure ↑↑↓↓ (will be discussed in the following section), not only *T* and *I*, but also *T I* are broken. Thus, Ca_3CoMnO_6 is a real multiferroic with magnetic point group 3*m*. Like polar point groups, the 58 magnetoelectric point groups including their allowed polarization directions coefficients (α_{ij}) are given in table 1.1 taken from ref. [8].

Table 1.1 Magnetoelectric point groups and their coefficients.

Magnetoelectric point groups	Magnetoelectric coefficients (α_{ij})	Examples	Ref.
$1, \bar{1}'$	$\begin{pmatrix} \alpha_{11} & \alpha_{12} & \alpha_{13} \\ \alpha_{21} & \alpha_{22} & \alpha_{23} \\ \alpha_{31} & \alpha_{32} & \alpha_{33} \end{pmatrix}$	Fe_3O_4 (1)	[10]
$2, m', 2/m'$	$\begin{pmatrix} \alpha_{11} & 0 & \alpha_{13} \\ 0 & \alpha_{22} & 0 \\ \alpha_{31} & 0 & \alpha_{33} \end{pmatrix}$	Ni-I Boracite (m')	[11]
$2', m, 2'/m$	$\begin{pmatrix} 0 & \alpha_{12} & 0 \\ \alpha_{21} & 0 & \alpha_{23} \\ 0 & \alpha_{32} & 0 \end{pmatrix}$	ErOOH $(2'/m)$	[12]
$222, m'm'2, m'm'm'$	$\begin{pmatrix} \alpha_{11} & 0 & 0 \\ 0 & \alpha_{22} & 0 \\ 0 & 0 & \alpha_{33} \end{pmatrix}$	Cu-Cl Boracite $(m'm'2)$	[13]
$22'2', 2mm, m'm2', m'mm$	$\begin{pmatrix} 0 & 0 & 0 \\ 0 & 0 & \alpha_{23} \\ 0 & \alpha_{32} & 0 \end{pmatrix}$	Ni-Cl Boracite $(m'm2')$	[14]
$3, \bar{3}', 4, \bar{4}', 4/m', 6, \bar{6}', 6/m'$	$\begin{pmatrix} \alpha_{11} & \alpha_{12} & 0 \\ -\alpha_{12} & \alpha_{11} & 0 \\ 0 & 0 & \alpha_{33} \end{pmatrix}$		
$4', \bar{4}, 4'/m'$	$\begin{pmatrix} \alpha_{11} & \alpha_{12} & 0 \\ \alpha_{12} & -\alpha_{11} & 0 \\ 0 & 0 & 0 \end{pmatrix}$		
$32, 3m', \bar{3}'m', 422, 4m'm', \bar{4}'2m', 4/m'm'm', 622, 6m'm', \bar{6}'m'2, 6/m'm'm'$	$\begin{pmatrix} \alpha_{11} & 0 & 0 \\ 0 & \alpha_{11} & 0 \\ 0 & 0 & \alpha_{33} \end{pmatrix}$	Cr_2O_3 $\overline{(3}'m')$	[15]
$4'22, 4'mm', \bar{4}2m, \bar{4}2'm', 4'/m'mm'$	$\begin{pmatrix} \alpha_{11} & 0 & 0 \\ 0 & -\alpha_{11} & 0 \\ 0 & 0 & 0 \end{pmatrix}$	$DyPO_4$ $(4'/m'mm')$	[16]
$32', 3m, \bar{3}'m, 42'2', 4mm, \bar{4}'2'm, 4/m'mm, 62'2', 6mm, \bar{6}'m2', 6/m'mm$	$\begin{pmatrix} 0 & \alpha_{12} & 0 \\ -\alpha_{12} & 0 & 0 \\ 0 & 0 & 0 \end{pmatrix}$		
$23, m'3, 432, \bar{4}'3m', m'3m'$	$\begin{pmatrix} \alpha_{11} & 0 & 0 \\ 0 & \alpha_{11} & 0 \\ 0 & 0 & \alpha_{11} \end{pmatrix}$		

1.4 Origin of multiferroic properties

1.4.1 Independent origin (Type-I multiferroic)

Three major routes are developed for combining ferroelectricity and magnetic order in a single material or a combination of materials. In the first case, finding a single phase material which has spontaneous ferroelectric and magnetic ordering is the most interesting one as it deals with new mechanisms and has very rich physics. Although there are active research in this field for nearly two decades, the total number of known multiferroics are not very large. It is because there are some fundamental contradictions in the requirement for magnetic ordering and ferroelectricity. The transition metal which has *d*-electron will reduce the tendency for off-center ferroelectric distortion in the materials. Therefore the empty *d*-orbital, apparently, is crucial for the observation of ferroelectricity [17]. Due to the interaction between the filled *p*-orbital of the oxygen atom and the empty *d*-orbital in the transition metal, the empty *d*-orbital will contribute to the bonding of the transition metal ion with the oxygen ligands. This leads to a lowering of energy and resulting in a displacement of the transition metal towards the ligand. When the *d*-orbital contains an electron, the overlap of the *p*-orbital and the *d*-orbital on the transition metal will not result in a reduction of the energy. Because the electron from the *d*-orbital would go to the antibonding orbital due to the electrons already present in the bonding state and oppose the energy gain thus the ferroelectricity does not occur. Alternative ways of inducing the polar ordering in magnetic ordered materials are discussed in the following sections.

1.4.1.1 Lone pair effect

The aforementioned contradictory picture makes the research on multiferroic so interesting and fascinating. It has taken many decades to notice the other routes of overcoming the d^0 problem. In 2003, $BiFeO_3$ was discovered to be a multiferroic where the Bi^{3+} ion has a lone pair ions which causes the ferroelectricity. The lone pairs are formed as clouds of two electrons which are not bound to any other atoms and induce a strong local polarization that can result in ferroelectricity (figure 1.3(a)). The electric polarization prefers to align along the [111] direction, as shown by the arrow. The ferroelectric Curie point is 1100 K. A typical ferroelectric loop observed at room temperature in $BiFeO_3$ is shown in figure 1.3(b). On the other hand, the weak magnetic moment at room temperature can be observed due to a small residual moment in a canted spin structure. The Fe^{3+} (d^5) ions order independently to the dielectric ordering to form an antiferromagnetic structure below 643 K. Since the two phenomena have independent origin, they have weaker coupling. However, as this material hosts both the ferroic ordering above room temperature, it has very high potential for the practical applications. Perhaps the most studied multiferroic material is $BiFeO_3$ till now. There are lot of research is still continuing to make this compound in viable form for the practical devices. Very recently, a spiral kind of magnetic ordering is found in this material which allows some additional electric polarization and promise a good coupling between the two ordering [18]. A more discussion on this material is given in chapter 6 (Bi_2FeAlO_6) where we have substituted Al^{3+}-ions in Fe^{3+}-ions under high pressure and temperature, maintaining its polar structure as well as magnetic character.

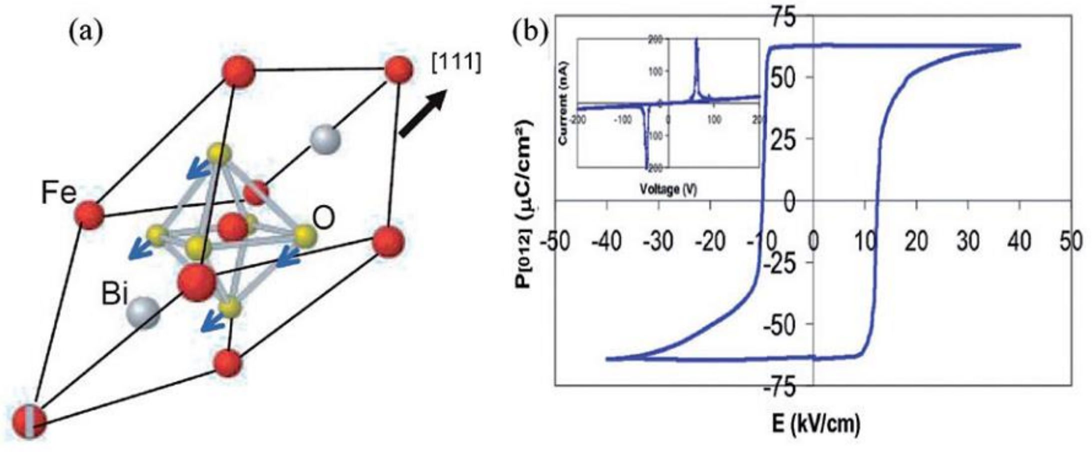

Figure 1.3 (a) $BiFeO_3$ lattice structure, Bi ion shifted towards (111) direction. The polarization direction along (111) indicated by an arrow. (b) *P*(*E*) loop measured in $BiFeO_3$ single crystal [19] (Copyright © 2007 American Institute of Physics.)

1.4.1.2 Geometric frustration

Hexagonal manganites are one among the well-known multiferroic materials where the ferroelectric and magnetic ordering appears through different routes. These materials have the chemical formula $AMnO_3$ in which ‘A’ is a lower size rare-earth ion (Ho to Lu and yttrium). In the hexagonal structure ($P6_3cm$), the Mn^{3+} ions are surrounded by a triangular bipyramid of oxygen atoms forming a layered arrangement which is separated by the layer of Y-ions. Here the ferroelectricity occurs due to buckling of MnO_5 bipyramid and vertically shifting of Y-ions from the mirror plane (high temperature centrosymmetric phase $P6_3/mmc$), keeping the constant distance to the interconnected apical oxygen (O_T ions) and change of two Y–O_P (in-plane oxygen) ~2.8 A° bond length to ~2.3 A° and 3.4 A°, leading to a net electric polarization (figure 1.4) [20]. Here the polarization occurs as a by-product of complex lattice distortion which is different from the previous one (lone pair effect) where ferroelectric transition comes from the polar structural instability associated with the electronic pairing. Thus this class of materials is called as improper ferroelectric. A more discussion on proper and improper ferroelectricity is presented in chapter 5 where we have investigated hybrid improper ferroelectricity in doubly ordered perovskite oxides ($AA'BB'O_6$). The ferroelectric transition in $YMnO_3$ occurs at a high temperature nearly 1000 K. On the other hand, the magnetic ordering occurs through the Mn^{3+} ordering below 100 K. Thus there is no magnetoelectric coupling present in these materials.

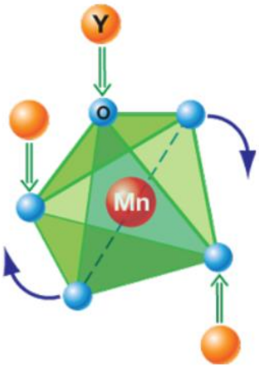

Figure 1.4 Tilting of a rigid MnO_5 block resulting in net electric polarization with a magnetic Mn^{3+} at the center. Because of the tilting, the Y-O bonds form dipoles (green arrows). (Adapted from ref. [21])

Another family of geometrically frustrated multiferroic system is $BaMF_4$ (M = Mn, Fe, Co and Ni) which crystallizes in orthorhombic structure. Ferroelectricity comes from alternating rotations of MF_6 octahedra in the *bc* plane and the displacement of the Ba cations along the *c*-axis [22]. Magnetism originates due to magnetic M-ions. Thus the ferroelectric phase transition and magnetic transition occurs at different temperature T_C = 1200-1500 K and T_N = 100 K [23].

1.4.1.3 Incorporation of magnetic ordering in a ferroelectric material

The second scheme towards achieving multiferroic materials is to integrate magnetic ordering in a ferroelectric material or vice versa. This is mainly made through substitutions of magnetic ions in a ferroelectric material. As already mentioned in the previous section, the transition metal *d*-electrons are essential for magnetism, a large number of study is devoted towards this strategy where the transition metals containing d-electrons have been incorporated in the non-magnetic ferroelectric structures. For example $Pb_2(CoW)O_6$, that showed both magnetic ordering and ferroelectricity where Co^{2+} ions are incorporated in the ferroelectric $PbWO_3$. Several materials have been prepared as multiferroics following this strategy [24, 25]. However, due to the fact that the ferroelectricity and magnetic ordering have their origin in the different atoms, the magnetoelectric coupling in this case is also small. Moreover, due to the dilution of the magnetic ions, the materials lose their magnetic interaction strength thus have a rather low Curie or Néel temperatures.

1.4.1.4 Heterostructures of ferroelectric and magnetic layer

A large amount of effort has been devoted in this third strategy, where a heterostructure of ferroelectric layer and magnetic layer have been utilized to make magnetoelectric functioning at the interfaces [26-31]. This process is also quite promising since it can have a direct application in device. However it is beyond our scope of the thesis thus we will be discussing multiferroics of only single phase materials.

1.4.2 Magnetism induced ferroelectric (Type-II multiferroic)

This class of multiferroic materials are the most demanding and generated broad interest in the condensed matter physics as well as in the technological aspects. In this case, the electric polarization is induced by various frustrated magnetic ordering thus possibility of a fair coupling among P and M. In general terms, microscopic mechanism of spin-induced multiferroicity can be categorized into three types. (i) symmetric spin exchange interaction, (ii) antisymmetric spin exchange interaction and (iii) spin–ligand interaction (spin-dependent *p–d* hybridization).

1.4.2.1 Symmetric exchange interaction

In this case, the dimerization of atoms possessing different valence states induces the ferroelectric polarization. The periodic array of dipole moments produces the ferroelectric ordering. Below certain types of magnetic ordering, the crystal structure deforms due to the change in bond length caused by the magnetic ordering and the dipoles are formed [32]. If the charge on magnetic ions are equivalent along the chain, this dimerization does not produce any electric polarization. When the two different charged magnetic ions are alternating, electric polarization is induced. The electric polarization can appear even without the dimerization when the different magnetic (S = 1/2) sites are alternating, as given by the following equation [32]. This provides an unique route for the spin induced ferroelectricity.

$$P = \sum_i \alpha(-1)^i S_i \cdot S_{i+1}$$

The multiferroicity originating from the exchange striction does not require the relativistic spin-orbit interaction. It was theoretically explained by I. A. Sergienko, C. ¸Sen, E. Dagotto [33]. When the spin sites arranged with alternating A–B-type stacking as up–up–down–down sequence, the electric polarization should be induced via the exchange striction [32, 34]. This typical up-up-down-down spin arrangement in a spin chain occurs due to the presence of competing nearest-neighbor ferromagnetic (J_F) and next-nearest-neighbor antiferromagnetic (J_{AF}) interactions when the ratio of these two interactions is $|J_F/J_{AF}| > ½$ [34]. If $¼ < |J_F/J_{AF}| < ½$, a spiral magnetic ground state is favorable which will be discussed in the next section [34]. A prototypical example is $Ca_3Co_{2-x}Mn_xO_6$ ($x \approx 0 .96$) which crystallizes in a centrosymmetric structure ($R\bar{3}c$) where Co^{2+} and Mn^{4+} ions order alternatively and possess up-up-down-down spin order below its antiferromagnetic ordering ($T_N \sim 16.5$ K). Thus electric polarization occurs along the chain axis due to exchange interaction (shown in Figure 1.5) [35].

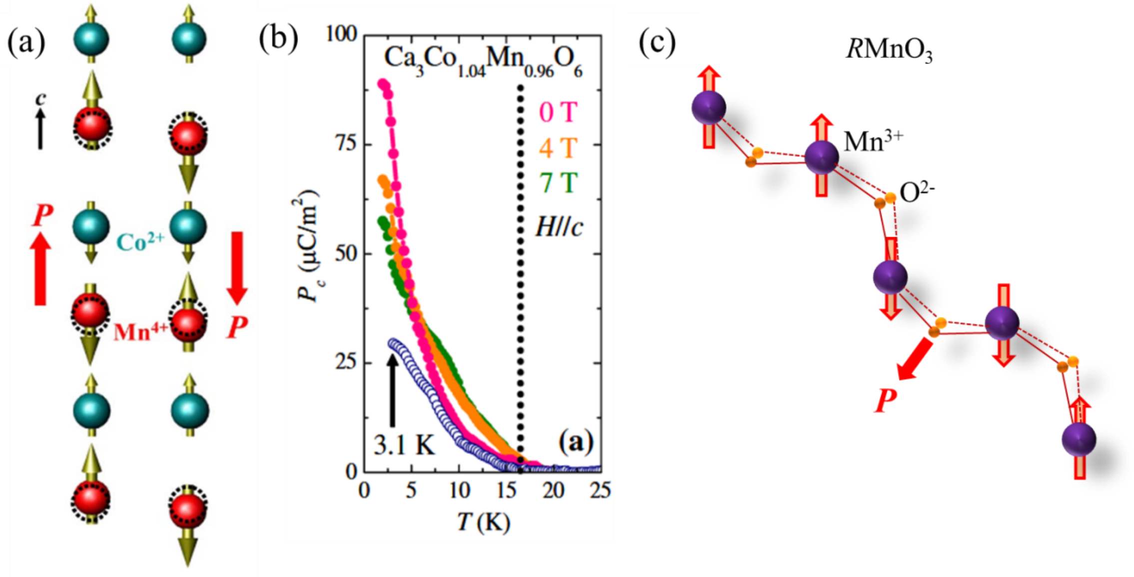

Figure 1.5 (a) Chains of up-up-down-down spin order and alternating charge ordering in $Ca_3Co_{2-x}Mn_xO_6$ ($x \approx 0.96$). Electric polarization induced along the chain through symmetric exchange striction. (b) Polarization measured in single crystal along chain direction ($P \parallel c$) (adapted with permission from ref. [35], © (2008) by the American Physical Society). (c) Up-up-down-down zigzag chain in orthorhombic $RMnO_3$ (R = Ho to Lu) and polarization direction.

Another scenario for this mechanism is when the M–X–M bond (M is the transition metal ion and X is the ligand ion) is arranged in zigzag fashion, and the spin forms up–up–down–down sequence. For example, orthorhombic $RMnO_3$ (R = Ho to Lu) perovskite stabilized under high pressure, where Mn–O–Mn networks along the orthorhombic *b*-axis are of zigzag type, shows the displacements of the bridging oxygen ion and produces net electric polarization along the *a*–axis (figure 1.5(c)). This magnetic structure is known as *E*-type AF, and the exchange-striction induced polarization can be up to 5000 μC/m^2 which is relatively much larger compared to other spin induced polarization as will be discussed in the following sections [33].

Besides, a prototypical exchange-striction induced multiferroic material is rare-earth mixed-valence manganese oxide family, RMn$_2$O$_5$. These compounds possess an orthorhombic *Pbam* structure where the Mn^{4+}O$_6$ octahedra form edge-sharing chains along the *c*-axis, connected by pairs of Mn^{3+}O$_5$ pyramids. The zigzag AF chains in the commensurate magnetic phase containing almost collinearly arranged Mn^{4+} and Mn^{3+} spins in the *ab* plane holds exchange-striction mechanism and produces ferroelectric polarization along *b*-axis below the magnetic ordering temperature. However, there exists another contribution of spin-induced polarization which is a spin-current model since this material has incommensurate cycloidal magnetic structure at a lower temperature. The exchange interaction in the orthoferrite (RFeO$_3$, R = Gd, Tb and Dy) between the R(4f) moment and Fe(3d) spins also induces a displacive type ferroelectric transition below the R magnetic ordering at low temperature [36, 37]. It is important to mention that the magnetic structure should be commensurate with the crystal structure for the exchange interaction induced electric polarization. Since we will be presenting the multiferroic properties in some rare-earth manganites, we have briefly discussed the phase diagram of rare earth manganites in the following section.

1.4.2.2 Spin-current or inverse DM interaction mechanism

In this case, the polarization is induced under the influence of spin-orbit interaction (SOI) in specific non-collinear spin structure. For antisymmetric exchange interaction, the spin current can be viewed as flowing between the canted spin sites S_i and S_j. This model was first proposed by Katsura and Nagosa [38]. Two non-collinear spins coupled by the exchange interaction lead to the spin current between the sites *i* and *j*, and induce the electric polarization (P) as given by,

$$P = \eta e_{ij} \times (S_i \times S_j)$$

where e_{ij} being a unit vector connecting two sites and η is a coupling constant proportional to the SOI in the weak coupling case (figure 1.6). This term is often called the inverse Dzyaloshinskii–Moriya (DM) interaction, in which the intervening ligand atom can displace [39] which can be understood in the following way, the DM interaction tries to make the spin more canted where as the inverse DM interaction is the crystal response against the DM interaction which leads to the distortion e.g. displace the ligand from its center of inversion thus balance the magnetic frustration and a macroscopic polarization appears.

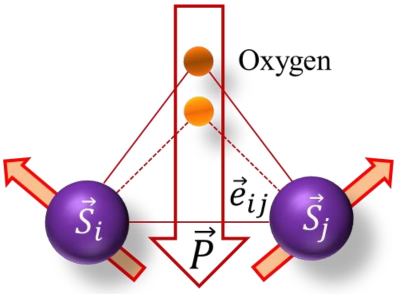

Figure 1.6 Shift of oxygen atom due to inverse DM interaction and induced polarization.

This spin-current model has been a very useful mechanism in recent studies of multiferroics since the spiral or cycloidal and transverse-conical spin orders, are most common in the spin-driven multiferroics which produce spontaneous *P* irrespective of magnetic modulation vectors, namely commensurate or incommensurate. In the earlier case, symmetric exchange interaction requires a commensurate spin structure. In figure. 1.7(a) various non-collinear spin structure along with the polarization direction is drawn based on the inverse DM interaction model.

The strong magnetoelectric coupling in multiferroic was first experimentally observed in orthorhombic perovskite manganites $R\text{MnO}_3$ (R = Tb, Dy, $\text{Eu}_{1-x}\text{Y}_x$) which show spiral/cycloidal magnetic ground state. The origin of spiral spin order is due to the frustrated magnetic interaction of nearest-neighbor (J_{FM}) ferromagnetic and next-nearest-neighbor (J_{AFM}) anti-ferromagnetic in the *ab* plane due to the smaller size rare-earth ions as described in the previous section. In the case of TbMnO_3 or DyMnO_3, the compound first undergoes the collinear sinusoidal antiferromagnetic spin order with the magnetic *q* vector q_m = (0.25–0.45)b^* (in the *Pbnm* setting) as can be seen in the $R\text{MnO}_3$ phase diagram figure 1.8. With lowering temperature, it changes to the cycloidal (transverse-spiral) spin order with the spin moments lying within the *bc* plane. This spin structure induces the electric polarization along *c*-axis according to the spin-current model. The sign of polarization or equivalently the spin helicity (rotation sense S_i x S_j) can be controlled by the direction of the electric field E during the poling process. The magnetism induced electric polarization in $TbMnO_3$ is shown in figure 1.7(e and f).

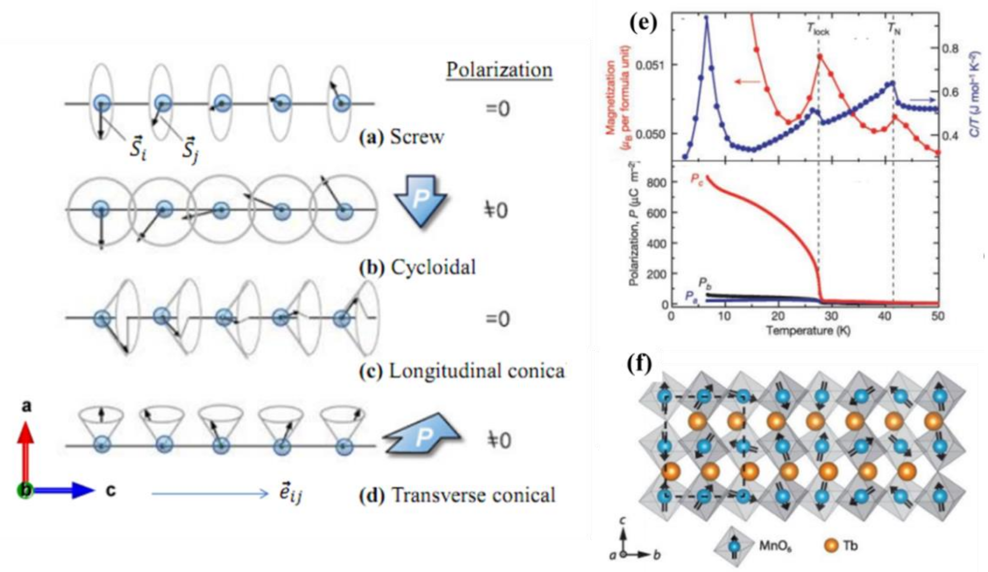

Figure 1.7 (a to d) Various types of non-collinear magnetic spin structure and the allowed electric polarization according to the inverse-DM interaction model (adapted from ref. [40], © (2009) by John Wiley and Sons. (e) Electric polarization below the magnetic ordering temperature T_{lock}. Adapted with permission from ref. © [41](2003) by the Nature Publishing Group). (f) Cycloidal magnetic structure of $TbMnO_3$ (adapted from Ref. [42], © (2014) by the AAAS).

The spin induced multiferroicity based on the cycloidal (transverse spiral) spin ordering has been observed in several materials such as $Ni_3V_2O_8$ [43], $LiCu_2O_2$ [44, 45], CuO [46] and $MnWO_4$ [47, 48]. Appart from the cycloidal ordering, the polarization can occurr in the transverse conical spin structure for example in $CoCr_2O_4$ and certain hexaferrites. For the comparison to other spin induced multiferroics, the schematic picture of the spin-current model is shown in figure 1.9(d-f) which is taken from ref. [32].

1.4.2.2.1 Phase diagram of *R*MnO_3

Rare-earth manganites *R*MnO_3 have very rich phase diagram based on both crystal and magnetic spin structure. Perovskite *R*MnO_3 adopts an orthorhombic perovskite structure for the higher size rare-earth ions (*R*= La-Dy) and hexagonal structure for small rare-earth ions (Ho-Lu and Y) under ambient pressure. The orthorhombic structure crystallizes in *Pbnm* space group while the hexagonal structure favors polar $P6_3cm$ polar space group which is Type-I multiferroic as mentioned above. However, under high pressure, the hexagonal phase can go to the orthorhombic perovskite structure. The structure of the orthorhombic manganites deviates from that of the ideal cubic perovskite structure due to mainly two factors. First one is so-called $GdFeO_3$ distortion through tilting of the MnO_6 octahedra and another one is Jahn-Teller (JT) distortion in which the octahedra themselves are deformed. The main driving force of $GdFeO_3$ type distortion is the ratio of A-site and B-site cation size i.e the Goldschmidt tolerance factor $\tau = \frac{R_A+R_O}{\sqrt{2}(R_B+R_O)}$.

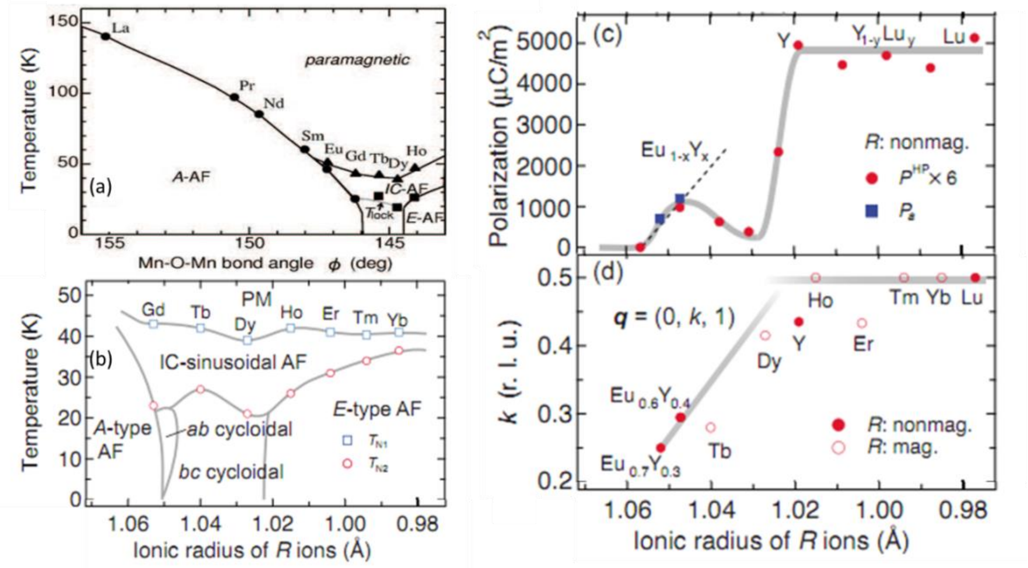

Figure 1.8 (a) magnetic ordering temperatures and Mn-O-Mn bond angle phase diagram of $RMnO_3$. Mn-O-Mn bond angle varies with the size of rare-earth ions. A more $GdFeO_3$ distortion occurs with the lower size of rare-earth ions thus the bond angle decreases. Along with the bond angles, the FM and AFM interaction strength also varies according to the Goodenough-Kanamori rule. Adapted from ref. [49]. (b) Various magnetic ordering phases in different rare-earth manganite with the rare-earth ionic radius. (c) Electric polarization corresponding to the various magnetic ordering depending on the rare-earth ionic radius. (d) Corresponding magnetic propagation vector q = (0, k ,1) of the rare-earth manganites. Adapted from ref. [50].

The $GdFeO_3$ distortion is generated in order to compensate the small rare-earth cations ionic radius; hence the distortion increases with decreasing the rare-earth ionic radii. The amount of $GdFeO_3$ distortion can be evaluated by the average Mn-O-Mn bond angle [49, 51, 52]. The John-Teller distortion comes from the orbital degeneracy of the $Mn^{3+}(d^4)$ cation in an octahedral crystal field. In order to overcome the orbital degeneracy, the octahedra have a tendency to distort the structure through shifts of the oxygen ions. Depending on the Mn-O-Mn bond angle, the Mn^{3+} spins order antiferromagnetically at different temperatures. Figure 1.8 shows the phase diagram of antiferromagnetic ordering temperature of $RMnO_3$ as a function of Mn-O-Mn bond angle.

The antiferromagnetic ordering has several magnetic ground states depending on the nearest-neighbor (NN) and next-nearest-neighbor (NNN) magnetic interaction in the *ab* plane. For the large ionic radius rare-earths (La to Sm), there is a strong ferromagnetic (FM) coupling between NN Mn-spins (J_F) in the *ab* plane and weak antiferromagnetic (AF) coupling (J_{AF}) along the *c*-axis, which corresponds to the so-called *A*-type AF structure. For small ionic radius, the NNN AF interaction increases in the *ab* plane in addition to the NN FM interaction due to more octahedral tilting. Thus *A*-type ordering vanishes and an incommensurate, sinusoidal structure appears below ~ 40 K for *R*= Tb and Dy. With the lowering of temperatures the interaction ratio (J_F/ J_{AF}) further increases and a spiral spin configuration with a commensurate propagation vector (0, q^{Mn}, 0) arises below a so-called lock-in temperature (T_{lock}) where the ferroelectricity occurs which is discussed in the previous section [49, 53]. With the further lower size of *R*-ions (Ho-Lu and Y), it undergoes *E*-type AF structure below the T_{lock}, where the spin order as up-up-down-down along a zig-zag chain and induces the ferroelectric polarization through symmetric exchange striction as mentioned in the last section [33, 54]. Since in our thesis we will be dealing with manganite multiferroics, we have shown various competitive magnetic states such as *A*-type AFM, cycloidal spin ordering lying in *ab* or *bc* plane, *E*-type magnetic ordering and incommensurate sinusoidal magnetic ordering in *O*-RMnO$_3$ in figure 1.8(b). Figure 1.8(c) shows the electric polarization corresponding to the particular magnetic ordering. Figure 1.8(d) shows the k-vector of the corresponding manganites.

1.4.2.3 *p–d* hybridization

This mechanism requires a specific lattice structure in addition to the SOC effect. A local polar bond arises between the transition metal and ligand depending on the transition metal spin direction. However, the modulation of the local polarization cancels out macroscopically in most of the cases. When the sum over the crystal lattice sites does not entirely cancel out, a macroscopic polarization appears. The longitudinal component of *P* for a pair of *M* (metal) and *L* (ligand) is expressed as

$$\vec{P}^{pd} \propto (\vec{S} \cdot \vec{e})^2 \vec{e}$$

with $\vec{e}$ being the vector from a transition metal to ligand [55].

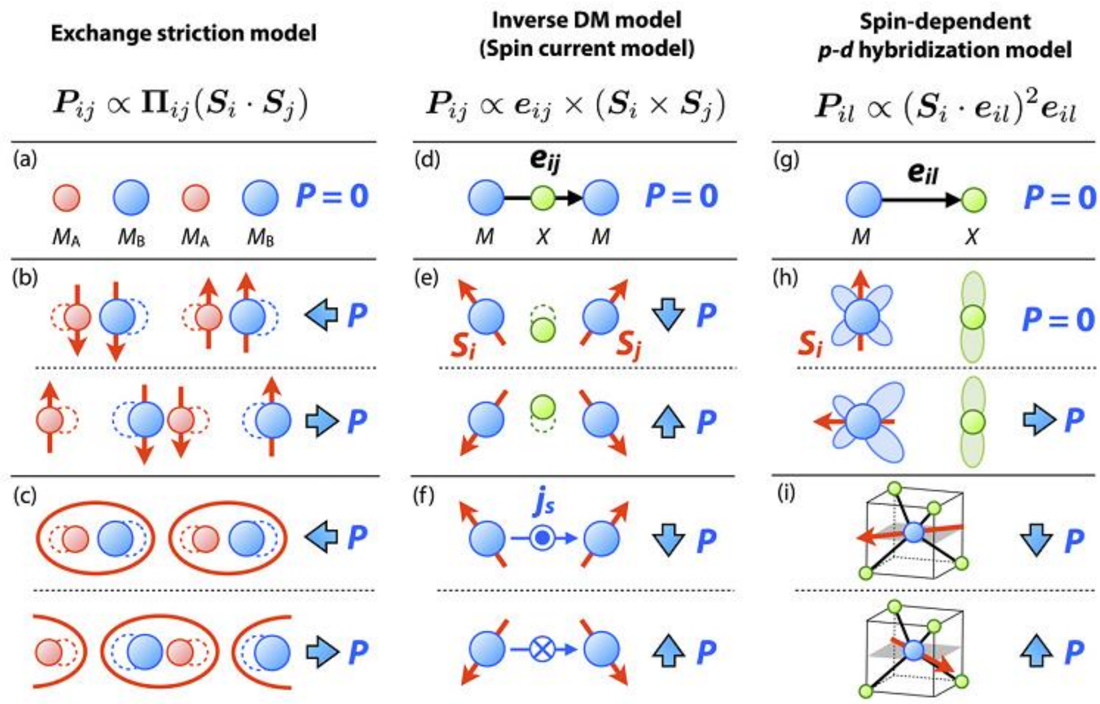

Figure 1.9 Schematic representation of various mechanism of spin-induced multiferroics. (a)-(c) shows exchange-striction model based multiferroicity. S_i and S_j represent the spin orientations at each magnetic site. (a) different charges are ordered without any spin. (b) spins arranged in down-down-up-up fashion thus atoms are shifted from the center position and induces polarization along the bond direction. (c) dimer-singlet formation; (d)–(f) spin-current model arising from the antisymmetric spin exchange interaction or inverse DM model, e_i is the unit vector connecting the adjacent spins (d) M –X –M clusters, P appears zero according to the equation. (e) a shift of ligand to maximize the energy gain by DM interaction producing polarization (f) an effective electric field caused by spin current j_s (with spin polarization $S_i \times S_j$ flowing between two magnetic sites producing the polarization; and (g)–(i) spin-dependent *p–d* hybridization mechanism due to the relativistic SOC. Here the M and X indicate magnetic and ligand ions, respectively. e_{il} is the unit vector connecting the M and X. (g) The spin-dependent *p–d* hybridization model considering a single pair of M and X sites and local P is induced along the bond direction. (h) the spin-dependent modulation of covalency between the magnetic *d* orbital and ligand *p* orbital. (i) for some appropriate crystallographic lattice MX_4 tetrahedra which can avoid cancellation and cause macroscopic P. (Adapted from ref. [32], © (2014) IOP Publishing)

The realization of this spin-dependent *p–d* hybridization model was first demonstrated in the triangular lattice antiferromagnets [56]. Based on this mechanism the ferroelectricity was observed in layered triangular lattice, e.g. delafossite and CdI_2 structure which consists of a layer of transition metal ions (M) sandwiched by layers of ligand anions (oxygen or halogen; X = Cl , Br, I). Considering the proper screw structure of transition metal spins in a layer, the two-fold rotational symmetry perpendicular to the screw axis can be broken due to *p-d* hybridization thus a polarization occurs. For example, $CuFeO_2$ shows a proper screw magnetic structure with incommensurate $q\sim0.21$ for $7\ \mathrm{T} < H_c < 12$

T below T_N (11 K) and polarization was confirmed in this screw magnetic phase [57, 58]. The appearance of polarization in the 120° magnetic phase is reported for delafossite $ACrO_2$ (A = Cu, Ag) with easy-axis anisotropy and in $RbFe(MoO_4)_2$ with easy-plane anisotropy [59, 60]. We have presented a *p-d* hybridization mechanism based multiferroicity in a mineral $MnSb_2S_4$, in chapter 6 where we have discussed the *p-d* hybridization mechanism in more detailed. The figure 1.9(g-i) shows the schematic picture of *p-d* hybridization induced polarization. Various spin induced multiferroics based on the three different model is given in table 1.2 taken mainly from a review [32].

Table 1.2 List of prototype spin induced multiferroics based on the three mechanisms.

Mechanism	Magnetic order	Compound	Ref
Spin current	Cycloidal	$RMnO_3$ (R = Tb, Dy)	[41]
		$LiCu_2O_2$	[45]
		$Ni_3V_2O_8$	[43]
		$MnWO_4$	[47, 48]
		$CuCl_2$, $CuBr_2$	[61]
		CuO	[46]
	H-induced conical	$CoCr_2O_4$, $ZnCr_2Se_4$	[62]
		$Ba_{0.5}Sr_{1.5}Zn_2Fe_{12}O_{22}$	[63]
Exchange striction	Collinear antiferromagnetic	RMn_2O_5	[64]
		O-$RMnO_3$ (R = Ho-Lu)	[33, 54]
		Ca_3CoMnO_6	[35]
	Weak ferromagnetic	$GdFeO_3$, $DyFeO_3$	[37, 65]
p-d hybridization	Proper screw	$CuFeO_2$, MnI_2, NiI_2	[58, 66, 67]
	120°	$CuCrO_2$, $AgCrO_2$	[59]
		$RbFe(MoO_4)_2$	[60]
	Collinear antiferromagnetic	$RFe_3(BO_3)_4$	[68]
	Skyrmion	Cu_2OSeO_3	[69]

1.5 Difficulties of finding intrinsic multiferroics

Finding intrinsic ferroelectric signature is one of the major challenges in the field of multiferroics study. It is mainly because the multiferroics containing magnetic ions has *d*- orbital electrons, mostly are not good insulators. They are more conductive in nature due to several conduction mechanisms such as electronic conduction, hopping conduction, variable-range hopping or Mott variable-range hopping with localized charge carrier states. In general there are mainly two methods in measuring the ferroelectric polarization. In first case, polarization *vs.* electric field loop is recorded. This requires a very good insulating sample and a sufficient amount of electric polarization to detect. Another way is to record pyroelectric current while heating the sample across the ferroelectric ordering after poling the sample with electric field. It is necessary to polarize the sample across the ferroelectric transition. Finally, the polarization can be calculated through integrating the current with time. In most of the magnetic origin (Type-II) multiferroic, this is the feasible way of detecting the polarization since the value of polarization is lower in such cases and occurs at low temperature. However in literature, there are many cases where the pyrocurrent interpretation is made erroneously. There can be many factors influencing the polarization such as thermally stimulated free charge carriers (TSFC). In chapter 3, we have introduced all such intricacy and shown a different method in order to determining a true ferroelectric signature.

1.6 Scope of the thesis

Although study on multiferroics have been pursued more than a decade, the challenges towards achieving right materials for the technological application and the understanding of complex magnetic structure and related mechanisms of multiferroics is quite far. In this thesis, we have studied way out to overcome some challenges of determining an intrinsic ferroelectric polarization in magnetic spin-driven multiferroics. Subsequently, we have studied some mixed rare-earth manganite multiferroics where we found various magnetic ground-state spin structures evolving at low temperature through the competing magnetic interactions. The electric polarization developments associated with the magnetic structures are intriguing. Further, we have worked on doubly ordered perovskite materials with chemical formula $AA'BB'O_6$, which was promising multiferroics based on theoretical calculation and crystal structure determination and we found the polar signature using high pressure synthesis technique on the lower size rare-earth ions at the A'-site. We have achieved good piezoelectric property with the doping of Al at Fe site using high pressure synthesis technique in the $BiFeO_3$ multiferroics. Also we have found spin induced multiferroicity in a non-oxide mineral called Clerite ($MnSb_2S_4$) which we explained through *d-p* hybridization. In addition, we have worked out the ground state magnetism of a frustrated spinel system $CoAl_2O_4$ through finding magnetoelectric effect in the good quality single crystal grown using floating zone furnace.

References

[1] P. Curie, Journal de physique théorique et appliquée **3**, 393 (1894).

[2] L. Landau and E. Lifshitz, English edition: Pergamon Press, Oxford (1960).

[3] I. Dzyaloshinskii, Soviet Physics JETP **10**, 628 (1960).

[4] D. Astrov, Sov. Phys. JETP **11**, 708 (1960).

[5] G. Rado and V. Folen, Phys. Rev. Lett. **7**, 310 (1961).

[6] H. Schmid, Ferroelectrics **162**, 317 (1994).

[7] C. Giacovazzo, Fundamentals of crystallography (Oxford university press, USA, 2000).

[8] K. Siratori, K. Kohn, and E. Kita, Acta Physica Polonica A **81**, 431 (1992).

[9] R. Saha, S. Ghara, E. Suard, D. H. Jang, K. H. Kim, N. Ter-Oganessian, and A. Sundaresan, Phys. Rev. B **94**, 014428 (2016).

[10] K. Siratori, E. Kita, G. Kaji, A. Tasaki, S. Kimura, I. Shindo, and K. Kohn, Journal of the Physical Society of Japan **47**, 1779 (1979).

[11] M. Clin, J.-P. Rivera, and H. Schmid, Ferroelectrics **108**, 207 (1990).

[12] A. N. Christensen and S. Quezel, Solid State Commun. **10**, 765 (1972).

[13] M. Haida, K. Kohn, and J. Kobayashi, Journal of the Physical Society of Japan **39**, 1625 (1975).

[14] J.-P. Rivera, H. Schmid, J.-M. Moret, and H. Bill, J. Magn. Magn. Mater. **6**, 211 (1974).

[15] D. Astrov, Sov. Phys. JETP **13**, 729 (1961).

[16] G. T. Rado, Phys. Rev. Lett. **23**, 644 (1969).

[17] N. A. Hill, (ACS Publications, 2000).

[18] N. Waterfield Price, R. D. Johnson, W. Saenrang, A. Bombardi, F. P. Chmiel, C. B. Eom, and P. G. Radaelli, Phys. Rev. Appl **8**, 014033 (2017).

[19] D. Lebeugle, D. Colson, A. Forget, and M. Viret, App. Phys. Lett. **91**, 022907 (2007).

[20] B. B. Van Aken, T. T. Palstra, A. Filippetti, and N. A. Spaldin, Nat. Mater **3**, 164 (2004).

[21] D. Khomskii, Physics **2**, 20 (2009).

[22] C. Ederer and N. A. Spaldin, Phys. Rev. B **74**, 024102 (2006).

[23] G. Smolenskiĭ and I. Chupis, Soviet Physics Uspekhi **25**, 475 (1982).

[24] M. J. Pitcher, P. Mandal, M. S. Dyer, J. Alaria, P. Borisov, H. Niu, J. B. Claridge, and M. J. Rosseinsky, Science **347**, 420 (2015).

[25] P. Mandal, M. Pitcher, J. Alaria, H. Niu, P. Borisov, P. Stamenov, J. Claridge, and M. Rosseinsky, nature **525**, 363 (2015).

[26] T. Nozaki *et al.*, Nat. Phys. **8**, 491 (2012).

[27] S. Valencia *et al.*, Nat. Mater **10**, 753 (2011).

[28] A. Mardana, S. Ducharme, and S. Adenwalla, Nano lett. **11**, 3862 (2011).

[29] M. Liu *et al.*, Advanced Functional Materials **19**, 1826 (2009).

[30] C. Vaz, J. Hoffman, Y. Segal, J. Reiner, R. Grober, Z. Zhang, C. Ahn, and F. Walker, Phys. Rev. Lett. **104**, 127202 (2010).

[31] J. Heron *et al.*, Phys. Rev. Lett. **107**, 217202 (2011).

[32] Y. Tokura, S. Seki, and N. Nagaosa, Rep. Prog. Phys **77**, 076501 (2014).

[33] I. A. Sergienko, C. Şen, and E. Dagotto, Phys. Rev. Lett. **97**, 227204 (2006).

[34] S.-W. Cheong and M. Mostovoy, Nat. Mater **6**, 13 (2007).

[35] Y. Choi, H. Yi, S. Lee, Q. Huang, V. Kiryukhin, and S.-W. Cheong, Phys. Rev. Lett. **100**, 047601 (2008).

[36] Y. Tokunaga, Y. Taguchi, T.-h. Arima, and Y. Tokura, Nat. Phys. **8**, 838 (2012).

[37] Y. Tokunaga, S. Iguchi, T. Arima, and Y. Tokura, Phys. Rev. Lett. **101**, 097205 (2008).

[38] H. Katsura, N. Nagaosa, and A. V. Balatsky, Phys. Rev. Lett. **95**, 057205 (2005).

[39] M. Mostovoy, Phys. Rev. Lett. **96**, 067601 (2006).

[40] Y. Tokura and S. Seki, Adv. Mater. **22**, 1554 (2010).

[41] T. Kimura, T. Goto, H. Shintani, K. Ishizaka, T.-h. Arima, and Y. Tokura, nature **426**, 55 (2003).

[42] T. Kubacka *et al.*, Science, 1242862 (2014).

[43] G. Lawes *et al.*, Phys. Rev. Lett. **95**, 087205 (2005).

[44] S. Park, Y. Choi, C. Zhang, and S. Cheong, Phys. Rev. Lett. **98**, 057601 (2007).

[45] S. Seki, Y. Yamasaki, M. Soda, M. Matsuura, K. Hirota, and Y. Tokura, Phys. Rev. Lett. **100**, 127201 (2008).

[46] T. Kimura, Y. Sekio, H. Nakamura, T. Siegrist, and A. Ramirez, Nat. Mater **7**, 291 (2008).

[47] K. Taniguchi, N. Abe, T. Takenobu, Y. Iwasa, and T. Arima, Phys. Rev. Lett. **97**, 097203 (2006).

[48] A. Arkenbout, T. Palstra, T. Siegrist, and T. Kimura, Phys. Rev. B **74**, 184431 (2006).

[49] T. Kimura, S. Ishihara, H. Shintani, T. Arima, K. Takahashi, K. Ishizaka, and Y. Tokura, Phys. Rev. B **68**, 060403 (2003).

[50] S. Ishiwata, Y. Kaneko, Y. Tokunaga, Y. Taguchi, T.-h. Arima, and Y. Tokura, Phys. Rev. B **81**, 100411 (2010).

[51] J. Alonso, M. Martinez-Lope, M. Casais, and M. Fernandez-Diaz, Inorg. chem. **39**, 917 (2000).

[52] J.-S. Zhou and J. Goodenough, Phys. Rev. Lett. **96**, 247202 (2006).

[53] T. Kimura, G. Lawes, T. Goto, Y. Tokura, and A. Ramirez, Phys. Rev. B **71**, 224425 (2005).

[54] B. Lorenz, Y.-Q. Wang, and C.-W. Chu, Phys. Rev. B **76**, 104405 (2007).

[55] T.-h. Arima, Journal of the Physical Society of Japan **76**, 073702 (2007).

[56] M. Collins and O. Petrenko, Canadian journal of physics **75**, 605 (1997).

[57] T. Nakajima, S. Mitsuda, S. Kanetsuki, K. Prokes, A. Podlesnyak, H. Kimura, and Y. Noda, Journal of the Physical Society of Japan **76**, 043709 (2007).

[58] T. Kimura, J. Lashley, and A. Ramirez, Phys. Rev. B **73**, 220401 (2006).

[59] S. Seki, Y. Onose, and Y. Tokura, Phys. Rev. Lett. **101**, 067204 (2008).

[60] M. Kenzelmann *et al.*, Phys. Rev. Lett. **98**, 267205 (2007).

[61] S. Seki, T. Kurumaji, S. Ishiwata, H. Matsui, H. Murakawa, Y. Tokunaga, Y. Kaneko, T. Hasegawa, and Y. Tokura, Phys. Rev. B **82**, 064424 (2010).

[62] Y. Yamasaki, S. Miyasaka, Y. Kaneko, J.-P. He, T. Arima, and Y. Tokura, Phys. Rev. Lett. **96**, 207204 (2006).

[63] T. Kimura, G. Lawes, and A. Ramirez, Phys. Rev. Lett. **94**, 137201 (2005).

[64] N. Hur, S. Park, P. Sharma, J. Ahn, S. Guha, and S. Cheong, nature **429**, 392 (2004).

[65] Y. Tokunaga, N. Furukawa, H. Sakai, Y. Taguchi, T.-h. Arima, and Y. Tokura, Nat. Mater **8**, 558 (2009).

[66] T. Kurumaji, S. Seki, S. Ishiwata, H. Murakawa, Y. Tokunaga, Y. Kaneko, and Y. Tokura, Phys. Rev. Lett. **106**, 167206 (2011).

[67] T. Kurumaji, S. Seki, S. Ishiwata, H. Murakawa, Y. Kaneko, and Y. Tokura, Phys. Rev. B **87**, 014429 (2013).

[68] T. Kurumaji, K. Ohgushi, and Y. Tokura, Phys. Rev. B **89**, 195126 (2014).

[69] S. Seki, X. Yu, S. Ishiwata, and Y. Tokura, Science **336**, 198 (2012).

Chapter 2

Experimental techniques

Summary

This chapter deals with a brief description of the various synthetic procedure carried out in the thesis. It also describes with the experimental setup and the basic operation principles used for various structural and physical properties of the materials investigated.

2.1 Introduction

In the present work, we have synthesized different types of multiferroic perovskite, double perovskite, spinel and some other materials mainly in powder form, and in some cases single crystal form. This chapter describes the experimental techniques used for the synthesis of powder as well as single crystal using floating zone furnace and characterization using powder X-ray as well neutron diffraction technique. It also describes all the measurement technique of magnetic, electric and spectroscopic properties which we have used in the thesis.

2.2 Sample Preparation

2.2.1 Powder sample

Conventional solid-state reaction route is a well-established technique for the preparation of bulk ceramic materials [1]. This technique is known for its versatility in the synthesis of various types of oxides as well as other ceramics. Ceramic materials possess relatively high melting point and hence can be prepared at very high temperatures. The solid-state reaction method depends on the inter-diffusion between the ions and therefore it is necessary to use fine reactants powders. The important factor in this reaction mechanism is the diffusion coefficient (D), which is given by the Fick’s law [2],

$$J = -D\frac{d\varphi}{dx}$$

where J is the flux of diffusing elements and $\frac{d\varphi}{dx}$ is the concentration gradient at the reaction interface. The diffusion coefficient (D) depends on the temperature of the reaction. The reaction temperatures are usually kept as high as 500°C to 1500°C, in order to maximize the difussion length, and the reaction would occur at an appreciable rate. The thermodynamic factor is also important for the solid state reaction. It decides whether or not a particular reaction should happen according to the change in free energy involved in the reaction. Apart from the commercially available muffle furnace and tubular furnaces (maximum temperature up to 1500 °C), two tubular furnaces fabricated by us which were able to heat up to 1150 °C, were used for the solid state synthesis reactions. A more detailed destription on the fabrication is given in the last section of this chapter.

2.2.2 High-pressure solid-state reaction

For the solid-state reaction, sometimes, only the high temperature is not an enough condition to stabilize the required phase of the materials. Applying pressure in addition to the high temperature helps to synthesize some materials. We have used cubic anvil type high-pressure apparatus where we could apply up to 4.5 GPa pressure for synthesizing several materials investigated here. The apparatus consists of mainly three parts; pressurizing unit where we have six identical cubic anvils made of tungsten carbide placed into the die, one pressure controlling unit and one temperature controlling unit (see figure 2.1).

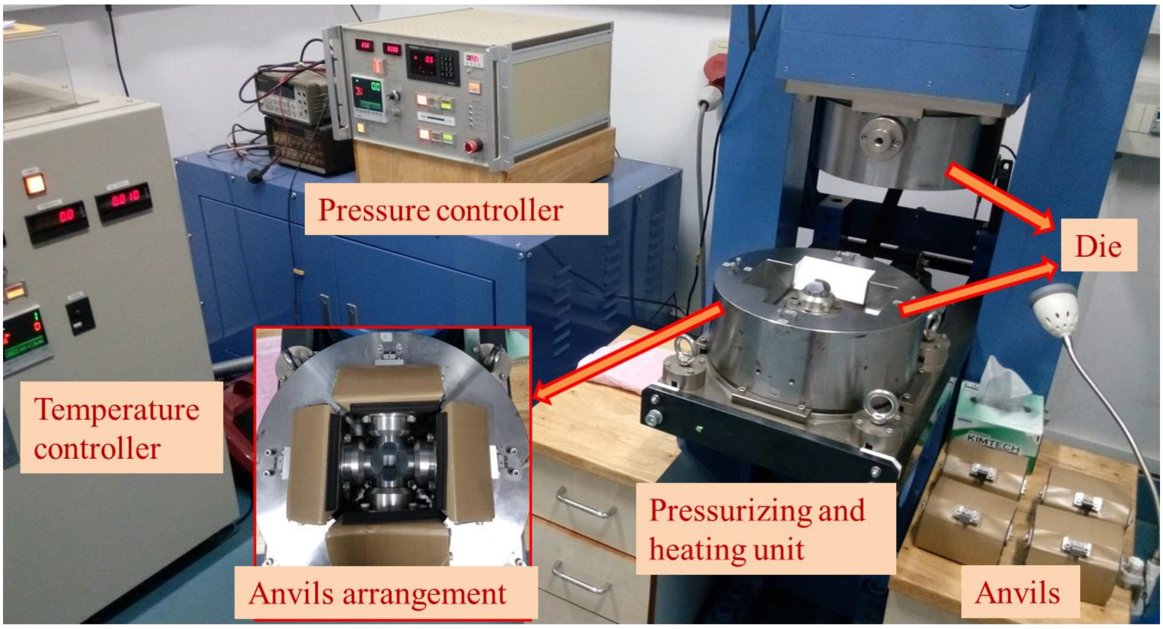

Figure 2.1 High-pressure apparatus showing its various controlling units, pressurizing and heating unit, and anvils arrangement in the die.

To prepare the sample, at first we need to make a thoroughly grounded mixture of the ingredients of a total amount of approximately 300 to 400 mg. We can choose either gold capsule or we can prepare BN capsule and sleeve to place the precursor in a cylindrical shape. The sample assembly will be then covered with another sleeve and pellet made of (80%)NaCl+(20%)ZrO_2. The whole assembly will then be kept into a cylindrical graphite heater and will be inserted into the pyrophyllite stone. Molybdenum top and bottom electrodes are used for the electrical conduction. Figure 2.2 shows the complete sample cell assembly. The pyrophyllite stone is heated at 700 °C before the use for high pressure. The whole cell assembly is kept inside the cubic anvils with proper alignment so that the compression limit of the pyrophyllite reaches uniformly for all the six anvils. The pressure can be increased slowly to the required amount (≤ 4.5 GPa). Once the pressure is stabilized, the temperature is increased slowly from the temperature controller unit up to 1000 °C and can be kept for dwelling for the sample reaction. Finally, the temperature can be either quenched by switching off the heating in order to arrest the high-pressure metal stable phase or can be cooled down to room temperature slowly. Once the temperature reaches room temperature, the pressure is released slowly to the ambient condition and the sample is taken out. Since at high pressure, the reaction rate is higher, we kept the dwelling time for a maximum of one hour for all the sample preparation. Caution and care are necessary for all the steps involved in this technique. Since there is no direct in-situ measuring thermocouple at the sample cell, we had performed a test of reaction in the pyrophyllite where we inserted the thermocouple manually and recorded the temperature with respect to the heater power supplied from the temperature controller unit. From this calibration curve, we choose the required power for any temperature. We performed a similar test for the pressure calibration using Bi-metal resistance measurement with pressure. A pressure-induced transition occurs at 2.5 GPa in Bi, where a resistivity change can be recorded.

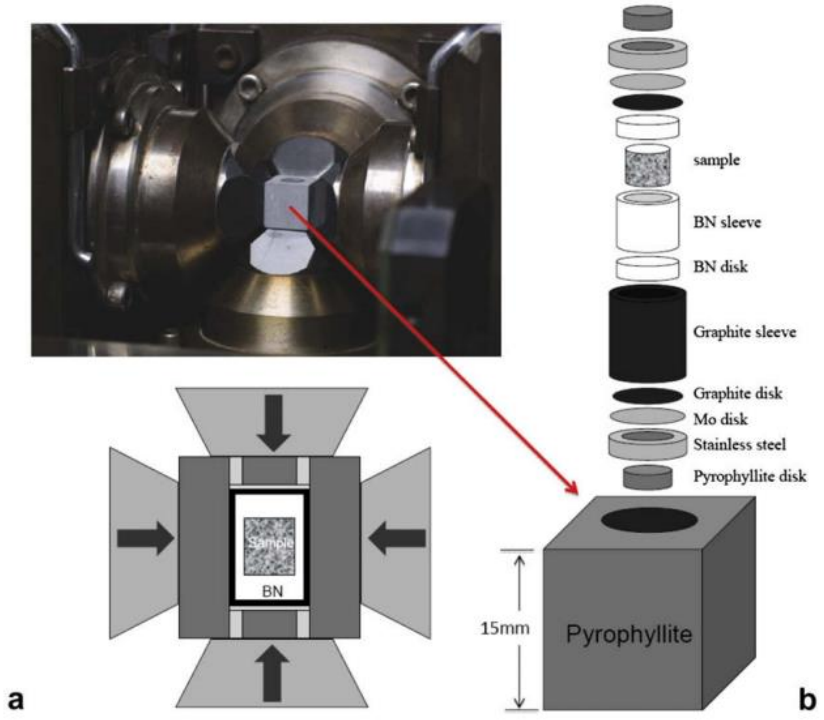

Figure 2.2 (a) Top image of cubic type anvils in the high pressure apparatus. Bottom, sample attachment with the anvils (side view). (b) Pyrophyllite cell assembly containing sample and various additive components. (adapted from Ref. [3])

2.2.3 Single crystal growth

Single crystal growth generally involves melting and controlled solidification of the melt for the nucleation and growth. The materials presented here possess very high melting points higher than 1800 °C. Optical Float Zone method is employed for the growth of single crystals as it can provide a large crystal size and crucible free high-temperature growth (figure 2.3(a)). In this method, we need to make first a pure powder form of the required sample. The important thing in this method of crystal growth is to find out the melting temperature of the sample and whether it melts congruently or incongruently. If the powder sample melts uniformly without decomposing into another phases, is called congruently melting. The sample grown in our study was melted congruently, therefore, we will be describing only this process.

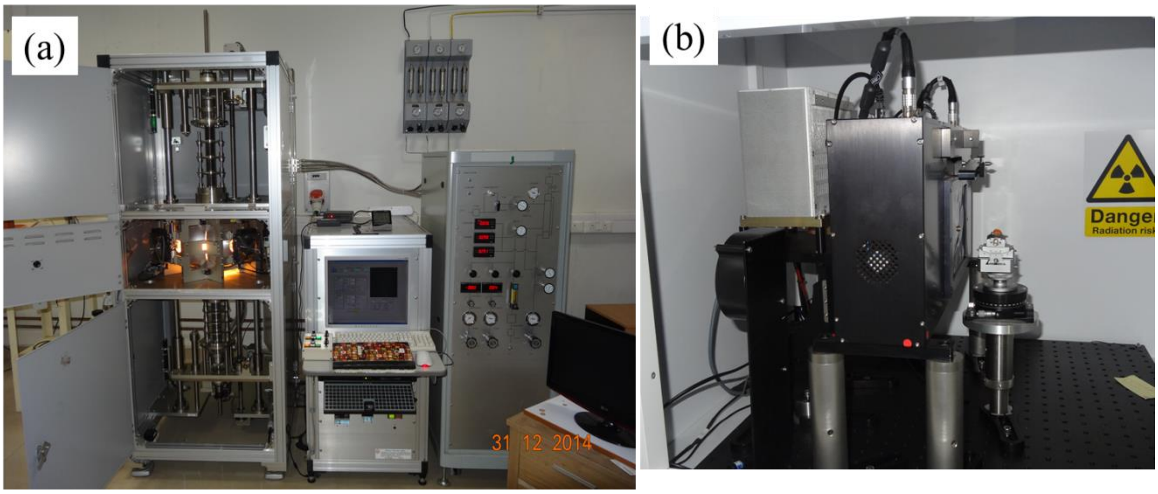

Figure 2.3 (a) Flouting zone image furnace. Left unit contains feed rod movement assembly, lamp-mirror-sample zone and seed rod movement assembly. Middle unit controls the sample movement, rotation and lamp power. Third unit controls the gas atmosphere and pressure. (b) Laue diffractometer for orienting the crystal.

2.2.3.1 Preparation of Ceramic Rods

For growth in the Optical float-zone furnace, polycrystalline ceramic rods are required. To prepare such ceramic rods, long silicon tubes are inserted in the custom-made pair of L-shape wand made of aluminum. The polycrystalline powder is filled in the silicon tube which is kept inside the pair of the wand and sample is packed evenly using a funnel and a small hammer. Once the packing is done (up to 5-8 cms), the holes are plugged with cotton and rubber cap. The whole assembly is transferred to hydrostatic press, and pressurized at 70 MPa. This procedure is essential to obtain uniform and dense rods. After pressurization, the rod is extracted from the silicon tube carefully using a glass rod and placed on a ceramic plate or boat and sintered at 1100 to 1400 °C for 18 hours. High density polycrystalline rods are thus obtained after sintering.

2.2.3.2 Optical Float-Zone Method

Figure 2.3 shows the four-mirror floating zone image furnace used for crystal growth. The furnace has four elliptical mirrors, each having two focal points in such a way that one focus is common to all four mirrors. At the other focus of each mirror, four halogen lamps with equal power are situated. This arrangement allows radiations from all the lamps to focus at the common focal point situated at the middle as shown in the figure 2.4 (a) and (b). At this point, temperatures as high as 2200 °C can be achieved depending on the lamp used. There are four different power rating lamps available and can be used as per the temperature requirements. The four mirror arrangement provides almost a circular distribution of the isothermal curve. It can be mentioned here that there is no direct measurement of temperature at the focal point using any thermocouple; however the lamp power actually determines the temperature. The polycrystalline sample rods as prepared previously are used as both feed (5-8 cm) and seed (3 cm) rods. The seed rod is fixed on a ceramic holder using nichrome wire. Feed rod is suspended by the same nichrome wires. The entire assembly is enclosed in a high-pressure quartz tube which facilitates maintaining different gas atmosphere capable with up to ~10 bar pressure. The ceramic ingots are melted as the lamp power is increased. When they form a convex shape the molted regions are brought closer and fused together. During the whole growth cycle, both feed and seed rods are rotated continuously in opposite directions. The volume of the molten region is maintained in such a way that the length of molten region is approximately equal to the diameter of the ceramic rod which allows better stability of the melting. After stabilizing the melt region, growth was proceeded by translation of the mirror-stage with a fixed rate typically 1 to 6 mm/h. The process is terminated when the end-position of the seed rod comes enough closer to the melting zone i.e. no more seed rod is left to melt. The lamp power is decreased quickly just below the melting power so that the melt zone is frozen. While doing so, the rotation of feed and seed rod is slowly brought to zero before freezing of the zone. Further, the lamp power is slowly reduced to zero and waited until the hot zones reach to room temperature. The sample was removed by opening the quartz tube. Typically, several growth runs are made before the parameters like growth rates, rotation speeds and ambience are optimized for good quality single crystals.

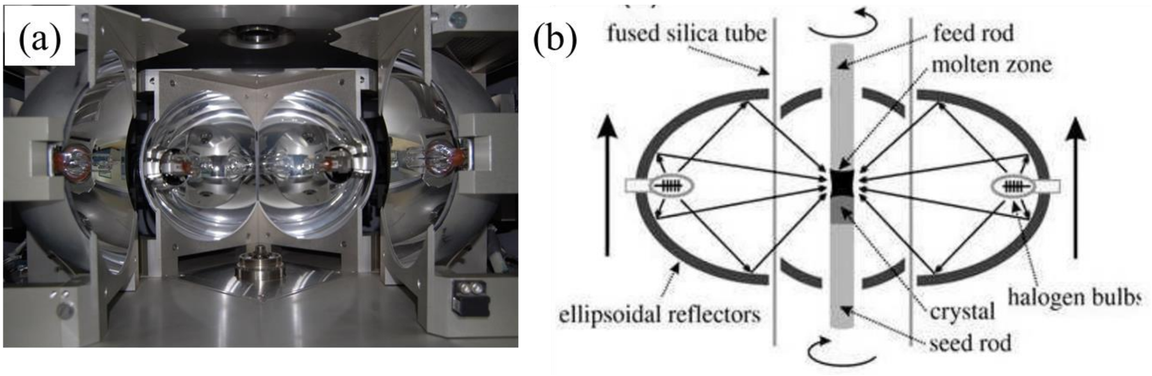

Figure 2.4 (a) Elliptical mirrors and lamp arrangement. (b) Optical path for the lamp and mirrors.

2.3 Sample Characterization

2.3.1 Powder X-ray and Neutron Diffraction

X-ray diffraction is the basic and widely used technique in the structural analysis since its discovery in 1925 by W. L Bragg. In all the samples investigated in the thesis, X-ray diffraction on powder samples were performed using a laboratory Bruker D8 Advance X-ray diffractometer and PANalytical Empyrean alpha-1 diffractometer (monochromatic $CuK\alpha_1$). The basic X-ray diffractometer parts consist mainly of an X-ray tube, a sample mounting stage and a detector. When X-rays falls on the powder sample, which consists of grains arranged randomly in all possible orientation, some of the X-rays will be scattered by the atoms of the first layer or plane (Figure 2.5), and the rest of the X-rays will pass through the first layer and will be scattered by the following layers. For this scattering to occur, the spacing between the atomic layers or crystallographic planes should be of the order of the wavelength of the incident X-ray beam. Constructive interference will happen only when these scattered rays coming from two different planes are in the same phase, and it will give a peak in the X-ray diffraction pattern. The constructive interference will occur with the Bragg's condition, $2d\ sin\theta = \lambda$, where d is the spacing between the consecutive crystallographic planes, λ is the wavelength of the X-rays, θ is the incident angle as shown in figure 2.5.

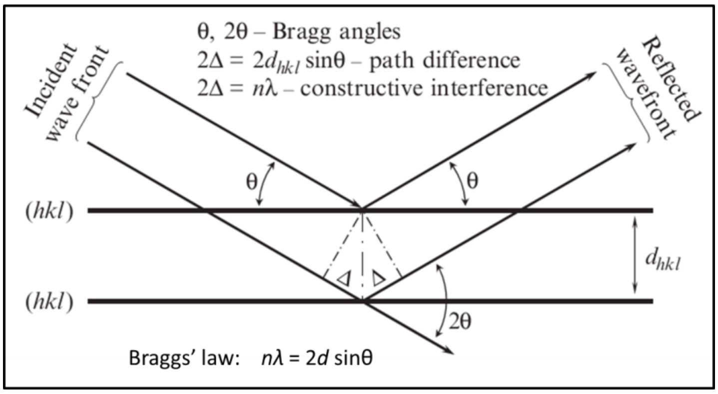

Figure 2.5 Schematic diagram of X-ray diffraction (Bragg's law); adapted from "Fundamentals of Powder Diffraction and Structural Characterization of Materials" book [4].

Thus, when Bragg's law is satisfied by some particular sets of planes, peaks will appear at certain 2θ positions and consequence as X-ray diffraction pattern of intensity versus 2θ, which are unique for different materials. Thus the distance between the planes is function of the lattice parameter and can be determined by analyzing the X-ray diffraction pattern. By analyzing the powder X-ray diffraction data using various tools, the complete crystal structure can be determined as will be described in the following section. The phase purity of a known compound can also be checked by comparing its X-ray diffraction data with the pattern available in various databases such as Inorganic Crystal Structure Database (ICSD). In the same way, the impurity phases also can be identified.

For some particular compounds, it may be difficult to index the peaks using the laboratory X-ray diffraction pattern due to the overlap of two or more close peaks. In such circumstances, the synchrotron X-ray diffraction experiments can resolve this issue, which has the ability to tune the wavelength. The synchrotron X-rays can also provide high intense peak with a better resolution due to the higher intensity of the synchrotron X-ray beams. Therefore, synchrotron X-ray pattern can be indexed accurately which can provide accurate structural parameters. Sometimes neutron diffraction experiment is necessary for the crystal structure determination when the compound contains some light elements such as oxygen, carbons, hydrogen, etc. The X-rays cannot detect the position of the light elements since X-ray scattering occurs by the electron cloud only. On the other hand, neutrons interact with the nucleus of the atom and can determine the position of the light elements more accurately. Further, since neutron possesses an intrinsic magnetic moment, it can interact with the moment of an atom in the compound and thus from neutron diffraction experiments one can obtain the magnetic structure. We have performed neutron diffraction experiments in WISH diffractometer at RAL, Didcot, UK. This neutron beam was appropriate for our experiments where we wanted to investigate the complex magnetic structure in Gd-160 isotope enriched $Gd_{0.5}Dy_{0.5}MnO_3$ sample.

2.3.2 Rietveld Refinement

The x-ray or neutron diffraction data can be treated using Rietveld refinement mathematical tools by which the complete structural parameters of the materials can be obtained [5, 6]. In this method, the recorded diffraction pattern is compared with a calculated pattern using few numbers of parameters. The intensity at each point of the experimental data (y_{io}) is compared with the corresponding calculated point (y_{ic}) in the model by minimizing a residual function S through the least square process. The calculated intensity at a point can be given by [7],

$$y_{ic} = S\sum_{k} m_k L_k |F_k|^2 G(\Delta\theta_{ik}) + y_{ib}$$

where S is the scale factor, m_k is the multiplicity factor, L_k is the Lorentz polarization factor for reflection k, F_k is the structure factor, $G(\Delta\theta_{ik})$ is the reflection profile function where $\Delta\theta_{ik} = 2\theta_i - 2\theta_k$ and $2\theta_k$ is the calculated position of the Bragg peak, y_{ib} is the background intensity.

The structure factor F_k can be written as,

$$F_{hkl} = \sum_{j=1}^{m} N_j f_j e^{2\pi i(hx_j+ky_j+lz_j)}$$

$$|f|^2 = e^{\frac{-Bsin^2\theta}{\lambda^2}}$$

Where *f* is the atomic form factor and *B* is the Debye-Waller temperature factor.

The residual function *S* is given by the following equation [5],

$$S = \sum_{i} W_i |y_{io} - y_{ic}|^2$$

where W_i is an weight factor, which depends on the standard deviation in the peak intensity and background intensity.

The important parameters for the y_{ic} are the reflection profile function and structure factors (F_k). The reflection profile function (peak shape) depends on many parameters such as the radiation source, wavelength distribution, detector etc., Different functions can be used for the peak shape function. Among these, the pseudo-Voigt (pV) function is mostly used since it is a combination of Lorentzian and Gaussian part which provides a good fitting,

$$pV = \eta L + (1-\eta)G; with\ 0 \leq \eta \leq 1$$

where L is the Lorentzian function and G is the Gaussian function, which is given by,

$$L = \frac{C_1^{\frac{1}{2}}}{\pi H_k}\left\{1 + C_1\left(\frac{\Delta\theta_{ik}}{H_k}\right)^2\right\}^{-1}$$

$$G = \frac{C_0^{\frac{1}{2}}}{\sqrt{\pi} H_k} e^{-C_0\left(\frac{\Delta\theta_{ik}}{H_k}\right)^2}$$

where $C_0$and C_1 are constants and H_k is the full width at half maxima (FWHM) of the kth reflection.

The FWHM (H_k) for Gaussian and Lorentzian peak function are given by [7],

$$(H_k)_G = (U\ tan^2\theta + V\ tan\theta - W)^{1/2}$$

$$(H_k)_L = Xtan\theta + \frac{Y}{cos\theta}$$

The parameters U, V, W and X, Y can be refined during pattern matching of the diffraction data. The refinement was performed using ‘Full-Prof’ software package [6] except for the magnetic structure determination through Time-Of-Flight data where ‘Jana’ software has been exploited [8]. In both cases, this parameter can be varied sequentially to obtain a good matching of the experimental data. The refinement quality can be judged through the following R-factor (R_p, R_{wp} and R_E) parameters,

$$R_p(\text{profile}) = \frac{\sum|y_{io} - y_{ic}|}{\sum y_{io}}$$

$$R_{wp}(\text{Weighted profile}) = \left(\frac{w_i(y_{io} - y_{ic})^2}{\sum w_i y_{io}^2}\right)^{\frac{1}{2}}$$

$$R_{pE}(\text{expected}) = \left\{\frac{N - P}{\sum w_i y_{io}^2}\right\}^{1/2}$$

The overall quality of the fitting can be understood by the χ^2 parameter,

$$\chi^2(\text{Goodness of fit}) = \left(\frac{R_{wp}}{R_E}\right)^2 = \frac{\sum w_i(y_{io} - y_{ic})^2}{(N - P)}$$

where N and P are the number of profile points and number of refined parameters, respectively. In the refinement process, at first, the peaks are indexed and the possible space groups are found along with the lattice parameters. With each possible space group and lattice parameter, the profile matching is performed to see the correct space group. Here we need to see the χ^2 value which should be close to one. This step is called as Lebail fitting. At the final stage, a possible structural model with the atomic position should be provided in order to fit the experimental data. This step is called as Rietveld refinement [6]. The crystal structure was drawn using the software Vesta [9].

2.4 Physical Property Measurements

2.4.1 Magnetization measurements

2.4.1.1 dc magnetization

The magnetic measurements presented in this thesis were performed using Superconducting Quantum Interference Device (SQUID) equipped in (Magnetic Property Measurement System) MPMS3 (see figure 2.6) or Vibrating Sample Magnetometer (VSM) option in Physical Property Measurement System (PPMS) (figure 2.7) provided by quantum design. The basic principle of the measurements is due to Faraday's law of induction which states that the induced voltage in a closed circuit is proportional to the rate of change of magnetic flux through the circuit. The magnetic flux (φ) through a coil of n turn with area A is given by $\varphi = AB$, where B is the magnetic field. The induced voltage (V) in the coil is given by,

$$V = -n\frac{d\varphi}{dt} = -nA\frac{dB}{dt}$$

when B is induced by the moving sample inside a coil, the magnetic moment which would be proportional to it can be detected.

Superconducting Quantum Interference Device

SQUID has a very high sensitivity to measure the sample's magnetic moment. It consists of thin insulating layers sandwiched between two superconducting layers to form two parallel Josephson junctions. A superconducting ring made of Josephson junctions that form an integral part of a dc-SQUID is shown in figure 2.6(c).

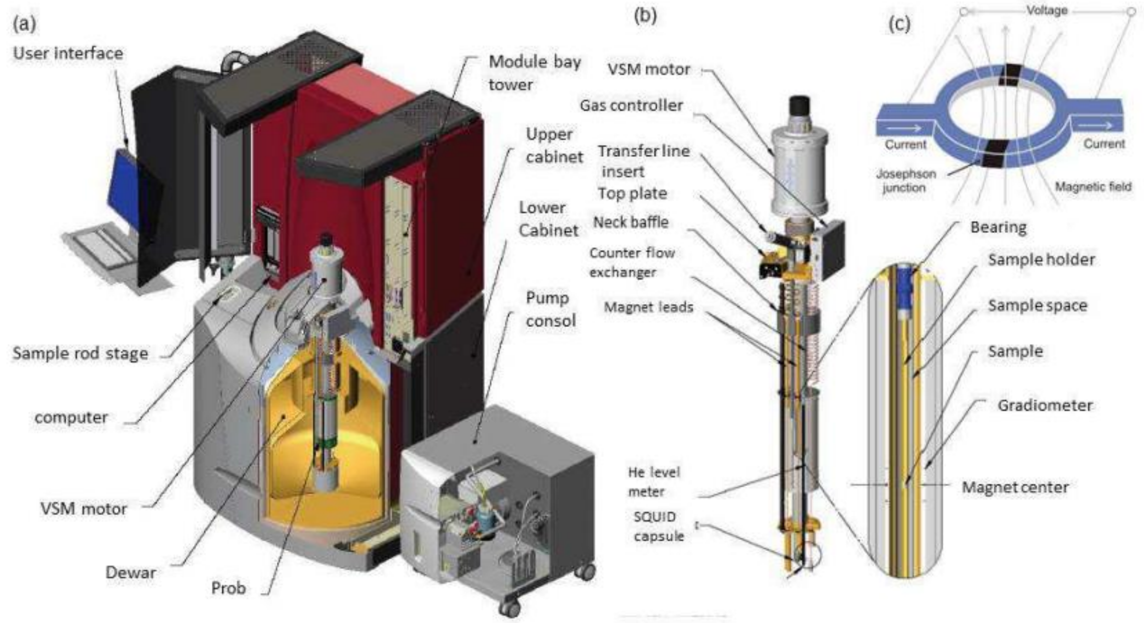

Figure 2.6 (a) Schematic diagram of a Quantum Design SQUID-VSM showing important parts; Adopted from (b) Picture of the SQUID-VSM probe. (adapted from ref. [10]) (c) Schematic of the two Josephson junctions.

A constant biasing current is maintained in the SQUID device while the measured voltage oscillates with changes in phase at the two junctions depending on the change in magnetic flux due to sample movement. Thus the sample magnetic moment can be measured.

There are two different modes available for the magnetization measurements: Vibrating sample magnetometer (VSM) mode and dc mode [10]. In VSM mode, the sample vibrates sinusoidally up and down with very high frequency while in dc scan mode the sample is moved up and down uniformly instead of oscillation. Thus, to get a good quality data, dc scan mode is preferred. The instrument operates in the temperature range, 1.8 K to 400 K with the applied field varying from 0 T to 7 T. A superconducting magnet made of a solenoid of superconducting wires is used to generate the required magnetic fields. Both superconducting magnet and sample chamber are contained in a Dewar and cooled with liquid He [10].

Vibrating Sample Magnetometer (PPMS)

This unit consists of a linear motor for vibrating the sample, a pick-up coil for detection of the moment, electronic controls for transporting the motor stage and detecting the response from the coil and an automation platform [10]. The magnetization of the order of less than 10^{-6} emu can be resolved by the use of compact gradiometer pick-up coils. The unit is adaptable in PPMS as an option control. It can measure magnetic moment in the temperature range 1.8 K to 400K with magnetic field 0 to ±9T. However, in a special oven option, the magnetization can be measured up to 1000 K. In this case, the sample chamber would be under high vacuum, and a sample mounting flat wand, made of ceramic material, is equipped with a fine control heater and thermometer. A typical VSM head along with pick-up coil and linear motor unit is shown in Figure 2.7. The measurement is performed by oscillating the sample at the center of the pick-up coil, and the induced voltage is measured. A sinusoidal oscillation is given to the sample thus the time-dependent induced voltage is,

$$V_{coil} = 2\pi fCmA\, sin(2\pi ft)$$

where f is the frequency of oscillation, C is the coupling constant, m is the dc magnetic moment of the sample, and A is the amplitude of oscillation.

dc magnetization is usually measured in three different conditions of the sample depending on the requirements; Zero-field-cooling (ZFC), Field-cooled cooling (FCC) and Field-cooled warming (FCW or FC). In the ZFC protocol, the sample is cooled from high temperature (from paramagnetic phase) to the lowest temperature in the absence of magnetic field. At the low temperature, the field is applied, and the measurements are taken while warming the sample. In FCC protocol, the required magnetic field is applied at a high temperature, and measurement is performed while cooling in the presence of the magnetic field. For FCW case, the sample is cooled under magnetic field and the measurements recorded during heating of the sample. To observe the magnetic ordering temperature of the specimen, ZFC and FCW are performed. The differences in all these measurement protocols will be presented in the thesis with various sample studies. The magnetization at constant temperature is also measured as a function of the magnetic field to obtain the *M*(*H*) isotherms.

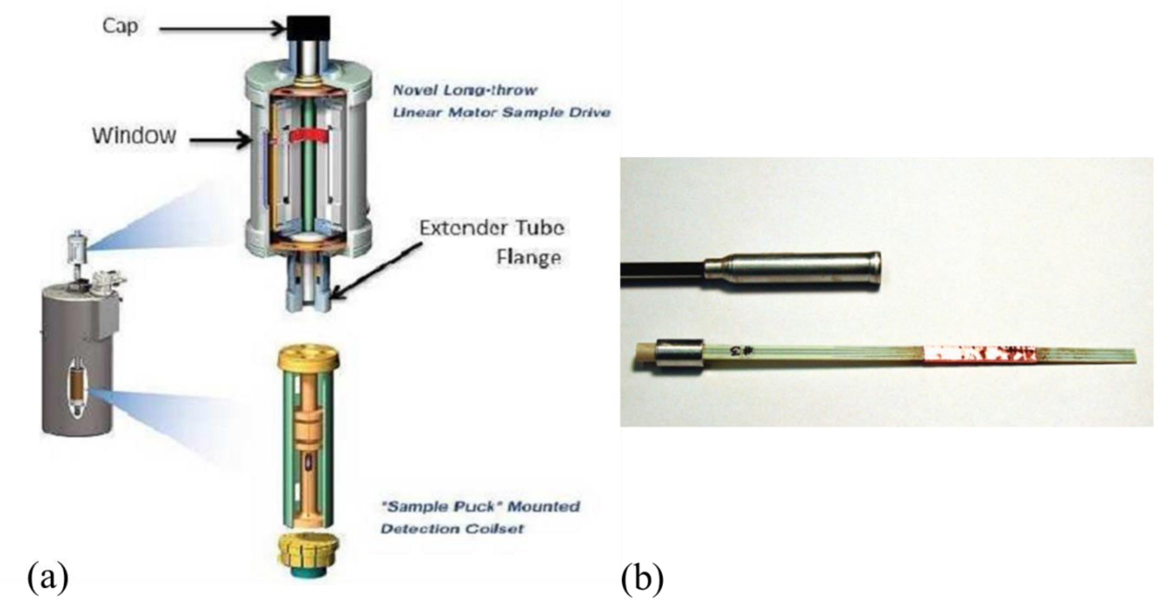

Figure 2.7 (a) Schematic of VSM probe, Linear Motor Module. (b) Oven sample rod: zirconia sample holder. Adapted from ref. [11].

2.4.1.2 ac susceptibility

For the magnetization-dynamics study, the ac susceptibility measurements are performed. In many cases, the ac susceptibility measurements are important such as for the spin-glass study where we need to see the dynamics of the magnetic domains in a time scale which is not possible to see in the dc magnetization study. In ac susceptibility measurements, the sample remains static and a small ac magnetic field ($H = H_0 \exp(i\omega t)$) is applied to the sample in presence or absence of dc bias magnetic field where H_0 and ω are the amplitude and frequency of the applied ac magnetic field, respectively. In small ac field, the susceptibility is defined as

$$\chi = \mathrm{d}M/\mathrm{d}H$$

For applied ac field $H = H_0 \exp(i\omega t)$, the measured voltage signal is given as

$$V = N_S \alpha S v_d M/dH(i\omega H_0 \exp(i\omega t))$$

where, N_S is number of turns in the secondary coils, α is a ratio of the cross-section of the sample to that of the secondary coil ($\alpha \leq 1$) and S is the cross-section of the secondary coil. The induced voltage in the secondary is proportional to the ac susceptibility of the sample.

In the case of higher frequency of the applied ac magnetic field, the ac magnetization of the sample cannot follow the driving frequency and lags behind the applied ac field. Thus, the ac magnetic susceptibility yields two quantities, magnitude of the susceptibility and the phase shift of the induced signal with respect to the driving signal. The susceptibility can be measured as a complex quantity with an in-phase component χ' (real part) and an out-of-phase component χ'' (the imaginary part which indicates the dissipative processes in the sample).

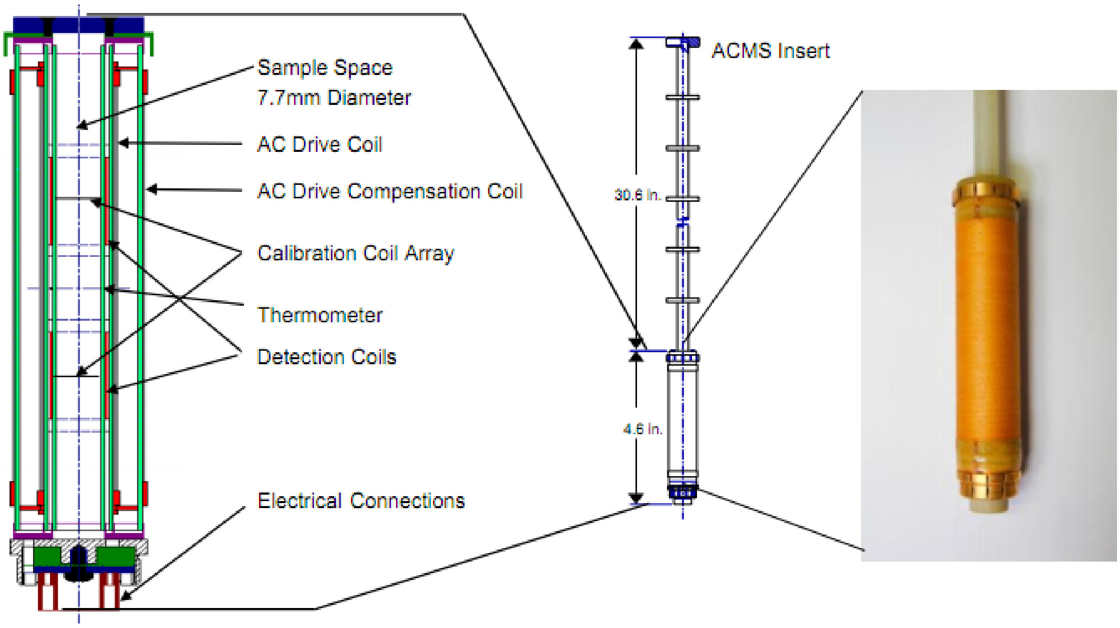

Figure 2.8 Schematic diagrams of the different parts of ACMS coil. Adapted from ref. [12]

The AC susceptibility measurements presented in the thesis was performed in PPMS ACMS option. The basic susceptometer consists of one long primary and two secondary coils. The ac magnetic field is generated by the primary coil (ac drive coil) which induces magnetic flux inside one secondary coil (AC Drive Compensation Coil). This secondary coil is wound in opposite direction so that the voltage induced by primary coil is cancelled out. The total magnetic flux has contributions from primary coil and the magnetization induced in the sample. Another secondary coil (pick-up coil) which consists of a combination of two coils (top and bottom) is tuned to detect signals only from the sample (see figure 2.8) [12]. The measurements are performed by five-point BTBCC (bottom-top-bottom-center-center) measurement process in the PPMS [12]. The signals from the detection coil in first three readings are amplified and digitized by an analog to digital (A/D) converter and saved as response waveform. The real and imaginary components of each response waveform are obtained by fitting the data and comparing with the driving signal. Finally, the calibration readings are used to get the real and imaginary part of the ac susceptibility of the sample [12].

2.4.2 Heat Capacity

Specific heat measurements are carried out using Heat capacity option in Physical Property Measurement System (PPMS) from Quantum Design. Figure 2.9 (a) shows a schematic of the specific heat option in PPMS [13]. Specific heat at a particular temperature is determined by measuring the relaxation time of the sample after heating. A high vacuum (10^{-6} torr using cryopump) is maintained in the sample chamber so that the calorimeter sample puck is isolated from the sample chamber. For heat capacity measurements, a cycle of consecutive heating and cooling of the sample is performed.

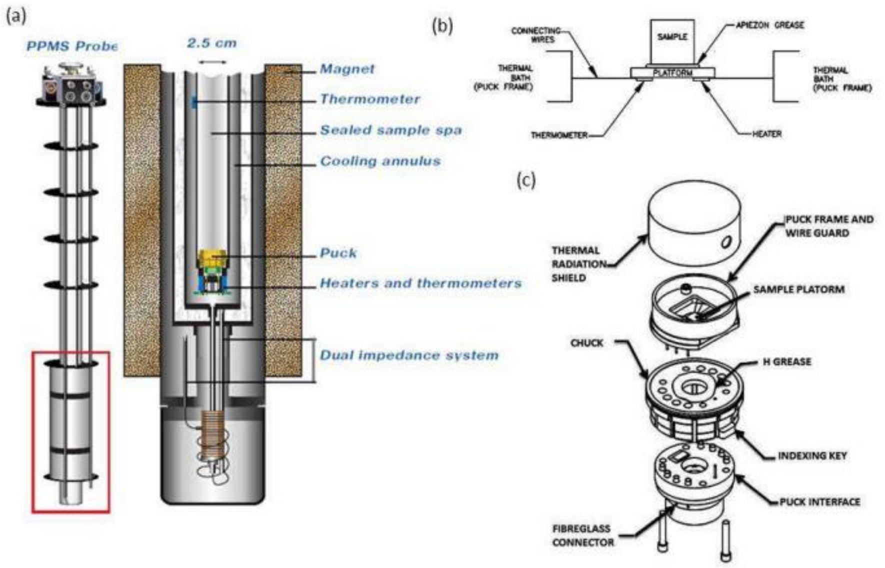

Figure 2.9 (a) Detailed view of sample chamber (b) schematic of specific heat sample mounting stage (c) detailed image of sample mounting puck. Adapted from ref. [13].

At first, a known amount of heat is supplied to the sample for a constant time, and then it is allowed to cool naturally at the same time. The temperature response is recorded during heating and cooling cycle, and it is fitted by the program available in MultiVu software for the full cycle with a model and finally provides the heat capacity of the sample [13]. At first addenda heat capacity measurement is performed, where a small amount of Apiezon grease is applied on the puck sample platform. After the addenda measurement, the sample preferable with a thin pellet geometry (~2.5 mm X 2.5 mm X 0.5 mm) is placed in the sample platform so that the Apiezon grease holds the sample and makes a good thermal contact of the sample to the calorimeter puck, and total heat capacity is measured, which includes the heat capacity of the sample, grease and sample platform. The sample heat capacity is then obtained by subtracting addenda heat capacity from total heat capacity automatically by the MultiVu software in PPMS [13].

In general, the heat capacity data exhibits a peak at the long-range magnetic ordering temperature or any structural transition where a change of entropy occurs at the phase transitions. The change in magnetic entropy associated with the long-range magnetic ordering can be calculated by subtracting lattice contribution from total heat capacity. The lattice contribution can be obtained by measuring heat capacity of an isostructural nonmagnetic sample or by using a Debye-Einstein model. In some cases, the heat capacity becomes very important to observe the magnetic ordering transition where the overall magnetization is dominated by a high magnitude of the paramagnetic moment which will be noticed in the thesis chapters.

2.4.3 Dielectric property

Dielectric constant is an important electrical property of the materials used in electrical device purposes. The dielectric constant of a substance can be determined by measuring the capacitance of a given parallel plate shapes. Electrical contacts are made using copper wire attached with silver paste to the two parallel flat surfaces of the sample coated with the silver paste. In some specific cases, in order to avoid the contact capacitance effect, sputtered gold contacts are made and connect with the wires using silver paste. We found a less noisy data in dielectric constant using PELCO high-performance silver-paste. Therefore, we have used it in most of the study in the thesis. The dielectric constant is a complex quantity,

$$\varepsilon_r = \varepsilon_r' - i\varepsilon_r'' \qquad\qquad loss = tan\delta = \frac{\varepsilon_r''}{\varepsilon_r'}$$

Here ε_r' and ε_r'' are the real and imaginary parts of dielectric constant, respectively. The real dielectric constant can be obtained from the following equation,

$$\varepsilon_r' = \frac{C\ d}{\varepsilon_0\ A}$$

where, ε_0 is the permittivity of free space (8.854×10^{-12} Fm−1), *A* is the area of the parallel electrodes and *d* is the distance between the electrodes. The measurements were performed using Agilent LCR meter (model E4980A) and Agilent 4294A Precision Impedance Analyzer. The sample was inserted into the PPMS where we could measure it from 2 to 350 K with magnetic field 0 to ±9 T (figure 2.10).

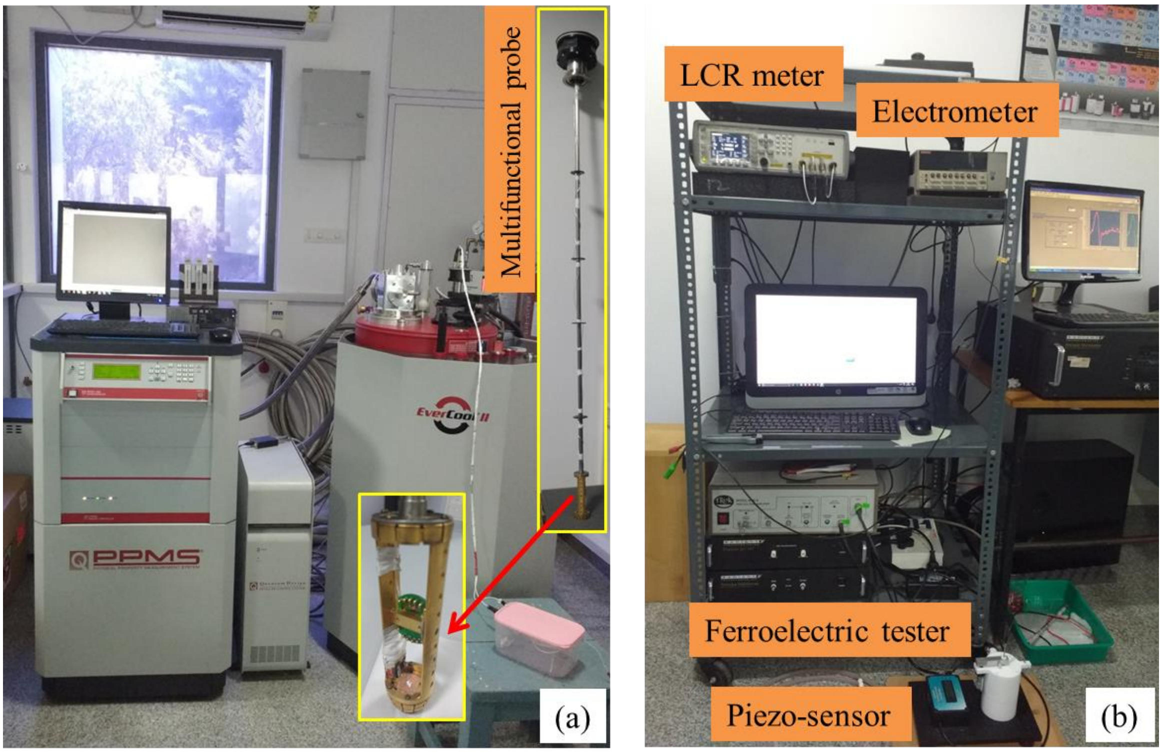

Figure 2.10 (a) PPMS including the multifunctional probe (b) various measuring devices; LCR meter, Electrometer, Ferroelectric tester, Piezoelectric displacement sensor.

2.4.4 *P*(*E*) hysteresis loop

In a ferroelectric material, the polarization is measured conventionally through a polarization versus electric field. It is usually measured using a Sawyer-Tower circuit which is shown in figure 2.11(a). In general, for *P*(*E*) loop measurements a triangular voltage pulse is applied to the sample with a given frequency. Since the sample is connected in series with a known capacitor, the charge accumulated in the sample will be same as the known capacitor which can be calculated by measuring the voltage across the known capacitor. The polarization is the charge per unit area, therefore, it can be obtained as

$$C = \frac{Q}{V}$$

$$P = \frac{Q}{A} = \frac{C_1 V_1}{A}$$

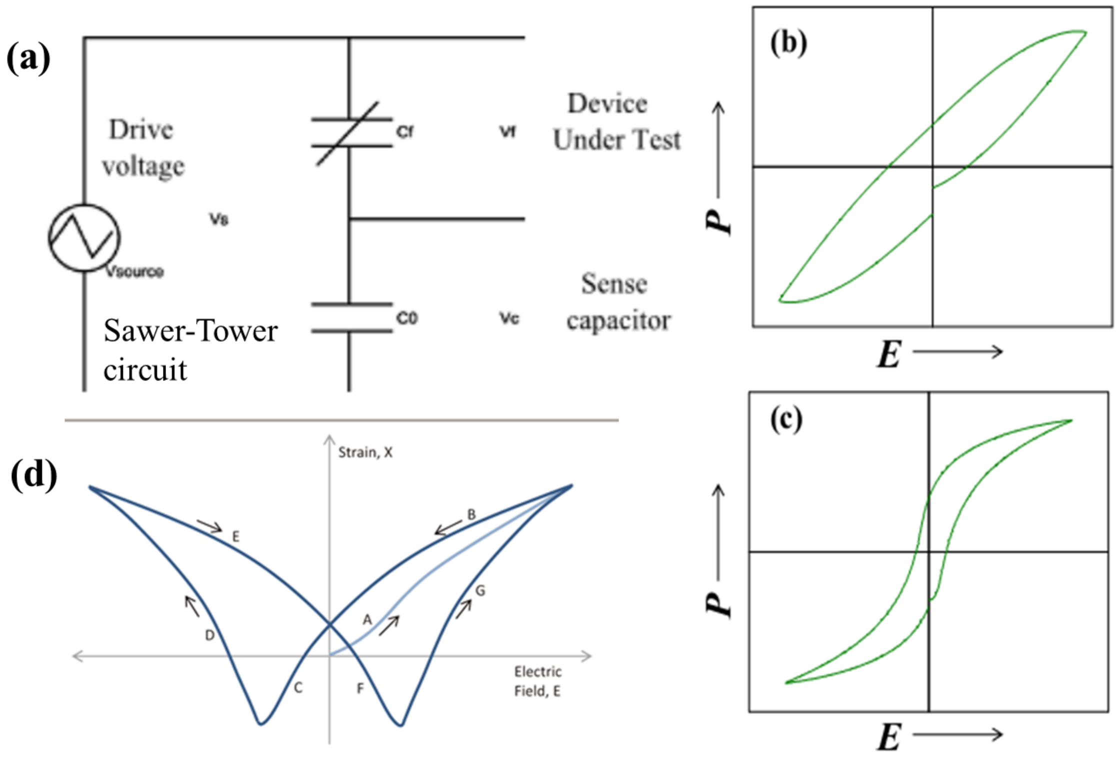

Figure 2.11 (a) Sawer-Tower circuit diagram for the ferroelectric loop measurements. (b) Unsaturated loop due to conductivity in the sample. (c) A typical ferroelectric loop measured in $BaTiO_3$ prepared in the lab. (d) Strain (displacement) behavior of a ferroelectric material (PZT) with an electric field.

A typical ferroelectric loop is shown in the figure 2.11(c) where we see saturation of polarization. It is very important to note that sometimes the observed loop may not be intrinsically due to ferroelectric. The sample's resistive and capacitive character often shows a lossy banana kind of loop which can sometimes be misinterpreted as a ferroelectric loop (figure 2.11(b)). A review based on those results is referred [14]. In order to avoid such circumstances, a modified *P*(*E*) loop called as Double Wave Method (DWM) was introduced where two consecutive positive (P') and up (P") and two consecutive negative (N') and down (N") pulse is given in order to measure the intrinsic ferroelectric polarization [15]. In this case, the first positive pulse contributes for the ferroelectric polarization as well as the leakage contribution however the second positive pulse should only contain the leakage contribution since the ferroelectric polarization current only occurs when the polarization states are switched. Thus by subtracting the polarization from P' and P", we can obtain only the intrinsic ferroelectric polarization. Similarly, we can obtain the negative polarization by subtracting the contribution from N' to N". A pre-poling positive and negative pulse is given in order to polarize the material before the measurement pulses. A typical waveform of the PUND measurement is shown in figure 2.12.

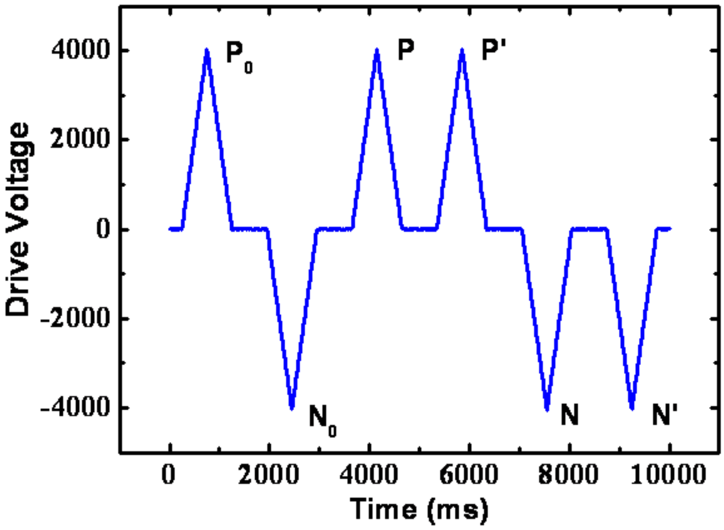

Figure 2.12 The drive voltage profile for measuring the polarization in PUND method.

2.4.5 Piezoelectric loop measurement

Piezoelectricity roots from the Greek word *piezo* for pressure. It means that a piezoelectric material develops a potential across its boundaries when subjected to mechanical stress (pressure), and vice versa, i.e., when an electric field is applied to the material, a mechanical deformation (strain) results. This property was discovered in 1880 by Pierre and Jacques Curie during their study of the effects of pressure on the generation of electrical charge by crystals such as Quartz, Tourmaline, and Rochelle salt. The microscopic origin of the piezoelectric effect is the displacement of ionic charges within a crystal structure. In comparison to the ferroelectricity, piezoelectricity requires only broken inversion symmetry, i.e. there need not be switching of polarization under ac electric field. Here we have measured the converse piezoelectric response, i.e. by applying an electric field, the strain in the material was measured using piezoelectric measurement set up of Precision Multiferroic tester by Radiant Technology (figure 2.10(b)). To measure the strain (displacement) in the sample, an optical probe is used. A typical piezoelectric loop of PZT is shown in figure 2.11(d). A well sintered insulating material is prerequisite for this measurement. Similar to the ferroelectric loop measurements, a silver paste was used to make the electrodes. Silicon oil was used to apply the high voltage.

2.4.6 Pyroelectric current measurement

The electric polarization of a ferroelectric material can be obtained by measuring pyroelectric current across the ferroelectric ordering temperature. The pyroelectric current exhibits an asymmetric peak at the ferroelectric transition. In this measurement, the sample is first poled with an electric field while cooling the sample across the ferroelectric ordering temperature. After that, the external electric field is removed and the electrodes are shorted for sufficient time in order to remove all the stray charges accumulated at sample electrode interfaces. Then the electrometer is connected to the sample and record the current while warming the sample with a constant rate. The pyrocurrent peak amplitude depends on the warming rate. This pyrocurrent is integrated with time, and the polarization can be obtained. Since in this measurement the sample is poled across the transition temperature, the material can be polarized even with a lower electric field, and a very small polarization signature also can be detected in this process which may not be possible in the normal $P(E)$ measurement described before. Thus in the case of multiferroic materials, where the polarization is comparatively low, and the transition temperature is at low-temperature pyrocurrent measurement has become a standard protocol for the polarization measurements. The switching of polarization can also be checked by reversing the poling field sign. However the pyrocurrent also sometimes get affected by some extrinsic contributions. Such as thermally stimulated depolarization current (TSDC) due to free or trapped charges can result a peak in the pyroelectric current data, which is in general broad and symmetric [16, 17]. Such peaks should not be attributed to the ferroelectric transition. It can be distinguished from the peak associated with a ferroelectric transition by measuring it under different heating rates. If the peak is due to the TSDC, it shifts to higher temperature with increasing heating rates, while if it is associated with a ferroelectric transition, it doesn't shift with increasing heating rate [17]. A schematic figure for a pyrocurrent at a ferroelectric transition is shown in figure 2.13. We have devised a new technique which is called as DC-bias current measurement in order to distinguish intrinsic pyrocurrent peak from the TSFC peaks which will be described in chapter 3[18].

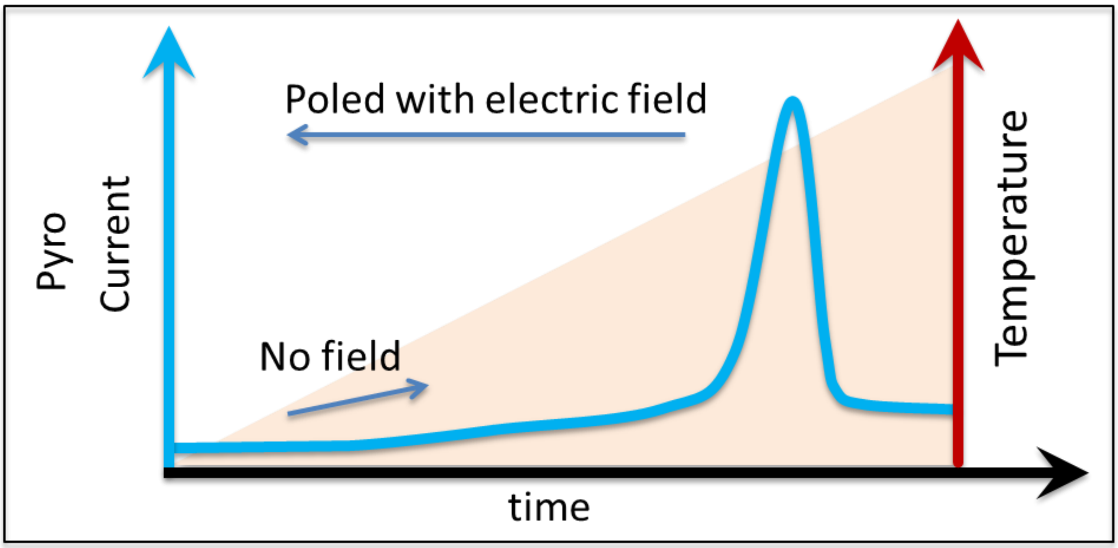

Figure 2.13 Typical feature of pyrocurrent.

2.5 Fabrication of tube furnace

Since our main sample preparation method was the solid state reaction which involves lot of heat treatment in the furnaces, it is necessary to have a number of high temperature furnaces in hand to continue the work more efficiently. In the beginning of my thesis work I found that we need the high temperature furnace quite frequently and the access was limited. I thought of fabricating the high temperature furnace in our laboratory. Specifically, we needed more tubular furnace because this furnace can be used for both cases, gas passing reaction as well as in air. I started fabricating the tube furnace using mostly the scrapped materials for example the broken ceramic tubes, thermal glass wool and some of the items from our central work shop. The most imported thing for a furnace is the heating element, good thermal insulation and a proper design with electrical circuit arrangements. As a heating element we have used high quality Kanthal wire

(FeCrAl alloy) from which we made a long coil with a resistance of nearly 30 Ohm. The coil was wrapped on the ceramic tube covering nearly 16-inches in length. Further, the coil was embedded with high temperature cement as a uniform layer. After curing the whole unit of coil, it is ready to be used as a heating element. This heating element was wrapped further with glass wool blanket for good thermal insulation. A cabinet was made to hold the heating element units and left some space at the bottom for arranging the electrical units. I choose to use to the programming controller so that we can use the furnace for required heating rate, dwelling time and cooling rate. A solid state relay (SSR) was used to supply the power to the furnace according to the requirement for the desired temperature profiles provided in the controller. This furnace was capable of heating maximum 1200 °C, we used K-type thermocouple as a temperature sensor. After the fabrication, the performance was tested and temperature was calibrated using an additional temperature sensor. We found temperature equilibrium for more than 5-inches at the center zone of the tube which was sufficient for our reaction. We made total two similar furnaces which are being used in the lab very regularly for more than four years for ≤1150 °C. The cost for the whole furnace was reasonable (approximately 350 USD each). Another important factor is that the power consumption in these small furnaces are also economic (<2 kW). In order to achieve the first cooling in the furnace (as the natural cooling process is slow) so that it can be ready for the next heating cycle as well as we can optimize the unnecessary gas passing during cooling, we have also integrated a cooling fan which can work as per the desired cooling rate as close as possible.

Figure 2.14 Laboratory fabricated furnaces usable up to 1150 °C according to the temperature profile given in the controller.

References

[1] A. R. West, Solid State Chemistry and its Applications, 2nd ed. (John Wiley & Sons, 2014).

[2] R. C. Ropp, *Solid state chemistry* (Elsevier, 2003).

[3] P. M. Shirage *et al.*, Physica C: Superconductivity **469**, 355 (2009).

[4] V. Z. Pecharsky, Peter, *Fundamentals of powder diffraction and structural characterization of materials* (Springer Science & Business Media, 2008).

[5] H. Rietveld, J. Appl. Crystallogr. **2**, 65 (1969).

[6] J. Rodriguez-Carvajal, in *satellite meeting on powder diffraction of the XV congress of the IUCr* (Toulouse, France:[sn], 1990).

[7] C. Giacovazzo, Fundamentals of crystallography (Oxford university press, USA, 2000).

[8] V. Petříček, M. Dušek, and L. Palatinus, Zeitschrift für Kristallographie-Crystalline Materials **229**, 345 (2014).

[9] K. Momma and F. Izumi, J. Appl. Crystallogr. **41**, 653 (2008).

[10] Magnetic Property Measurement System - MPMS 3 User's Manual (Quantum Design).

[11] Physical Property Measurement System - VSM Oven Option - User’s Manual (Quantum Design).

[12] Physical Property Measurement System - AC Measurement System (ACMS) Option -User’s Manual (Quantum Design).

[13] Physical Property Measurement System - Heat Capacity Option - User’s Manual (Quantum Design). .

[14] J. Scott, J. Phys. Condens. Matter **20**, 021001 (2007).

[15] M. Fukunaga and Y. Noda, Journal of the Physical Society of Japan **77**, 064706 (2008).

[16] S. McKeever and D. Hughes, J. Phys. D App. Phys. **8**, 1520 (1975).

[17] Y. Kohara, Y. Yamasaki, Y. Onose, and Y. Tokura, Phys. Rev. B **82**, 104419 (2010).

[18] C. De, S. Ghara, and A. Sundaresan, Solid State Commun. **205**, 61 (2015).

Chapter 3

Thermally stimulated free charge carriers and intrinsic ferroelectric polarization in multiferroic materials: A study on $TbMnO_3$*

Summary

This chapter is focused on the determination of the intrinsic ferroelectric polarization in the multiferroic materials through pyrocurrent measurement. Nowadays, pyrocurrent measurements have become a standard protocol and mostly used to investigate the signature of ferroelectricity as well as to estimate the polarization. However, there are some factors especially thermally stimulated charge carriers which manifests the pyrocurrent feature that is very similar to the ferroelectric and thus it becomes sometimes erroneous to attribute the pyrocurrent results as ferroelectricity. The clear signature of multiferroic behavior distinguished from trapped charges related behavior has been demonstrated through investigating a renowned multiferroic $TbMnO_3$. Interplay between the ferroelectric polarization and the trap charge related internal field is shown. A simple way of tracing ferroelectric signature, the so called DC-bias method, has been introduced.

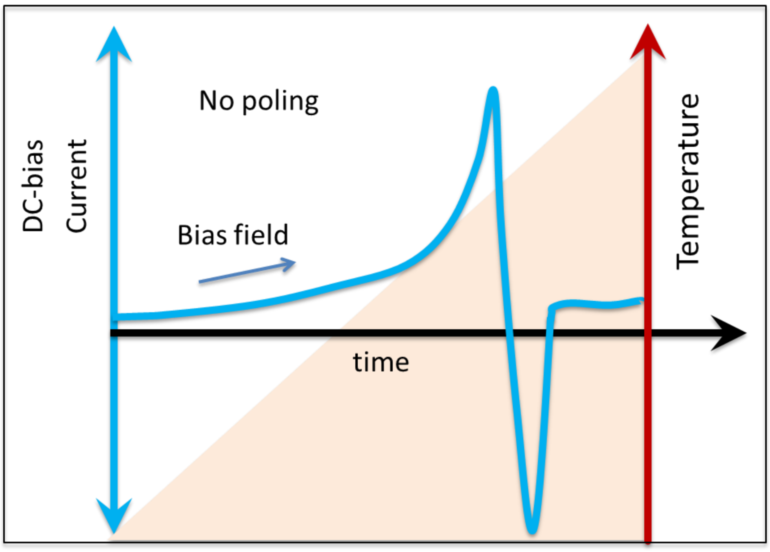

---

*This work has appeared in C. De *et al.* *Solid State Commun.* **205**, 61 (2015), © (2015) Elsevier Ltd.

3.1 Introduction

Since the discovery of spin-induced ferroelectricity in RMnO$_3$ (R = Gd, Tb and Dy), there have been immense efforts to find out new single phase magnetoelectric multiferroic materials in which a coupled ferroelectricity and magnetism coexist [1-7]. These materials have received much attention because of their interesting fundamental science and potential for applications [8-13]. But finding new multiferroic materials with an efficient magnetoelectric coupling at room temperature is a quite challenging task because of difficulties in combining ferroelectricity and magnetism in the same phase as discussed in the introduction [14]. So far, there are only a handful of families of materials that have been discovered to show this phenomenon in which either the ferroelectric transition is far below room temperature or the polarization is lower than that required for applications [5, 15]. Besides, the leakage current in most of these materials becomes a major issue for studying their ferroelectric properties [16, 17]. Usually, the standard Sawyer– Tower circuit has been used for the measurement of $P(E)$ loops to determine ferroelectric properties in conventional ferroelectric materials which are good insulators [18, 19]. However, this method seems to be not suitable for multiferroic materials because of their feeble ferroelectric polarization and a considerable leakage current. A modified $P(E)$ loop method known as Positive-Up and Negative-Down (PUND) has been employed in determining the intrinsic ferroelectric polarization by separating out the leakage contribution [17, 20, 21]. However, the most widely used method to study ferroelectric properties in multiferroic materials is the pyroelectric current measurements [1, 22-25]. Though the measurement of pyrocurrent is simple, the analysis becomes complicated when the sample contains thermally stimulated free charge (TSFC) carriers in the vicinity of ferroelectric ordering temperature [26]. It should be mentioned that many materials have been proposed as multiferroics in the literature based on pyrocurrent which are not intrinsic.

To understand the actual nature of pyrocurrent behavior for a multiferroic material, a thorough investigation has been performed in a prototype multiferroic material TbMnO$_3$. In this compound, the Mn^{3+} moments undergo an incommensurate sinusoidal antiferromagnetic ordering at 42 K and a commensurate cycloidal ordering at 28 K and finally Tb^{3+} orders below 7 K. Below the commensurate cycloidal ordering, a spontaneous electric polarization appears because of breaking of inversion symmetry due to inverse Dzyaloshinskii–Moriya interaction [1-3, 7]. In this chapter, a formation of an internal electric field (E_{int}) by TSFC carriers at higher temperature and its effect on the pyrocurrent peak at the ferroelectric ordering temperature is discussed in detailed through investigating the pyrocurrent properties over a broad range of temperature. Particularly, when the sample is poled across the ferroelectric transition in a wide temperature range (T_{Pole}: 130–10 K) by a positive external electric field (E_{ext} = 4 kV/cm), we observed two pyrocurrent peaks in the negative direction (-I_{pyro}). The one at the ferroelectric transition (T_C ~ 26 K) is sharp whereas the other peak located in the paraelectric state (~ 80 K) is relatively broad and symmetric. This broad peak is a manifestation of the existence of E_{int} field due to TSFC charge carriers. Intriguingly, the sample poled only in the paraelectric state (T_{Pole} : 130–50 K) by the same positive field (E_{ext}) also exhibits a pyro-current peak at T_C with the same polarity (I_{pyro}). This unusual behavior of pyrocurrent is explained by the internal field (E_{int}). Finally, it has been demonstrated that a simple DC-biased current measurement can be useful in understanding the origin of pyrocurrent and thus identifying true ferroelectric behavior.

3.2 Experiments

The polycrystalline sample of $TbMnO_3$ was prepared by standard solid state synthesis route. Stoichiometric amount of Tb_4O_7 (preheated at 950°C for 12 hours) and Mn_2O_3 were mixed in an agate mortar and pestle. The mixture was heated at 1100°C, 1200°C and 1300°C in air for 24 hours sequentially. Finally, the mixture was pelletized and sintered at 1350°C in air for 24 hours. Phase purity was confirmed by analyzing the powder X-ray diffraction data collected using the Bruker D8 Advance X-ray diffractometer. Magnetic measurements were carried out on a SQUID VSM magnetometer and heat capacity and electrical measurements with a Physical Property Measuring System (PPMS), Quantum Design, USA. Pyroelectric and DC-biased current measurements were recorded at 4 K/min rate using the Keithley Electrometer/High resistance meter (model 6517A). Dielectric properties were measured using the Agilent (E4980A) Precision LCR meter attached to the PPMS. Electrical contacts were made using silver paint.

3.3 Results and discussion

3.3.1 Magnetization and heat capacity and dielectric property

Figure 3.1(a) shows the specific heat divided by temperature (C/T) and magnetization (M), data measured under field cooled condition with 100 Oe, as a function of temperature (T). Since the sample is polycrystalline in nature and the Tb^{3+} moments are higher than Mn^{3+} moments, the magnetization anomalies associated with ordering of Mn^{3+} ions are not observed and only an ordering corresponding to the Tb^{3+} ions is observed around 7 K [27]. However, Mn^{3+} spin associated anomalies can be seen clearly in (C/T) data where the anomaly near 40 K corresponds to the sinusoidal antiferromagnetic ordering and near 25 K corresponds to the cycloidal ordering of Mn^{3+} ions. Tb^{3+} ordering at 7 K is also observed in the C/T data.

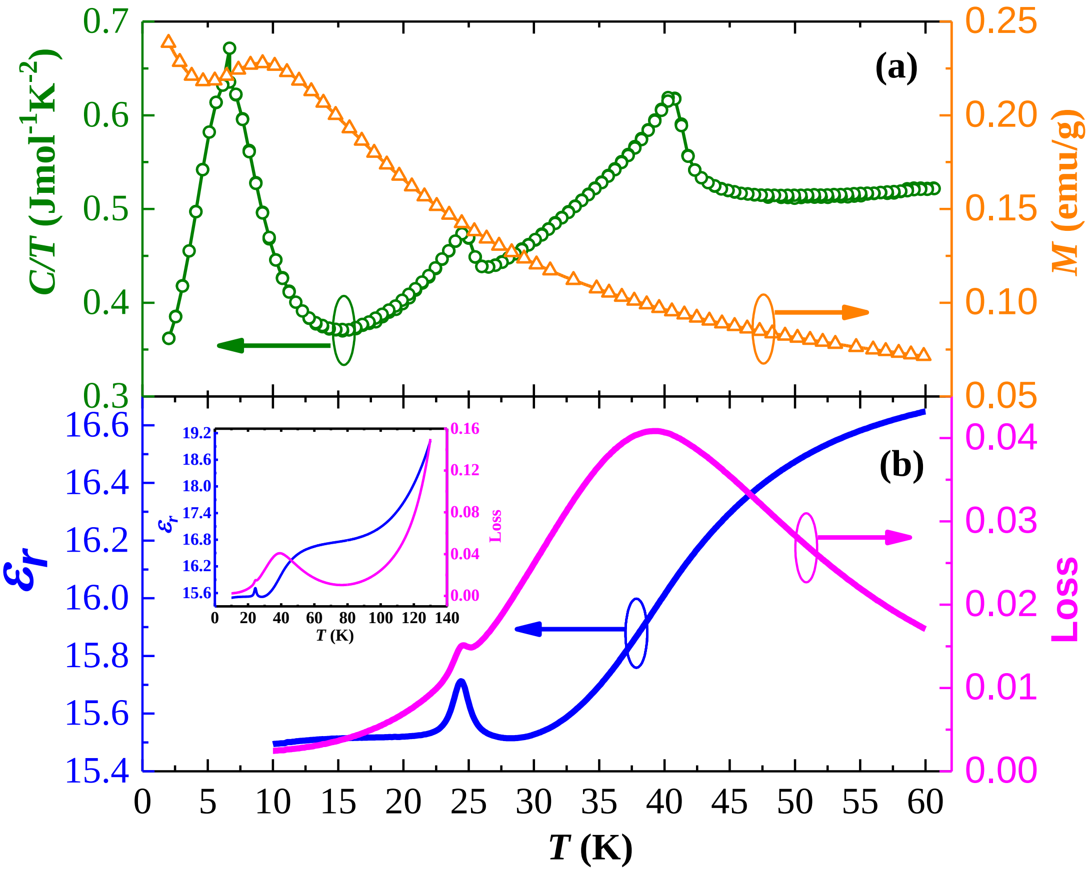

Figure 3.1 (a) Specific heat divided by temperature (C/T) (left axis) and magnetization (M) (right axis) vs. temperature (T). (b) Dielectric constant $\Delta\varepsilon_r$ (left axis) and loss (tan δ) (right axis) as a function of temperature. The inset shows the dielectric data up to 130 K.

Results of dielectric measurements carried out at 50 kHz are shown in figure 3.1(b) where the dielectric constant (left axis) and loss data (right axis) show anomaly at the ferroelectric ordering temperature around 25 K. It can be understand that being a polycrystalline sample, the ferroelectric T_C is slightly decreased to 25 K from a value of 28 K, as observed in single crystal sample [1]. The broad peak in the loss data and the step-like feature in the dielectric constant at around 40 K are due to Debye like relaxation associated with the magnetic Mn^{3+} ion. A similar relaxation behavior is also present in $DyMnO_3$ in the same temperature region [28]. Notably, this dielectric anomaly has correlation with the magnetic ordering and will be discussed in Chapter 4 in single crystal study of $Gd_{0.5}Dy_{0.5}MnO_3$. The inset of figure 3.1(b) shows the dielectric data up to 130 K. Above 80 K, the rise in the dielectric constant and loss is due to the Maxwell–Wagner relaxation associated with the barrier layer capacitor at the grain boundaries [29-32].

3.3.2 Pyrocurrent and DC-bias current

Figure 3.2 shows pyrocurrent (I_{pyro}) data recorded while warming the sample with a rate of 4 K/min from 10 K to 130 K, after poling the sample from 130 K to 10 K (T_{pole}) with $E_{ext} = 4\ \mathrm{kV/cm}$. Before recording the pyrocurrent, electrodes were kept shorted for 30 min at 10 K to remove stray charges. We observe two distinct negative pyrocurrent peaks. The low temperature peak at 26 K is sharp whereas the high temperature peak at 80 K is relatively broad and symmetric. Evidently, the low temperature peak is the depolarization current due to ferroelectric transition where the anomaly in the dielectric constant as well as in heat capacity is also observed. By a careful observation on the high temperature side of this peak, it can be seen that the current goes to the positive direction at the vicinity of the T_C, as shown in the inset. This behavior is unusual because the depolarization current should remain negative for a positive poling field ($E_{ext} = 4\ \mathrm{kV/cm}$). It can be inferred that the positive component of the peak is related to the presence some negative field concealed in the sample.

Since we do not see any dielectric anomaly at around 80 K and the magnetic ordering is far below 80 K and also the crystal structure is centrosymmetric (P*bnm*), we suggest that the high temperature peak can be related to some trapped charges accumulating at the electrode interface and the grain boundaries. In order to further confirm the non-ferroelectric origin of this peak, the pyrocurrent was measured at different warming rates of 0.5, 2 and 4 K/min respectively as shown in the figure 3.3.

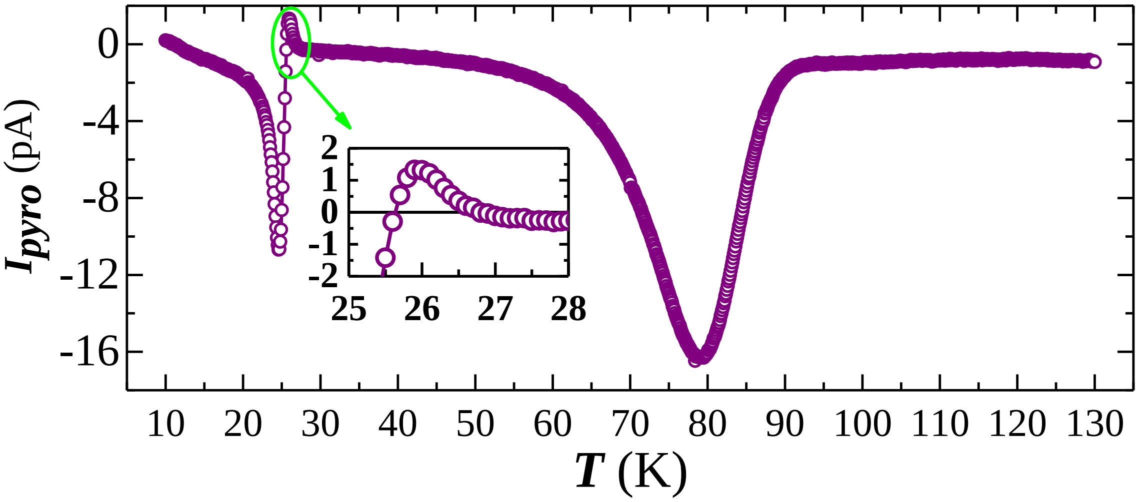

Figure 3.2 Pyro-current versus temperature data after poling with E_{ext} = 4 kV/cm and T_{Pole}:130 K to 10 K.

We found that the high temperature pyrocurrent peak shifts towards the high temperature with increasing heating rate which is a typical behavior of thermally stimulated free charge carriers [33]. On the other hand, the low temperature peak remains unchanged which is consistent with the fact that the depolarization current due to ferroelectricity should always vanish at the T_C. It can be noted here that there may be a minute gradual change of the pyro-peak with the warming rate which should be due to the thermal lag between the sample temperature and the PPMS temperature sensor. The variation of warming rate was chosen towards the lower rate so that the thermal lag can be avoided as much as possible. It can be mentioned here that in the PPMS, due to presence of Helium exchange gas in the normal purge-seal operation, this thermal lag is small. From this experiment, it was confirmed that the high temperature peak is related to some other charges accumulating below the peak temperature in presence of the field cooling during the poling. These charges are called as TSFC carriers. An internal field denoted as E_{int} can be created due to freezing of the charges during the poling process. During the pyrocurrent measurement while warming, the depolarization of the charges exhibits a peak in pyrocurrent.

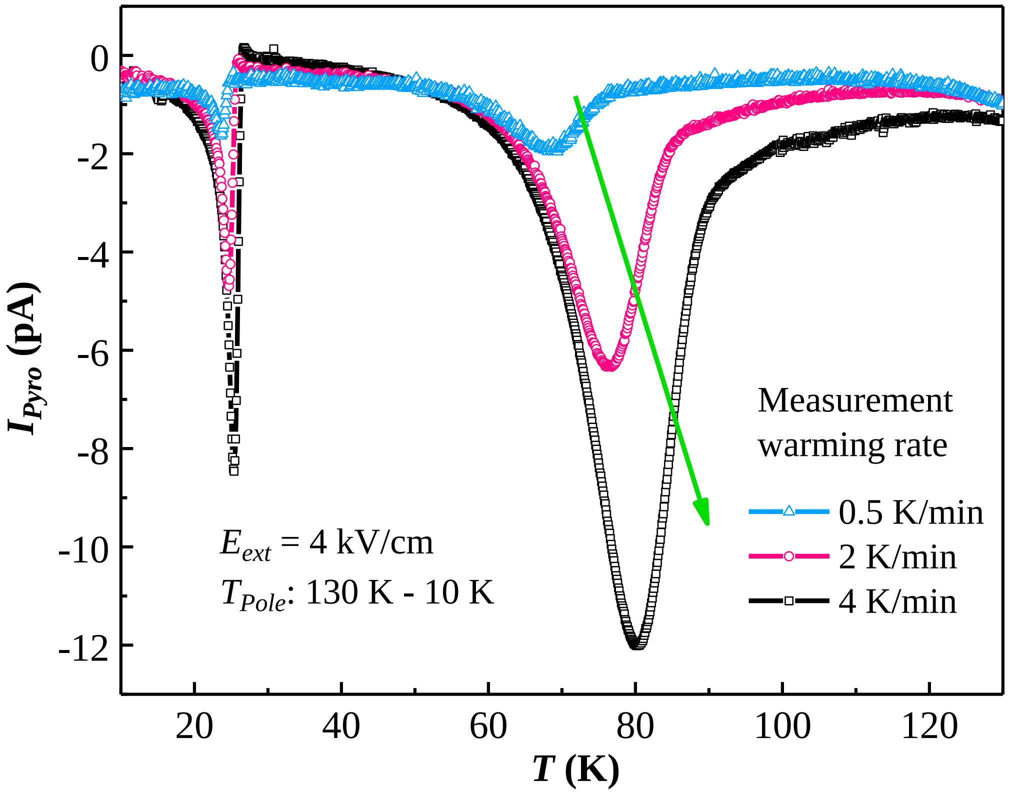

Figure 3.3 Pyrocurrent measured at different warming rate after poling the sample from 130 to 10 K.

In order to distinguish these two pyrocurrent peaks in an easy way, another measurement procedure is introduced for the first time. In contrast to the conventional pyrocurrent method, in this case a DC-bias field (+ 2, + 4 and + 8kV/cm) is applied to the sample after cooling the sample to the lowest temperature (10 K, in the present case) without applying any field. The current (I_{DC}) was recorded while warming the sample from 10 K and the results are shown in figure 3.4 in two parts. Interestingly, at the temperature corresponding to the low temperature pyrocurrent peak, the I_{DC} shows a broad positive peak and a sharp negative peak whose magnitude increases with increasing applied field. The observation of positive and negative component of this peak resembles the low temperature pyrocurrent peak, including the small positive component (figure. 3.2). However, the origin of both positive and negative peak is different. For obvious reason, while warming the sample from 10 K, the positive peak in DC-biased current (+I_{DC}) arises due to polarization of ferroelectric dipoles for approaching the ferroelectric ordering and the consecutive negative peak results from depolarization current just below the T_C. For pyrocurrent data (figure. 3.2), the negative component of the low temperature pyrocurrent peak arises from depolarization current while the positive component has its origin at the negative internal field ($-E_{int}$) due to TSFC carriers which acts somewhat similar manner of the DC-biased current. A detailed discussion on this scenario is given in the subsequent section.

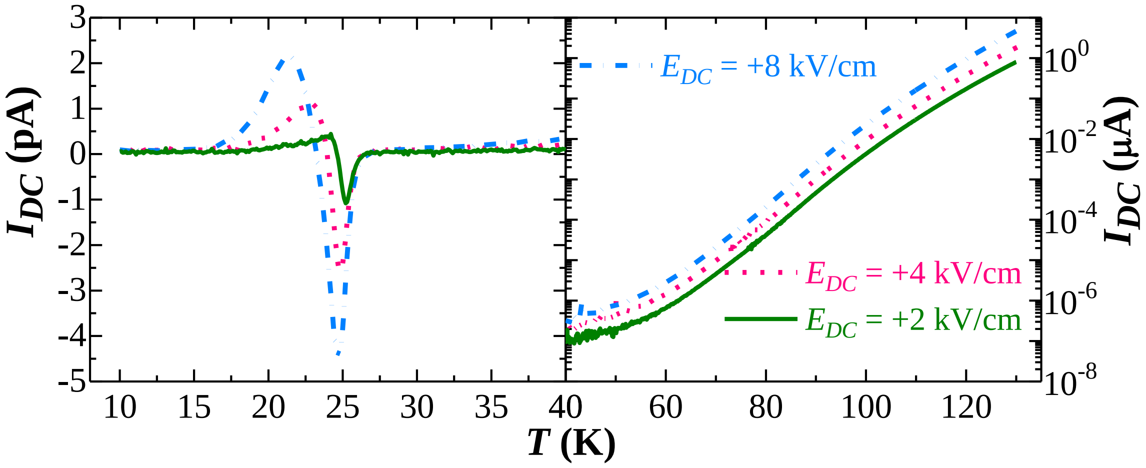

Figure 3.4 Variation of DC-biased current (I_{DC}) with temperature at different bias field in two different temperature ranges with the left axis on a linear scale and the right axis on a log scale.

More importantly, the I_{DC} does not show any feature corresponding to the high temperature pyrocurrent peak in the paraelectric state confirming its non-ferroelectric origin. Thus, these results demonstrate that the DC-biased current measurement can differentiate the pyrocurrent peak arising from ferroelectricity and that due to TSFC carriers. In fact, we observe a broad pyrocurrent peak in several non-ferroelectric materials as RMnO$_3$ (R = Nd, Sm and Eu) (shown in figure 3.5), garnet $Sm_3Fe_5O_{12}$ (data not shown) and NaRMnWO$_6$ (R = La, Nd and Tb) (will be discussed in Chapter 5) [34], but we did not observe corresponding peak in DC-biased current. Therefore, we imply that the presence of pyrocurrent does not always indicate ferroelectricity and one must be careful while analyzing the pyrocurrent of any leaky materials, particularly when the pyrocurrent peak appears close to magnetic ordering [35-37]. By analyzing the shape of pyrocurrent peaks observed in ferroelectric and non-ferroelectric materials, we suggest that the sharp lambda-like pyrocurrent is indicative of ferroelectricity. The relatively broad and symmetric peak may indicate that it can be due to TSFC carriers. The TSFC carriers related pyro-peak can arise at different temperatures, depending on the activation energy of any charged transition metal ions in the material. A schematic diagram of DC-bias current for a ferroelectric transition has been shown in the beginning of this chapter.

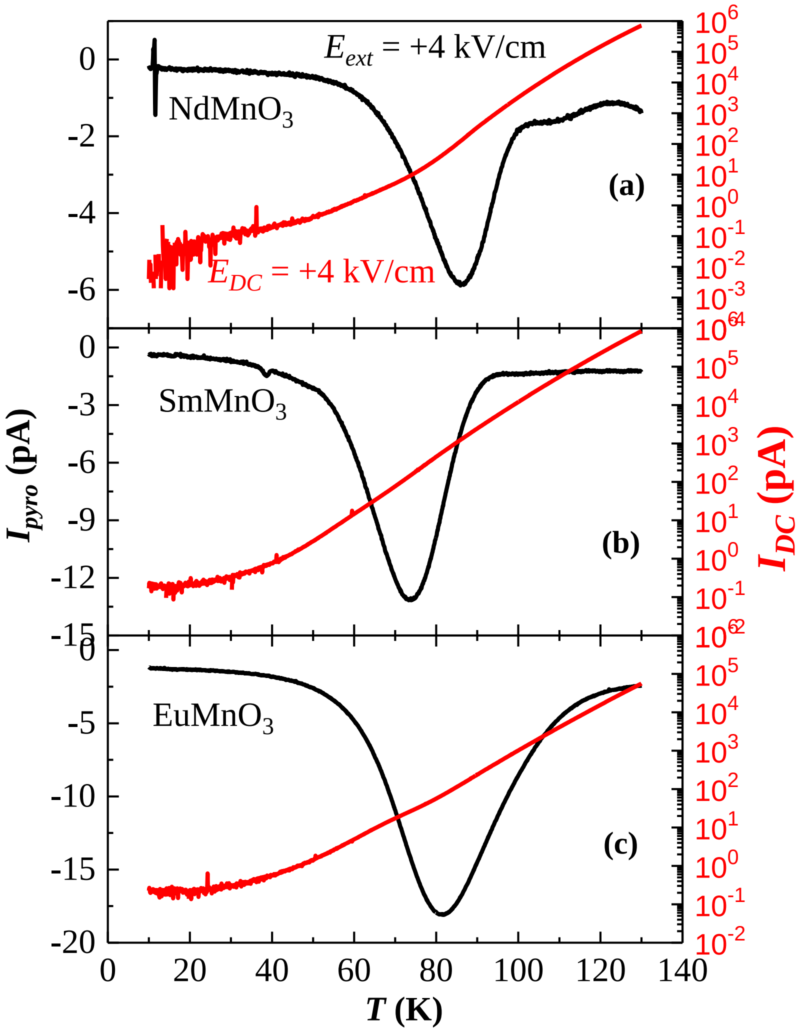

Figure 3.5 Pyrocurrent behavior in other non multiferroic manganite. (a), (b) and (c) shows the data for NdMnO$_3$, SmMnO$_3$ and EuMnO$_3$ respectively. Right axis shows the DC-biased current measured with +4 kV/cm.

3.3.3 Internal field due to TSFC carriers

Now, we demonstrate that the positive component of the low temperature peak of figure 3.2 is caused by a negative internal field. For this purpose, we have measured pyrocurrent under different poling temperature region with the same positive poling field (4 kV/cm) and heating rate adapted in figure 3.2 and the results are shown in figure 3.6. For the poling temperature range, T_{Pole}: 50 –10 K, the pyrocurrent measured from 10 to 130 K is shown in figure 3.6(a).

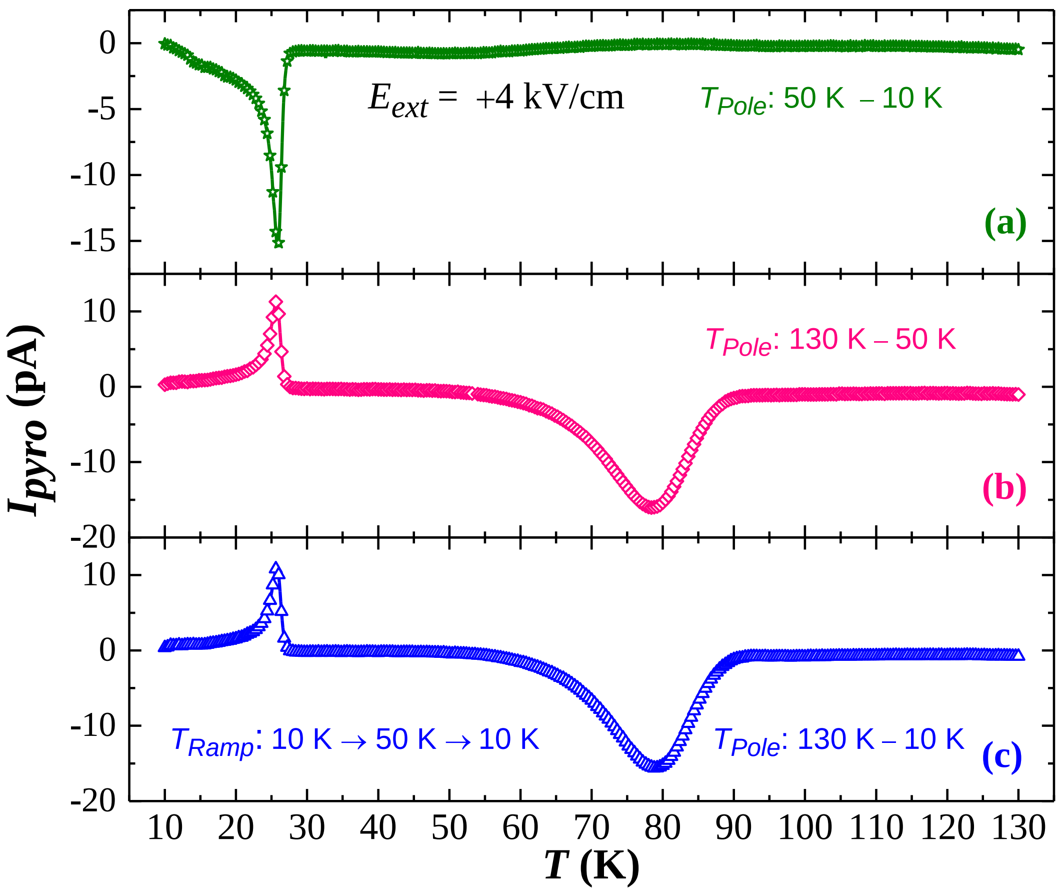

Figure 3.6 Temperature pro file of I_{pyro} recorded under the same poling field (E_{ext} = 4 kV/cm) but different poling temperature range (T_{Pole}). (a) T_{Pole}: 50– 10 K, (b) Pole:130– 50 K and (c) T_{Pole}:130– 10 K. In the last case, the sample was warmed across the T_C to T = 50 K in short circuit condition and cooled to 10 K prior to the I_{pyro} measurement from 10 to 130 K.

It can be seen that there is only one pyrocurrent peak with negative polarity (-I_{pyro}) due to depolarization of dipoles at the ferroelectric transition without any positive component. The fact that we do not observe the positive component in the low temperature pyrocurrent peak and also the absence of high temperature pyrocurrent peak in the paraelectric state confirms that the positive component of the first peak is related to the high temperature pyrocurrent peak. Further, the external poling below 50 K should not produce E_{int}, if the freezing temperature of the TSFC carrier is above 60 K as seen in the peak onset of the high temperature pyrocurrent. Therefore, the observed pyrocurrent is the result of only the positive external field (E_{ext}).

In order to study the effect of E_{int} alone if at all exists, the sample was poled only in the paraelectric state (T_{pole}: 130 - 50 K) and shortened the electrodes at 50 K. Then the sample was cool down to 10 K in short-circuit condition across T_C. Since the sample was cool down in the absence of E_{ext} across the ferroelectric transition, we do not expect pyropeak at T_C. In contrast, we observed a pyropeak at T_C with the same polarity (I_{pyro}), as that of the E_{ext} (figure 3.6(b)). On the other hand, a broad negative pyro-current peak in the paraelectric state (80 K) is observed which is a manifestation of the presence of E_{int} due to TSFC carriers, as discussed before. Thus, it is obvious from these measurements that the positive pyro-current peak (I_{pyro}) arises from the negative internal field (E_{int}) which in turn is created by positive external field (E_{ext}).

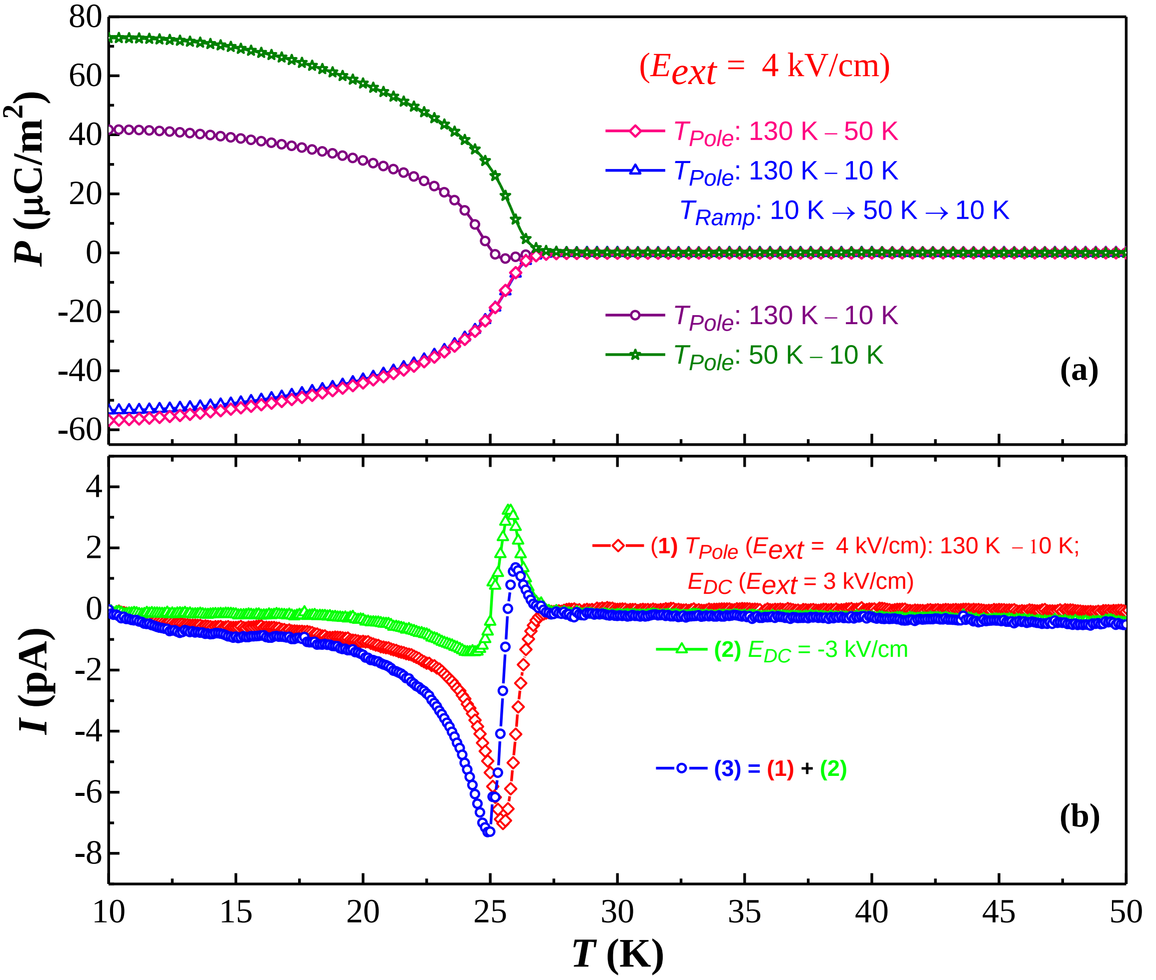

Figure 3.7 (a) Polarization data (T < 50 K) obtained from integrating the pyro-current data (Figure 3.6) with time. Different colors/symbols show the polarization for different poling procedures mentioned in the figure. (b) Results of DC-biased current (I_{DC}) measurements under different bias field (E_{DC}): (1) I_{DC}(◊)measured under E_{DC} = (3 kV/cm) after poling from 130 to 10 K with 4 kV/cm. (2). I_{DC} (△) measured under E_{DC} = -3 kV/cm. (3). Data (○) obtained by adding the IDC data 1 (◊) and 2 (△) which is equivalent to I_{pyro} in Figure 3.2.

The presence of E_{int}, and its polarity with respect to E_{ext}, is further confirmed by the following warming and cooling experiments in the temperature range of 10–50 K. After poling from 130 to 10 K, the sample was short-circuited and warmed to a temperature (50 K) above T_C and then cool down again to 10 K. In this process, the positive depolarization current (-I_{pyro}) would disappear at T_C during the first warming cycle and therefore, we should not see depolarization current in the subsequent warming measurement. Indeed, we still observe a pyrocurrent peak at T_C (figure 3.6(c)) with positive polarity (I_{pyro}) which remains unchanged for further cooling and warming cycles between 50 and 10 K. This peak disappears only when the sample is warmed above the high temperature peak where the E_{int} field disappears. This is a kind of memory effect of the ferroelectric polarization which itself is an interesting subject and studied in detail in Chapter 4. These results further confirm the presence of the E_{int} field and its opposite polarity with respect to the E_{ext}, when the sample is poled in the paraelectric state (130 K) and cool down to 50 K or below. We have estimated the strength of E_{int} with respect to E_{ext} from polarization data (figure 3.7(a)) obtained from the pyro-current data shown in figure 3.2 and figure 3.6. It is found that the strength of the internal poling field is nearly three fourth of the external field ($E_{int} \approx 0.75E_{ext}$).

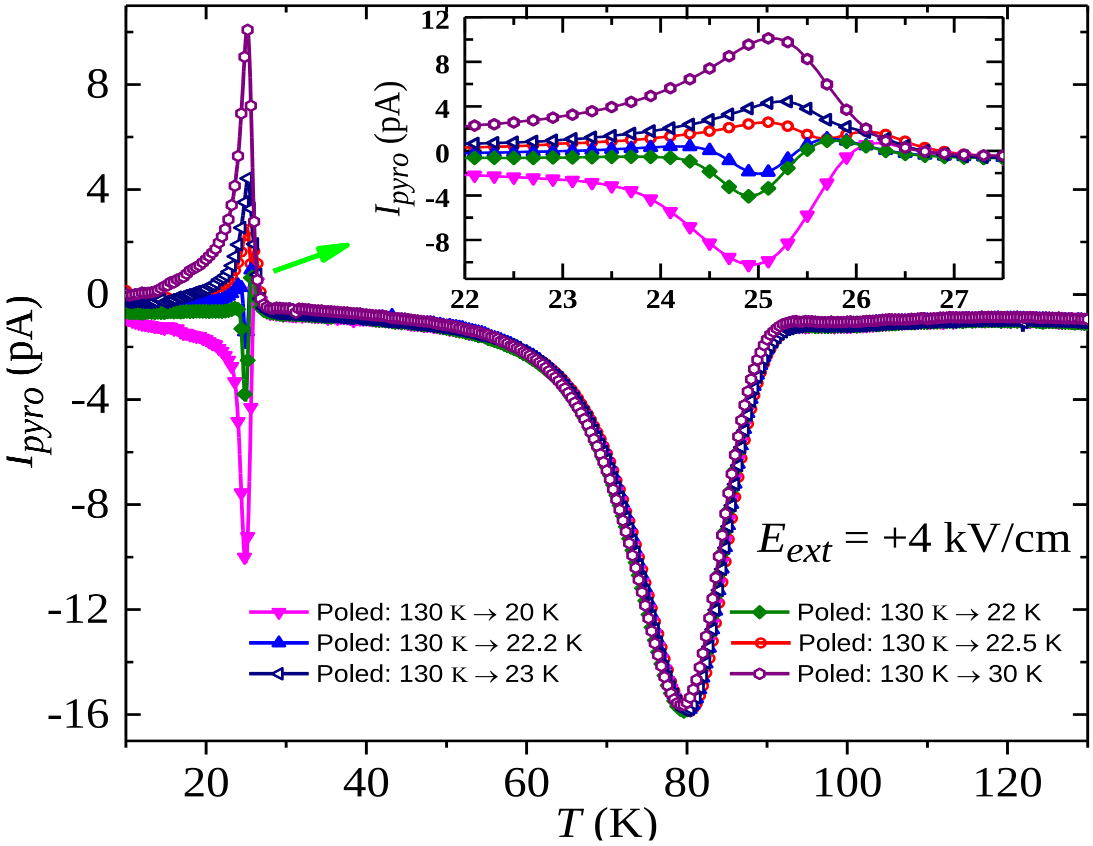

Figure 3.8 Pyrocurrent measured from 10 to 130 K after poling the sample form 130 K to various temperatures. Inset shows a magnified region near T_C.

Knowing the fact of the interplay of the internal field to the ferroelectric polarization, we have performed a study of pyrocurrent with varying the poling temperature range. From this study we see an almost compensation of ferroelectric polarization for the poling from 13 to 22.5 K because of two almost equal and opposite E_{ext} and E_{int} field present across the T_C while cooling the sample. This result is shown in figure 3.8.

3.3.4 Schematic of ferroelectric dipoles and TSFC carrier

The behavior of pyrocurrent due to the E_{ext} (figure 3.6(a)), E_{int} (figure 3.6(b)) and their combined effect (figure 3.2) can be better understood from the orientation of ferroelectric domains with respect to the poling field, as shown in the diagram (figure 3.9). In this diagram, as the crystallographic directions are randomly oriented to the applied electric field, we have considered the dipolar orientation of each grain along the applied field direction. The diagram in figure 3.9(a) represents the effect of E_{ext} on the orientation of ferroelectric dipoles (green color). This corresponds to the negative depolarization current as shown in figure 3.6(a). Figure 3.9(b) depicts the formation of the E_{int} due to TSFC carriers when the sample is cooled under the external poling field across the temperature range, 130 –50 K. Under an applied field (E_{ext}), the charge carriers accumulate near the grain boundaries and frozen-in during cooling and thus form electric dipoles. These charges act as an internal poling field below the freezing temperature (T ≈ 60 K), and remain even after removing the E_{ext} field. During this process, the free charge carriers move to oppositely charged electrodes, the polarity of ($\mp$) the E_{int} is opposite ($\pm$) to that of the E_{ext}. The effect of negative internal field (-E_{int}) alone on the ferrelectric dipoles is shown in figure 3.9(c) in red color, which corresponds to the positive pyrocurrent (I_{pyro}) peak observed in figure 3.6(b). Finally, we discuss the behavior of pyrocurrent shown in figure 3.2, where the sample was cooled across the T_C under both $+E_{ext}$ and -E_{int} fields simultaneously. In this case, we may anticipate that the resultant pyrocurrent may be the effect of the sum of the pyrocurrent behavior under external (figure 3.6(a)) and internal poling fields (figure 3.6(b)). In fact, it is rather a combination of pyrocurrent due to the effective external field ($E_{eff} = E_{ext} - E_{int}$) and DC-biased current corresponding to the internal field. Figure 3.9(d) represents ferroelectric domain orientation in the temperature interval $10\text{ K} < \text{T} < T_C$ after the simultaneous electric poling (+ E_{ext} and -E_{int}), where we see that there are two oppositely aligned ferroelectric domains. The bigger domains (green color) are formed because of the effective external field E_{eff} during the poling (130 –10 K) process. Upon warming in short-circuit condition; the polarized dipoles in the bigger domains would give a negative depolarization current resulting in random orientation of dipoles.

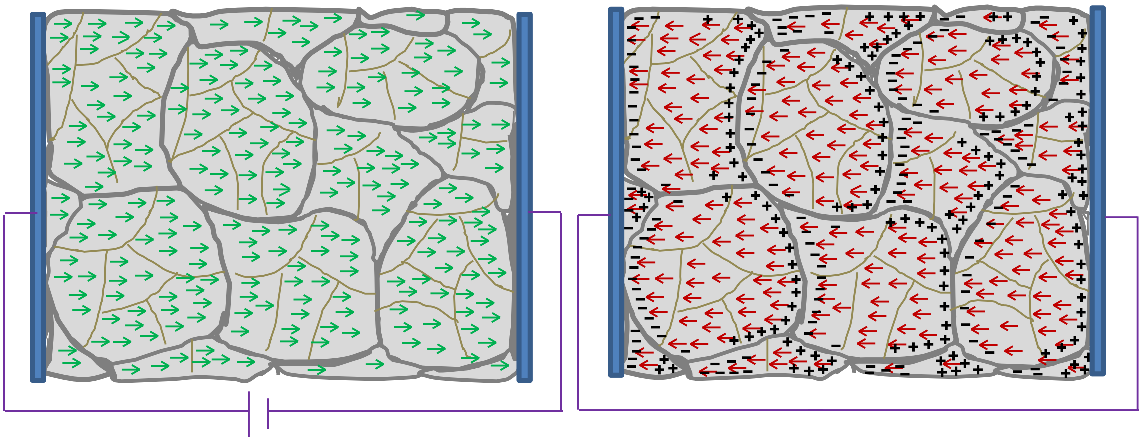
(a) Poled: 50 K → 10 K; T < T_C

(c) Poled: 130 K → 50 K; T < T_C

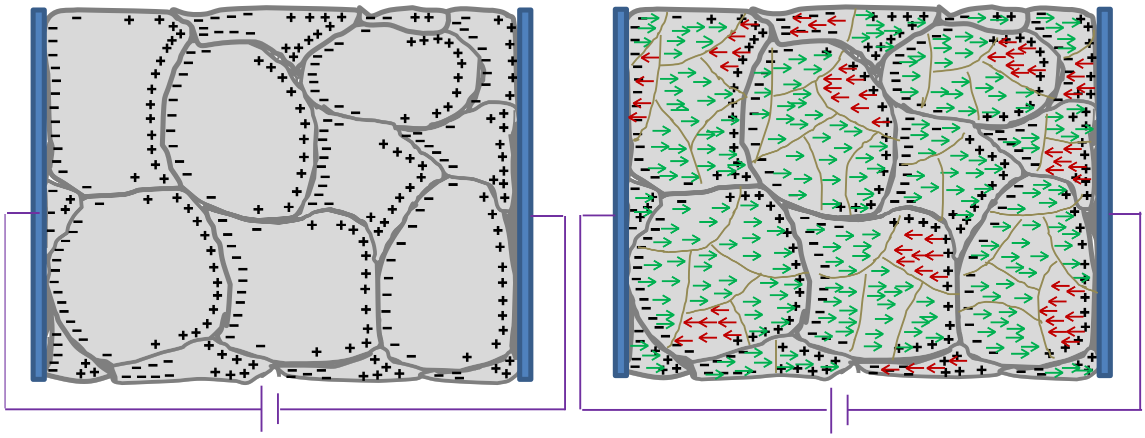
(b) Poled: 130 K → 50 K ; T < 50 K

(d) Poled: 130 K → 10 K; 10 K< T < T_C

Figure 3.9 Schematic diagram showing orientation of ferroelectric domains and polarization of TSFC carriers for different poling temperature range. (a) Ferroelectric dipole orientation due to external field (poled below 50 K), (b) formation of internal field after poling the sample from 130 to 50 K, (c) ferroelectric dipole orientation due to only internal electric field (poled from 130 to 50 K and cool down to 10 K) and (d) oppositely aligned ferroelectric domains due to the simultaneous presence of internal and external fields (poled from 130 to 10 K).

At the same time, the presence of (-E_{int}) field will align the random oriented dipoles in the opposite direction. This situation is similar to switching of ferroelectric polarization under opposite electric field except in the present case where it is driven by the thermal energy. As a result, the polarization current due to internal field will initially add up to the depolarization current. Close to the T_C, both the depolarization and polarization current, due to switching of polarization will cease and depolarization current resulting from -E_{int}

would give rise to positive component of the pyrocurrent peak ($+I_{pyro}$). In order to prove this hypothesis, we have carried out two different DC-biased current measurements. In the first measurement, the current data was recorded under the DC-bias field of +3 kV/cm after the sample was poled from 130 to 10 K under the poling field of +4 kV/cm. This experiment was carried out to nullify the effect of (-E_{int}) by applying a positive DC-bias of magnitude equivalent to $E_{int} \approx 0.75 E_{ext}$. This should be equivalent to pyrocurrent behavior under the poling field of $E_{eff} \simeq$ (1 kV/cm). In the second experiment, to obtain the effect of internal field (-E_{int}) alone on pyrocurrent, the current was measured under a DC-bias of -3 kV/cm which is equivalent to -E_{int}. This would give rise to a polarization and depolarization current while warming the sample during the pyrocurrent measurement. Results of these two experiments are shown in figure 3.7 (b) where we have shown the sum of these two DC-biased current data (open circle) which reproduces the pyrocurrent behavior observed in figure 3.2.

3.4. Conclusion

In conclusion, pyroelectric current measurements on a polycrystalline $TbMnO_3$ demonstrate that the internal electric field generated by thermally stimulated free charge carriers manifests itself as a pyrocurrent peak in the paraelectric state. The differences between the nature of pyrocurrent due to ferroelectricity and the free charge carriers have been discussed, which would be helpful in characterizing multiferroic materials. The effect of interplay of internal and external poling fields on ferroelectric polarization has been explained by combined pyrocurrent and DC-biased current measurement. More importantly, we have shown that a simple DC-biased current measurement can distinguish pyro-current peaks originating from ferroelectric polarization and free charge carriers. Further, it is important to note that a number of materials have been shown as an intrinsic multiferroic or magnetoelectric in the literature exploiting the DC-bias technique. Also it has been shown that the internal electric field can even switch the polarization in opposite direction due to relaxation of the ferroelectric dipoles when subjected to keep for a long time just below the T_C after poling with the external as well as internal field simultaneously.

References

[1] T. Kimura, T. Goto, H. Shintani, K. Ishizaka, T. Arima, and Y. Tokura, Nature **426**, 55 (2003).

[2] H. Katsura, N. Nagaosa, and A. V. Balatsky, Phys. Rev. Lett. **95**, 057205 (2005).

[3] M. Staruch, G. Lawes, A. Kumarasiri, L. F. Cotica, and M. Jain, Appl. Phys. Lett. **102** (2013).

[4] T. Kimura, Y. Sekio, H. Nakamura, T. Siegrist, and A. P. Ramirez, Nat. Mater. **7**, 291 (2008).

[5] S.-W. Cheong and M. Mostovoy, Nat. Mater. **6**, 13 (2007).

[6] Y. Tokunaga, Y. Taguchi, T.-h. Arima, and Y. Tokura, Nat. Phys. **8**, 838 (2012).

[7] T. Kimura, G. Lawes, T. Goto, Y. Tokura, and A. P. Ramirez, Phys. Rev. B **71**, 224425 (2005).

[8] H. Schmid, Ferroelectrics **162**, 317 (1994).

[9] W. Kleemann and P. Borisov, in *Smart Materials for Energy, Communications and Security*, edited by I. Luk'yanchuk, and D. Mezzane (Springer Netherlands, 2008), pp. 3.

[10] H. Béa, M. Gajek, M. Bibes, and A. Barthélémy, J. Phys.: Condens. Matter **20**, 434221 (2008).

[11] N. A. Spaldin and M. Fiebig, Science **309**, 391 (2005).

[12] J. Wang *et al.*, Science **299**, 1719 (2003).

[13] J. Dho, X. Qi, H. Kim, J. L. MacManus-Driscoll, and M. G. Blamire, Adv. Mater. **18**, 1445 (2006).

[14] N. A. Hill, J. Phys. Chem. B **104**, 6694 (2000).

[15] T. Kimura, Annual Review of Condensed Matter Physics **3**, 93 (2012).

[16] Y. Kitagawa, Y. Hiraoka, T. Honda, T. Ishikura, H. Nakamura, and T. Kimura, Nat. Mater. **9**, 797 (2010).

[17] S. M. Feng, Y. S. Chai, J. L. Zhu, N. Manivannan, Y. S. Oh, L. J. Wang, Y. S. Yang, C. Q. Jin, and K. H. Kim, New J. Phys. **12**, 073006 (2010).

[18] C. B. Sawyer and C. H. Tower, Phys. Rev. **35**, 269 (1930).

[19] J. F. Scott, J. Phys.: Condens. Matter **20**, 021001 (2008).

[20] M. Fukunaga and Y. Noda, J. Phys. Soc. Jpn. **77**, 064706 (2008).

[21] Y. Chai, Y. Oh, L. Wang, N. Manivannan, S. Feng, Y. Yang, L. Yan, C. Jin, and K. H. Kim, Phys. Rev. B **85**, 184406 (2012).

[22] G. Lawes *et al.*, Phys. Rev. Lett. **95**, 087205 (2005).

[23] O. Heyer, N. Hollmann, I. Klassen, S. Jodlauk, L. Bohatý, P. Becker, J. A. Mydosh, T. Lorenz, and D. Khomskii, J. Phys.: Condens. Matter **18**, L471 (2006).

[24] S. Jodlauk, P. Becker, J. A. Mydosh, D. I. Khomskii, T. Lorenz, S. V. Streltsov, D. C. Hezel, and L. Bohatý, J. Phys.: Condens. Matter **19**, 432201 (2007).

[25] R. D. Johnson, L. C. Chapon, D. D. Khalyavin, P. Manuel, P. G. Radaelli, and C. Martin, Phys. Rev. Lett. **108**, 067201 (2012).

[26] Y. Kohara, Y. Yamasaki, Y. Onose, and Y. Tokura, Phys. Rev. B **82**, 104419 (2010).

[27] M. Staruch, D. Violette, and M. Jain, Mater. Chem. Phys. **139**, 897 (2013).

[28] F. Schrettle, P. Lunkenheimer, J. Hemberger, V. Y. Ivanov, A. A. Mukhin, A. M. Balbashov, and A. Loidl, Phys. Rev. Lett. **102**, 207208 (2009).

[29] L. G. D. Silveira, G. S. Dias, L. F. Cótica, J. A. Eiras, D. Garcia, J. A. Sampaio, F. Yokaichiya, and I. A. Santos, J. Phys.: Condens. Matter **25**, 475401 (2013).

[30] Y. A. Park, K. M. Song, and N. Hur, J. Korean Phys. Soc. **53**, 3356 (2008).

[31] P. Lunkenheimer, V. Bobnar, A. Pronin, A. Ritus, A. Volkov, and A. Loidl, Phys. Rev. B **66**, 052105 (2002).

[32] P. Lunkenheimer, S. Krohns, S. Riegg, S. Ebbinghaus, A. Reller, and A. Loidl, The European Physical Journal Special Topics **180**, 61 (2009).

[33] X. Zhang *et al.*, Appl. Phys. Lett. **104**, 062903 (2014).

[34] C. De, T. H. Kim, K. H. Kim, and A. Sundaresan, Phys. Chem. Chem. Phys. **16**, 5407 (2014).

[35] A. Ruff, S. Krohns, F. Schrettle, V. Tsurkan, P. Lunkenheimer, and A. Loidl, Eur. Phys. J. B **85**, 1 (2012).

[36] N. Ikeda *et al.*, Nature **436**, 1136 (2005).

[37] M. Maglione and M. Subramanian, Appl. Phys. Lett. **93**, 032902 (2008).

Chapter 4

Part-I

Effect of rare-earth on multiferroic properties of $R_{0.5}Dy_{0.5}MnO_3$ (R = Eu and Gd)*

Summary

This chapter involves various intriguing multiferroic states induced by the rare-earth magnetism which is primarily observed in two polycrystalline material $R_{0.5}Dy_{0.5}MnO_3$ (R = Eu and Gd), then confirmed by single crystal of $Gd_{0.5}Dy_{0.5}MnO_3$. The microscopic origin is corroborated by time of flight neutron diffraction data recorded in a Gd-160 isotope enriched powder sample. It exhibits a spontaneous electric polarization P_a as well as P_c which results from the cycloidal spins lying on the (102) lattice plane. Below 10 K, a short-range magnetic ordering of rare-earth ions triggers the Mn-cycloidal plane to a helical spin state with a small cycloidal component, which is consistent with the suppression of both P_a and P_c but with a small remnant polarization. Application of external magnetic field ($H||a$) suppresses P_a but enhances P_c due to combined action of rotation of cycloidal plane and field induced long range ferromagnetic ordering of R-ions. Remarkably, a large polarization (P_a ~ 2500 μC/m^2) is observed at 2 K under an applied magnetic field ($H||b$) of 4 T.

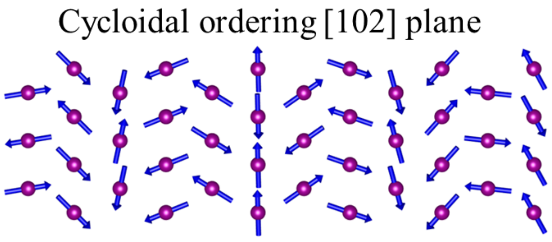

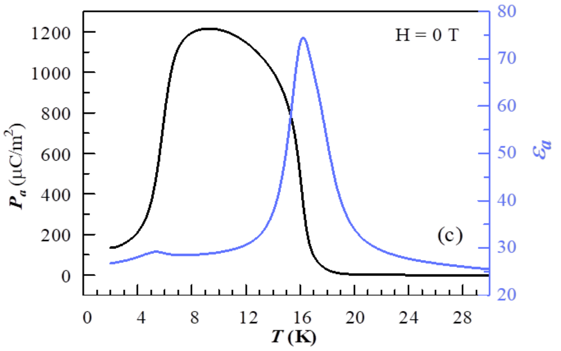

---

*Paper based on this work **C. De** and A. Sundaresan, *App. Phys. Lett.* 107, 052902 (2015), © (2015) by the AIP Publishing. **C. De** *et al.* to be communicated (2018).

4.1 Introduction

There has been a resurgence of interest in multiferroic materials showing simultaneously present magnetic and ferroelectric orders with a promising cross linking between them, which is an important parameter for applications such as magnetoelectric memory, spintronics, sensors and magnetoelectric microwave devices [1-10]. Coexisting magnetic and electric dipole order are often found in frustrated magnets where the electric polarization is induced by unconventional spin states breaking inversion symmetry of the crystal lattice. These materials also show complex phase diagrams due to competition between magnetic states with close free energies as discussed in the section "rare-earth manganite phase diagram" in Chapter 1. In orthorhombic rare-earth (*R*) manganites *R*MnO$_3$ (*R* = Dy, Tb and Gd), ferroelectricity is associated with the cycloidal spiral ordering of the Mn spins [1, 2, 11, 12] (see figure 1.7). According to the inverse Dzyaloshinskii-Moriya mechanism and the spin current model of the magnetically induced ferroelectricity, the electric polarization vector lies in the spiral plane and is perpendicular to the spiral wave vector [13-15]. The orientation of the plane, in which the spins rotate depends on the ionic size of R-ion and applied magnetic fields [16]. For example, *R*MnO$_3$ with *R* = Tb and Dy show the cycloidal spiral state with the wave vector along the *b*-axis and spins lying onto the *bc* plane, which induces a polarization, P_c, in the *c*-direction due to the symmetry $Pbn2_11$'(0b0)000s [17, 18]. Under an applied magnetic field along the *b*-axis, the polarization vector re-orients from the *c*- to *a*-direction due to flop of spiral spins from the *bc* to the *ab* plane where the symmetry changes to $P2_1nm1$'(0b0)000s [11]. GdMnO$_3$ is close to the borderline separating the nonpolar collinear A-type antiferromagnetic (AFM) state from polar non-collinear spiral states (phase diagram is shown in Chapter 1, figure 1.8) [11]. Its precise location in the phase diagram remains a controversy and the nature of various competing phases is not well understood. Magnetization and single-crystal synchrotron x-ray data suggest that below 23 K Mn spins order in the A-type AFM state which is weakly ferromagnetic and paraelectric [19, 20]. This contradicts a small electric polarization observed in a narrow temperature interval around the Gd ordering temperature (~ 6.5 K) [11, 12]. Moreover, magnetic field applied along the *b*-axis induces a ferroelectric state below 23 K with the electric polarization, P_a, comparable to that in Tb and Dy compounds. In this state, both Mn and Gd spins show a commensurate modulation along the *b*-axis [19, 20]. The field-induced ferroelectricity is believed to originate from the *ab* cycloidal plane [20, 21].

Indeed, in a related compound, $\mathrm{Gd_{0.7}Tb_{0.3}MnO_3}$ the *ab* cycloidal state with the polarization parallel to the *a* axis was observed by neutron diffraction study [22].

In addition to the strong effect of the size of rare-earth ions on competing exchange interactions between $\mathrm{Mn^{3+}}$ spins, and thus the magnetic structure and dielectric properties of rare-earth manganites, the coupling between the R-ion and $\mathrm{Mn^{3+}}$ magnetic subsystems also plays an important role. In the case of $\mathrm{TbMnO_3}$, the electric polarization mainly comes from the Mn-magnetic subsystem. On the other hand, in $\mathrm{DyMnO_3}$, an incommensurate magnetic ordering of Dy-ions, which is induced by the spiral ordering of Mn-spins and with the same wave vector, gives a significant contribution to the total electric polarization. This is evident from the large polarization drop below the commensurate magnetic ordering of Dy-ions ($T_N^{Dy} = 7$ K) when the rare-earth ions no longer contribute to the electric polarization and only the polarization induced by Mn-spins remains [23]. These facts prompted a number of systematic studies of orthorhombic manganites with mixed R-ions [24, 25], which revealed rich phase diagrams resulting from competition of collinear and non-collinear, commensurate and incommensurate magnetic phases that can coexist in spatially uniform and phase separated states. A transition from *bc* cycloidal to *E*-type antiferromagnetic phase and coexistence of these two phases were well demonstrated in $\mathrm{Dy_{1-x}Ho_xMnO_3}$ [25]. A phase conversion of cycloidal (*bc* plane) to *E*-type ordering induced by the application of external pressure were evidenced in $\mathrm{TbMnO_3}$ leads to a large polarization (~1.0 $\mu\mathrm{C/cm^2}$) [26]. Yet, multiferroic properties of manganites near the phase boundary between the *ab* and *bc* cycloidal phases as well as effects of the interplay between the Mn and R magnetic orders are not well understood.

In order to shed light on the aforementioned scenario, we primarily investigated magnetic and dielectric properties of two mixed rare-earth manganites namely $\mathrm{Eu_{0.5}Dy_{0.5}MnO_3}$ (EDMO) and $\mathrm{Gd_{0.5}Dy_{0.5}MnO_3}$ (GDMO) in polycrystalline form. In the first compound, the average size of A-cations would be more than $\mathrm{Tb^{3+}}$ and in the second compound, it is almost same as $\mathrm{Tb^{3+}}$ thus both the compounds lie very close boundary of the *ab* and *bc* cycloidal spin structure in the rare-earth manganite phase diagram as shown in chapter 1 (figure 1.8). Indeed, we observe ferroelectric polarization in both the compounds below a cycloidal magnetic ordering as evidenced by the heat capacity data in comparison with our existing $\mathrm{TbMnO_3}$ data which is already presented in chapter 3.

While both GDMO and EDMO showed double peak structure in dielectric as well as in the pyrocurrent corresponding to the simultaneous presence of polarization along a- and c-direction, a remarkable increase in polarization under magnetic field was found in GDMO compound. For a detailed study of multiferroic character, including the various crystallographic directions in this mixed rare-earth manganite, we have grown the high quality large single crystal of $\mathrm{Gd_{0.5}Dy_{0.5}MnO_3}$ using floating zone furnace. For powder neutron diffraction study, we have synthesized polycrystalline $^{160}\mathrm{Gd_{0.5}Dy_{0.5}MnO_3}$ for the microscopic spin structures associated with the various multiferroic phases evidenced in our electric polarization measurements. The ferroelectric state of this material shows polarization both along the a- and c-axes, which is consistent with the fact that the cycloidal plane lies in [102] plane, as revealed by neutron diffraction. Intriguingly, the short-range magnetic ordering of R-ions suppresses the ferroelectric spiral state of $\mathrm{Mn^{3+}}$ spins and induces a helical spin structure with a cycloidal component that results in a weak but finite electric polarization. We discuss the complex temperature and field dependence of the electric polarization of GDMO in terms of contributions of $\mathrm{Mn^{3+}}$ and R-spins. Further, we have studied a novel multiferroic memory effect in the single crystal sample which is presented in Part-II of this chapter.

4.2 Experiments

Polycrystalline samples were prepared by standard solid state reaction method. Rare earth oxides were preheated for overnight before using them. Stoichiometric amount of Eu_2O_3, Gd_2O_3, Dy_2O_3, Tb_4O_7 and Mn_2O_3 were taken in a agate mortar and pestle and thoroughly mixed. The mixtures were heated at 1100, 1200 and 1300 °C subsequently in air. Finally the powder was pressed into pellets and sintered at 1400 °C in air. Phase purity of the samples was checked by X-ray diffraction (XRD) patterns using a PANalytical Empyrean alpha-1 diffractometer build with monochromatized Cu $K\alpha_1$ radiation. Single crystals were grown by the floating zone method as described in detail in chapter 2. The single phase polycrystalline powder samples as prepared via solid state reaction have been used for the single crystal growth. The phase purity of the single crystal was confirmed by P-XRD technique after grounding the single crystal sample. Crystal homogeneity was confirmed by optical microscopy under polarized light and scanning electron microscopy (Zeiss Ultra Plus, Germany). Using Laue diffractometer along with orient express software, three plate-like samples cut along the principle axes

[100], [010] and [001] with a dimension of about 2 mm × 2 mm × 0.3 mm were used for the physical property measurements. Neutron diffraction measurements were made on polycrystalline sample containing ^{160}Gd isotope on the high-resolution powder diffractometer “WISH” at ISIS, UK [27]. The Jana2006 software were used to perform the Rietveld refinements of the neutron data whereas group theoretical calculation were carried out with the help of the ISODISTORT software [28, 29]. Magnetic measurements were performed in VSM SQUID. Heat capacity was measured in Physical Property Measurement System (PPMS). Dielectric constant measurement was performed using Agilent E4980A Precision LCR meter. Pyrocurrent was measured using Keithley Electrometer (6517A). For the pyroelectric current measurement, the sample was cooled across the transition temperature with applied electric field. At the low temperature the electrodes were shorted. After waiting about 30 min, the electrometer was connected to the sample and the current was measured while heating the sample with 4 K/min rate without applying any electric field. For the DC-bias current measurement, the sample was cooled down to the lowest temperature without an electric poling and the current is recorded while warming the sample in presence of an electric field. This procedure enables to obtain both the polarization and depolarization currents in a single measurement at the transition temperature which is already discussed in detail in chapter 3 [30]. This technique has already been applied in several multiferroic studies [31-33].

4.3 Results and discussions

4.3.1 Results on polycrystalline EDMO and GDMO

Figure 4.1 shows Rietveld refined powder X-ray diffraction pattern using orthorhombic structure model for all the three compounds. Table 4.1 shows the obtained cell parameters which are in accordance with the parent compounds. A more detailed crystal structure parameter obtained through neutron diffraction study is given in the following section. Figure 4.2(a, b and c) shows specific heat divided by temperature (C/T) (left-axis) and magnetization (M) data, measured under field cooled warming (100 Oe) condition (right-axis), with temperature for EDMO, GDMO and TMO, respectively. Since the rare-earth paramagnetic moments are higher than the Mn^{3+} antiferromagnetic moment, we do not observe magnetic anomaly at magnetic ordering temperatures of Mn^{3+}ions. On the other hand, the (C/T) data clearly show the incommensurate sinusoidal antiferromagnetic ordering (T_N), commensurate cycloidal ordering (T_C) and R^{3+} ordering [1], except that the rare-earth moments in EDMO do not order down to 2 K which can be accounted to the substitution of non-magnetic rare-earth (Eu^{3+}).

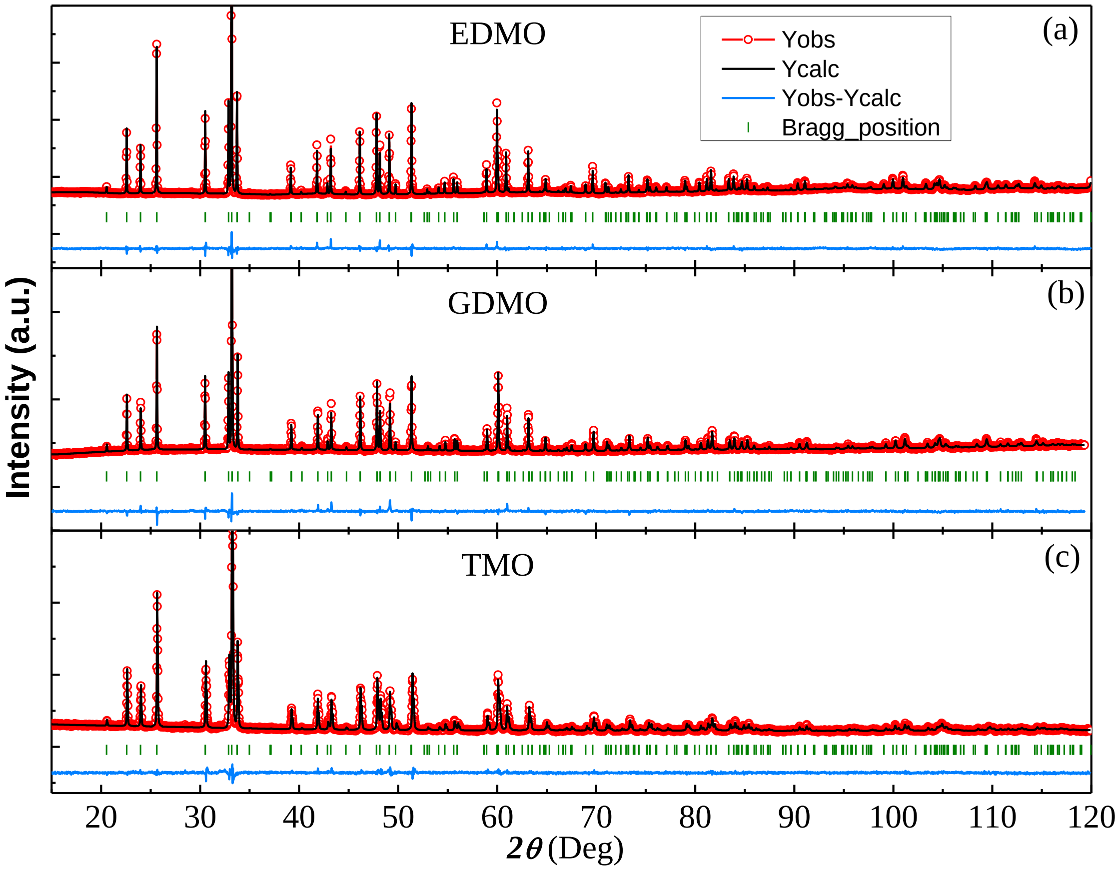

Figure 4.1 X-ray diffraction pattern of (a) $Eu_{0.5}Dy_{0.5}MnO_3$ (b) $Gd_{0.5}Dy_{0.5}MnO_3$ (c) $TbMnO_3$ at room temperature. Rietveld refinement was carried out using *Pbnm* space group.

Table 4.1 Lattice parameters for all the three compounds obtained from the refinement.

Compound name	a (Å)	b (Å)	c (Å)	V (Å^3)
$Eu_{0.5}Dy_{0.5}MnO_3$	5.31020(6)	5.85375(7)	7.41499(8)	230.492(4)
$Gd_{0.5}Dy_{0.5}MnO_3$	5.29950(8)	5.85520(9)	7.40597(11)	229.804(6)
$TbMnO_3$	5.30207(2)	5.84313(8)	7.40737(9)	229.486(5)

The center panels (d, e and f) show dielectric constant (left-axis) and loss data (right-axis) measured at 50 kHz with different external magnetic fields (0, 4 and 8 T). For EDMO and GDMO, the zero field dielectric and loss data show a broad doublet peak which becomes a single peak with a slight positive shift of temperature under applied magnetic field. On the other hand, only a single peak in dielectric and loss data is observed for TMO which becomes broad in presence of magnetic field. Pyrocurrent data of the samples recorded at

4 K/min from 10 to 30 K at 0, and 8 T field, after poling the samples with an electric field (E = 8 kV/cm, H⊥E) from 35 to 10 K, is displayed in bottom panels (g, h and i).

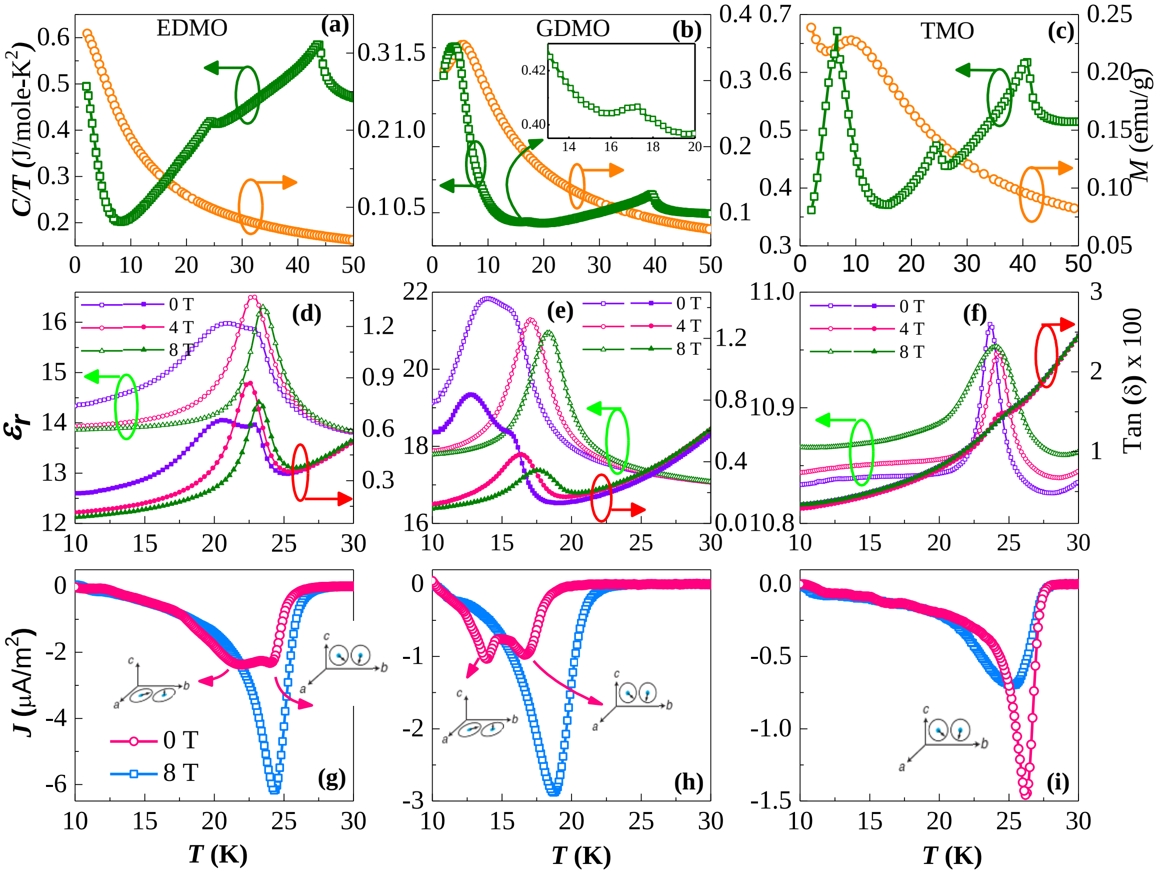

Figure 4.2 First, second and third column represents the data of $Eu_{0.5}Dy_{0.5}MnO_3$, $Gd_{0.5}Dy_{0.5}MnO_3$ and $TbMnO_3$, respectively where left-axis in a, b and c shows heat capacity divided by temperature and the right axis shows magnetization *vs.* temperature data. Left-axis in (d, e and f) shows dielectric constant and the right-axis shows loss *vs.* temperature. (g, h and i) shows pyroelectric current *vs.* temperature data.

From these data, we infer that the ferroelectric transition temperatures (T_C) for EDMO, GDMO and TMO are 26, 18 and 27 K, respectively. This is in agreement with the heat capacity and dielectric anomaly. It is interesting to note that the zero field pyrocurrent data for both EDMO and GDMO show two peak features but a single peak for TMO, similar to that observed in dielectric and loss data. We suggest that the two peak feature in dielectric and pyrocurrent data indicates the presence of polarization in both *a*- and *c*-directions. This indicates possible coexistence of both *ab* and *bc* cycloidal phases due to fluctuation of compositions of Gd and Dy or the cycloidal plane lies in a different plane which allows the polarization along both the directions or there could be a temperature dependent reorientation of cycloidal spins. The thermal hysteresis observed in dielectric constant peak while cooling and warming suggests that the phase transition between the two cycloidal phases can be of first order (figure 4.3).

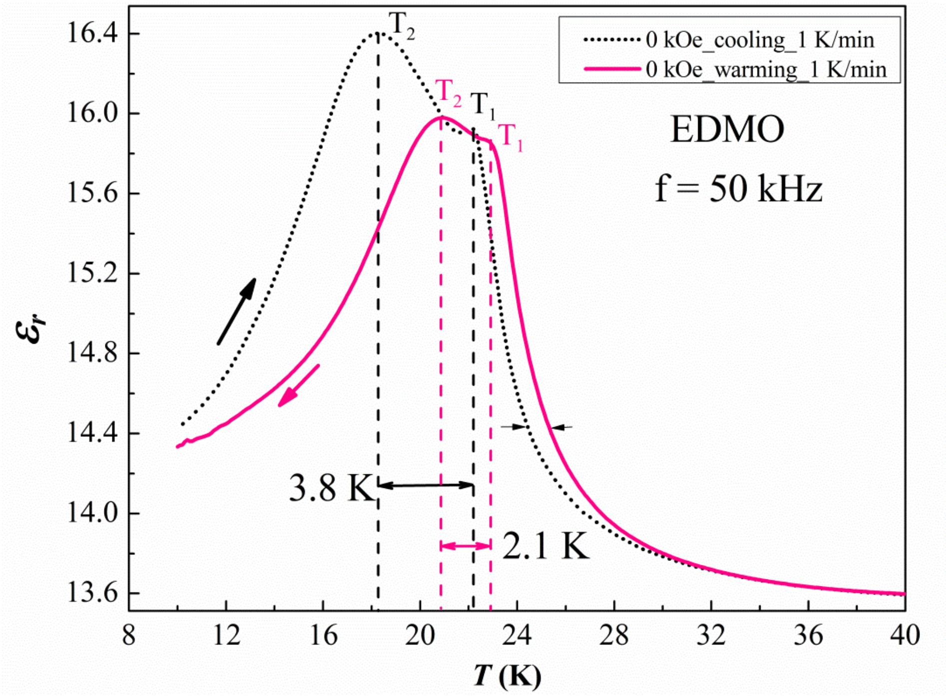

Figure 4.3 Dielectric constant while warming and cooling in EDMO.

It requires a single crystal study to confirm the actual case which we have presented in the following sections. Based on the theoretically obtained magnetoelectric phase diagram of temperature versus J_2 (NNN exchange interaction), we attribute the low temperature peak to *ab* and high temperature peak to *bc* cycloidal ordering and the corresponding polarization direction should be along *a* and *c*-axis [18]. Under an applied magnetic field (8 T), the two peak feature disappears and becomes a single peak with enhanced pyrocurrent and significant increase of T_C. In contrast, the magnitude of the single peak observed for TMO is decreased with magnetic field without any significant change in T_C (figure 4.2). Figure 4.4 (a, b and c) shows magnetodielectric (MD) data measured at 50 kHz while sweeping the magnetic field from -7 T to +7 T at different temperatures for all the three samples. It is interesting to notice the distinct behavior of MD in EDMO and GDMO from TMO. Above T_C, all the three samples exhibit positive MD and it reaches a maximum around T_C. Below T_C, the MD in TMO remains positive and at 10 K, it levels off above 40 kOe as shown in figure 4.4(c). In contrast, the mixed rare earth samples show a crossover from positive to negative at the intermediate temperatures between the double peak in the pyrocurrent data observed in figure 4.2 [2]. Positive MD shows a broad maximum, corresponding to a critical field, which shifts to lower field with decreasing temperature. This behavior may indicate a change in direction of polarization. Further a large MD (12%) can be observed in GDMO.

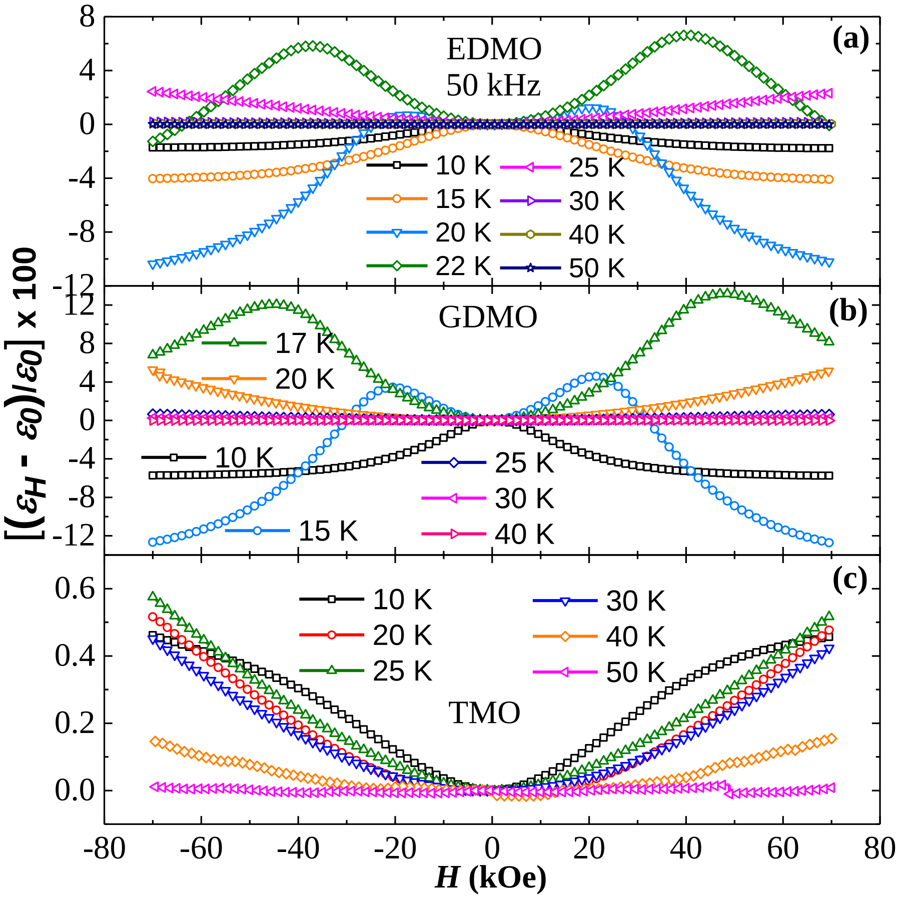

Figure 4.4 Magnetodielectric data of (a) $Eu_{0.5}Dy_{0.5}MnO_3$ (b) $Gd_{0.5}Dy_{0.5}MnO_3$ and (c) $TbMnO_3$ measured at 50 kHz at various temperatures.

Figure 4.5(a, b and c) shows temperature dependent polarization data, at different magnetic fields, obtained by integrating the pyrocurrent (inset), recorded after poling the samples with E = 8 kV/cm (H⊥E). In TMO, it is known that the polarization changes its direction from *c*- to *a*-axis when magnetic field is applied along the *b*-direction [1, 11]. However, the observed polarization along *a*-direction could be smaller because of the lack of complete flop of *bc* cycloidal phase due to high domain wall formation energy, determined by the competition between Zeeman energy and magnetic anisotropy [34-36]. In the present case, the polycrystalline TMO shows only a small decrease in polarization (ΔP =12% at 8 T) with magnetic field which could be accounted to the same reason figure 4.5(c).

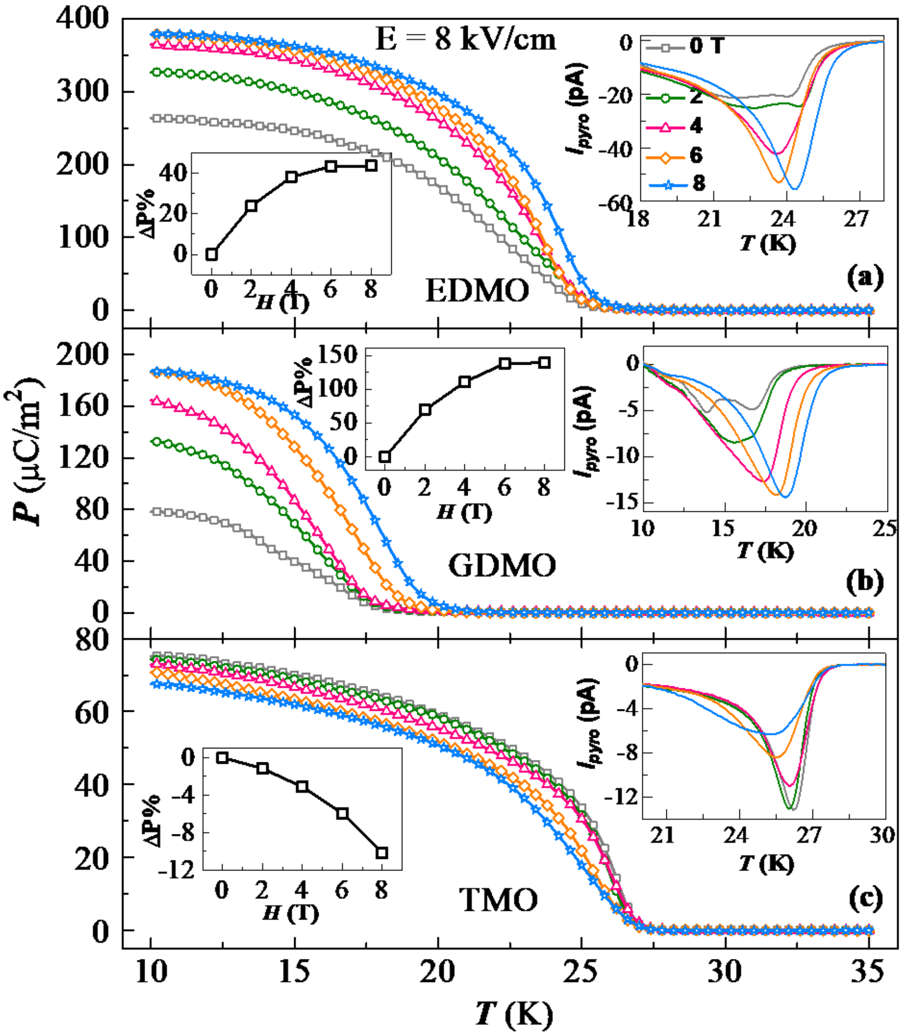

Figure 4.5 Polarization data of (a) EDMO (b) GDMO and (c) TMO measured at various magnetic fields. Inset (right side) shows pyrocurrent data. Inset (left side) shows normalized $\triangle P = [((P(H)-P(0))/P(0))x100]$ change of polarization under magnetic field.

In contrast, a dramatic change of polarization is observed in the two mixed rare-earth manganites, shown in figure 4.5(a and b). While the magnitude of the polarization at zero field is fairly large (almost four times that of TMO) in EDMO, a remarkable enhance of polarization (>140% at 8 T) is observed in GDMO (figure 4.5(b)). It is clear from the polarization data (shown in the insets of figure 4.5) that the two peaks gradually becomes a single peak and there is a magnetic field tunability of polarization in the mixed rare-earth compounds. This intriguing magnetoelectric properties demand a further study which may answer all the findings. However, from the polycrystalline sample we cannot see the polarization along the particular directions as well as the effect of magnetic field applied along various directions which is necessary to know the detailed magnetoelectric properties in this mixed rare-earth manganites. Therefore, we choose $Gd_{0.5}Dy_{0.5}MnO_3$ to grow single crystal since it has the highest magnetic field tunability of ferroelectric polarization.

4.3.2 Results on single crystal $Gd_{0.5}Dy_{0.5}MnO_3$

4.3.2.1 Crystal Laue pattern and images

The as grown crystal and Laue diffraction pattern for (100), (010) and (001) direction and thins cut sample with crystallographic directions is shown in figure 4.6 which were used for the electrical as well as magnetic property measurements.

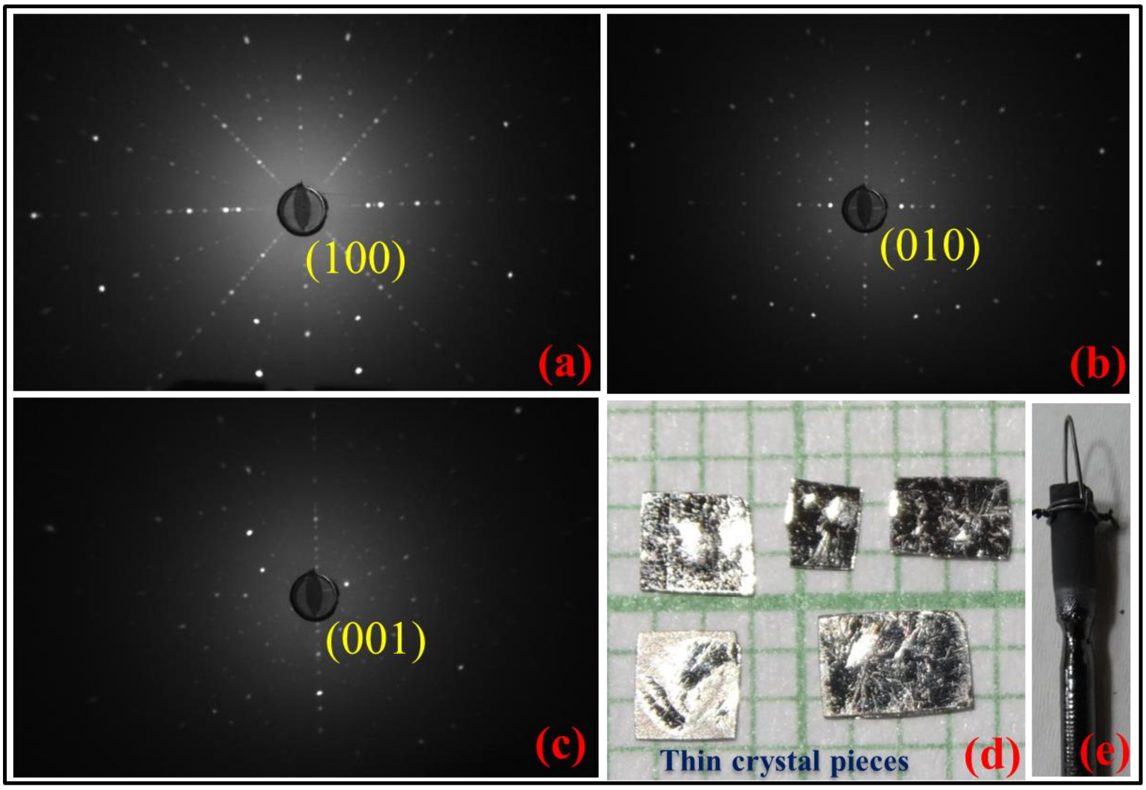

Figure 4.6 Laue diffracted pattern for (a) along (100), (b) along (010) and (c) along (001) directions. (d) Thin oriented crystal pieces (e) as grown crystal.

4.3.2.2 Magnetic phase transitions

Figures 4.7(a) and (b) show temperature dependence of heat capacity divided by temperature (C/T) and magnetization, $M(T)$ along the three crystallographic axes. Heat capacity data show three anomalies that can be associated with the collinear incommensurate ordering ($T_N^{Mn} = 39.5$ K), cycloidal ordering ($T_C = 16.5$ K) of Mn spins and ordering of R-ions at $T_N^R = 5$ K, as observed in the polycrystalline sample (see figure

4.2(a-c)) [1]. However, it should be noted that the C/T anomaly and the corresponding $M(T)$ anomaly at T_N^R are significantly broad (figure 4.7(b)). The large suppression of heat capacity peak at T_N^R under a magnetic field $H_b = 8$ T and the nature of $M(H)$ data (inset of figure 4.7(b)) indicates metamagnetic nature of R-ion ordering. The suppression of magnetization peak and the critical field of metamagnetic transition can be seen in figure 4.7(c and d). On the other hand, the anomaly at T_C becomes more prominent increasing by 3 K under $H_b = 8$ T (figure 4.7 (a)). The broad peak near 5 K disappears at higher magnetic field as seen in figure 4.7(c). A clear peak near 2 T at 2 K is corresponding to the critical field of metamagnetic transition as seen in figure 4.7(d)

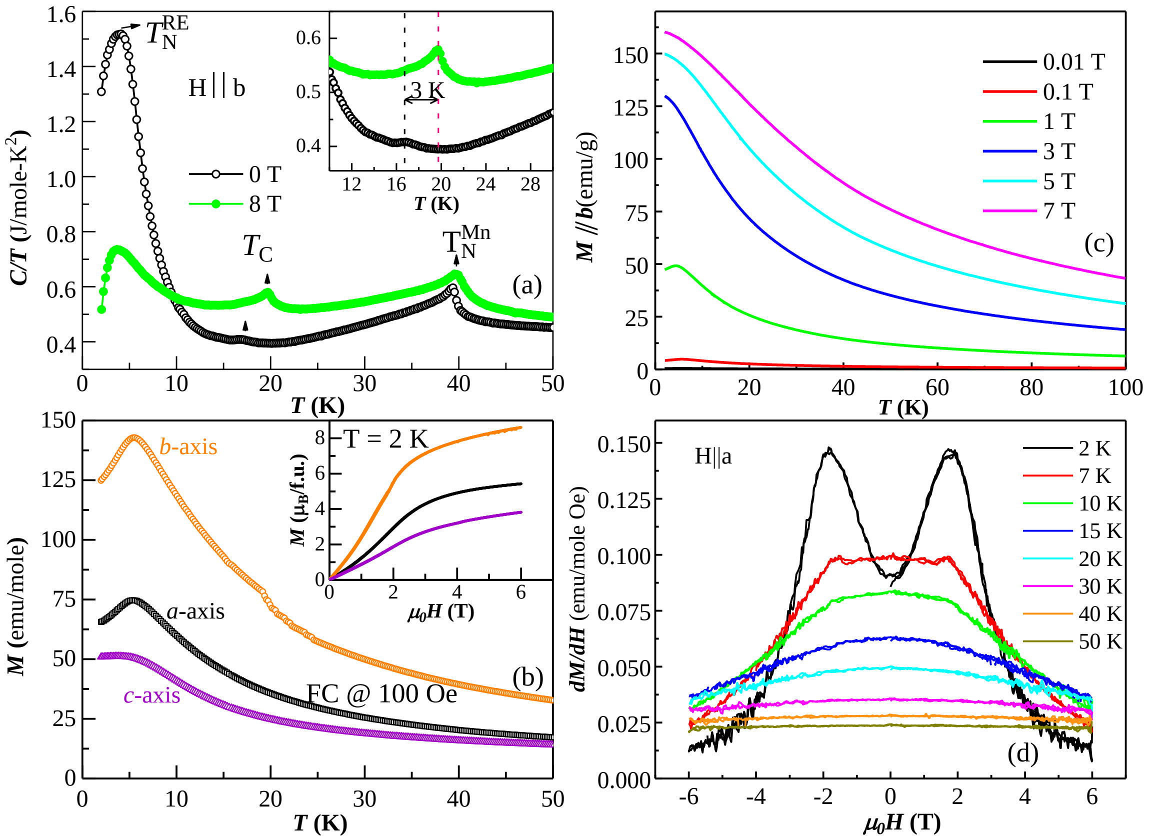

Figure 4.7 (a) and (b) show the heat capacity divided by temperature and magnetization as a function of temperature, respectively. Three anomalies corresponding to the Mn-spiral spin, cycloidal ordering and R-ion ordering at T_N, T_C, and T_N^{RE} can be clearly seen. (c) Magnetization along b-direction at various field. (b) Derivative of magnetization with field obtained from $M(H)$ along a-axis.

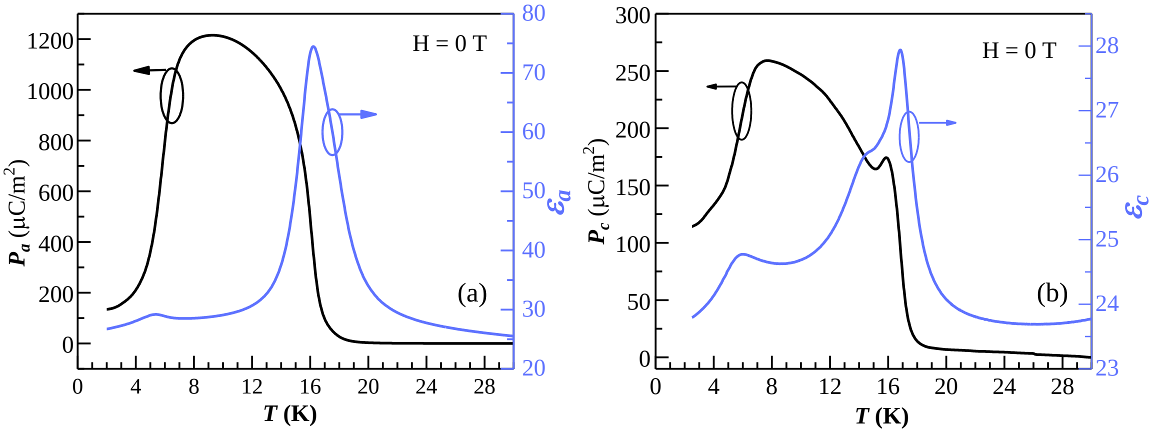

Figure 4.8 (a) and (b) show electric polarization P_a and P_c and ε_a and $\varepsilon_c$versus temperature, respectively.

4.3.2.2 Temperature-dependent spontaneous electric polarization

First, we discuss the unusual behavior of spontaneous electric polarization in the temperature range 2–30 K, measured after an electric poling (5.6 kV/cm) from 30 to 2 K. Figure 4.8(a) and (b) show development of spontaneous polarization both along the *a* and *c* directions (P_a and P_c), respectively below the cycloidal ordering temperature. This is consistent with the anomaly in the dielectric permittivities (ε_a and ε_c) along the *a*- and *c*-axis as shown in the respective figures. Intriguingly, the polarization P_a drops sharply at low temperatures from 1200 μC/m^2 at 7 K to a remnant polarization of ~ 100 μC/m^2 at 2 K. On the other hand, P_c drops from 200 μC/m^2 to 100 μC/m^2 in the same temperature interval. The decrease of electric polarization below 7 K indicates that the magnetic ordering of *R*-ions triggers the transition of the Mn magnetic subsystem into a non-ferroelectric (or a weakly ferroelectric) state. The suppression of the spiral ordering of Mn spins by the *R* magnetic ordering is unique to this compound. The simultaneous presence of P_a and P_c in GDMO may results from phase separation or by fluctuations of the local concentration of Gd/Dy-ions or the spiral plane to an intermediate plane between *ab* and *bc* induced by rare-earth anisotropy. This behavior is in agreement with the previous results on polycrystalline $Gd_{0.5}Dy_{0.5}MnO_3$ where we observed a double peak structure in the pyrocurrent as well as in the dielectric permittivity, ε (figure 4.2)[37]. The presence of dielectric anomaly in both ε_a and ε_c at around rare-earth ordering (~5 K) indicates that the low temperature state may be a new polar phase (see figure 4.9).

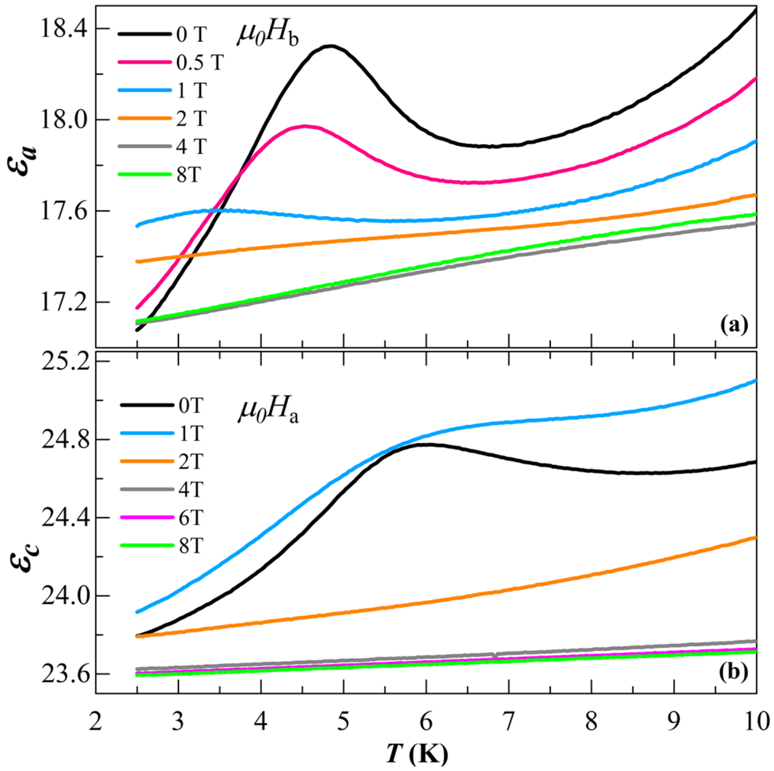

Figure 4.9 Dielectric constant at low temperature along *a* and *c*-direction under magnetic field along *b* and *a*-direction.

4.3.2.3 Effect of magnetic field (*H*||*a*) on the polarization (*P_a* and *P_c*)

When magnetic fields applied along the *a*-direction, P_a is suppressed while P_c increases along with the recovery of the low temperature polarization (figure 4.10(a, b)), so that P_c at 7 K and 2 T roughly equals P_a in zero field and *vice versa*. It is should be noted that there is a sudden decrease and increase of polarization in P_a and P_c, respectively, between 1 and 2 T. This behavior is due to continuous rotation of cycloidal plane from [102] plane towards *bc* plane. This is different from what is observed in $TbMnO_3$ and $DyMnO_3$ where $H||a$ forces the polarization to rotate from the *c*-axis to the *a*-axis because of the flop of cycloidal plane from *bc* to *ab* plane. As in $DyMnO_3$, ε_a and ε_c show high sensitivity to the applied magnetic field near the flop transition (see insets of Figure 4.10) – the so-called giant magneto-capacitance effect [2]. The ferroelectric Curie temperature increases by about 4 K under the magnetic field of 8 T.

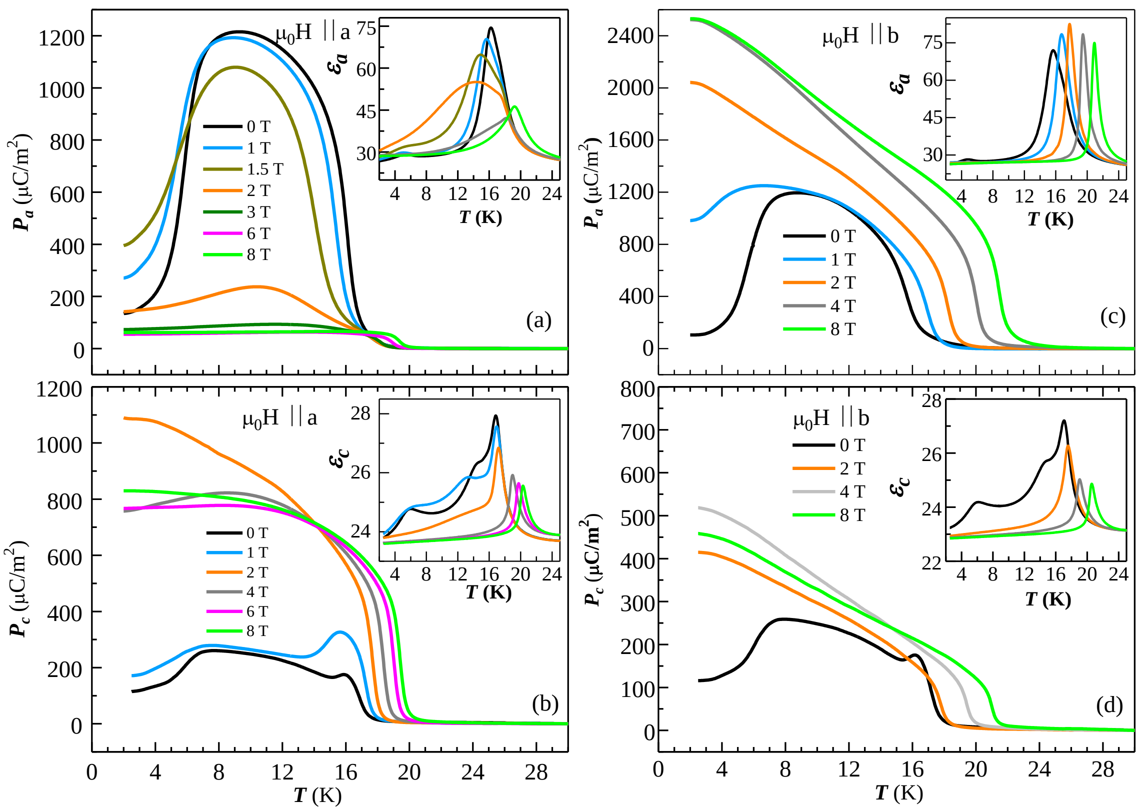

Figure 4.10 (a) and (b) show the suppression and enhancement electric polarization of P_a and P_c when magnetic field is applied along *a*-direction. (c) And (d) shows temperature-dependence of P_a and P_c under applied field along *b*-direction.

4.3.2.4 Effect of magnetic field ($H||b$) on the polarization (P_a and P_c)

When magnetic fields applied along the *b* axis, both the Curie temperature and polarization (P_a and P_c) increase monotonously with $H||b$ (Figure 4.10(c, d)). At $H||b =$ 8 T and 2 K, $P_a = 2500$ μC·m^{-2}, which is twenty five times larger than the zero-field value and is comparable to the polarization in the *ab* spiral state of $DyMnO_3$ induced by $H||b$ [11]. While $H||b$ in $TbMnO_3$ and $DyMnO_3$ induces the flop transition from the *bc*-spiral to the *ab*-spiral state [2, 11], no flop transition is found in GDMO: remarkably, the polarization along the *c*-axis, P_c, also increases: at $H||b = 8$ T it is five times larger than in zero field (figure 4.10(c)). Similar behavior is observed in $H||c$ is similar to that in $H||b$, except that the growth of P_a is less dramatic as shown in figure 4.11 for P_a, P_c ($H||c$)). Along *a*-axis, the increasing of polarization as well as T_C is higher compared to the *c*-axis. Furthermore, P_a has a maximum around 3 T and decreases upon a further increase of magnetic field. This behavior shows a good agreement with the dielectric constant under $H||c$, as seen in figure 4.11 (c, d). The polarization along *b*-direction (figure 4.12) shows a tiny polarization compared to the other direction of polarization which can be due to the small miss cut angle of the sample.

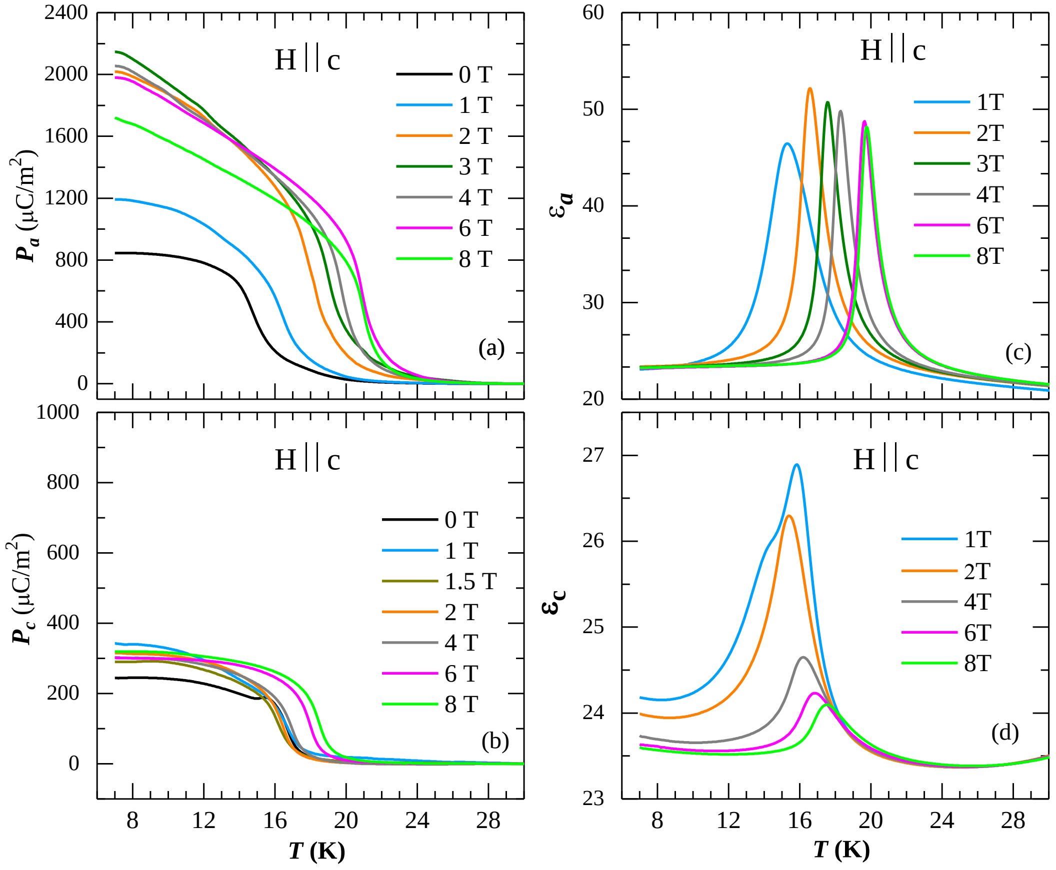

Figure 4.11 (a) and (b) Polarization and (c) and (d) shows dielectric constant along *a* and *c*-direction under magnetic field along *c*-direction.

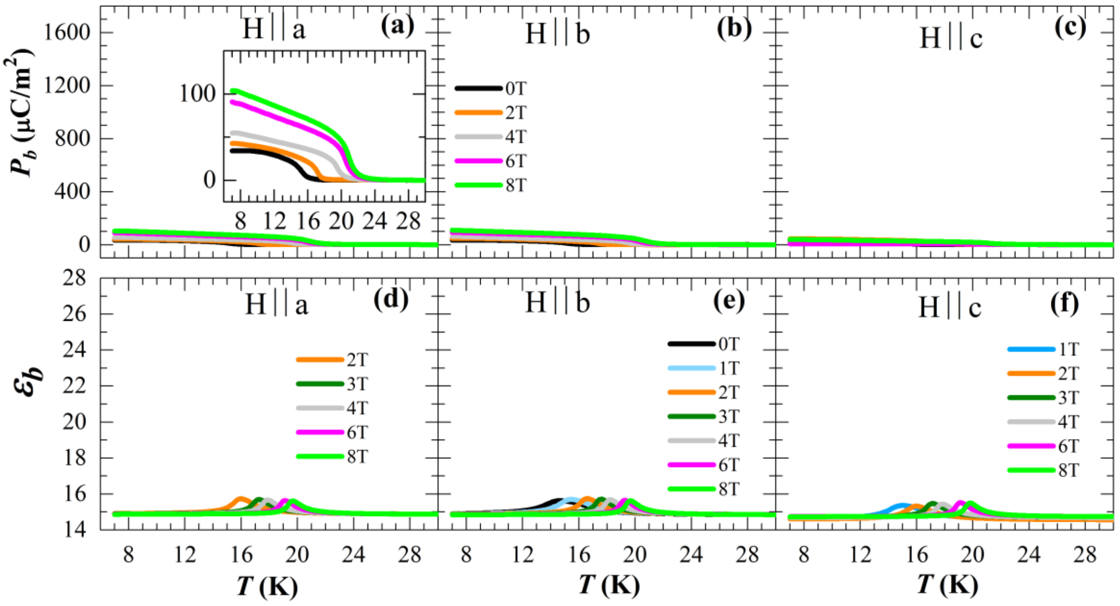

Figure 4.12 P_a and ε_b under magnetic field along *a*, *b* and *c*-direction.

4.3.2.5 Neutron diffraction results in polycrystalline $^{160}Gd_{0.5}Dy_{0.5}MnO_3$

Paramagnetic state:

In order to understand the unusual temperature and magnetic field dependence of spontaneous polarization, we have carried out neutron powder diffraction studies in ^{160}Gd substituted GDMO. The refinement of the nuclear structure with the *Pbnm*1*'* space group shows good agreement between the observed and calculated data as seen from the Rietveld plots in figure. 4.13. The refinement of the average occupancy in the A-site is in agreement with the nominal composition. The details of the crystal structure refinement are given in the table 4.2 and 4.3).

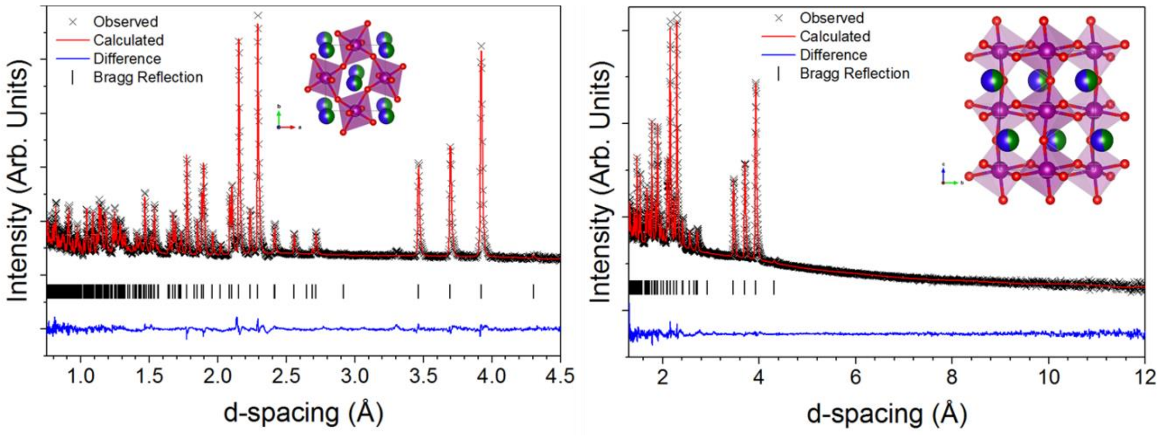

Figure 4.13 Rietveld plots of the paramagnetic structure of $Gd_{0.463}Dy_{0.537}MnO_3$ against the WISH data collected in the detector banks with average 2θ of 152.8° (left) and 58.3° (right). A projection of the crystal structure is shown in inset for the *ab* plane (left) and *bc* plane (right). The purple, blue/green and red spheres indicate the manganese, dysprosium/gadolinium and oxygen position respectively.

Table 4.2 Crystal structure parameters and reliability factor for the $Gd_{0.463}Dy_{0.537}MnO_3$ in the paramagnetic phase.

Chemical formula	$Gd_{0.463}Dy_{0.537}MnO_3$
Z	4
Superspace group	*Pbnm1'*
a(Å)	5.29614(3)
b(Å)	5.83834(3)
c(Å)	7.39621(4)
Volume(Å^3)	228.695(2)
R_p (all banks)	0.0193
R_{WP} (all banks)	0.0195

Table 4.3 Atomic positions, occupancies, and isotropic atomic thermal displacements for the $Gd_{0.463}Dy_{0.537}MnO_3$ structure in the paramagnetic phase.

Atom	x	y	z	Occupancy	U_{iso}
Gd	0.98232(10)	0.08177(7)	0.25	0.4634(14)	0.00210(13)
Dy	0.98232(10)	0.08177(7)	0.25	0.5366(14)	0.00210(13)
Mn	0.5	0	0	1	0.0040(4)
O1	0.10657(16)	0.46558(15)	0.25	1	0.0052(3)
O2	0.70360(14)	0.32621(12)	0.05190(9)	1	0.0061(2)

Spin density wave state:

Below $T_N^{Mn} = 39.5$ K, a set of new reflections, ascribable to magnetic ordering of the Mn sublattice, are observed and could be indexed with a propagation vector k= (0 0.308(4) 0). The attempt to refine the observed diffraction pattern with a superspace group deriving from a single irreducible representation, corresponding to a spin density wave aligned with one of the unit cell directions, gives poor results. For this reason the combination of two irreducible representation were tested and the best refinement is obtained with the *P2₁/m1'(αβ0)00s* superspace group (see figure 4.14). The detailed description of the symmetry analysis is provided in table 4.4 and table 4.5.

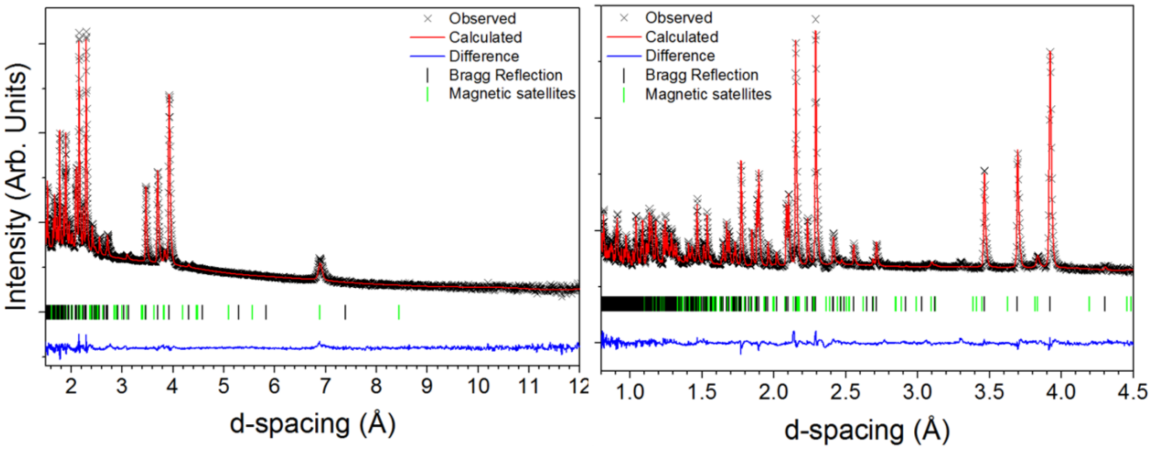

Figure 4.14 Rietveld plots of the spin density wave structure of $Gd_{0.463}Dy_{0.537}MnO_3$ at 25K against the WISH data collected in the detector banks with average 2θ of 58.3° (left) and 152.8° (right).

Table 4.4 Crystal parameters and reliability factor for the $Gd_{0.463}Dy_{0.537}MnO_3$ structure in the spin density wave phase at 25 K.

Chemical formula	$Gd_{0.463}Dy_{0.537}MnO_3$
Z	4
Superspace group	*P2₁/m1'(αβ0)00s*
Irreducible Representation	$m\Sigma_1 \oplus m\Sigma_3$

Order Parameter Direction	*P (a,0|b,0)*
a(Å)	5.29660(3)
b(Å)	5.83765(3)
c(Å)	7.39489(5)
gamma (degree)	89.993(13)
k	(0 0.308(4) 0)
Volume(Å^3)	228.648(2)
R_p (all banks)	0.0197
R_{WP} (all banks)	0.0199

Table 4.5 Atomic positions, occupancies, isotropic atomic thermal displacements and magnetic parameter for the $Gd_{0.463}Dy_{0.537}MnO_3$ structure in the spin density wave phase at 25 K. The nuclear position occupancies and thermal displacement were fixed as the paramagnetic structure.

Atom	x	y	z	Occupancy	U_{iso}
Gd_1	-0.01768	0.08177	0.25	0.4634	0.00210
Gd_2	0.51768	0.08177	0.25	0.4634	0.00210
Dy_1	-0.01768	0.08177	0.25	0.5366	0.00210
Dy_2	0.51768	0.08177	0.25	0.5366	0.00210
Mn_1	0.5	0	0	1	0.0040
Mn_2	0	0.5	0	1	0.0040
O1_1	0.10657	0.46558	0.25	1	0.0052
O1_2	0.39343	-0.03442	0.25	1	0.0052
O2_1	0.70360	0.32621	0.05190	1	0.0061
O2_2	0.7964	0.82621	0.4481	1	0.0061

Atom	$M_x$sin	$M_y$sin	$M_z$sin	$M_x$cos	$M_y$cos	$M_z$cos	M_{tot}
Mn_1	-	-	-	0.99(9)	2.66(3)	-	2.83(9)
Mn_2	-	-	-	0.99(9)	2.66(3)	-	2.83(9)

The magnetic structure is described by a non-polar spin density wave lying in the *ab* plane, approximately aligned with the (120) crystallographic direction, with an amplitude of 2.83(9) μ_B at 25 K (see figure 4.15).

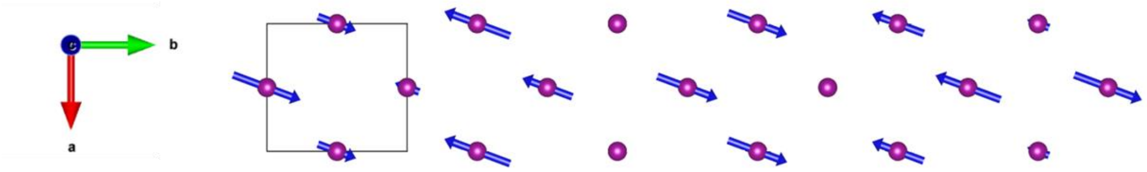

Figure 4.15 Projection in the *ab* plane of the spin density wave structure. For clarity only one [110] Mn layer is given and the staking is antiferromagnetic along the c-direction. The spins are aligned along the (120) crystallographic direction.

Cycloidal state:

By crossing T_C, a strong and abrupt increase of the magnetic intensity indicates a change in the spin configuration as also suggested from the pyrocurrent measurements as well as from the heat capacity data. As observed in the other RMnO$_3$ compounds[1], this transition is related to the appearance of a cycloidal spin structure. The best refinement (figure 4.16) of the neutron diffraction data at 11 K was obtained in the *Pn1'(0β0)0s* superspace group deriving from the use of all four irreducible representations of the parent space group. The refinement results are provided in table 4.6 and 4.7).

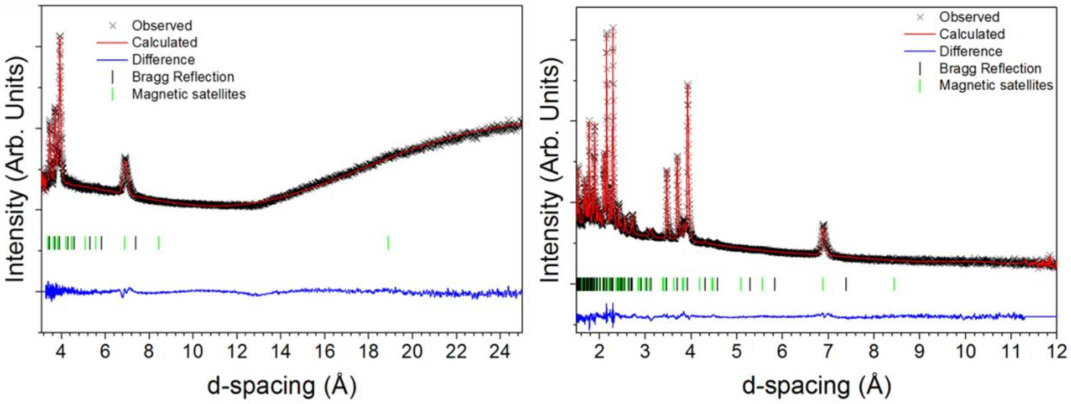

Figure 4.16 Rietveld plots of the Cycloidal structure of $Gd_{0.463}Dy_{0.537}MnO_3$ at 11K against the WISH data collected in the detector banks with average 2θ of 27.1° (left), 58.3° (right).

Table 4.6 Crystal parameters and reliability factor for the $Gd_{0.463}Dy_{0.537}MnO_3$ structure in the Cycloidal phase at 11 K.

Chemical formula	$Gd_{0.463}Dy_{0.537}MnO_3$
Z	4
Superspace group	*Pn1'(0β0)0s*
Irreducible Representation	$m\Sigma_1 \oplus m\Sigma_2 \oplus m\Sigma_3 \oplus m\Sigma_4$
Order Parameter Direction	*P(a,0|0,b|0,c|d,0)*
a(Å)	5.29665(4)
b(Å)	5.83746(4)
c(Å)	7.39453(5)
k	(0 0.309(4) 0)
Volume(Å^3)	228.631(3)
R_p (all banks)	0.0204
R_{WP} (all banks)	0.0218

Table 4.7 Atomic positions, occupancies, isotropic atomic thermal displacements and magnetic parameter for the $Gd_{0.463}Dy_{0.537}MnO_3$ structure in the cycloidal phase at 11 K. The nuclear position occupancies and thermal displacement were fixed to the paramagnetic structure values. The Fourier coefficients of the magnetic modulation are expressed in polar coordinates.

Atom	x	y	z	Occupancy	U_{iso}

Gd_1	-0.01768	0.66823	0.75	0.4634	0.00210
Gd_2	0.51768	0.16823	-0.25	0.4634	0.00210
Dy_1	-0.01768	0.66823	0.75	0.5366	0.00210
Dy_2	0.51768	0.16823	-0.25	0.5366	0.00210
Mn_1	-0.5	0.75	0	1	0.0040
Mn_2	0.5	0.75	-0.5	1	0.0040
O1_1	-0.89343	0.28442	0.75	1	0.0052
O1_2	0.39343	0.78442	-0.25	1	0.0052
O2_1	-0.2964	0.42379	0.9481	1	0.0061
O2_2	-0.2036	-0.07621	0.5519	1	0.0061
O2_3	-0.7036	0.07621	1.4481	1	0.0061
O2_4	0.2036	0.57621	0.0519	1	0.0061

Atom	$M_r$sin	$M_p$sin	$M_t$sin	$M_r$cos	$M_p$cos	$M_t$cos	M_{tot}
Mn_1	2.80(16)	90	90	2.80(16)	0	128(1)	2.80(9)
Mn_2	2.80(16)	-90	90	2.80(16)	180	51(1)	2.80(9)

The refined magnetic structure is schematically shown in figure 4.17(a), (b) and (c) and consists of a cycloidal structure lying in the (102) plane of the nuclear structure with an ordered moment of 2.80(9) μ_B at 11 K. The tilting of the manganese cycloidal plane, ~40 degrees for the *ab* plane, is allowed by the magnetic point group *m1'* and it is in agreement with the observation of a spontaneous polarization in both the *a* and *c* directions. Moreover, taking into account the inverse spin current mechanism [13-15] the induced polarization should lie along the (20-1) direction, in agreement with the hierarchy of the measured polarization along *a* and *c*-direction, with $P_a > P_c$. The *Pn1'(0β0)0s* magnetic superspace groups actually allows the cycloidal plane to freely rotate around the *b*-axis without symmetry breaking. This can easily explain the almost continuous change of the polarization from P_a to P_c, above T_N^R, when magnetic field is applied along *a*-direction. Interestingly the value of the propagation vector along the b direction remains unchanged between the spin density wave and the cycloidal phase in contrast with the other orthorhombic rare earth manganites.

Pseudo-helix state:

Below 10 K, a clear rise of diffuse scattering in the diffraction data is observed (figure 4.18) indicating the setting in of short range correlations. From the intensity of the diffuse scattering, heat capacity and magnetization data (figure 4.7(a), (b)) it is possible to conclude that below T_N^R, a short range ordering of the rare earth ions develops. Moreover, a new set of satellite reflection is observed, which can be indexed with the same propagation vector as the cycloidal. In particular, the observation of the 000+k and 110-k magnetic reflections, absent in the cycloidal phase, suggests the presence of sizable magnetic component perpendicular to the k-vector characteristic of helical phase.

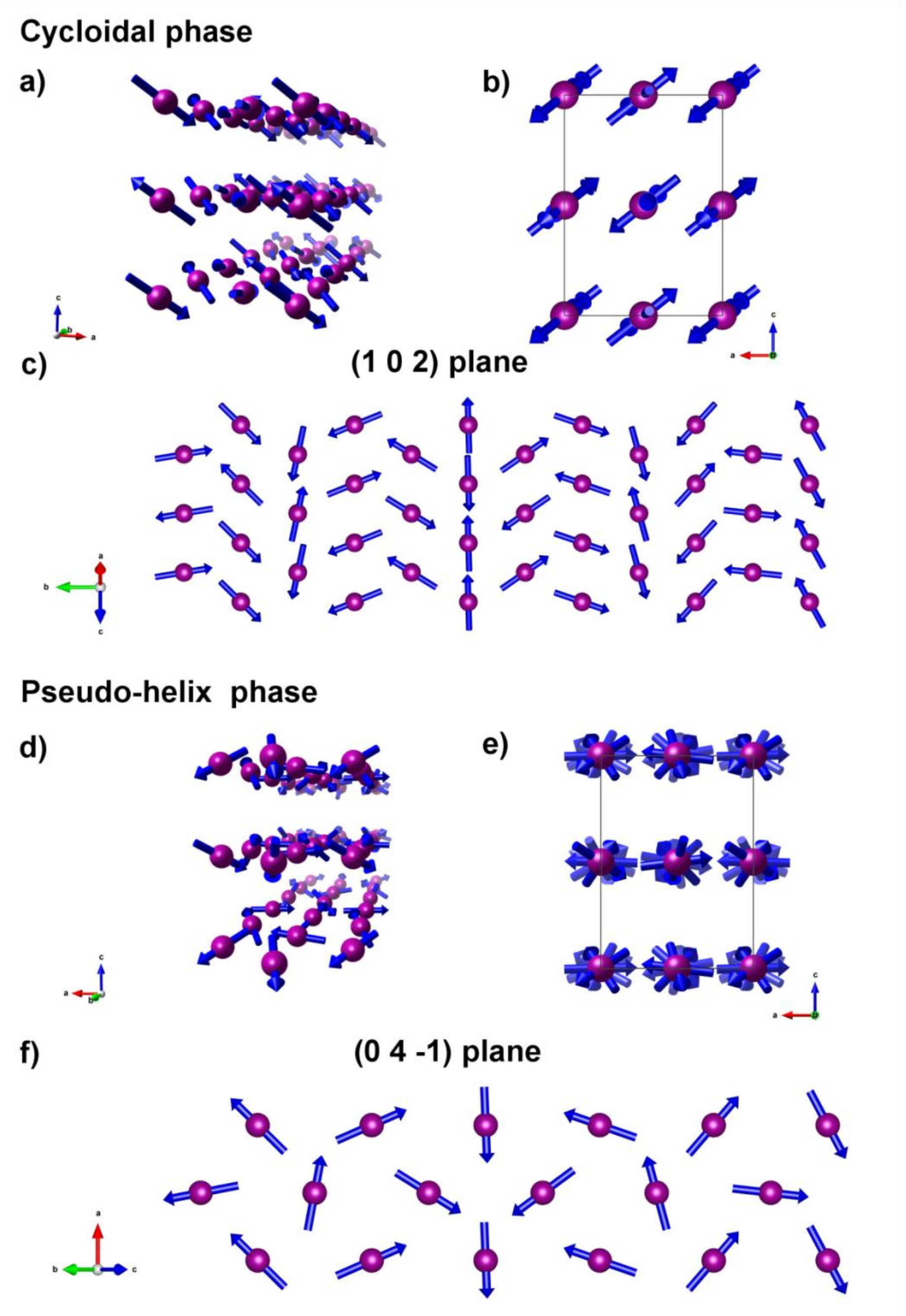

Figure 4.17 Magnetic structures of the cycloidal phase (a), (b) and (c) and for the p-helix phase (d),(e) and (f) in different projections. (a) 3D view of the cycloidal phase: (b) projection of the cycloidal structure in the ac plane showing the spins in the (102) plane; (c) projection along the [102] direction showing the rotation of the cycloidal structure in the (102) plane. (d) 3D view of the p-helix phase, (e) projection of the p-helix structure in the *ac* plane showing the perpendicular component to k, (f) projection along the [041] direction showing the rotation of the Mn spins in the (04-1) plane.

The best refinement of the neutron data at base temperature was obtained in the *Pn1'(0β0)0s* superspace group as seen figure 4.19) and the resulting magnetic structure is drawn in figure 4.17(d), (e) and (f). The details of the refinement are shown in table 4.8 and 4.9. The structure is characterized by a spiral spin arrangements with the spin rotating in the (041) and (04-1) planes, alternating along the *c*-axis (figure 4.17 (e, f)), with an ordered moment of 3.17(11) μ_B.

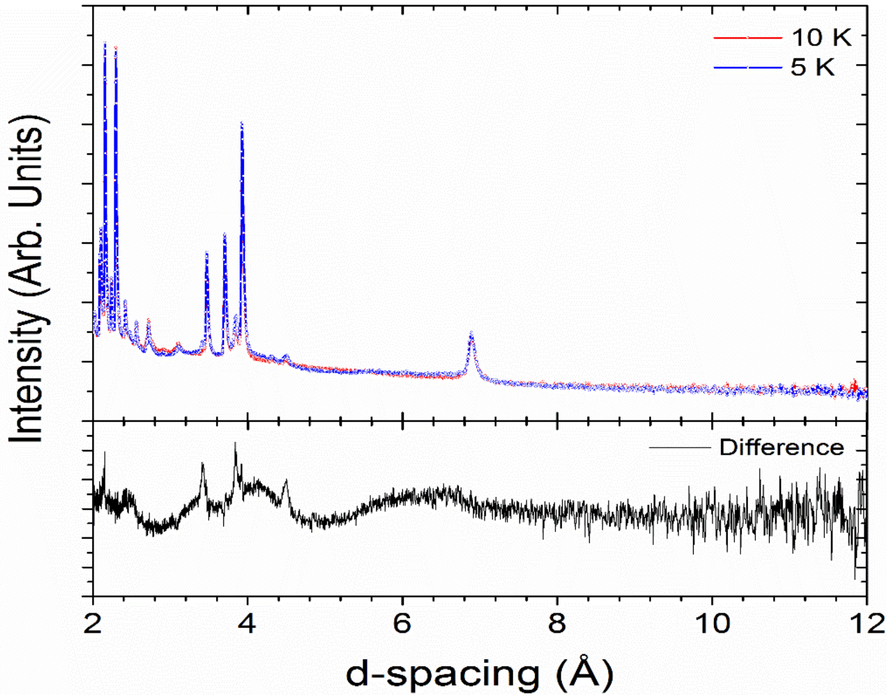

Figure 4.18 Plot of the time of fight neutron diffraction data collected in the detector banks with average 2θ of 58.3°at 11 K (red line), at 1.5 K (blue line) and the difference plot between the two temperatures (black line). From the difference plot the diffuse scattering in the low temperature data can be observed.

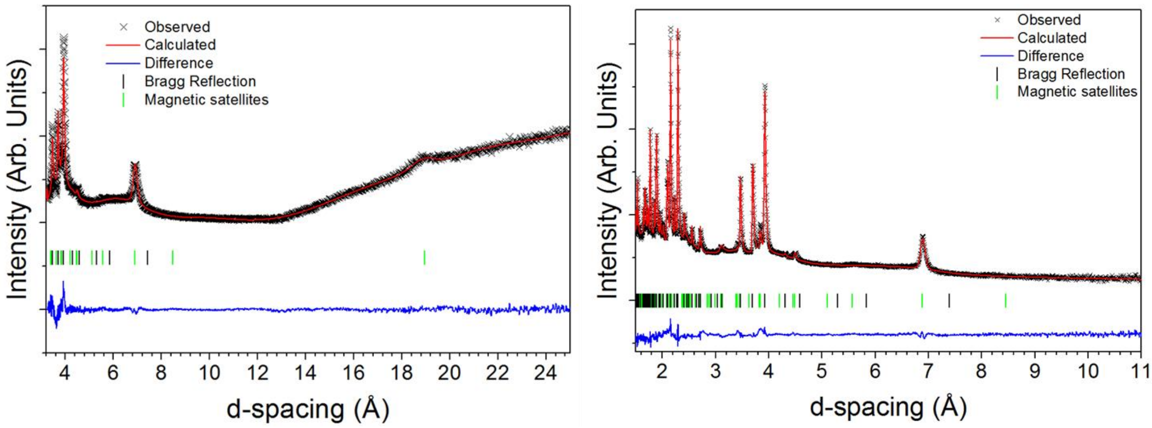

Figure 4.19 Rietveld plots of the pseudo-helix structure of $Gd_{0.463}Dy_{0.537}MnO_3$ at 1.5K against the WISH data collected in the detector banks with average 2θ of 27.1° (left), 58.3° (right).

This spiral structure can be decomposed in a large non-polar helical component perpendicular to the propagation vector and a smaller polar cycloidal component. The magnetic structure and the point group *m1'* are consistent with the pyrocurrent measurements that indicate a strong decrease of the spontaneous polarization but still a finite value for P_a and P_c. Owing to the larger helical component, we will call this phase pseudo-helix (p-helix) for the rest of the chapter. It is worth stressing that the p-helix phase is still described in the same superspace group as the cycloidal one meaning that the phase transition between the two phases can occur with a continuous rotation or with a sudden jump of the cycloidal plane in an isostructural phase. Unfortunately, the diffraction data among the two phases possess the same propagation vector, which do not allow us discriminating between the two cases. Figure 4.20 (a, b and c) shows the integrated intensity versus temperature of some magnetic reflections characteristics of each phase, highlighting the different transitions temperatures. It is interesting to note that the intensity of the 110-k and 000+k reflections, characteristic of the p-helix phase, increases below T_C following an almost linear dependence, typical of a secondary (induced) order parameter. It is therefore, likely that the rotation of the cycloidal plane from the (102) plane to the (041)/(04-1) is induced from the short range ordering of the R ions in the A site.

Table 4.8 Crystal parameters and reliability factor for the $Gd_{0.463}Dy_{0.537}MnO_3$ structure in the p-helix phase at 1.5 K.

Chemical formula	$Gd_{0.463}Dy_{0.537}MnO_3$
Z	4
Superspace group	*Pn1'(0β0)0s*
Irreducible Representation	$m\Sigma_1 \oplus m\Sigma_2 \oplus m\Sigma_3 \oplus m\Sigma_4$
Order Parameter Direction	*P(a,0|0,b|0,c|d,0)*
a(Å)	5.29630(4)
b(Å)	5.83720(5)
c(Å)	7.39510(6)
k	(0 0.309(4) 0)
Volume(Å^3)	228.624(3)
R_p (all banks)	0.0230
R_{WP} (all banks)	0.0268

Table 4.9 Atomic positions, occupancies, isotropic atomic thermal displacements and magnetic parameter for the $Gd_{0.463}Dy_{0.537}MnO_3$ structure in the pseudo-helix phase at 1.5 K. The nuclear position occupancies and thermal displacement were fixed to the paramagnetic structure values. The Fourier coefficients of the magnetic modulation are expressed in polar coordinates.

Atom	x	y	z	Occupancy	U_{iso}
Gd_1	-0.01768	0.66823	0.75	0.4634	0.00210

Gd_2	0.51768	0.16823	-0.25	0.4634	0.00210
Dy_1	-0.01768	0.66823	0.75	0.5366	0.00210
Dy_2	0.51768	0.16823	-0.25	0.5366	0.00210
Mn_1	-0.5	0.75	0	1	0.0040
Mn_2	0.5	0.75	-0.5	1	0.0040
O1_1	-0.89343	0.28442	0.75	1	0.0052
O1_2	0.39343	0.78442	-0.25	1	0.0052
O2_1	-0.2964	0.42379	0.9481	1	0.0061
O2_2	-0.2036	-0.07621	0.5519	1	0.0061
O2_3	-0.7036	0.07621	1.4481	1	0.0061
O2_4	0.2036	0.57621	0.0519	1	0.0061

Atom	$M_r$sin	$M_p$sin	$M_t$sin	$M_r$cos	$M_p$cos	$M_t$cos	M_{tot}
Mn_1	3.17(2)	-90	49.8(6)	3.17(2)	180	90	3.17(11)
Mn_2	3.17(2)	90	49.8(6)	3.17(2)	0	90	3.17(11)

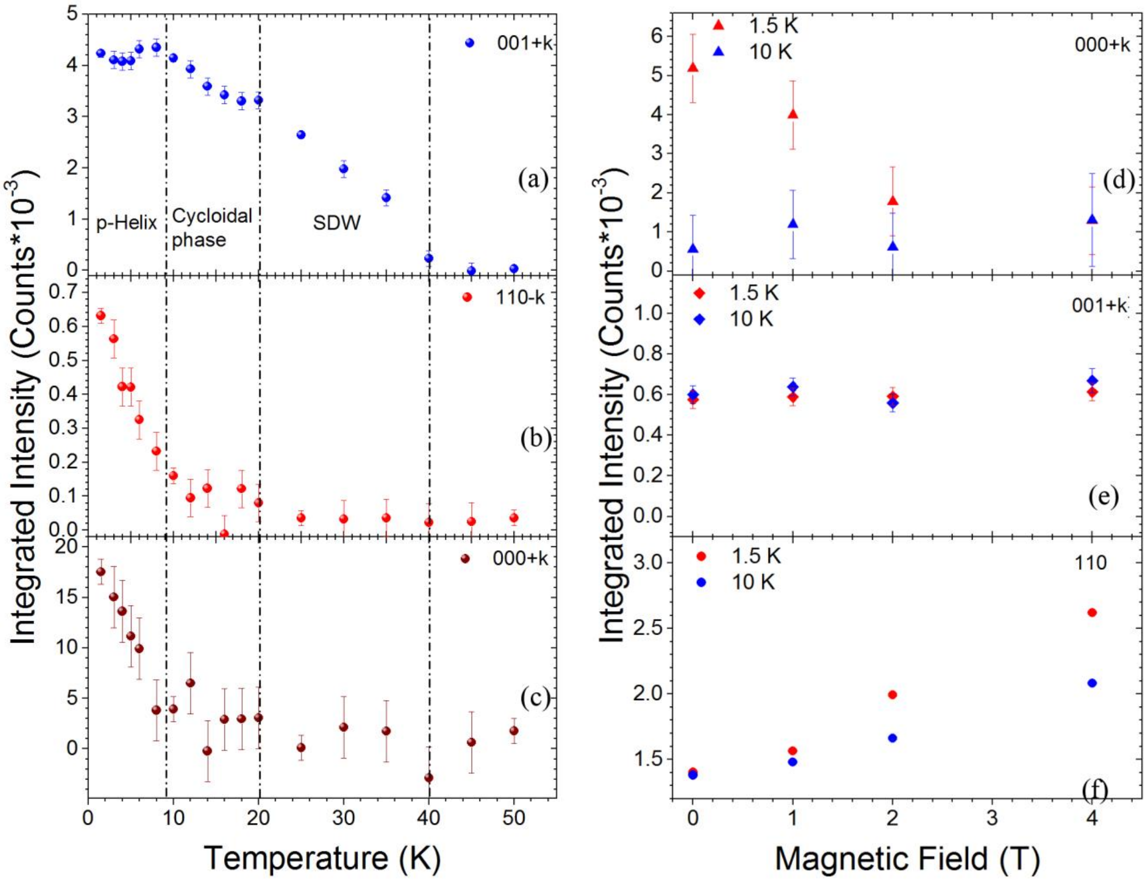

Figure 4.20 Integrated intensity of magnetic reflections characteristic of each magnetic phase as function of temperature (a), (b), (c) and applied magnetic field (d), (e) and (f).

In order to investigate the role of the short range ordering of the *R*-ions on the Mn spin ordering and to investigate the strong increase in the electric polarization in the p-helix phase under external magnetic field, a series of in field powder neutron diffraction experiment were performed. The increase of the applied magnetic field induces a clear decrease of the diffuse scattering with a concomitant increase of the diffracted intensity on some nuclear reflections as shown in figure 4.21. These magnetic contributions, with a k= 0 propagation vector, are ascribable to a ferromagnetic polarization of the R ion as also observed in the macroscopic magnetization measurements displayed in the inset of figure 4.7(b). As shown in figure 4.20, from the integrated intensity of the 110 reflection, the ferromagnetic polarization of the *R*-ion can be obtained both above and below T_N^R. More interesting is the effect of the applied field on the Mn sublattice ordering. Figure 4.20(d, e and f) shows the integrated intensity of the 000+k and 001+k satellite reflection, characteristic of the p-helix and cycloidal phase respectively, versus the applied field above and below T_N^R. It clearly demonstrate that the application of an external magnetic field below T_N^R induces the transition from the p-helix phase to the cycloidal one as indicated from the vanishing of the 000+k satellite reflection, explaining also the strong increase of the polarization along the a- and c-axis. On the contrary, the application of the magnetic field above the short range ordering of the *R*-ion, does not change the cycloidal plane of the Mn spins, as shown from the integrated intensity of the magnetic satellites at 11 K (figure 4.20).

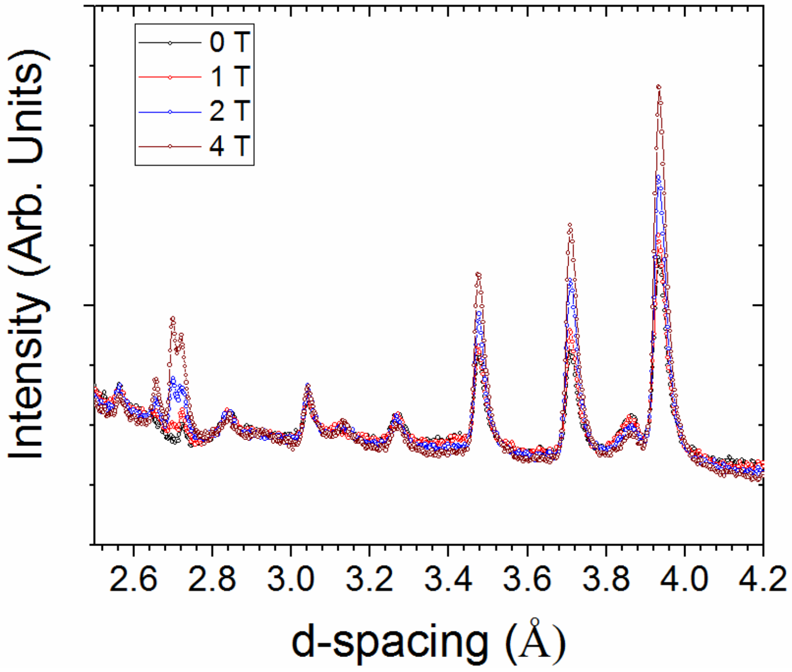

Figure 4.21 Magnetic field dependence of the time of fight neutron diffraction data collected in the detector banks with 2θ = 156° at 1.5K. The rise of magnetic intensity on the nuclear reflection clearly indicates a ferromagnetic ordering of the R ions above 2T.

4.3.2.6 Electric polarization in the *p*-helix phase

We consider that the relatively small remnant polarization (~100 μC/m^2) is associated with the p-helix state. The presence of such a small polarization is demonstrated by our detailed pyroelectric current measurements, as discussed below. The first evidence comes from pyrocurrent measurements with different poling intervals (figure 4.22(a)). For the poling intervals 8-2 K and 7-2 K, we see negative (T_{N2}) and positive (T_{N3}) pyrocurrent peaks corresponding to the appearance and disappearance of Mn polarization, respectively, similar to those observed for 30-2 K poling interval (the inset in figure 4.10(c)), except that the pyrocurrent values are smaller because the poling is done well below the Curie temperature. On the other hand, for the poling interval 6.5 - 2 K, we observe only a negative peak at T_{N3}.

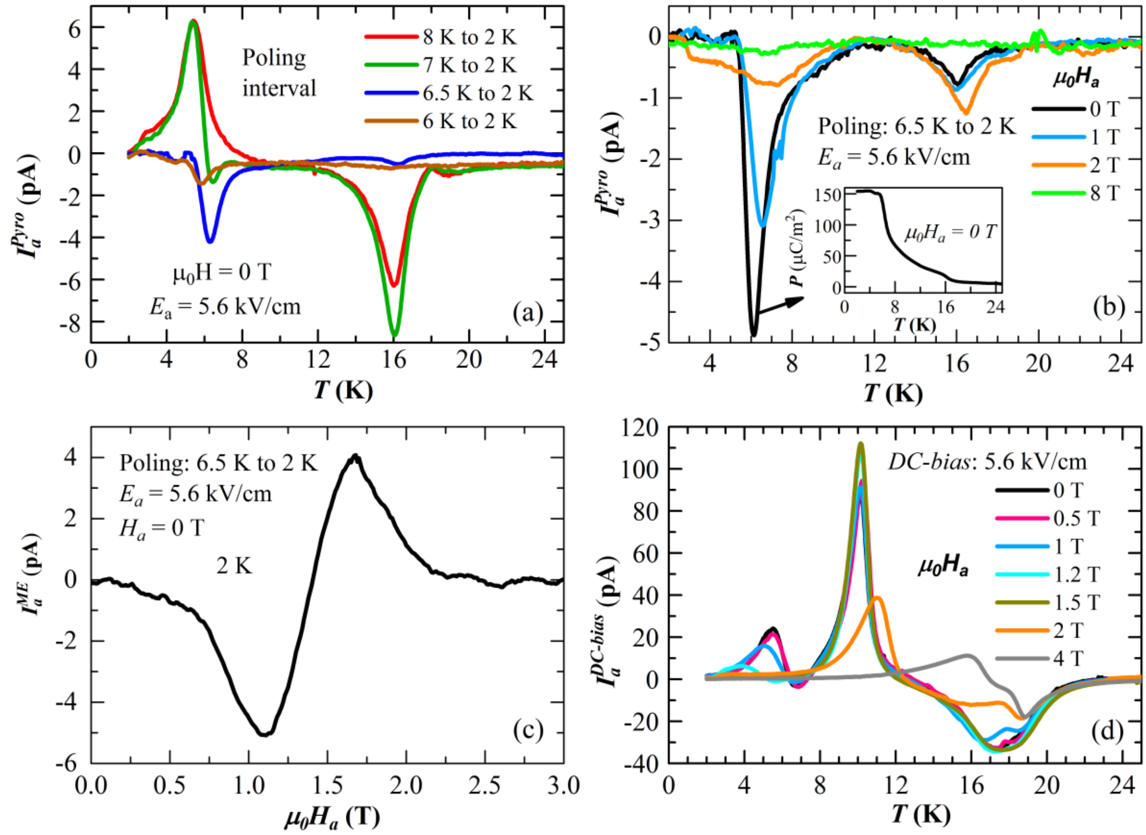

Figure 4.22 (a) Pyrocurrent data recorded along the *a*-axis for different poling intervals between 8 K to 2 K with 5.6 kV/cm. Negative peak appears at rare-earth ordering when the poling field is applied from 6.5 K to 2 K. (b) Pyrocurrent measured along the *a*-axis under various H_a after poling from 6.5 to 2 K. Inset shows polarization along the *a*-axis in zero magnetic field poled between 6.5 K to 2 K (c) magnetoelectric current recorded at 2 K while ramping the field from 0 to 3 T after poling the sample from 6.5 to 2 K with 5.6 kV/cm in zero magnetic field. (d) DC-bias current measured along the *a*-axis with 5.6 kV/cm at various magnetic field along the *a*-axis.

This negative peak is not related to the disappearance of Mn polarization but indicates a polar state associated with the helical ordering. In order to further explore the polar nature of the low-temperature phase, we have measured pyrocurrent under various magnetic fields for the same poling interval. Figure 4.22(b) shows the suppression of the low-temperature polarization by magnetic field related to changes in the R-spin structure, which correlates with the meta-magnetic behavior shown in figure 4.8. The small negative pyrocurrent peaks at T_{N2} in figure 4.22(b), corresponding to the Mn spiral ordering, are induced by the depolarization current at T_{N3}. At $H_a = 8$ T, the low-temperature polar phase disappears and so does the peak at T_{N2}. It can be noted here that the polarization obtained by integrating the pyrocurrent in zero field (inset of figure 4.22(b)) is comparable to the remnant polarization at 2 K (figure 4.10). The ferroelectric nature of the low-temperature state ($T < T_{N3}$) is further supported by the magnetic field dependence of the current measured at 2 K (figure 4.22(c)) showing a negative peak at ~1.1 T and a positive peak at ~1.5 T. These peaks correspond to disappearance of the low-temperature polarization and appearance of the spiral-induced polarization, respectively.

To further confirm the presence of small polarization in the low-temperature state, we have exploited the DC-bias measurement [38] which is already described in the previous chapter in details. The sample was cooled down to 2 K and the current I_a was recorded in presence of an applied electric field (5.6 kV/cm) while warming in various magnetic fields ($H \| a$) (figure 4.22(d)). In zero field, we observe a positive peak at 6 K followed by a small negative peak near 7 K, corresponding to the polarization and depolarization currents, respectively This confirms the independent origin of ferroelectric order in the low-temperature state and is consistent with the dielectric anomaly at T_{N3} (figure 4.9). Similarly, we observe the polarization and depolarization currents due to the spiral ordering of Mn-spins at 10.5 K and 17 K, respectively. Under magnetic field, we see that the low-temperature polarization peaks are suppressed and only the peaks associated with the Mn spiral ordering remain.

4.3.3 Discussion on various polar states

We summarize the temperature and magnetic field dependence of polarization in figure 4.23. In the case of magnetic field applied along the a-direction, P_a and P_c at 10 K clearly demonstrate the change in magnitude of $P_a > P_c$ to $P_c > P_a$ which is due to rotation of cycloidal plane towards the *bc*-plane. At 2 K, P_a is small because of the p-helical ground state with a cycloidal component. With increasing magnetic field, it exhibits a maximum around 1.5 T which is due to field induced ferromagnetic ordering of *R*-ions that results in the recovery of cycloidal polarization.

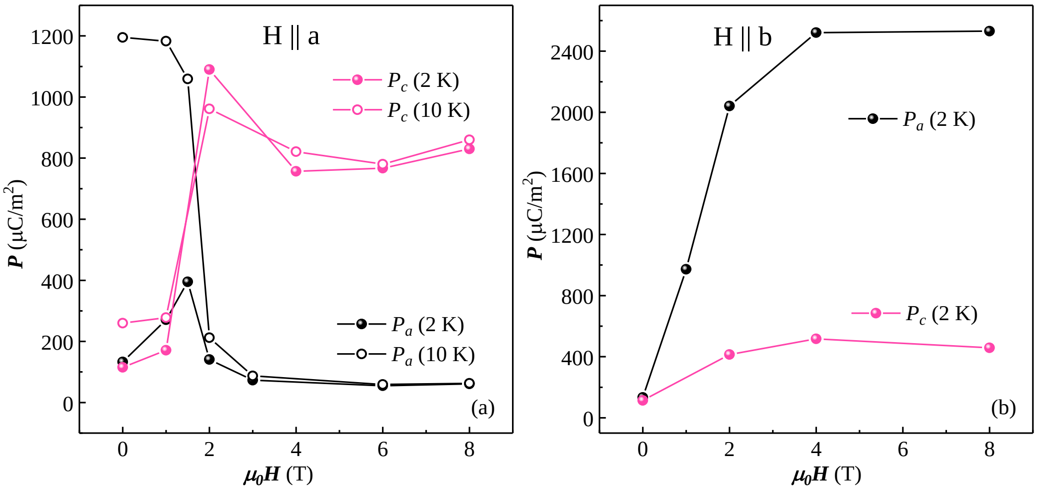

Figure 4.23 Electric polarization P_a and P_c under $H||a$ and $H||b$.

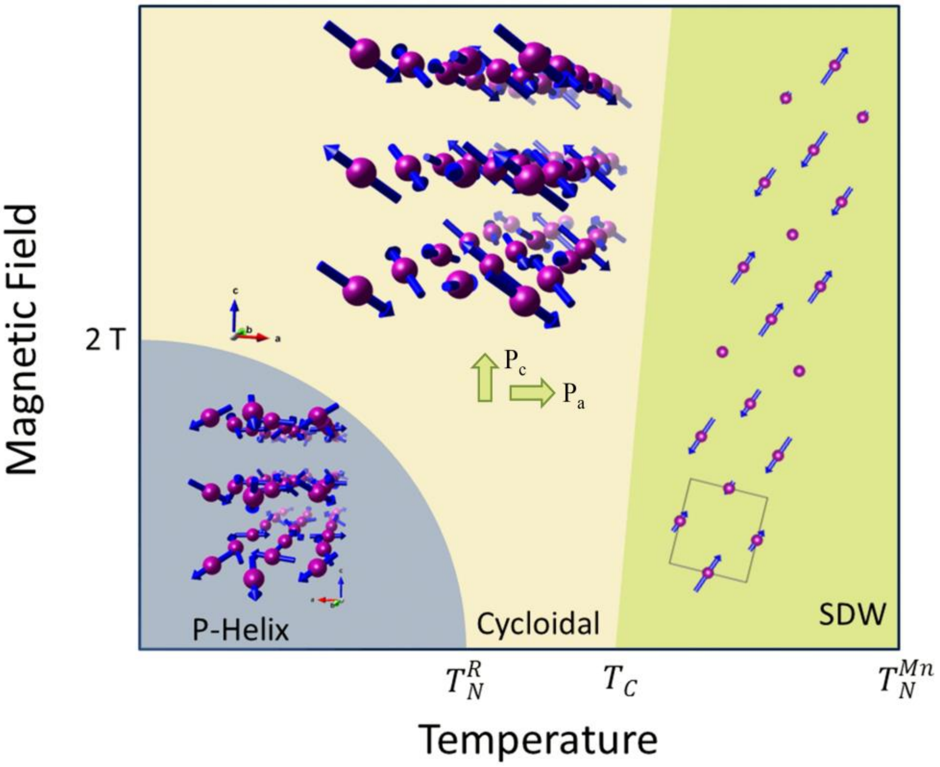

Figure 4.24 Schematic phase diagram of various magnetic phases with temperature and magnetic field.

However, the polarization remains low because of the suppression of high temperature cycloidal polarization. P_c follows switching behavior at 10 K with $P_a \sim P_c$ to $P_c > P_a$. On the other hand, P_a under $H||_b$ shows a gigantic enhancement reaching a value (2500 μC/m^2) that corresponds to the maximum polarization reported for DyMnO$_3$. A schematic phase diagram is provided in figure 4.24 in order to show the various competitive magnetic phase with magnetic field and temperature.

This large enhancement of the polarization may result from the exchange striction mechanism of magnetoelectric coupling [39], which is described phenomenologically by the term,

$$H_{me} = gP_a(\boldsymbol{A} \cdot \partial_b \boldsymbol{G} - \boldsymbol{G} \cdot \partial_b \boldsymbol{A}), \qquad (1)$$

where $\boldsymbol{A} = (A_a, A_b, A_c)$ and $\boldsymbol{G} = (G_a, G_b, G_c)$ are the Mn vector order parameters in the Bertaut notation [40] and $\partial_b = \frac{\partial}{\partial y}$. The scalar products in Equation (1) are invariant under rotations of spins for a fixed crystal lattice, reflecting the non-relativistic origin of this magnetoelectric coupling term. The relativistic spin-orbit coupling gives rise to a spin canting responsible for the admixture of the G-type antiferromagnetic order of Mn^{3+} spins to the *ab* spiral with the incommensurate A-type order: the A_a component of the spiral induces G_b and C_c orders, which both belong to Γ_1 representation, and the A_b component of the spiral induces G_a and F_c orders (Γ_4 representation). We note that this mechanism of polarization enhancement is only effective in the *ab* spiral state: a similar coupling for the *bc* spiral state, $g'P_c(\boldsymbol{A} \cdot \partial_b \boldsymbol{F} - \boldsymbol{F} \cdot \partial_b \boldsymbol{A})$, is expected to induce a much weaker polarization, because the magnitude of the F-type order is small compared to that of the G-type order due to the antiferromagnetic interaction between the Mn^{3+} spins in neighboring *ab* layers [41]. The large increase of the spiral ordering temperature under $H||b$ may result from a decrease of the relative magnetic anisotropy along the *a*- and *b*-axes, which controls the difference between T_{N1} and T_{N2} [15].

4.4 Conclusions

In conclusion, we have shown a possible coexistence of polarization along both *a*- and *c*-axis in the mixed rare-earth manganites Eu$_{0.5}$Dy$_{0.5}$MnO$_3$ and Gd$_{0.5}$Dy$_{0.5}$MnO$_3$ through polycrystalline sample study. These materials exhibited giant magnetic tunability of polarization and large magnetodielectric coupling. From the single crystal study of

$Gd_{0.5}Dy_{0.5}MnO_3$, and neutron study of polycrystalline Gd-160(GDMO) we have confirmed that the polarization indeed exist along both a-and c-direction due to the cycloidal plane lying on the [102] plane. Applied magnetic field ($H||a$) around 2 T rotates the cycloidal plane abruptly but without breaking the symmetry and thus changes the P_a/P_c ratio by more than an order of magnitude. Magnetic fields applied along the b and c axes result in a monotonous increase of both P_a and P_c. An unusually strong effect is observed for $H||b$: $P_a(8\text{ T})$ at 2 K is 25 times larger than $P_a(0\text{ T})$. The unique feature of this compound is that the short range rare-earth ordering suppresses the polar spiral ordering of Mn spins and gives rise to a new helical state with a smaller electric polarization. Applied magnetic fields at 2 K induce ferromagnetic ordering of R-ions which results in the recovery of polarization due to cycloidal ordering.

Part-II

Multiferroic memory effect*

Summary

Memory effect of polarized ferroelectric domain state in a nonpolar paraelectric collinear magnetic phase has been reported in few multiferroics. Using magnetoelectric and dielectric-relaxation study, in a single crystal of $Gd_{0.5}Dy_{0.5}MnO_3$ multiferroic, we prove the presence of memory effect beyond the collinear magnetic ordering temperature. Our study reveals that a Debye-like relaxation behavior corresponding to localized charge carries/defect dipoles in the lattice can explain this novel memory effect. A correlation of dielectric relaxation behavior to the magnetic ordering is found in a wide range of temperature including non-collinear spin-induced ferroelectric, a collinear antiferromagnetic state as well as a considerable extend into the paramagnetic state. Hence we inevitably have discussed the previous conjecture of the memory effect of small ferroelectric embryo hypothesis along with our defect dipole model.

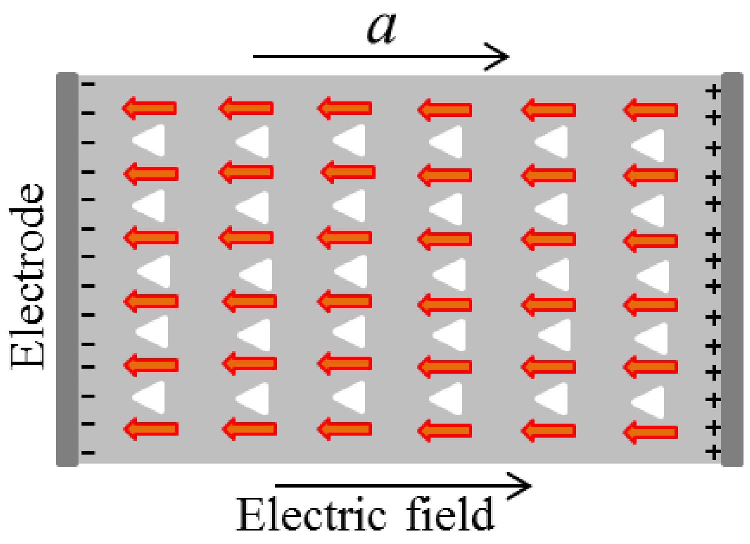

---

*Paper based on this work **C. De** and A. Sundaresan, to be communicated (2018).

4.5 Introduction to the memory effect

Multiferroics, anticipated to be a potential candidate for future storage devices, are currently a major area of research in condense matter physics where both the ferroelectric and magnetic polarization coexists and allow a strong pairing amongst them [6, 7, 9, 10, 26, 42]. Besides, researcher has paid attention to these materials due to potential applications in the spintronics, sensors and magnetoelectric microwave devices as well as for fundamental physics [3-5, 43, 44]. Recently, in cycloidal magnetic ordering induced multiferroic materials such as $MnWO_4$, $YMnO_3$-thin film and rare-earth(*R*) manganite etc., an intriguing memory effect was observed where the materials can store their polarization domain states in a disordered non-ferroelectric state [45-47]. Specifically, when the material is polarized macroscopically by external electric field, the polarized single ferroelectric domain state should remain only in the ferroelectric region as the ferroelectric dipoles would be randomly oriented beyond T_C. Remarkably, it was first observed in $MnWO_4$ by K. Taniguchi *et al.* that the ferroelectric polarization state could be retrieved from the paraelectric collinear antiferromagnetic state by magnetic field cycling and it was proposed that there could be small ferroelectric embryo that is microscopically polarized chiral domains state preserved in the paraelectric collinear antiferromagnetic ordering state due to higher magnetic frustration [45]. Later, I. Fina *et al.* had found a similar memory effect in the collinear antiferromagnetic ordering region in another chiral ordered multiferroic $Sm_{0.5}Y_{0.5}MnO_3$ material and argued the same hypothesis. The presence of such non collinear domains or chiral component in the collinear phase was proven to be expected in *R*-manganite multiferroic as the polar transition between non-collinear to collinear to be an order-disorder type [48]. This was supported through various studies such as, a fluctuating ferroelectric region in the sinusoidal phase anticipated through a model calculation showing a dynamic short range order (cycloidal type) in the collinear sinusoidal range (T_C < T <T_N) [35]. Terahertz spectroscopic studies also evidenced a non-zero dielectric contributions of electromagnons in the sinusoidal phase [44, 49]. From soft x-ray scattering study, the transition of incommensurate and commensurate state (T_C or $T_{lock\text{-}in}$) in $TbMnO_3$ was found to be among two non collinear state of Mn^{3+} ions, suggesting the presence of microscopic non-collinear state in a collinear matrix [50]. Therefore the observation of memory effect was explained quite satisfactorily through the small embryo model. Later, through the neutron diffraction of electric field poled chiral domain state in $MnWO_4$, it was found that the polarized domains can remember their chirality even in paramagnetic state [51]. We found the memory effect up to a deep paramagnetic state in the mixed rare-earth manganites in polycrystalline phase, although no origin could be inferred in the polycrystalline study [37]. Thus the study on the memory effect in multiferroic materials is still not clear and a detailed study on the memory effect and its mechanism is still missing.

In this part, we unambiguously confirm the presence of memory effect above T_N i.e. in the paraelectric as well as paramagnetic region in the single crystal of $Gd_{0.5}Dy_{0.5}MnO_3$ (GDMO) multiferroic. We demonstrated a typical relaxation behavior in the memory effect temperature range corresponding to localized charge carriers consisting of Mn-ions. We have shown how an internal electric field created due to such charge carriers and can polarize the ferroelectric dipoles. Finally, a model consisting of different type of dipoles present in the material is provided to explain the memory effect over the whole temperature range.

4.6 Results and discussion

4.6.1 Observation of memory effect

Heat capacity divided by temperature *vs.* temperature data in the earlier part ensured the three consecutive magnetic ordering at $T_N^{Mn} = 39.5$ K, $T_{Cy}^{Mn} = 16$ K (T_C), and $T_N^{RE} = 5$ K for sinusoidal antiferromagnetic, non collinear cycloidal ordering (ferroelectric onset, T_C), rare earth antiferromagnetic ordering, respectively at zero magnetic fields where the polarization occurs predominantly along a-axis at the transition from collinear sinusoidal to spiral ordering of Mn^{3+} spin. In order to demonstrate the memory effect, we first demonstrate the pyrocurrent behavior along a-axis in figure 4.25 under two measurement conditions. In the first case, the pyrocurrent was recorded in a conventional way as described in previous sections except the sample was poled up to 7 K from 30 K in order to avoid the intricacy of R-ion short range ordering which could influence the polarization as seen before. After the poling, the sample was warmed to 50 K with short circuit electrodes. The current was recorded in the second heating as shown in figure 4.25.

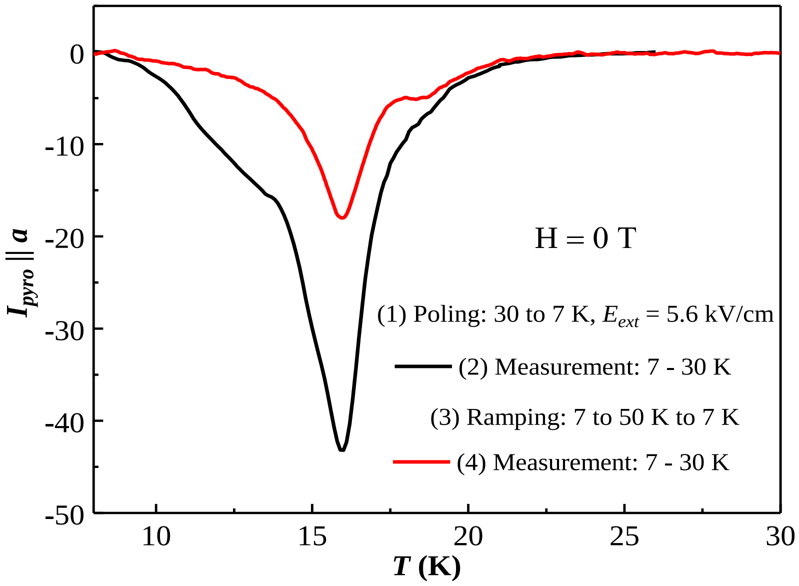

Figure 4.25 Pyrocurrent from 7 to 30 K, after poling the sample from 30 to 7 K. Red curve showing the data after ramping the sample from 7 to 50 K.

In order to reproduce the appearance of pyrocurrent even after warming the sample above the magnetic ordering temperature we have pursued the following measurement protocol. At first the sample was poled with electric field (E_{ext}) from 30 K to 7 K. Second, the electrodes were shorted at 7 K for 30 minutes to remove the stray charges on the sample-electrode interface. Third, current was recorded through continuously ramping the temperature from 7 K to various temperature (T_R = 25, 35, 45, 55, 65, 75, 80 and 90 K) and cooling back to 7 K (figure 4.26).Remarkably, a continuous polarization current peak while cooling (doted curve, denoted as C_n) and depolarization current peak while warming (continuous curve, denoted as W_n, the so-called pyrocurrent peak) at the ferroelectric onset (T_C ~16 K) is observed for T_R as high as 80 K which is almost double of the Mn^{3+} sinusoidal ordering. Above 80 K, no trace of the peak is found in both the cooling and warming cycle. Since the sample was poled with electric field only in the first cooling cycle from 30 to 7 K and the pyrocurrent peak is observed after warming the sample up to 80 K, the memory of the polarization state can be declared as restored from far above the Curie temperature ($T_C \sim 16\ K$).

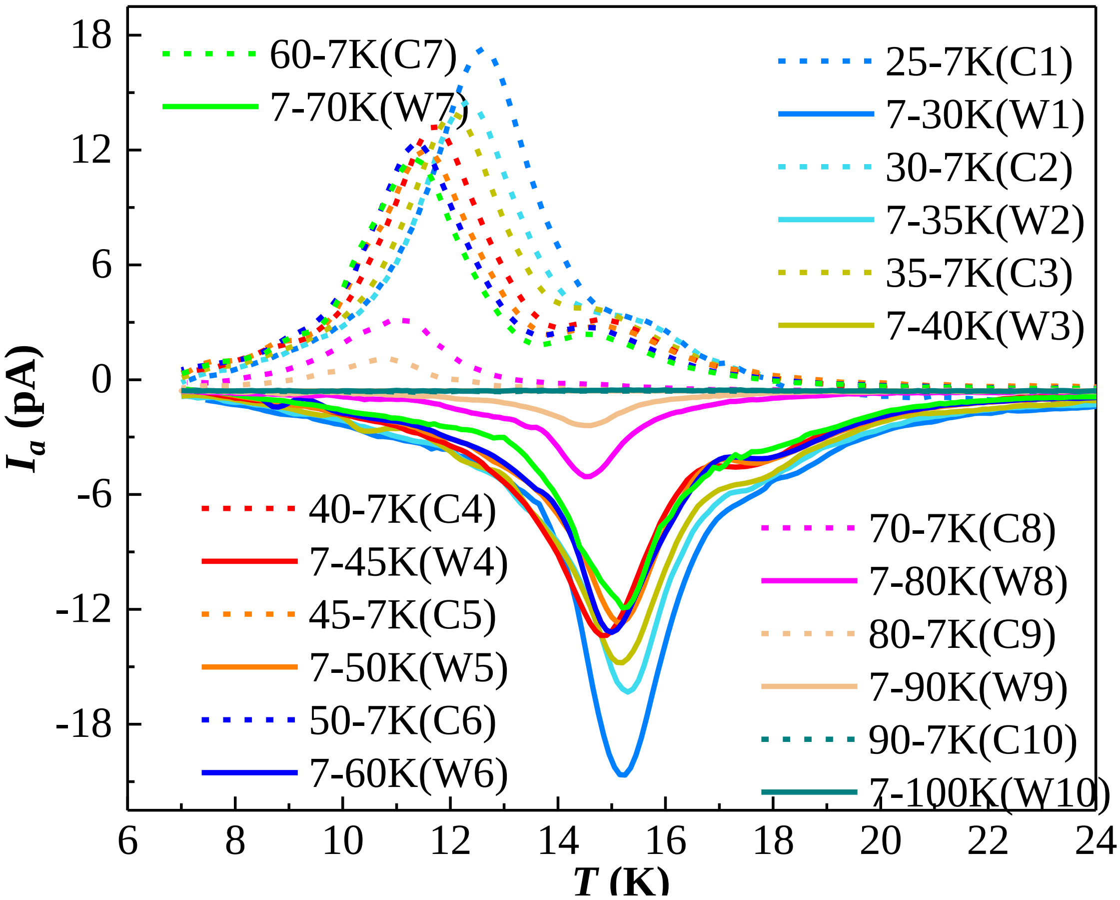

Figure 4.26 Pyrocurrent behavior while warming (continuous curve) and cooling (dotted curve) from 7 K to various temperatures (T_R) after initial poling the sample from 30 to 7 K with -5 kV/cm and 0 T.

For quantitatively examining the thermal remnant of polarization with different ramping temperature (denoted as P_{TR}), the experiment protocol is slightly modified. The first and second steps were same as mentioned before. Third, the temperature was ramped at T_R and cooled to 7 K by keeping the electrode shorted. Forth, the current was recorded while warming the sample from 8 to 30 K. This was followed for all the different T_R. In this way, we obtained the P_{TR} after integrating the pyrocurrent (inset), for all the T_R (figure 4.27(a and b)). The polarization obtained at 8 K, is shown as a function of T_R in figure 4.27(c). We notice that initially P_{TR} is decreased with increasing T_R up to nearly 35 K and then a step like increase which remained nearly constant up to 60 K and gradually vanishes at 80 K. Notably, this experiment have also shown the memory effect up to 80 K which signifies that the memory effect is secured below 80 K. Since the material shows the polarization along both a-and c-axis, we confirmed the memory effect along c-axis too and the result is shown in figure 4.28.

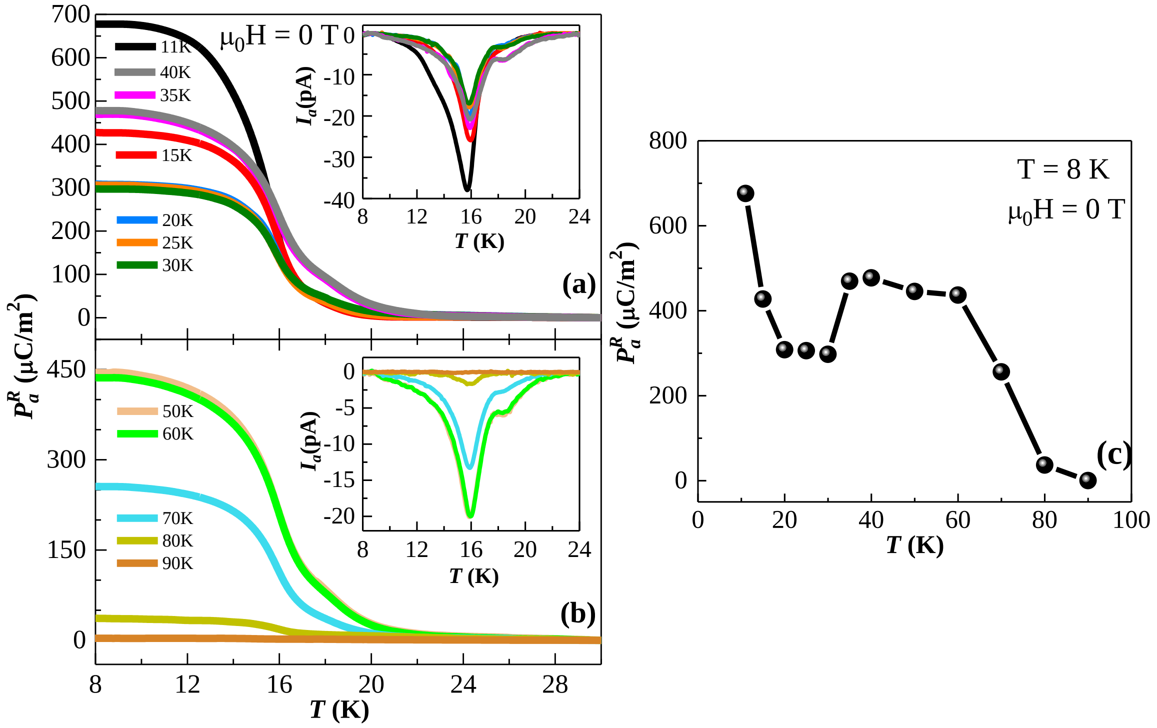

Figure 4.27 Polarization *vs.* temperature data along *a*-direction after poling the sample from 30 to 8 K with 5.6 kV/cm and 0 T magnetic field and short the electrode at 8 K for 30 min and ramp the temperature from 8 K to different T_R to 8 K. (a) shows the data for $T_R < T_N$ and (b) shows the data for $T_R > T_N$. Insets shows the corresponding recorded pyrocurrent data. (c) Thermal remnant polarization (P_{TR}) value at 8 K with temperature.

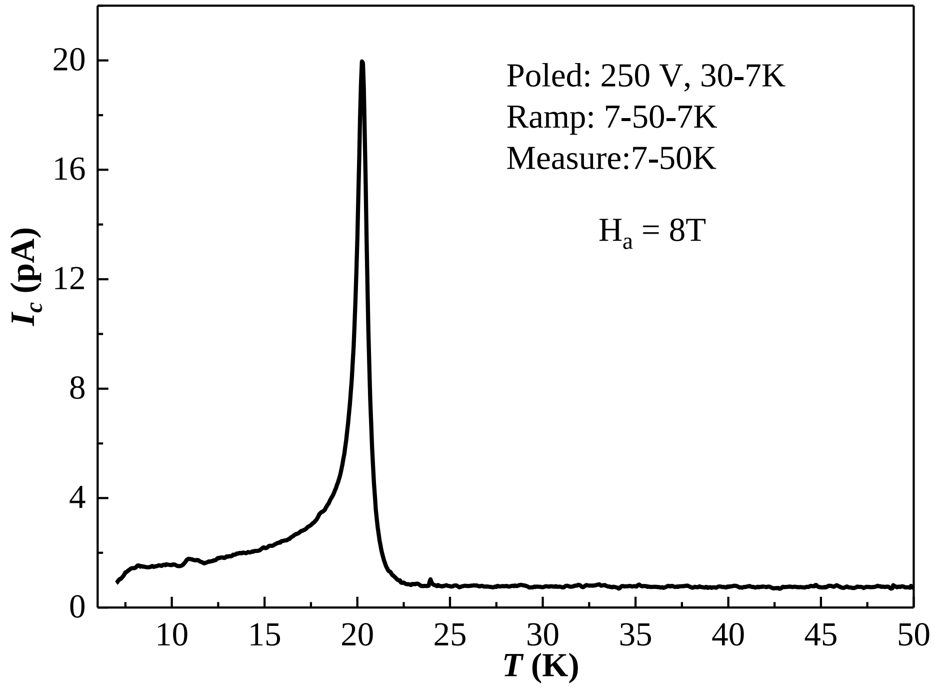

Figure 4.28 Memory effect along *c*-axis. Sample was poled from 30 to 7 K and followed by ramping to 50 K. Current was recorded while warming at 4 K/min from 7 to 50 K.

4.6.2 Dielectric relaxation

In order to investigate the origin of the memory effect, above T_N, we looked at the dielectric response with frequency along different directions. The frequency dependent dielectric constant along *c*-axis, shows a steps like behavior in the real part (ε') and corresponding peaks in the loss part in the temperature range of 20 to 100 K (figure 4.29). The frequency dependent thermal shift in the steps of ε′ and peaks in the loss corresponds to a typical relaxation behavior which was already observed in other rare-earth manganite multiferroic and attributed to a Debye like relaxation due to presence of localized charge carriers (LCC) in the crystal [2, 52, 53]. The relaxation time constant was fitted with inverse temperature according to both Arrhenius and Mott insulator related Variable Range Hopping (VRH) conduction mechanism for the comparison of fitting. We found that the VRH conduction mechanism has better agreement (figure 4.30(a)).

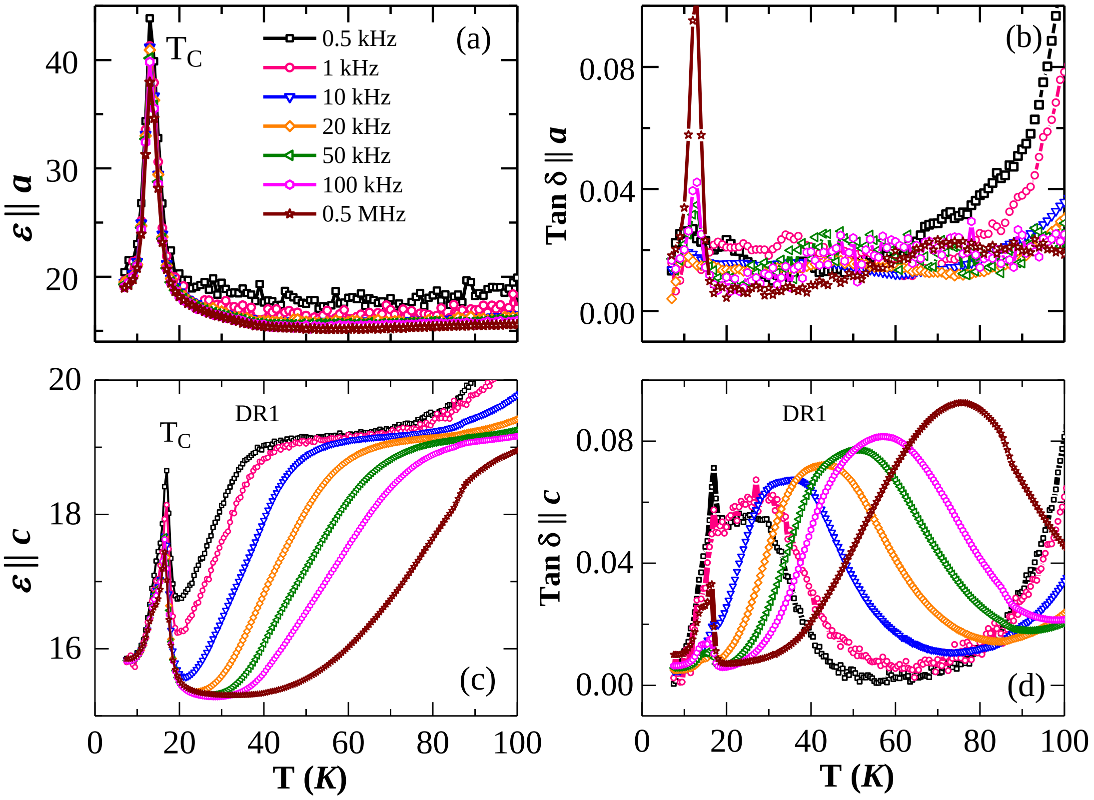

Figure 4.29 (a) Dielectric (b) loss data measured under various frequencies along c-axis.

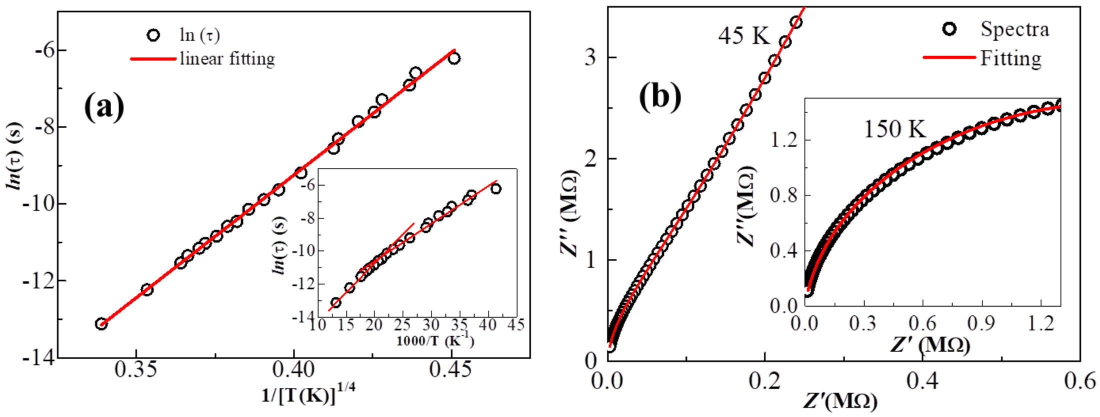

Figure 4.30 (a) Mott relation fitting. Inset shows Arrhenius fitting. (b) Cole cole plot.

Further, we notice a straight line like behavior with big slope in the complex impedance plot at 45 K (figure 4.30(b) which suggests the intrinsic nature of the relaxation. Importantly, this relaxation extends to a wide temperature range including FE, paraelectric and paramagnetic where we see the memory effect. Usually these LCC can be made up of trapped electrons accompanied by lattice distortion [54]. The electron hopping, associated with lattice distortion behaves like dipole reorientation under ac electric field and can show the dipolar relaxation behavior which we observe in our case. The ac dielectric constant along a-axis, shows an almost temperature independent behavior up to 100 K except the prominent peak at the cycloidal ordering temperature (T_C = 16 K) (figure 4.29 (a, b)).

The anisotropic behavior in dielectric relaxation data can be explained due to the John-Teller ions Mn^{3+} responsible for the relaxation [43, 49, 52]. Since the relaxation has anisotropic feature, we attempted to find out its correlation to the magnetic ordering. We do not see any distinct anomaly corresponding to the Mn^{3+} spin ordering at $T_N = 39.5$ K, however the anisotropy was noticed in the magnetization along the different axis above T_N in figure 4.7(b). This results suggests a short range magnetic correlation is present above T_N which is in agreement with earlier report where it has been shown that a non-zero contribution of the magnetic specific heat up to 200 K in the known multiferroic manganite $TbMnO_3$ ($T_N = 41$ K) [55]. Besides, a non-zero contribution of dielectric constant, related to electromagnon, was observed above T_N in the mixed rare-earth manganite [44]. Recently, S Elsässer et al had detected electromagnon signal corresponding to the local cycloidal spin order in $RMnO_3$ compounds even up to nearly twice of the global antiferromagnetic ordering of Mn^{3+} [56]. All these studies suggest that the localized charge carriers are strongly correlated to the local chiral magnetic domains and can exist up to some extend of higher temperature above the T_N. Here we consider that an internal electric field (E_{int}^{LCC}) corresponding to the dielectric relaxations due to the Mn^{3+} ions is produced with the application of external dc electric field E_{ext}.

The large relaxation behavior of the order of two decades arising above 90 K was noticed in the loss data along both c-axis (figure 4.29) and a-axis which can be attributed the Maxwell-Wagner type relaxation due to formation of Surface Barrier Later Capacitor (SBLC) at the sample and electrode interface [57]. The charges accumulated at the interface (Thermally Stimulated Free Charge carriers) under applied electric field can be frozen below the activation temperature and can act as an internal electric field (E_{int}^{TSFC}) below the freezing temperature (T_f). The consequences of this TSFC carrier related field at the electrode interface or grain boundary with ferroelectric polarization is already demonstrated in multiferroic $TbMnO_3$ [38, 58]. Here we observed a TSFC carrier related pyropeak at 90 K when the sample was poled from 150 to 40 K and measured from 40 to 150 K which confirms the presence of E_{int}^{TSFC} below $T_f \sim 70$ K (T_f has been considered as onset of the TSFC related pyro peak) (figure 4.31).

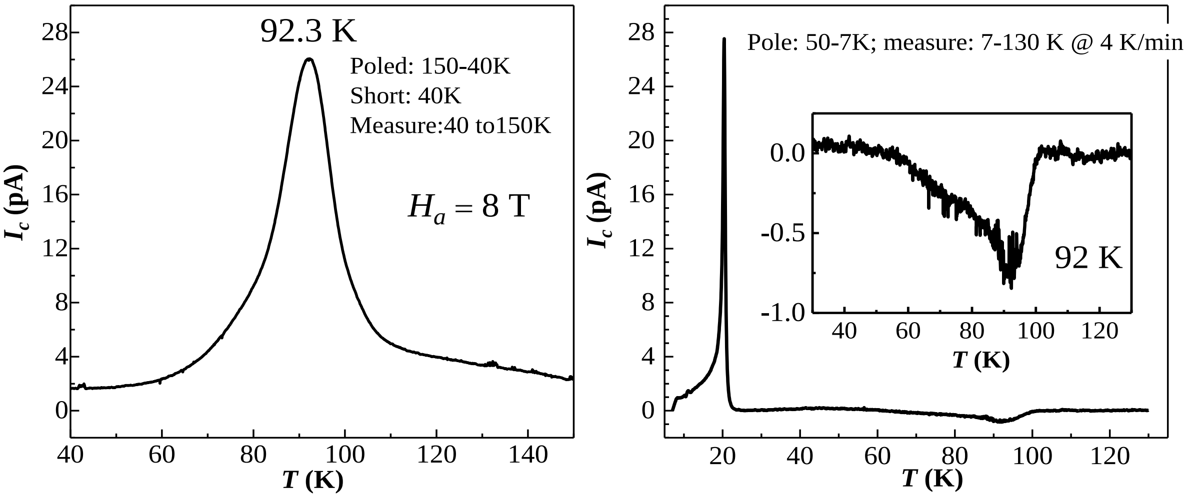

Figure 4.31 (a) TSFC related pyrocurrent peak. (b) the correlation between ferroelectric ordering pyropeak and TSFC carrier related pyropeak.

4.6.3 Origin of memory effect

In order to confirm the existence of E_{int}^{LCC} and the correlation of both E_{int}^{LCC} and E_{int}^{TSFC} to the memory effect, we recorded the pyrocurrent with different poling temperature intervals. First, we have applied E_{ext} (5.6 kV/cm) to the sample from 130 to 60 K and further cool down the sample to 7 K with $E_{ext} = 0$ and subsequently measured the pyrocurrent from 7 to 130 K. A positive pyrocurrent peak at T_C and a negative pyrocurrent peak at 90 K is observed. Since we know that the direction of the E_{int}^{TSFC} is opposite to the external field as demonstrated earlier [38], we confirm that such pyrocurrent behavior is related to E_{int}^{TSFC}. The similar feature of pyrocurrent is observed when the sample is poled at 70 K or above 70 K e.g poling from 100 to 45 K, 150 to 70 K and 70 to 45 K (figure 4.32). As the TSFC carriers become mobile above 70 K, the field applied only above 70 K produces small peaks or no peak in the pyrocurrent e.g. poling at 100 K for 15min (gray, left triangle curve in Fig. 3). Further, the TSFC charge carriers are almost immobile at low temperature (T<T_f), so the formation of E_{int}^{TSFC} should be negligible when the sample is subjected to E_{ext} at low temperature. Thus E_{int}^{TSFC} is unlikely to cause the memory effect which we observed after poling the sample below 30 K.

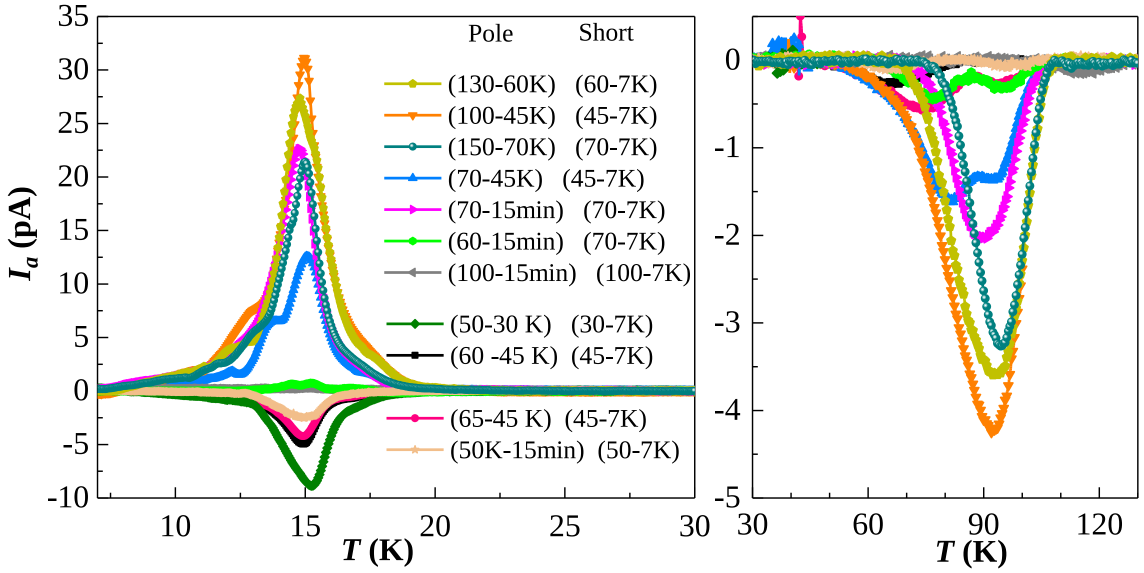

Figure 4.32 Pyro current data with different poling temperature interval. The poling field was set at 5.6 kV/cm for all the measurements.

Next, we applied the electric field in the range of 60 to 30 K and further cool down to 7 K without any external field and measured the pyrocurrent from 7 to 130 K. Intriguingly, we have observed a negative pyrocurrent peak at the T_C which is in the same direction of E_{ext} applied field but opposite to the E_{int}^{TSFC} (see figure 4.32). In this poling case, we do not expect any pyrocurrent peak at T_C as the field was applied above T_C or T_N

and below T_f. Thus, we argue that the internal electric field (E_{int}^{LCC}) is produced below T_f owing to the localized charge carriers as introduced before. This internal field actually can polarize the ferroelectric dipoles across T_C. It should be noted that E_{int}^{LCC} should be disappeared when a sufficient thermal energy is present. Since the TSFC carriers become mobile above 70 K, the localized charge carrier dipoles can also be dissociated along with TSFC carriers.

Now, we recall the thermal behavior of P_{TR} (figure 4.27(c)) where we see a step like increase above 30 K and gradual decrease above 60 K. This temperature profile resembles the activity of E_{int}^{LCC} with temperature and suggest that E_{int}^{LCC} is responsible for the memory effect. It should be noted here that the effect of ferroelectric poling above T_C resembles the role of defects in ferroelectric materials [59-63]. Such defects can be formed due to oxygen vacancy, compositional defects or localized lattice distortion. When the defects are charged with external electric field, they become Defect-Dipoles (DD) and can act as an intrinsic local internal bias field inside the grain. This causes occasionally domain pinning (double hysteresis), shifting of PE hysteresis loop in the ferroelectric materials through internal biasing field [63]. The ferroelectric dipoles align in the same direction of defect dipoles since the defects are present in the ferroelectric domain itself and can induce a preference to align the spontaneous ferroelectric domains in the same direction [63]. Thus, it can align the ferroelectric dipoles locally along the same direction as the external electric field. Since we learned that the localized charge carrier is correlated to the magnetic ordering in the sample, it is likely to imagine the presence of tiny polar region consisting of chiral magnetic domain is associated with the localized charge carriers even in the paramagnetic state. Therefore we propose the following mechanism for the observed memory effect.

A schematic diagram consisting of ferroelectric dipole, LCC dipole and sample/electrode interface dipole, is shown in figure 4.33. It depicts the stray charges at the electrode and sample interface, causing the internal electric field (E_{int}^{TSFC}) and has the direction opposite to the external electric field. The red color arrow represents the ferroelectric dipoles. The white arrow represents the local dipoles ordered in parallel to the ferroelectric dipoles. When the external electric field is applied above 30 K, it can polarize the local dipoles and the associated local microscopic chiral domains. While cooing the sample, despite removing the external field below 30 K, the local dipoles can be reformed as macroscopic ferroelectric domains and form a single domain state below the ferroelectric transition.

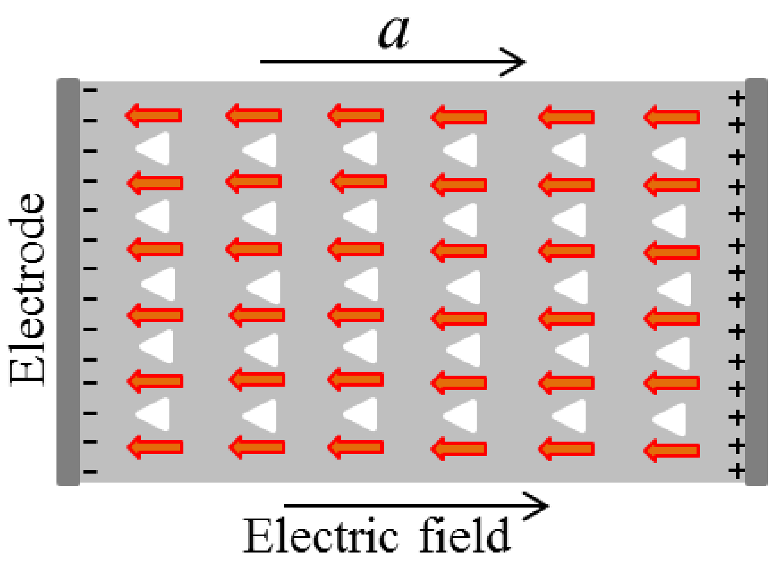

Figure 4.33 Schematic diagram of ferroelectric dipoles and defect dipoles.

Similarly when we apply field to the sample below 30 K, it polarize the macroscopic ferroelectric dipoles and while measuring the pyrocurrent or ramping the temperature above T_C in absence of external field, the local dipoles associated with the polar cycloidal domains can be formed which can carry the microscopic polarization and does not vanish even above T_N. If the T_R does not exceed $\mathrm{T}_{\mathrm{Mem}}^{\mathrm{Max}}$, the stored microscopic polarization can reformed into macroscopic ferroelectric dipoles while cooling the sample through T_C. In this way the LCC dipoles can be reformed as macroscopic ferroelectric dipoles in the cooling process thus a polarization current appears (figure 4.26 dotted curves) and the macroscopically polarized ferroelectric dipoles can deformed into the local dipoles in the warming process hence a depolarization curve appears (figure 4.26 continuous curves). This cyclic process between local dipoles and ferroelectric dipoles forming and deforming can continue until the T_R goes above T_{Max}^{Mem}. We argue that this memory effect may be observed in multiferroic materials due to unintended consequence of defects where the defects may not necessarily have any magnetic correlation. Thus the multiferroic materials can hold the polarization state even above their onset temperature which may enable it more suitable for the practical applications.

4.7 Conclusions

In conclusion, we demonstrated that the ferroelectric polarization state can be restored from a deep paramagnetic region without applying any electric or magnetic field. We have shown that the temperature profile of the magnetoelectric memory effect correspond to a relaxation behavior of magnetically active localized charge carriers in the lattice. The localized charge carriers are composed of small polar cycloidal domains. Our findings offer a new way of enabling the multiferroics to be operated even at higher temperatures.

References

[1] T. Kimura, T. Goto, H. Shintani, K. Ishizaka, T. Arima, and Y. Tokura, Nature **426**, 55 (2003).

[2] T. Goto, T. Kimura, G. Lawes, A. P. Ramirez, and Y. Tokura, Phys. Rev. Lett. **92**, 257201 (2004).

[3] H. Béa, M. Gajek, M. Bibes, and A. Barthélémy, J. Phys. Condens. Matter **20**, 434221 (2008).

[4] I. Kézsmárki, U. Nagel, S. Bordács, R. S. Fishman, J. H. Lee, H. T. Yi, S. W. Cheong, and T. Rõõm, Phys. Rev. Lett. **115**, 127203 (2015).

[5] S. Toyoda, N. Abe, S. Kimura, Y. H. Matsuda, T. Nomura, A. Ikeda, S. Takeyama, and T. Arima, Phys. Rev. Lett. **115**, 267207 (2015).

[6] N. A. Spaldin and M. Fiebig, Science **309**, 391 (2005).

[7] S.-W. Cheong and M. Mostovoy, Nat Mater **6**, 13 (2007).

[8] T. Kimura, Annu. Rev. Condens. Matter Phys. **3**, 93 (2012).

[9] Y. Tokura, S. Seki, and N. Nagaosa, Reports on Progress in Physics **77**, 076501 (2014).

[10] M. M. Vopson, Critical Reviews in Solid State and Materials Sciences **40**, 223 (2015).

[11] T. Kimura, G. Lawes, T. Goto, Y. Tokura, and A. P. Ramirez, Phys. Rev. B **71**, 224425 (2005).

[12] K. Noda, S. Nakamura, J. Nagayama, and H. Kuwahara, J. App. Phys. **97** (2005).

[13] H. Katsura, N. Nagaosa, and A. V. Balatsky, Phys. Rev. Lett. **95**, 057205 (2005).

[14] M. Mostovoy, Phys. Rev. Lett. **96**, 067601 (2006).

[15] I. A. Sergienko and E. Dagotto, Phys. Rev. B **73**, 094434 (2006).

[16] J. Hemberger, F. Schrettle, A. Pimenov, P. Lunkenheimer, V. Y. Ivanov, A. A. Mukhin, A. M. Balbashov, and A. Loidl, Phys. Rev. B **75**, 035118 (2007).

[17] Y. Yamasaki, H. Sagayama, T. Goto, M. Matsuura, K. Hirota, T. Arima, and Y. Tokura, Phys. Rev. Lett. **98**, 147204 (2007).

[18] M. Mochizuki and N. Furukawa, Phys. Rev. B **80**, 134416 (2009).

[19] T. Goto, Y. Yamasaki, H. Watanabe, T. Kimura, and Y. Tokura, Phys. Rev. B **72**, 220403 (2005).

[20] T. Arima, T. Goto, Y. Yamasaki, S. Miyasaka, K. Ishii, M. Tsubota, T. Inami, Y. Murakami, and Y. Tokura, Phys. Rev. B **72**, 100102 (2005).

[21] N. Aliouane *et al.*, J. Phys. Condens. Matter **20**, 434215 (2008).

[22] Y. Yamasaki *et al.*, Phys. Rev. Lett. **101**, 097204 (2008).

[23] O. Prokhnenko, R. Feyerherm, E. Dudzik, S. Landsgesell, N. Aliouane, L. C. Chapon, and D. N. Argyriou, Phys. Rev. Lett. **98**, 057206 (2007).

[24] S. Ishiwata, Y. Kaneko, Y. Tokunaga, Y. Taguchi, T.-h. Arima, and Y. Tokura, Phys. Rev. B **81**, 100411 (2010).

[25] N. Zhang, S. Dong, Z. Fu, Z. Yan, F. Chang, and J. Liu, Sci. Rep. **4**, 6506 (2014).

[26] T. Aoyama, K. Yamauchi, A. Iyama, S. Picozzi, K. Shimizu, and T. Kimura, Nat. Commun. **5**, 4927 (2014).

[27] L. C. Chapon *et al.*, Neutron News **22**, 22 (2011).

[28] V. Petříček, M. Dušek, and L. Palatinus, Zeitschrift für Kristallographie-Crystalline Materials **229**, 345 (2014).

[29] B. J. Campbell, H. T. Stokes, D. E. Tanner, and D. M. Hatch, Journal of Applied Crystallography **39**, 607 (2006).

[30] See the supplemental material for heat capacity and detailed magnetization, dielectric and pyrocurrent data.

[31] N. Terada, Y. S. Glazkova, and A. A. Belik, Phys. Rev. B **93**, 155127 (2016).

[32] B. Koteswararao, K. Yoo, F. Chou, and K. H. Kim, APL Mater. **4**, 036101 (2016).

[33] S. Ghara, N. Ter-Oganessian, and A. Sundaresan, Phys. Rev. B **95**, 094404 (2017).

[34] H. Murakawa, Y. Onose, F. Kagawa, S. Ishiwata, Y. Kaneko, and Y. Tokura, Phys. Rev. Lett. **101**, 197207 (2008).

[35] F. Kagawa, M. Mochizuki, Y. Onose, H. Murakawa, Y. Kaneko, N. Furukawa, and Y. Tokura, Phys. Rev. Lett. **102**, 057604 (2009).

[36] N. Abe, K. Taniguchi, H. Sagayama, H. Umetsu, and T. Arima, Phys. Rev. B **83**, 060403 (2011).

[37] C. De and A. Sundaresan, App. Phys. Lett. **107**, 052902 (2015).

[38] C. De, S. Ghara, and A. Sundaresan, Solid State Commun. **205**, 61 (2015).

[39] M. Mochizuki, N. Furukawa, and N. Nagaosa, Phys. Rev. B **84**, 144409 (2011).

[40] E. Bertaut, G. Rado, and H. Suhl, in Magnetism, Edited by Rado GT, Suhl H. New York: Academic **3**, 149 (1963).

[41] R. Kajimoto, H. Yoshizawa, H. Shintani, T. Kimura, and Y. Tokura, Phys. Rev. B **70**, 012401 (2004).

[42] S. Dong, J.-M. Liu, S.-W. Cheong, and Z. Ren, Adv. Phys. **64**, 519 (2015).

[43] A. Pimenov, A. Mukhin, V. Y. Ivanov, V. Travkin, A. Balbashov, and A. Loidl, Nat. Phys. **2**, 97 (2006).

[44] A. Pimenov, A. Loidl, A. Mukhin, V. Travkin, V. Y. Ivanov, and A. Balbashov, Phys. Rev. B **77**, 014438 (2008).

[45] K. Taniguchi, N. Abe, S. Ohtani, and T. Arima, Phys. Rev. Lett. **102**, 147201 (2009).

[46] I. Fina, V. Skumryev, D. O'Flynn, G. Balakrishnan, and J. Fontcuberta, Phys. Rev. B **88**, 100403 (2013).

[47] I. Fina, L. Fàbrega, X. Martí, F. Sánchez, and J. Fontcuberta, Phys. Rev. Lett. **107**, 257601 (2011).

[48] M. Schiebl, A. Shuvaev, A. Pimenov, G. Johnstone, V. Dziom, A. Mukhin, V. Y. Ivanov, and A. Pimenov, Phys. Rev. B **91**, 224205 (2015).

[49] A. Pimenov, A. Shuvaev, A. Mukhin, and A. Loidl, J. Phys. Condens. Matter **20**, 434209 (2008).

[50] S. Wilkins *et al.*, Phys. Rev. Lett. **103**, 207602 (2009).

[51] T. Finger, D. Senff, K. Schmalzl, W. Schmidt, L. Regnault, P. Becker, L. Bohatỳ, and M. Braden, Phys. Rev. B **81**, 054430 (2010).

[52] F. Schrettle, P. Lunkenheimer, J. Hemberger, V. Y. Ivanov, A. Mukhin, A. Balbashov, and A. Loidl, Phys. Rev. Lett. **102**, 207208 (2009).

[53] J. Yang *et al.*, App. Phys. Lett. **101**, 222904 (2012).

[54] S. Liu and R. Cohen, App. Phys. Lett. **111**, 082903 (2017).

[55] D. O'Flynn, M. R. Lees, and G. Balakrishnan, J. Phys. Condens. Matter **26**, 256002 (2014).

[56] S. Elsässer, M. Schiebl, A. Mukhin, A. Balbashov, A. Pimenov, and J. Geurts, New J. Phys. **19**, 013005 (2017).

[57] P. Lunkenheimer, S. Krohns, S. Riegg, S. G. Ebbinghaus, A. Reller, and A. Loidl, Eur. Phys. J. Special Topics **180**, 61 (2009).

[58] T. Ngo, U. Adem, and T. Palstra, App. Phys. Lett. **106**, 152904 (2015).

[59] P. Gao *et al.*, Nat. Commun. **2**, 591 (2011).

[60] Y. Pu, J. Zhu, X. Zhu, Y. Luo, M. Wang, X. Li, J. Liu, J. Zhu, and D. Xiao, J. App. Phys. **109**, 044102 (2011).

[61] S. M. Yang, S. J. Moon, T. H. Kim, and Y. S. Kim, Curr. Appl. Phys. **14**, 757 (2014).

[62] C. Folkman, S. Baek, C. Nelson, H. Jang, T. Tybell, X. Pan, and C. Eom, App. Phys. Lett. **96**, 052903 (2010).

[63] D. Lee, H.-S. Kim, S. Y. Jang, K. W. Joh, T. W. Noh, J. Yu, C. E. Lee, and J.-G. Yoon, Phys. Rev. B **81**, 012101 (2010).

Chapter 5

Magnetic and dielectric properties of the layered and rock-salt ordered NaRMWO$_6$ (R = La, Nd, Tb, Y and Ho; M = Mn, Fe and Co) double perovskites*

Summary

Various experimental work as well as theoretical calculation on structural basis has predicted that the double perovskites, NaRMnWO$_6$ (R = La, Nd, Tb) exhibiting simultaneous ordering of A-site cations (Na and R-ions) in layered arrangement and B-site cations (Mn and W) in rock salt structure crystallize in monoclinic polar $P2_1$ phase with a large electric polarization (~20 μC/cm^2 for La). Our studies such as, $P(E)$, PUND and piezoelectric reveal no sign of polar character on NaRMnWO$_6$ compounds for R-ions (La, Nd and Tb) of larger size. However, samples with the lower size of rare-earth (Y), prepared under high pressure and high temperature, the octahedral distortion is sufficiently high which could stabilize the polar structure. We have extended our investigation using different transition metals such as Fe, Co and Cu holding the same doubly ordered structure. A polar structure along with a strong magnetoelectric coupling below the antiferromagnetic ordering is also found for Co with lower size rare-earth (Ho) ion. This chapter will bring a comprehensive study and discussion of some possible polar double perovskite materials along with their electrical and magnetic properties.

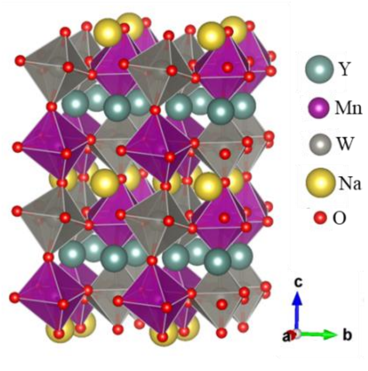

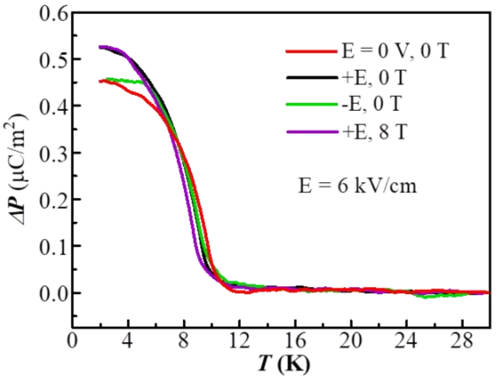

---

*This work has appeared in **C. De** *et al. Phys. Chem. Chem. Phys.* **16**, 5407 (2014) and C. De and A. Sundaresan, *Phys. Rev. B,* **97**, 214418 (2018), © (2018) by APS.

5.1 Introduction

In the history of ferroelectric research, there is a classical strategy of making polar, non-centrosymmetric oxides, wherein due to the lack of spatial inversion symmetry, ferroelectric polarization appears. Crystallographically, a material can be considered as polar if it is a member of one of the following 10 polar crystal classes (1, 2, 3, 4, 6, *m*, *mm*2, 3*m*, 4*mm* or 6*mm*) [1]. The materials constituting polar group, provides lot of fascinating and technologically useful properties such as ferroelectricity, piezoelectricity, second order non-linear optical behavior etc. In ferroelectric case, the polarization has to be switched with reversing the electric field whereas in piezoelectric case switching is not compulsory. Based on the origin of ferroelectric states, it can be divided into two categories.

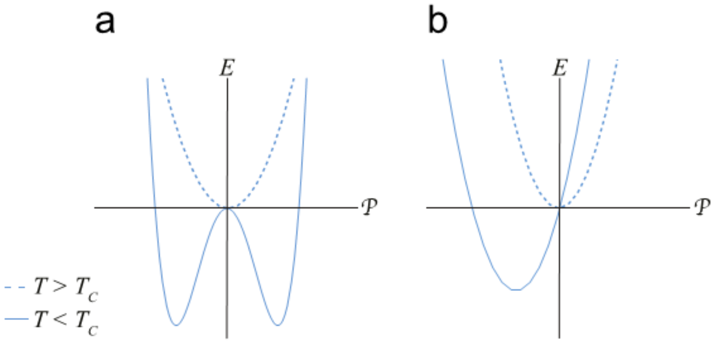

Figure 5.1 Energy behavior as a function of the polarization when T is above and below the Curie temperature (T_C) of the primary order parameter for (a) a proper and (b) an improper ferroelectric transition. Adopted from ref. [2] © Copyright from J. Solid State Chem. (2012).

In the case of proper ferroelectric, a polar lattice distortion occurs through a different symmetry between paraelectric and ferroelectric ground state. In this case, the energy has a characteristic double-well potential which can be switched using an electric field without any other structural distortions (figure 5.1(a)). The classical strategy for making proper ferroelectric materials is to incorporate second order Jahn-Teller (SOJT) distortion (octahedrally coordinated d^0 transition metals Ti^{+4}, Nb^{+5}, W^{+6} etc.) or stereo-active lone pair (Te^{+4}, Pb^{+2}, Bi^{+3}, Se^{+4} etc.) electrons in the materials, as for example $BaTiO_3$ and $BiFeO_3$ respectively. A perovskite structure is an ideal framework for adopting such elements. In the case of improper ferroelectric, the polarization remains in a single well potential where the minimum is shifted to a non-zero value (figure 5.1(b)) [2]. A large structural change occurs at the paraelectric to ferroelectric transition e.g., the unit cell volume increases by at least factor of two. For example, hexagonal manganite e.g. $YMnO_3$, the rotation of MnO_5 trigonal-bipyramids and buckling of the yttrium planes results in a tripling of the unit cell volume [3]. An electric field actually switches the sense of rotation-like distortion of the MnO_5 polyhedra. In particular, this rotational degree of freedom is greatly advantageous for designing the functional materials since it can allow a change in magnetic ordering through altering the bond angles.

5.1.1 Hybrid improper ferroelectricity in perovskites

Hybrid improper ferroelectricity (HIF) is a powerful mechanism where an electrical polarization can be obtained, for example, through assembling two nonpolar substances within a super-lattice [4-6]. For a perovskite structure, although octahedral rotations are associated with a lattice instability, the individual rotations cannot induce ferroelectricity as they are connected in three dimensional network [7]. It was predicted that a combination of non-polar octahedral rotations can induce the ferroelectricity through a trilinear coupling called as hybrid improper ferroelectricity [4, 8]. This prediction was well verified in several experimental studies. For example, in a combined theoretical and experimental study, by growing $(SrTiO_3)_n/(PbTiO_3)_m$ super-lattices, it was observed that for a small period super-lattices the polarization was increased with increasing the layer of $SrTiO_3$ which is a paraelectric substance [9]. The additional polarization was explained by a combination of two different octahedral rotations, R_1 and R_2, with different symmetries. Another significant example of hybrid improper ferroelectricity was demonstrated in Ruddlesden–Popper ($A_{n+1}B_n\,O_{3n+1}$) phase where one extra layer of A-O is inserted in every *n* perovskite unit cells. For *n*=2, $Ca_3Ti_2O_7$ and $Ca_3Mn_2O_7$ phases results in the polar $A2_1am$ space group through octahedral rotation. Using first principle calculation, $Ca_3Ti_2O_7$ and $Ca_3Mn_2O_7$ was shown to have a large polarization of P = 20 μC/cm^2 and 5 μC/cm^2 respectively [8] where $Ca_3Mn_2O_7$ induces a linear magnetoelectric effect through electric field tuning of oxygen rotation [10]. Besides, HIF was also demonstrated in $(Ca,Sr)_3Ti_2O_7$ crystals [11].

Simple perovskite oxides (ABO_3) are one of most curious and useful family of materials where both A and B cations of different valence and size can be accomodated and thus providing a large number of diverse and fascinating properties e.g. ferroelectricity [12], ferromagnetism, piezoelectricity [13], superconductivity [14], colossal magnetoresistance [15], ionic conductivity [16], Mott insulator [17] and multiferroicity [3, 18-20]. Recently, a family of doubly ordered perovskites with the formula, AA'BB'O$_6$ has fascinated solid state chemists owing to the unusual combination ordering of both the cations at A-and B-site in the perovskite structure [21, 22]. For example, in NaRMnWO$_6$ (R = La, Nd and Tb), Na and R ions order in a layered form at the A-site and Mn and W ions order in a rock-salt manner at the B-site [23]. Such double ordering in the stoichiometric compound is unusual [24] and is known usually in oxygen or cation deficient compounds [25, 26]. It was suggested that the layered ordering in the double perovskites provides bond instability which is compensated by the presence of highly charged d^0 cation on one of the B-site [22, 23]. In addition to the cation ordering, these compounds are expected to crystallize in polar space group $P2_1$ according to the x-ray and neutron diffraction analysis [27, 28]. This polar structure can be explained by particular octahedral tilting in the distorted perovskites structure. A combination of two non-polar octahedral rotation system (a^{0}a^{0}c$^+$ and a$^-$a$^-$c$^+$ in glazer notation) coupled through a trilinear coupling and the presence of layered cation ordering at the B-site causes the structure polar [29, 30]. Here the octahedral rotation depends on the Goldsmith tolerance factor ($t = \frac{r_A + r_0}{\sqrt{2}(r_B + r_o)}$) of the perovskite structure. The lower size of A-site cations (rare-earth ions) gives lower t value thus a larger distortion occurs in the structure. Based on density functional theory calculations and group theoretical analysis, a fairly large ferroelectric polarization 16 μC/cm^2 was obtained in NaLaMnWO$_6$ belonging to $P2_1$ structure [29]. With the lower size of rare-earths a larger polarization can be expected.

Besides, these double perovskite compounds exhibit antiferromagnetic ordering at low temperatures (T_N ranging from 10 to 15 K) due to the presence of magnetic ions at the B-site. A neutron diffraction study in NaLaMnWO$_6$ had shown that the Mn^{2+} ions order commensurately AFM (k = ½, 0, ½) as a consequence of Mn–O–W–O–Mn superexchange [28]. When Nd is replaced for La^{3+} ions, the magnetic sublattices order into an incommensurate (k = 0, 0.48, ½) structure where, Nd and Mn both ions order simultaneously at ~11 K. NaTbMnWO$_6$ showed two magnetic phase transitions upon cooling, one at 15 K and another ~9 K which is due to the coupling between two magnetic sublattices Mn^{2+} and Tb^{3+} [27, 28]. The wave vector at 11 K was found to be a combination of commensurate (½, 0, ½) and incommensurate (0, 0.427, ½) and behaves commensurate (½, 0, ½) at 6 K [28]. Therefore the presence of second order Jahn-Teller (d^0) W^{6+} ion and magnetic ions at the B-site makes this family of oxides potentially attractive for multiferroic properties. Nevertheless, the x-ray diffraction patterns of all these compounds could also be fitted with $P2_1/m$ centrosymmetric space group in addition to the $P2_1$ structure since they both have same extinction rule and a small difference in intensity which create the structure equivocal. Interestingly, a recent investigation on Co containing doubly ordered perovskites, Na*Ln*CoWO$_6$, has shown that the compound with larger *Ln* ions (*Ln*=La, Pr and Nd) crystallizes in nonpolar structures ($C2$/m) but the compounds with smaller *Ln*-ions (*Ln*=Sm-Yb) are in polar with $P2_1$ symmetry due to larger distortion in the structure [31].

In this chapter, at first we have attempted to investigate the electrical properties of the doubly ordered perovskites Na*Ln*MnWO$_6$ (*Ln*=La, Nd and Tb), Na*Ln*FeWO$_6$ (*Ln* = La and Nd) and Na*Ln*CoWO$_6$ (*Ln* = La and Nd) prepared under ambient pressure in order to explore possible ferroelectric properties. However, using the conventional $P(E)$ loop measurements, we found that none of these compounds showed ferroelectric loop at room temperature. For further confirmation, we have employed a modified $P(E)$ loop measurement technique, called Positive-Up and Negative-Down (PUND) [32] which could overcome the experimental difficulty present in the conventional *PE* method due to defects, porosity or high leakage current [33, 34]. We have also studied the physical properties such as magnetization, piezoelectricity, SHG [35], dielectric permittivity, dc and ac conductivity and pyroelectric current for all the synthesized compounds.

Later we have synthesized two more doubly ordered compounds NaYMnWO$_6$ and NaHoCoWO$_6$, under high pressure and high temperature, which could not be made under ambient condition. Rietveld refinement of x-ray diffraction data in these two compounds has good agreement with the polar ($P2_1$) structure. Both Mn^{2+} and Co^{2+} ions undergo antiferromagnetic ordering around 9 K similar to the other compounds. The $P(E)$ loop measurements in the paramagnetic polar state show almost a linear loop. However, pyroelectric measurements across the magnetic transition show a change in electric polarization (ΔP) without applying a poling electric field. Further, the polarization is not switchable upon reversing the direction of poling electric field. These results demonstrate the pyroelectric nature of these doubly ordered perovskites indicating a large energy barrier between the two polar states. Further, our attempt of synthesizing Na*R*CuWO$_6$ compounds was not successful in ambient pressure as well as high pressure (up to 4.5 GPa) and high temperature conditions used in the present investigations.

5.2 Experiments

Polycrystalline samples of Na*R*MnWO$_6$ (*R* =La, Nd and Tb), NaLaFeWO$_6$ and Na*R*CoWO$_6$ (*R* =La and Nd) were synthesized by the conventional solid state route at ambient pressure. The precursors MnWO$_4$, FeWO$_4$, CoWO$_4$ and CuWO$_4$ were first prepared by heating appropriate amount of Mn$_2$O$_3$, Fe$_2$O$_3$, Co$_3$O$_4$, CuO and WO$_3$ in air at 1200 °C for MnWO$_4$ and FeWO$_4$, 1100 °C for CoWO$_4$ and 800 °C for CuWO$_4$ for 40 h each. Stoichiometric amounts of rare-earth oxides (La$_2$O$_3$, Nd$_2$O$_3$ and Tb$_4$O$_7$ after preheating at 950°C for 10-12 h), MWO$_4$ and Na$_2$CO$_3$ were mixed using an agate mortar and pestle. An excess of 5wt% of Na$_2$CO$_3$ was taken to compensate the loss of sodium due to volatile nature of Na$_2$O for all the compounds. The compounds with lower size of rare-earth, NaYMnWO$_6$ and NaHoCoWO$_6$ were synthesized by solid state reaction under high pressure and high temperature using cubic anvil-type high pressure apparatus as described in chapter 2. As a source of Na, Na$_2$WO$_4$ was chosen which was prepared by heating the stoichiometric mixture of Na$_2$CO$_3$ and WO$_3$ at 800 °C for 12 h with several intermittent grinding. CoO precursor was prepared from Co$_3$O$_4$ by heating at 950 °C in Ar for 12 h. Purity of these precursors were confirmed by powder X-Ray diffraction (XRD) patterns before using for high pressure synthesis. Finally, the stoichiometric amount of Na$_2$WO$_4$ (preheated at 150 °C before using), Ho$_2$O$_3$ (preheated at 950 °C), CoO and WO$_3$ were thoroughly mixed for sufficient time. For high-pressure synthesis, the mixed powder was pressed into a cylinder and wrapped with gold foil. The sample assembly was placed in the six anvil system and pressurized up to 4.5 GPa. After reaching the desired pressure, the temperature was increased to 1000 °C and maintained for 1 hour followed by quenching to room temperature and then the pressure was decreased slowly. NaLaCuWO$_6$ has also been attempted under high pressure following the similar synthesis process. The individual preparation conditions including the unsuccessful materials are given in the table 5.1.

Powder X-ray Diffraction (P-XRD) data were collected using Bruker D8 Advanced X-ray diffractometer and analyzed by Rietveld method using Full-Prof Professional suite [36]. For NaYMnWO$_6$ and NaHoCoWO$_6$ compounds the P-XRD pattern were taken in PANalytical Empyrean alpha-1 monochromatic diffractometer at room temperature. Magnetization measurements were carried out on a Quantum Design's SQUID VSM and data were collected from 2 to 300 K with the increment of 3 K/min. Electrical measurements were performed in Quantum Design's PPMS that provides temperature and external magnetic field control. Agilent LCR meter (E4980A) and Keithley (6517B) Electrometer were used to measure dielectric and pyroelectric property. PELCO High performance silver paste was used to make the electrodes on the flat sample surface. For $P(E)$ and PUND measurement in NaRMnWO$_6$ (R = La, Nd and Tb) electrodes were made by gold sputtering. $P(E)$ loop, PUND, piezoelectricity measurements were performed using Radiant technology Precision Work station. SHG measurements were performed at room temperature in DCR-11 equipped with Laser of 1064 nm wavelength [35]. Thermogravimetric analysis (TGA) and Differential thermal analysis (DTA) was recorded up to 1000 °C under N_2 atmosphere at 3°C/min in Mettler TGA 850.

Table 5.1 List of compounds attempted and their detailed synthesis condition and quality.

compounds	Synthesis condition	Phases	Remarks
Successful compounds			
$NaLaMnWO_6$	1000 ºC in forming gas (5% H_2 and 95% Ar)	Pure	Yellow color
$NaNdMnWO_6$	1000 ºC (forming gas)	Pure	Yellow color
$NaTbMnWO_6$	980 ºC (in forming gas)	Small Tb_4O_7	Deep green
$NaLaFeWO_6$	1010 ºC (in forming gas)	Pure	Gray in color, more conductive
$NaLaCoWO_6$	1000 ºC (in air)	Small Na_2WO_4+ unknown impurity	First attempt at 980 °C had more impurity phase.
$NaNdCoWO_6$	980 ºC (in air)	Small Na_2WO_4 and WO_3	Heating cycles were unsuccessful for eliminating impurity.
$NaYMnWO_6$	1000 ºC under 4.5 GPa	Small Y_2WO_6	Green color, single crystalline grains, preferred orientation in the X-ray.
$NaHoCoWO_6$	1000 ºC under 4.5 GPa	Pure	Gray color sample. After grinding turned into light deep purple color. Well sintered.
Unsuccessful compounds			
$NaLaCuWO_6$	980ºC (in air)	Na_2WO_4 +CuO	No main phase obtained, $CuWO_4$ melted at 1000 ºC
$NaNdCuWO_6$	980ºC (in air)	Na_2WO_4 + Nd_2WO_6	No main phase obtained
$NaLaCuWO_6$	4.5 GPa, 1000ºC (Gold capsule)	$NaLaCuWO_6$+ Na2WO4+CuO	Green color, some amount of phase formed.
$NaBiCoWO_6$	550ºC (in argon)	$CoWO_4$ +Bi_2O_3 +Na_2WO_4	melted at 850 ºC. Not formed at even 700ºC and 600 ºC.
$NaBiCoWO_6$ (using$NaBiO_3$)	750 ºC (in argon)	Bi_2WO_6 +Na_2WO_4 phase not formed	To avoid two phases of Na_2CO_3 and Bi_2O_3 we used $NaBiO_3$
$NaBiCuWO_6$	550 ºC (in argon)	Bi_2WO_6 +Na_2WO_4 +Bi_2O_3	melted at 850ºC, Phase not formed at even 700ºC and 600ºC.

KBiCoWO$_6$	500 ºC (in argon)	Bi_2O_3 +WO_3 phase not formed	Potassium compounds are hygroscopic.
KBiCuWO$_6$	500 ºC (in argon)	CuWO4 + Bi2O3 + CuO	Target phase not formed
NaDyCuWO$_6$	900 ºC (in air)	Dy_2WO_6 +Na_2WO_4 +CuO + Dy_6WO_{12}	Phase not formed at even 800 ºC and 1000 ºC.
NaYCuWO$_6$	900 ºC (in air)	Y_2WO_6 + Na_2WO_4 +CuO	Phase not formed at even 800 ºC and 1000 ºC.

5.3 Results and discussion: Na*R*MWO$_6$ (for M = Mn, *R* = La, Nd and Tb; M = Co, *R* = La and Nd; M = Fe, *R* = La) synthesized under ambient pressure

5.3.1 Structural details of Na*R*MnWO6 (*R* = La, Nd and Tb)

Results of Rietveld refinement on the room temperature P-XRD data of Na*R*MnWO$_6$ are shown in figure 5.2 (a, b and c) for *R*= La, Nd and Tb respectively. The refinements are performed with the $P2_1$ space group motivated by the earlier report [23]. No impurity was observed in XRD for NaNdMnWO$_6$ and NaLaMnWO$_6$ whereas a little amount of Tb_4O_7 was present as a secondary phase in NaTbMnWO$_6$. Additional heating cycles were unsuccessful for eliminating this impurity. The lattice parameters of all these compounds, extracted from Rietveld refinement, are shown in table 5.3 and 5.4 which are consistent with the earlier report [23]. The lattice parameters are decreasing with the decreasing tolerance factor which is expected if the octahedral tilting distortion increases with the decreasing of tolerance factor. Tolerance factor is calculated based on the average cation size for both 'A' and 'B' sites with the respective coordinates. Depending on the synthesis temperature, the color of the Na*R*MnWO$_6$ (*R* = La, Nd, Tb) varies slightly. After first heating, they appeared deep green and turned to greenish-yellow when sintered at 1000 °C. The powder X-ray Diffraction patterns of these compounds with different color were indistinguishable.

Table 5.2 Structural details of the synthesized compounds

Compounds	(S.G)	a (Å)	b (Å)	c (Å)	β (deg)	volume (Å)^3	*t*
NaLaMnWO$_6$	$P2_1$	5.5976 (3)	5.5602(3)	8.0317 (3)	90.113 (3)	251.86 (2)	0.93
NaNdMnWO$_6$	$P2_1$	5.5114 (1)	5.5920 (2)	7.9839 (2)	90.373 (2)	246.06 (1)	0.91
NaTbMnWO$_6$	$P2_1$	5.4245 (3)	5.5847 (3)	7.9243 (4)	89.645 (2)	240.06 (2)	0.91
NaYMnWO$_6$	$P2_1$	5.3936(0)	5.5817(0)	7.9052(0)	90.336(0)	237.99(0)	0.90
NaLaCoWO$_6$	$C2/m$	7.8300(1)	7.8415(1)	7.8931(1)	90.167(1)	484.63(1)	0.96
NaNdCoWO$_6$	$C2/m$	7.7899(3)	7.7454(5)	7.8773(3)	90.187(2)	475.28(4)	0.94
NaHoCoWO$_6$	$P2_1$	5.3467(0)	5.5219(0)	7.7896(0)	90.282(0)	229.98(0)	0.92

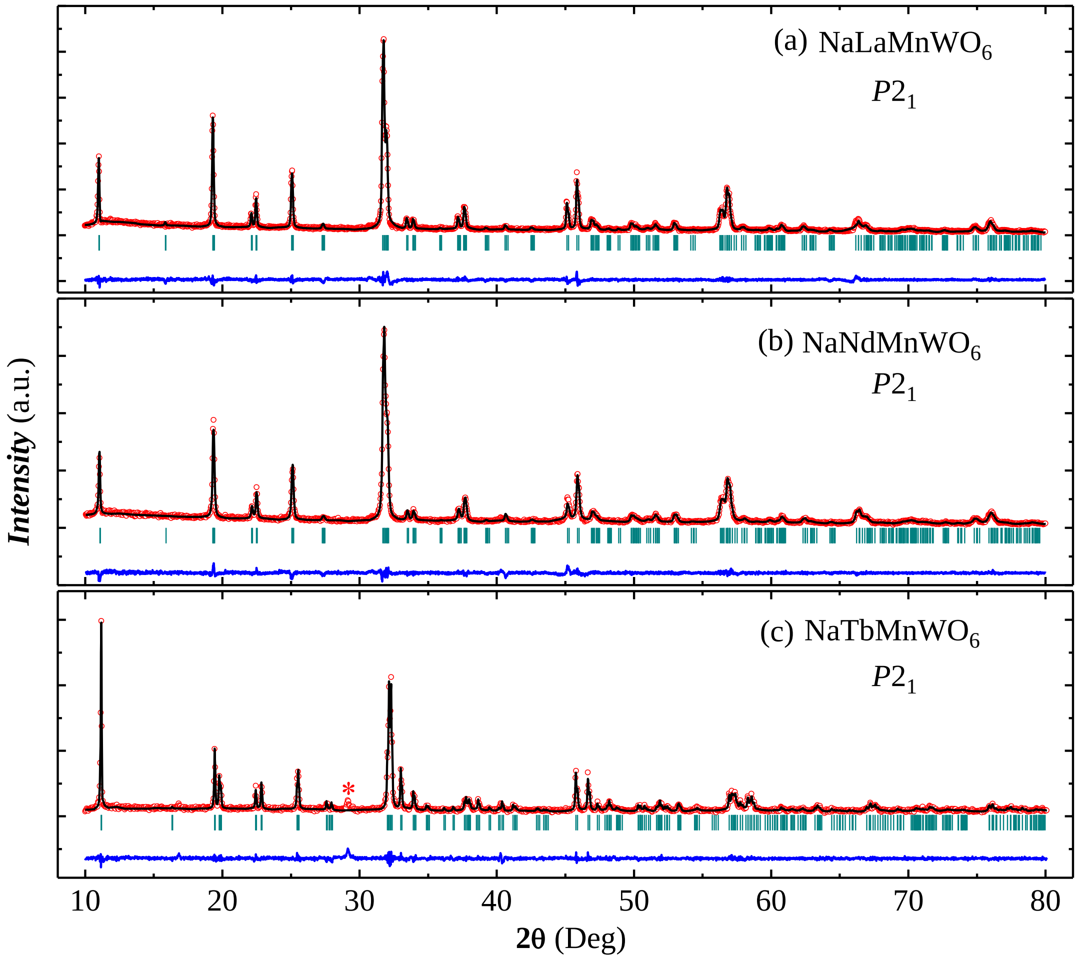

Figure 5.2 (a, b) Rietveld refinements on room temperature powder X-ray data of Na*R*MnWO$_6$ (*R* =La and Nd) using $P2_1$ space group. (c) Lebail fit of NaTbMnWO$_6$. Red circles, black line, blue lines and deep cyne vertical lines are representing observed, calculated, difference intensity and Bragg's positions, respectively. Asterisk in (c) shows impurity peak of Tb_4O_7.

Table 5.3 Structural parameters of NaLaMnWO$_6$ obtained from Rietveld refinement of X-ray diffraction data at room temperature. *Space group*: $P2_1$; a = 5.5976(3) Å, b = 5.6021(3) Å, c = 8.0317(3) Å, β = 90.113(3)°, Vol: 251.86(2)Å^3; χ^2 = 5.84; Bragg *R*-factor = 8.34 (%), R_f-factor = 16.8 (%)

Atom	Wyckoff position	*x*	*y*	*z*	B$_{iso}$	Occ.
Na	2a	0.233(8)	0.24(2)	-0.004(13)	1.29(5)	1
La	2a	0.257(2)	0.247(3)	0.501(3)	1.14(10)	1
Mn	2a	0.745(5)	0.268(4)	0.236(1)	0.52(14)	1
W	2a	0.752(2)	0.250	0.761(0)	0.19(6)	1
O1	2a	0.544(14)	0.523(14)	0.729(8)	1.0	1
O2	2a	0.483(14)	0.517(19)	0.311(7)	1.0	1
O3	2a	0.082(8)	0.018(10)	0.177(5)	1.0	1
O4	2a	0.039(12)	0.078(12)	0.750(8)	1.0	1
O5	2a	0.825(13)	0.321(15)	0.511(5)	1.0	1
O6	2a	0.699(13)	0.212(16)	-0.018(4)	1.0	1

Table 5.4 Structural parameters of NaNdMnWO$_6$ obtained from Rietveld refinement of X-ray diffraction data at room temperature. *Space group*: $P2_1$; a = 5.5114(1) Å, b = 5.5920(2) Å, c = 7.9839(2) Å, β = 90.365(2)°, Vol: 246.06(1)Å^3; χ^2 = 1.73; Bragg *R*-factor = 6.32 (%), R_f-factor = 8.13 (%)

Atom	Wyckoff position	*x*	*y*	*z*	B$_{iso}$	Occ.
Na	2a	0.247(9)	0.247(5)	0.000(7)	0.9	1
Nd	2a	0.260(2)	0.292(1)	0.500(1)	1.1	1
Mn	2a	0.746(4)	0.265(3)	0.238(1)	0.6	1
W	2a	0.759(1)	0.250	0.763(0)	0.19(6)	1
O1	2a	0.525(10)	0.517(11)	0.700(14)	1.0	1
O2	2a	0.512(9)	0.533(12)	0.298(13)	1.0	1
O3	2a	-0.067(8)	-0.083(9)	0.201(13)	1.0	1
O4	2a	-0.071(9)	-0.050(8)	0.806(7)	1.0	1
O5	2a	0.846(5)	0.235(8)	0.504(5)	1.0	1
O6	2a	0.647(4)	0.278(15)	-0.009(5)	1.0	1

The dark green color in the first heating could be due to presence of slight amount of Mn^{3+}, which was reduced to Mn^{2+} with the subsequent heating at higher temperatures.

A detailed crystallographic study was reported for the similar double perovskite compound based on HRTEM and neutron diffraction study where both 'A' site and 'B' site cation ordering was observed depending on the tolerance factor and octahedral rotation [23, 37, 38]. The assignment to the space group $P2_1/m$ (centrosymmetric) is consistent with the 'out of phase' rotation ($a^-a^-c^0$) of the octahedra. With the decreasing size of 'A' site cation gives another 'in phase' rotation ($a^0a^0c^+$) and finally it becomes ($a^-a^-c^+$) which corresponds to $P2_1$ (non-centrosymmetric) space group which is expected in our case. The presence of the additional rotation is important because it destroys the inversion center and allows the formation of a polar structure. However it is quite hard to resolve the difference in the structure of $P2_1$ and $P2_1/m$ using lab X-ray since the oxygen atom position cannot be determined very accurately.

As will be seen in the next section, our electrical property measurements such as *P*(*E*), PUND and *piezo* loop reveal the absence of ferroelectric polarization at room temperature in all the investigated (Na*R*MnWO$_6$, *R*=La, Nd and Tb) compounds [39, 40]. We have performed the refinement using $P2_1/m$ space group to the experimental pattern. We have shown the refinement details of NaLaMnWO$_6$ and NaNdMnWO$_6$ for $P2_1/m$ in table 5.5 and 5.6. Compared to the $P2_1$ space group, the $P2_1/m$ yielded a poor fit.

However, we consider that using neutron or synchrotron source on single crystal sample is necessary for the exact structure determination in these doubly ordered perovskite compounds. The difference in the structure observed in our X-ray diffraction experiments with the lower size of rare-earth (Y) will be presented later.

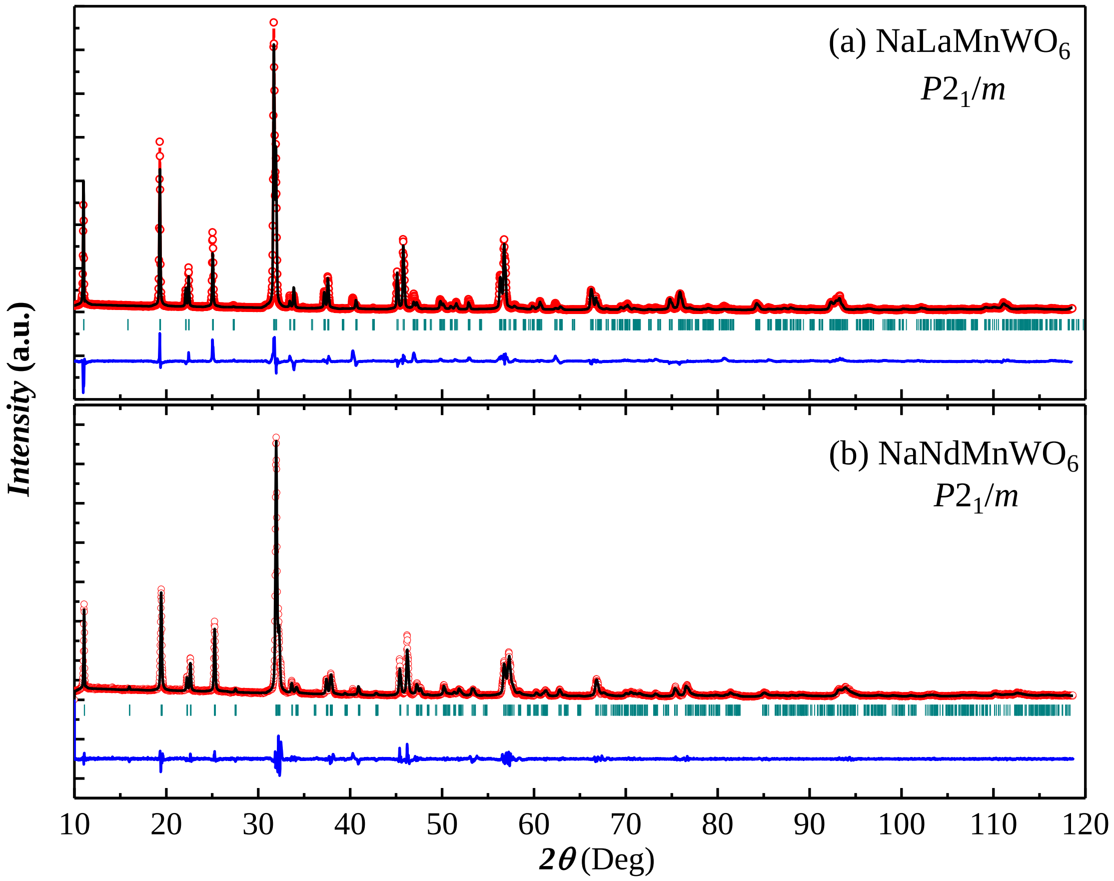

Figure 5.3 Powder X-ray diffraction pattern recorded at room temperature and the Rietveld refined pattern using $P2_1/m$ space group in (a) $NaLaMnWO_6$ (b) $NaNdMnWO_6$.

Table 5.5 Structural parameters of $NaLaMnWO_6$ obtained from Rietveld refinement of X-ray diffraction data at room temperature. *Space group*: $P2_1/m$; a = 5.6001(5) Å, b = 5.60353(5) Å, c = 8.0339(3) Å, β = 90.095(6)°, Vol: 252.11(4)Å^3; χ^2 = 6.14; Bragg R-factor = 14.6(%), R_f-factor = 14.6(%)

Atom	Wyckoff position	x	y	z	B_{iso}	Occ.
Na	2e	0.750	0.250	0.500	2.1(3)	1
La	2e	0.750	0.250	0.0	1.73(8)	1
Mn	2e	0.250	0.250	0.250	0.63(15)	1
W	2e	0.250	0.250	0.750	0.19(6)	1
O1	4f	0.002(7)	0.910(8)	0.250	1.0	2
O2	4f	0.546(7)	0.058(7)	0.250	1.0	2
O3	2e	0.250	0.250	0.012(4)	1.0	1
O4	2e	0.250	0.250	0.551(3)	1.0	1

Table 5.6 Structural parameters of $NaNdMnWO_6$ obtained from Rietveld refinement of X-ray diffraction data at room temperature. *Space group*: $P2_1/m$; a = 5.5417(3) Å, b = 5.5755(4) Å, c = 7.9922 (5) Å, β = 89.96(2)°, Vol: 246.94(3)Å^3; χ^2 = 8.92; Bragg R-factor = 19.2 (%), R_f-factor = 18.3 (%)

Atom	Wyckoff position	*x*	*y*	*z*	B_{iso}	Occ.
Na	2e	0.750	0.250	0.500	2.0(5)	1
La	2e	0.750	0.250	0.0	2.16(11)	1
Mn	2e	0.250	0.250	0.250	1.2(2)	1
W	2e	0.250	0.250	0.750	1.08(6)	1
O1	4f	-0.006(6)	0.598(5)	0.250	1.0	2
O2	4f	0.533(6)	0.040(6)	0.250	1.0	2
O3	2e	0.250	0.250	0.037(4)	1.0	1
O4	2e	0.250	0.250	0.544(4)	1.0	1

Powder x-ray pattern of Na*R*$CoWO_6$ (*R*= La and Nd) samples were also refined using FullProf and shown in figure 5.4. Although the x-ray data of $NaLaCoWO_6$ and $NaNdCoWO_6$ were fitted well with monoclinic polar space group $P2_1$, it was also possible to fit with non-polar crystal structure $C2/m$ [31]. Following the recent structural study of the Co compounds, we performed the structure refinement with *C*2/m. The compounds with lower *R*-ions were unsuccessful to prepare under ambient condition. We understand the unsuccessful synthesis attempts were mainly due to formation of Na_2WO_4 phase in preference to formation of a perovskite phase (as shown in table 5.1) as the coordination numbers of both tungsten and the alkali metal cation increases upon going from Na_2WO_4 to perovskite structure. High pressure synthesis route could help to stabilize the double perovskite phases as mentioned previously [22, 27]. On the other hand, the lower size rare-earth containing compounds have more tendencies to have the greater structural distortion leading towards the polar character. In order to see that, we have prepared double perovskite compounds with the lower size *R*-ion under high pressure and high temperature which will be presented later. The powder x-ray pattern of $NaLaFeWO_6$ along with the refinement using $P2_1$ space group is given in figure 5.5 which is in a good agreement with the earlier reports [41].

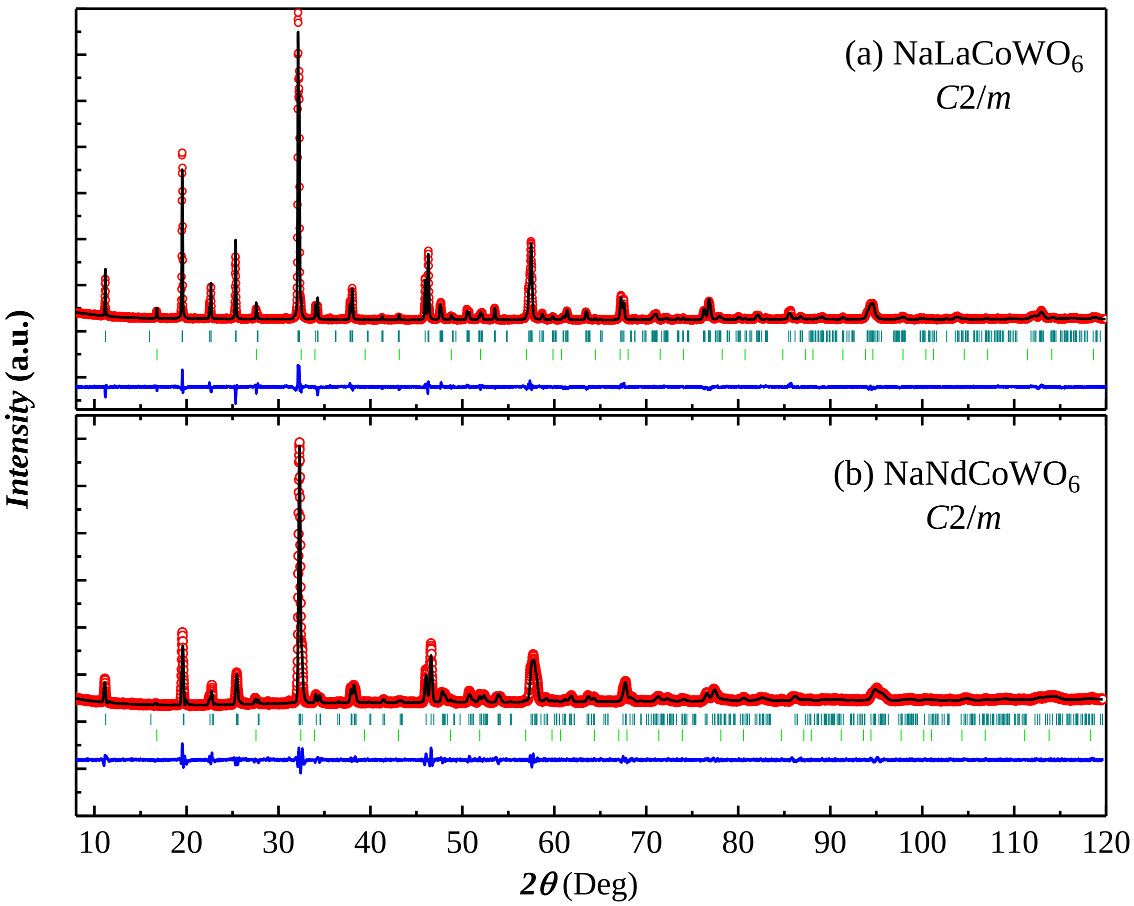

Figure 5.4 Powder X-ray diffraction pattern recorded at room temperature and the Rietveld refined pattern using *C*2/*m* space group in (a) $NaLaCoWO_6$ (b) $NaNdCoWO_6$. The second Bragg lines correspond to the impurity phase Na_2WO_4.

Table 5.7 Structural parameters of $NaLaCoWO_6$ obtained from Rietveld refinement of X-ray diffraction data at room temperature. *Space group*: *C*2/*m*; a = 7.8300(1) Å, b = 7.8415(1) Å, c = 7.8931(1) Å, β = 90.167(1)°, Vol: 484.63(1) Å^3; χ^2 = 3.72; Bragg *R*-factor = 7.43 (%), R_f-factor = 6.35 (%)

Atom	Wyckoff position	*x*	*y*	*z*	B_{iso}	Occ.
Na	4g	0.000	0.251(4)	0.500	0.90	1
La	4h	0.000	0.245(0)	0.000	0.60	1
Co	4i	0.746(1)	0.000	0.739(0)	0.50	1
W	4i	0.2478(4)	0.000	0.734(0)	0.51(3)	1
O1	4i	0.032(3)	0.000	0.570(3)	1.0	1
O2	8j	0.746(3)	0.279(1)	0.738(2)	1.0	2
O4	4i	0.469(4)	0.000	0.786(3)	1.0	1
O5	4i	0.809(2)	0.000	0.059(2)	1.0	1
O6	4i	0.666(2)	0.000	0.495(3)	1.0	1

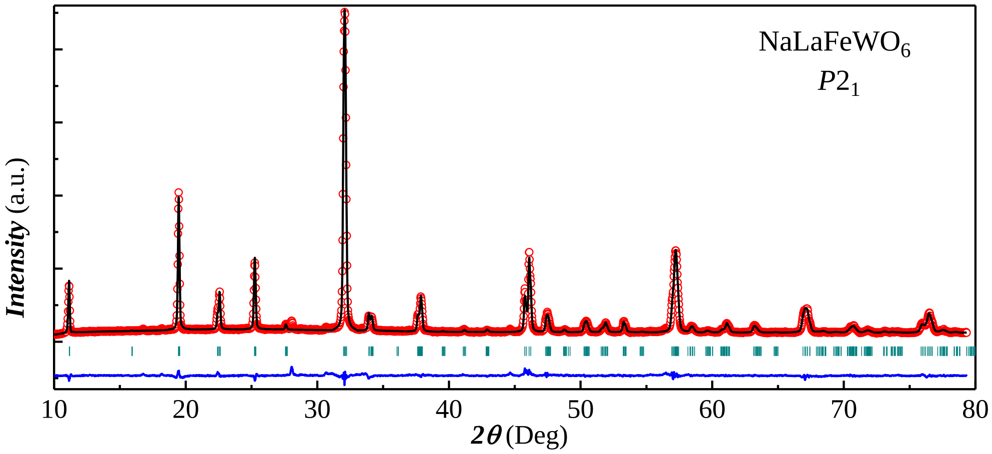

Figure 5.5 Powder X-ray diffraction pattern recorded at room temperature and the Rietveld refined pattern using $P2_1$ space group in $NaLaFeWO_6$

5.3.2 Magnetic properties

Magnetization measurements confirm the magnetic ordering of Mn-ions at low temperatures in the range of 6 to 15 K as shown in figure 5.6 (a, b and c) for $NaRMnWO_6$ where R = La, Nd and Tb, respectively. The Néel temperature for all the compounds has been shown in the table 5.8. From the Curie-Wiess plot, the Wiess constant and effective moment (μ_{eff}) have been calculated from the best fit linear regime (100 K to 300 K) and compared with the theoretical value shown in the table 5.8. This showed a good agreement with the reported value. Using the relation $\mu_{eff} = g(S(S + 1))^{1/2}$, μ_{eff} is 5.92 for Mn^{+2}, where g = 2.0023 and S = 5/2. For the sample containing magnetic rare-earth, the total magnetic moment is calculated by the formula $(\mu_{total})^2 = (\mu_R)^2 + (\mu_{Mn})^2$. The low temperature antiferromagnetic ordering can be explained by the long super-exchange path of Mn^{+2} i.e. Mn^{+2}-O-W^{+6}-O-Mn^{+2}. Therefore, the lower size rare-earth cation should give higher T_N as the average bond distance decreases. Apart from 15 K, antiferromagnetic ordering of Mn^{2+} in Tb sample, the second magnetic transition at 9 K can be due to the Tb^{3+} ordering through coupling of Mn^{2+} and Tb^{3+} ions. In contrast to the T_N, the Weiss constant decreases with the higher size of the rare-earth ions. This can be due to the fact that with lower size of rare-earth, the bond linearity in Mn^{+2}-O-W^{+6}-O-Mn^{+2} path decreases thus the orbital overlap decreases which reduces the exchange striction interaction [23]. The unusual increasing of T_N with the lowering interaction strength can be due to the competitive interaction of Mn-O-O-Mn in addition to the dominating Mn^{+2}-O-W^{+6}-O-Mn^{+2} interaction as mentioned in previous study [23].

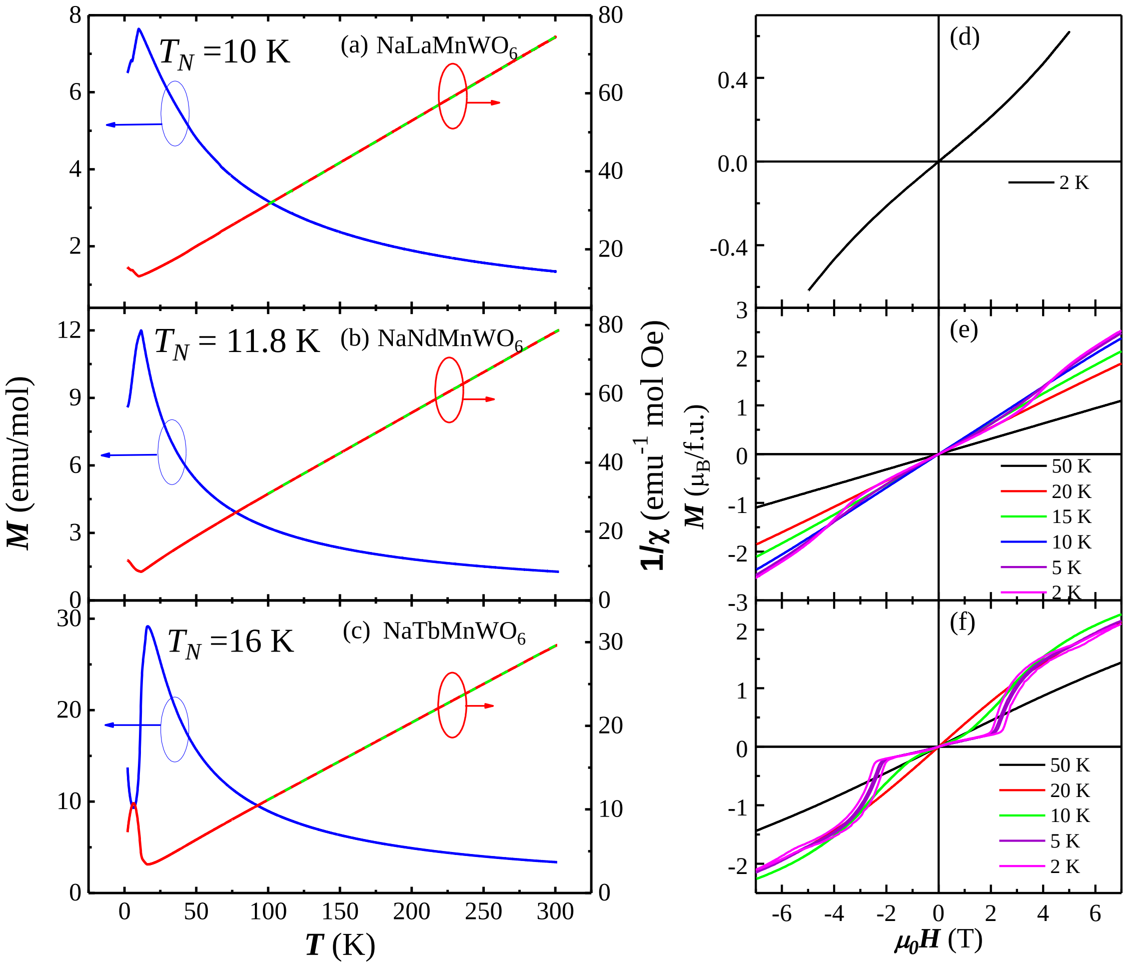

Figure 5.6 (a-c) Magnetization *vs.* temperature (blue on left-axis) and $1/\chi_m$ *vs.* temperature plot (red on right-axis) of Na*R*MnWO$_6$ (*R* = La, Nd and Tb). (d-f) Magnetization versus field at various temperatures in Na*R*MnWO$_6$ (*R* = La, Nd and Tb) respectively.

The *M*(*H*) loops measured in all the three samples are shown in figure 5.6 (d, e and f). Below the ordering temperature, the *M*(*H*) loops are that of collinear antiferromagnetic behavior. When the temperature is slightly higher than the antiferromagnetic ordering temperature, it shows small curvature which could be due to the short range ordering of the magnetic ions. At well below T_N, the curves bend with increasing field due to the saturation of magnetizations. For the magnetic rare-earth Nd and Tb, the *M*(*H*) loop shows metamagnetic transitions at low temperatures as we see a sudden change in the slope of the *M*(*H*) curve. The metamagnetic transition reprsents the magnetic field induced change of the magnetic structure in antiferromagnetic state [42]. When the magnetic field strength is sufficiently high, the magnetic moments can reorient and favors another magnetic structure. A magnetic field dependent neutron diffraction study is necessary to elucidate the change in the magnetic structure. The critical field of the transition can be derived by taking first derivative of the magnetization with respect to field. This has been illustrated in the next section with the context of magnetodielectric effect.

We have also performed the magnetization study in NaRCoWO$_6$ (R= La and Nd) and the results are shown in figure 5.7. Both these compounds show antiferromagnetic ordering similar to the Mn compounds. In the case of La, the antiferromagnetic ordering is at ~14 K and a step like increase is observed at ~90 K. This step feature can be due to some magnetic impurity present in the sample. This step feature as well as the discrepancy in the ZFC and FCW was unavoidable with repeated sample preparation and varying the sintering temperature.

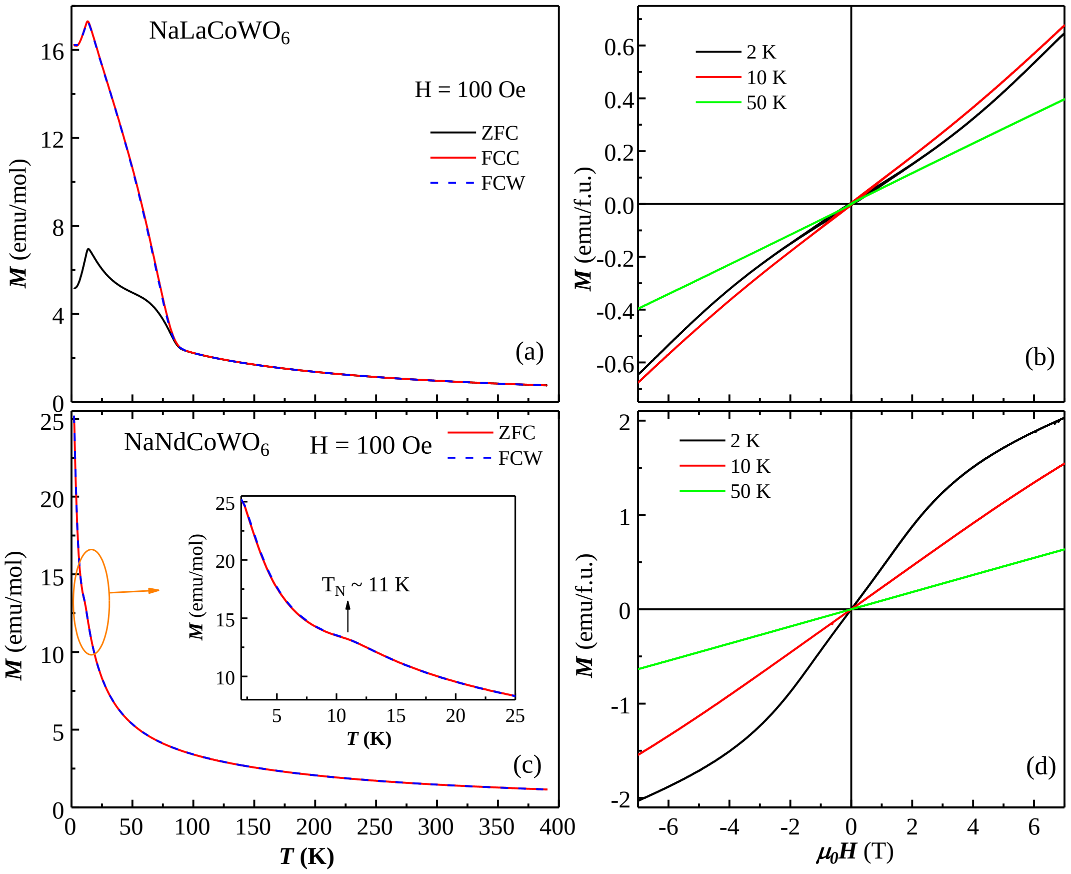

Figure 5.7 DC magnetization *vs.* temperature recorded under ZFC, FCC and FCW condition with 100 Oe for (a) NaLaCoWO$_6$ and (c) NaNdCoWO$_6$. Inset shows the magnified view around the transition temperature. (b) and (d) shows the $M(H)$ loop at different temperatures for NaLaCoWO$_6$ and NaNdCoWO$_6$ respectively.

In case of Nd, the antiferromagnetic ordering (~11 K) is immersed in the high paramagnetic moment of Nd-ions thus a very small cusp is observed (See inset of figure 5.7 (c)). The overlap of both ZFC and FCW data represents a long range antiferromagnetic ordering. The obtained μ_{eff} and curie temperatures (θ_c) are given in the table 5.8 which shows a good agreement with the theoretical value. For Co^{2+} ions, the magnetic moment was considered to be 4.9 μ_B/f.u. as a reference value instead of theoretical spin only value 3.87 μ_B/f.u. as it is most commonly observed in the salts where the orbital quenching cannot be ignored. We have also looked at magnetization *vs.* applied field curve in both the samples which confirms the antiferromagnetic character below the ordering temperature (figure 5.7 (b) and (d)). $NaLaFeWO_6$ compound shows antiferromagnetic ordering at ~25 K as shown in figure 5.8 which is in well agreement with the literature [41]. Reliable μ_{eff} value could not be obtained since the sample has magnetic impurity with higher magnetic ordering temperature.

Table 5.8 Weiss constant, μ_{eff} (experimental), μ_{eff} (theory/reference value), T_N (K) derived from the $M(T)$ data measured under FCW condition. $\mu_{eff}^{Tot} = \sqrt{(\mu_{TM-ion})^2 + (\mu_{R-ion})^2}$ where $\mu(Mn^{2+}) = 5.92\ \mu_B$ and $\mu(Co^{2+}) = 4.9\ \mu_B$.

Compound name	Weiss constant	μ_{eff} (μ_B)	μ_{eff} (μ_B) theory/ref	T_N (K)
$NaLaMnWO_6$	-46.44	6.05	5.92	10
$NaNdMnWO_6$	-28.17	6.8	6.94	11
$NaTbMnWO_6$	-24.05	11.3	11.38	15
$NaYMnWO_6$	-36.5	6.01	5.92	9
$NaLaCoWO_6$	-35.04	5.08	4.9	14
$NaNdCoWO_6$	-42.92	6.33	6.09	11
$NaHoCoWO_6$	-11.1	12.12	12.14	9

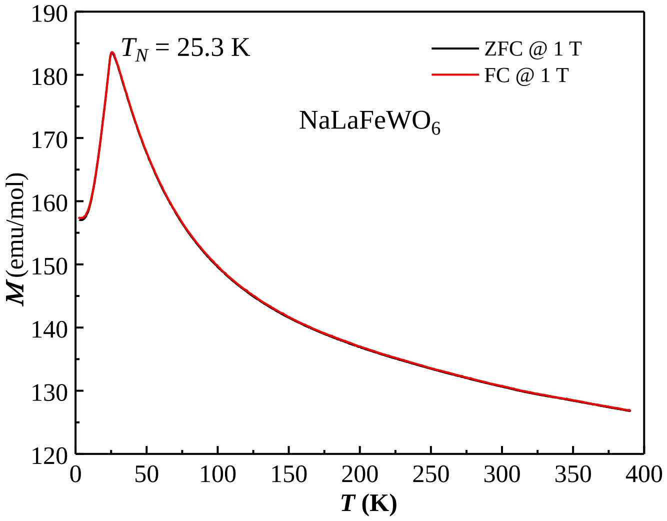

Figure 5.8 DC magnetization *vs.* temperature recorded under ZFC and FCW condition with 1 T in $NaLaFeWO_6$.

5.3.3 Polarization

In order to see the ferroelectric character, *P*(*E*) loop measurements carried out in $NaNdMnWO_6$ using a single wave (top panel) and PUND method (bottom panel) at several temperatures (15, 77, 150, 240, 250, 260, 270, 280 and 300 K) with voltage pulse of frequency 1000 Hz and 10 Hz are shown in figure 5.9 (a) and b), respectively. It can be seen that the single wave method gives either lossy or linear loop, which indicates a leaky material where other source of polarization such as capacitive and resistive dominates. With the conventional *P*(*E*) method, it would be difficult to separate out intrinsic ferroelectric polarization from other sources. To determine the intrinsic ferroelectric polarization, if any, we performed the PUND measurements, which allow subtraction of extrinsic contribution arising from leakage [32, 33] and the results are shown at the bottom panels of figure 5.9(a) and (b). It is obvious from these figures that there is no ferroelectric polarization in $NaNdMnWO_6$. Similar results were also found for the other La and Tb compounds.

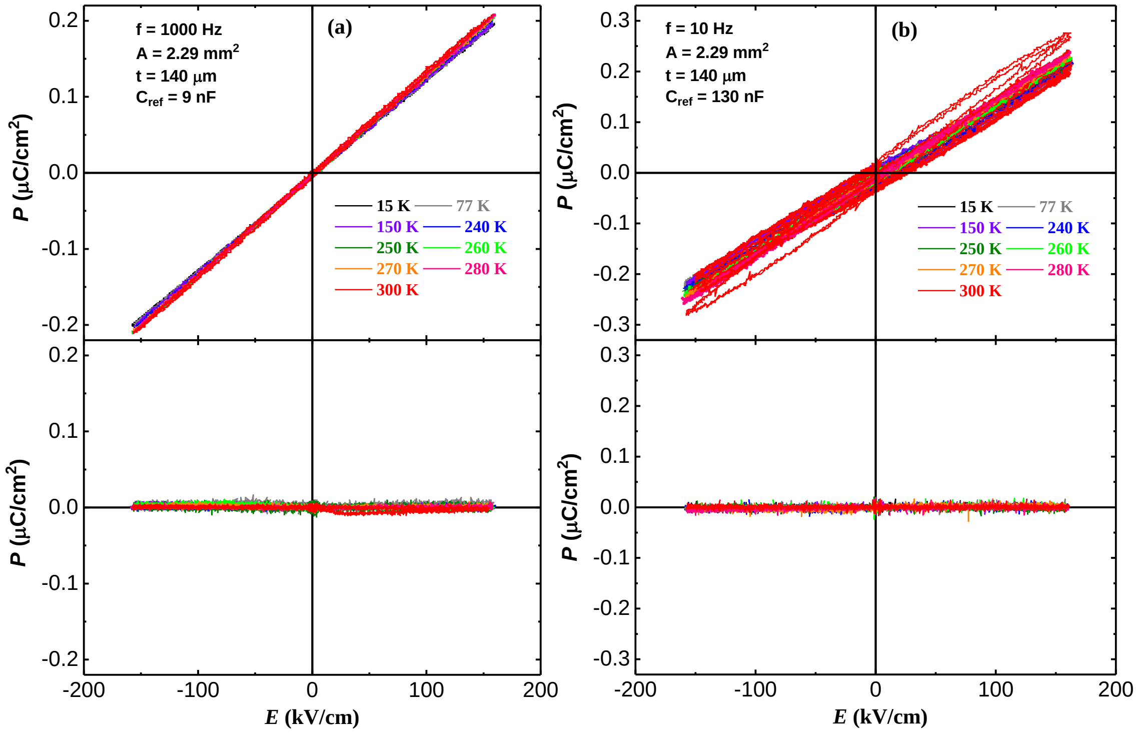

Figure 5.9 *P*(*E*) loop (upper panel), and PUND result (lower panel) of $NaNdMnWO_6$ measured with a voltage pulse frequency **(a)** 1000 Hz, **(b)** 10Hz. Different colors show the curve obtained at different temperature.

PUND results of $NaNdMnWO_6$ have been further analyzed from time dependent behavior of current (I) [43]. In figure 5.10(a) and 5.10(b), upper most panels show the first negative applied electric field pulse with time. Lower panels show the response of current to the first negative pulse (black curve) and second negative pulse (red curve) with time at various temperatures at (a) 1000 and (b) 10 Hz. For a ferroelectric material, we should observe a peak in the current curve in response to the first negative pulse which should be absent in the second negative pulse [44]. In the present data, we do not see any peak-like feature in both the first and second negative pulse. These results further confirm the absence of ferroelectricity.

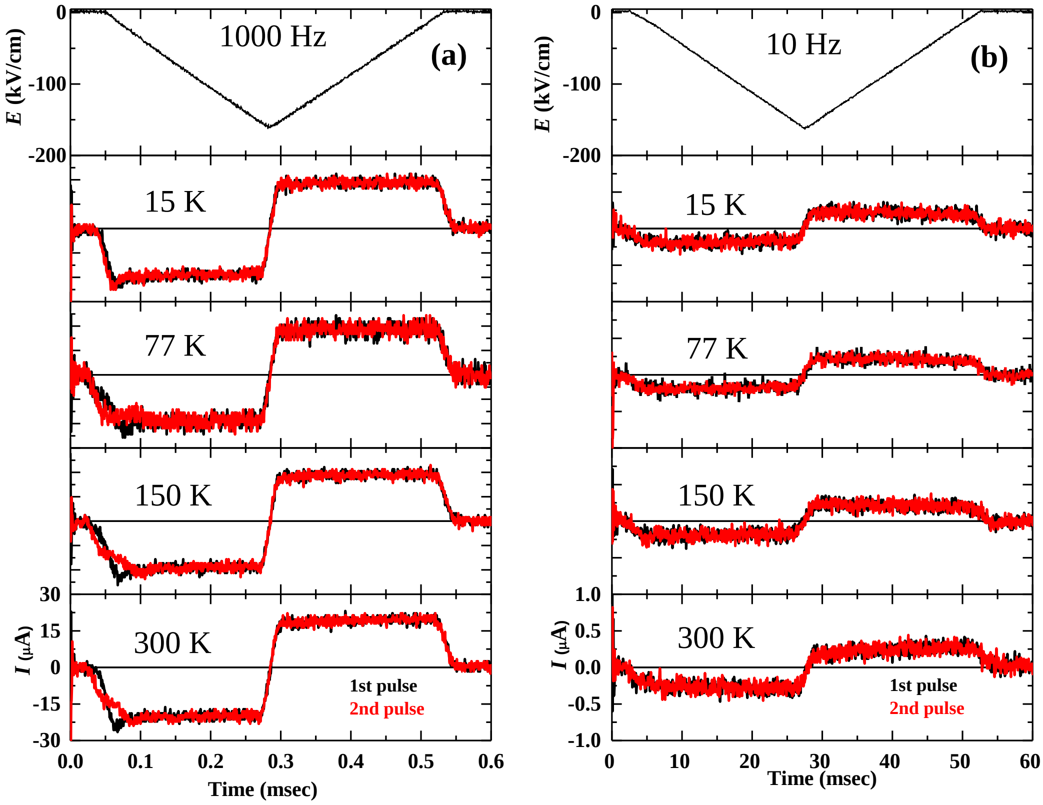

Figure 5.10 Time-dependent current curves for $NaNdMnWO_6$. Upper most panels represents the 1st and 2nd electric field pulse for PUND measurement at **(a)** 1000 Hz, **(b)** 10 Hz. Lower panels represent the corresponding current responses at various temperatures. Black curves show the response of 1st voltage pulse and red curves show the response of 2nd voltage pulse.

As these materials are expected to show ferroelectricity from the symmetry aspects, we have carefully performed two more symmetry related experiments on Na*R*MnWO$_6$ (*R* =La, Nd and Tb). Piezoelectric measurements measured at room temperature did not show any stress-strain loop [35]. SHG measurements [35, 45] carried out at room temperature also showed nearly zero signals compared to KDP and urea. On the other hand, the SHG measurement on isostructural compounds NaNdFeWO$_6$ and NaLaFeWO$_6$ has been reported to show a positive SHG signal with respect to α-SiO$_2$ [41]. The absence of ferroelectricity in these materials is in contrast to that expected based on neutron/X-ray diffraction studies and density functional theory calculations [29]. These contradicting results pose a question whether the actual crystal symmetry is polar ($P2_1$) or non-polar ($P2_1/m$ or $C2/m$). The suggestion of the polar space group ($P2_1$) is obtained from the analysis of Rietveld refinement on x-ray and neutron diffraction data on polycrystalline sample and bond valence optimization using SPuDs program assuming a random distribution of the A-site cation, suggesting a stable octahedral tilting (a$^-$a$^-$c$^+$) system [27]. $P2_1$ space group is expected for a$^-$a$^-$c$^+$ tilting along with both the cation ordering [22]. The present experimental results suggest that we may need to study synchrotron x-ray and neutron diffraction data from a single crystal and/or an analysis of electron microscopic study could help the actual structure determination. Another possibility could be that the compounds are only pyroelectric thus we do not see any switchable polarization.

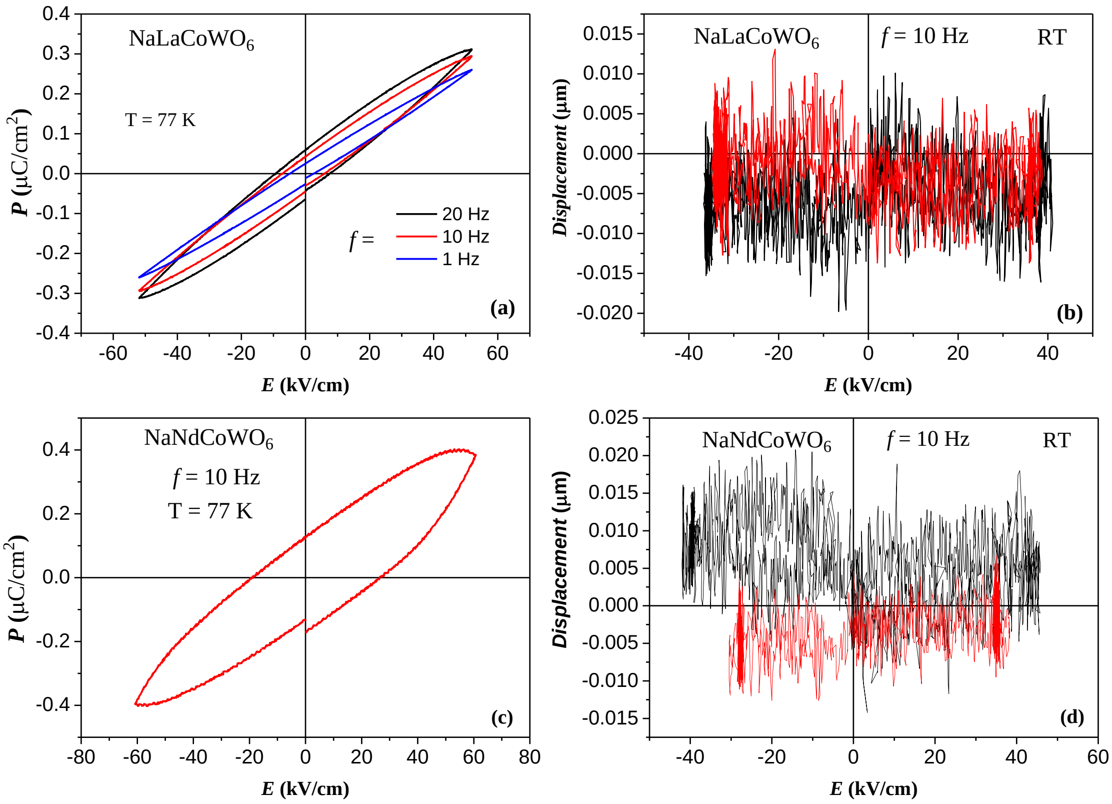

Figure 5.11 Polarization *vs.* electric field loop measured at 77 K and piezoelectric displacement loop measured at room temperature for (a, b) NaLaCoWO$_6$ and (c, d) NaNdCoWO$_6$.

We have also looked at the *P*(*E*) loop and piezoelectric displacement loop in other double perovskite samples such as $NaLaCoWO_6$, $NaNdCoWO_6$. From figure. 5.11, we see only a lossy *P*(*E*) loop measured at 77 K in both NaLaCoWO6 and NaNdCoWO6 samples. The absence of piezoelectric strain loop also signifies absence of polar character in the sample. The significant sample conductivity did not allow us to apply a sufficient high electric field in the sample. These results are in agreement with the non-polar space group *C*2/*m*, expected for the higher size rare-earth ions. We attempted to measure *P*(*E*) and piezoelectric loop in NaLaFeWO6 sample however the highly conductive nature did not allow us to measure even at 10 K [41].

5.3.4 Magnetodielectric effect at low temperature

In order to see the effect of magnetic ordering on the dielectric property we first looked at the dielectric constant around the magnetic ordering temperature. In $NaLaMnWO_6$, the dielectric constant data measured with 100 kHz, is shown in figure 5.12. We see only a broad anomaly below ~10 K which is in the vicinity of the magnetic ordering at 10 K. We believe that this dielectric anomaly is a consequence of the magnetic ordering of Mn^{2+} ions. Since the anomaly is quite small and broad, we took first derivative of ε_r with respect to temperature and shown in the inset of figure 5.12. The effect of magnetic field on the anomaly is negligible which indicates that the long-range ordering of Mn does not have any impact on the applied field up to 8 T. Besides, we do not see any anomaly in the loss data corresponding to the dielectric anomaly as shown in the inset of figure 5.12. These results demonstrate a spin phonon coupling at the magnetic ordering temperature in this double perovskite material. It is important to note such effect with a magnetic interaction through long super-exchange path. We know that the dielectric anomaly at the magnetic ordering temperature often leads to a magnetoelectric effect or a multiferroic behavior. Yet the presence of anomaly at zero magnetic field and the silent feature with magnetic field, suggested that it may not be a magnetoelectric case. In order to confirm the multiferroic behavior we have measured the pyrocurrent from the 2 to 20 K temperature range after poling the sample from 20 to 2 K. We did not observe any peak in the pyrocurrent which suggests that the dielectric anomaly is corresponding to only a magneto-structural coupling effect or the electric polarization might be very small.

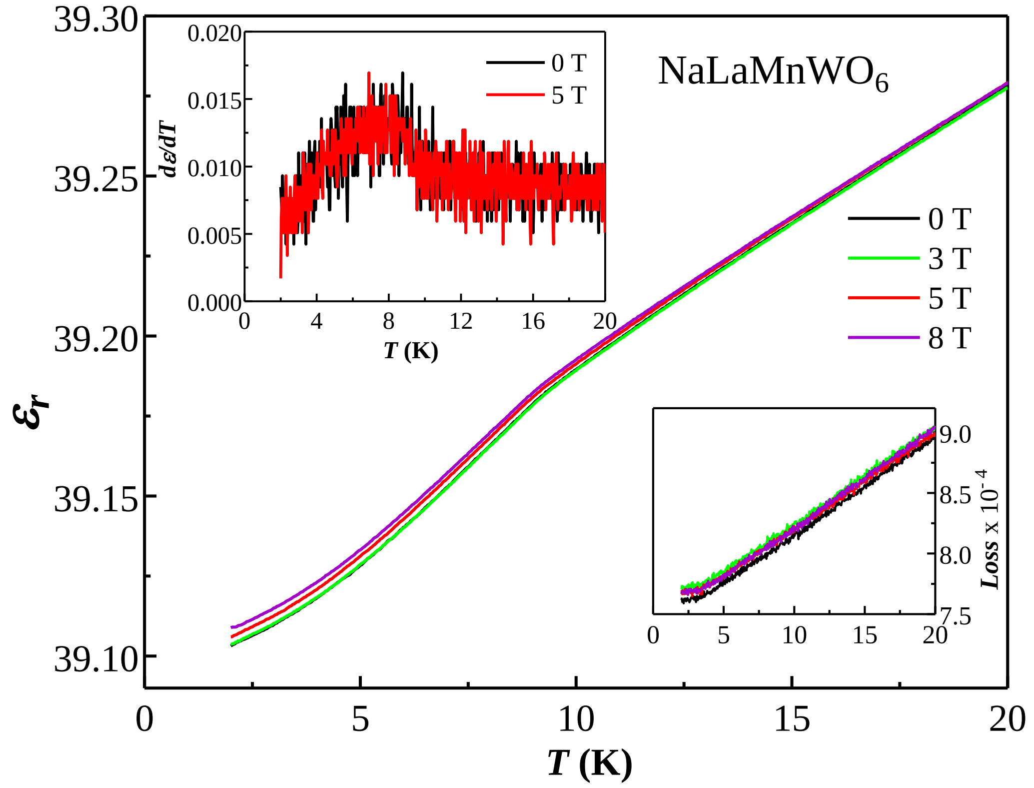

Figure 5.12 Dielectric data measure with 100 kHz from 2 to 20 K with 1 K/min in NaLaMnWO₆. Upper inset shows first derivative of dielectric constant w.r.t temperature and lower inset shows the corresponding loss data.

Further, we have measured the dielectric constant in the other two Mn-containing sample as well (figure 5. 13). With lowering the temperature, in NaNdMnWO6 we see first a monotonous decreasing trend which is similar to the La sample, however with further decreasing temperature a remarkably big step like anomaly arises below the magnetic ordering temperature (~11 K) at zero magnetic field, quite different from the La-sample. The dielectric anomaly comprises a small kink around 9.4 K and a prominent sharp triangular peak centered at ~ 5.5 K for both zero and 1 T magnetic field applied perpendicular to the electric potential. With increasing the magnetic field, the kink vanishes as seen in the 3 T curve and the sharp peak substantially broaden and becomes less pronounced yet does not shift the peak temperature with the increasing field. The strong anomalous behavior stands for a significant magnetodielectric effect. In order to probe the effect of magnetic fields on the dielectric response of NaNdMnWO₆, we have recorded isothermal magnetocapacitance at several temperatures including 2, 5, 10 and 15 K. The normalized magnetodielectric ($\Delta\varepsilon$) value is shown in figure 5.13 (c) where we see a hysteretic positive magnetodielectric effect at 2 K with a broad peak near 4 T. We attribute this behavior to the magnetic hysteresis as seen in the first derivative of isothermal magnetization versus field shown in figure 5.13 (e) where we can see a corresponding peak in dM/dH at ~ 4 T. Therefore we understand that the magnetodielectric effect can be entirely dertermined by the net magnetization of Mn and rare-earth Nd in this sample. At 5 K, the $\Delta\varepsilon$ has negative sign with highest value i.e. (-0.15%). These results confirm that that this sample has a magnetodielectric coupling below the ordering temperature.

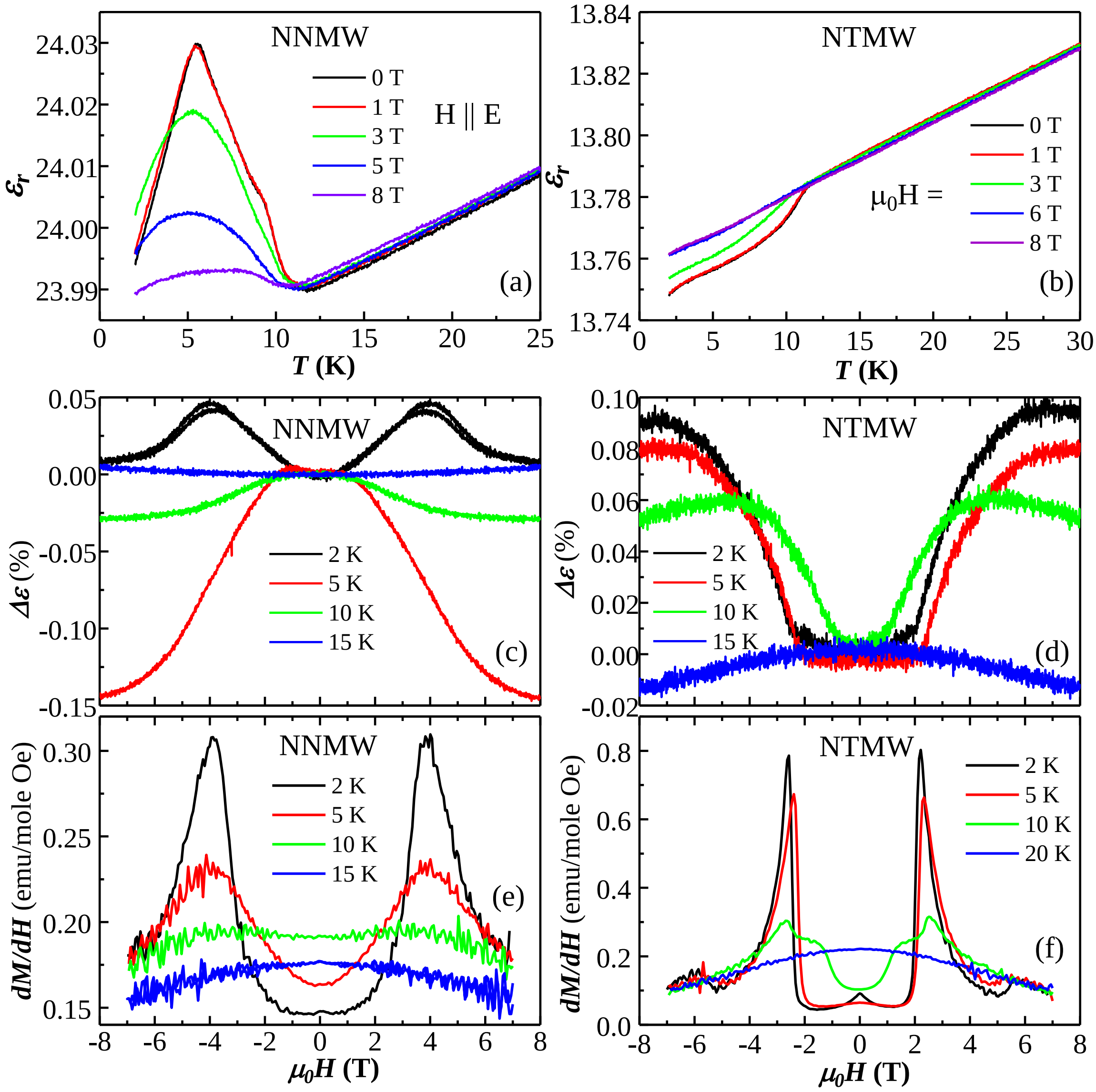

Figure 5.13 Dielectric constant measured at lower temperature across the magnetic ordering Magnetodielectric effect at 2, 5, 10 and 15 K and first derivative of magnetization with respect to field vs field for (a, c and e) $NaNdMnWO_6$ (NNMW)(b, d and f) $NaTbMnWO_6$ (NTMW).

Several factors can be responsible for contributing the magnetization induced change in the dielectric constant such as magnetoresistive effects [46], spin-phonon coupling [47], orbital degree of freedom [48], electromagnon scattering [49] and magnetostructural change [50] etc. We disregard the magnetoresistive origin since we did not observe any significant magnetoloss feature [51] and importantly we did not observe any relaxation behavior with a broad frequency range which is not shown for this sample but will be shown for other samples later. The value of $\Delta\varepsilon$ is comparable with the other magnetoelectric and multiferroic materials. Thus it is quite natural to expect magnetoelectric or magnetism induced multiferroic behavior in this compound. We have recorded the pyrocurrent as measured in the previous La-sample. However we did not see any peak feature near the dielectric anomaly suggesting the sample is only magnetodielectric. We argue that the non-collinear magnetic ordering (k = 0, 0.487, ½), as evidenced before form neutron diffraction study, responsible for the observed magnetodielectric coupling effect [28, 52]. The strong anomaly can be understood due to the simultaneous ordering of Nd and the Mn ions below 11 K. It is important to note that the rare-earth ordering has significant influence for the magnetodielectric effect. The magnetic field induced change in the rare-earth magnetic structure as evidenced by the metamagnetic transition may be responsible for the critical change in the dielectric constant as well as magnetization near ~4 T. A magnetic field dependent neutron diffraction study would be beneficial to understand the magnetic field effect on the spin structure.

A similar magnetodielectric study is performed in NaTbMnWO$_6$ sample as well and shown in figure 5.13 (b). For the similar crystal structure and a non-collinear spin structure (k= 0, 0.427, ½) in addition to the commensurate structure (k= ½, 0, ½), mentioned in the introduction, we can expect a similar magnetodielectric effect in this compound. Below 11 K, we observe a step like decreasing trend in the dielectric constant up to 1 T field. With increasing field the step size becomes less prominent and finally at 8 T, the dielectric constant becomes almost linear with the temperature which is similar to the case of La sample. This dielectric behavior is somewhat different from the Nd-sample, nevertheless, the presence of magnetism induced magnetodielectric effect is confirmed. In order to see the magnetic field effect we measured isothermal magnetocapacitance and shown in figure 5.13(d). At 2 K, we see a step like increase of $\Delta\varepsilon$ at above 2 T and saturation above 6 T. The behavior is almost same at 5 K except there is a minute change of critical field. At higher temperature, this behavior becomes less prominent i.e. the critical field as well as the saturation value becomes less. At 15 K, very near to the magnetic ordering (T_N = 16 K) the $\Delta\varepsilon$ shows a parabolic behavior with negative value which could be due to the similar effect in the magnetization as seen in figure 5.13(f) we see that the magnetization follows the same behavior. The intrinsic magnetodielectric feature is confirmed by the absence of field dependent behavior in the loss data (not shown). Therefore we attribute this magnetodielectric behavior to the net magnetization of the sample. We believe a similar spin-phonon coupling mechanism is responsible for this sample as well. The step like feature in the $\Delta\varepsilon$ at 2 and 5 K further indicates a change in the magnetic structure as observed in the magnetization data. A similar spin-phonon mediated magnetodielectric coupling was observed in Mn_3O_4 [53], $NiCr_2O_4$ [54], $SeCuO_3$ and $TeCuO_3$ [55] etc. It is important to note that we attempted to measure pyroelectric current in Tb-sample however did not find any polarization. Figure 5.14 shows the magnetodielectric behavior in $NaNdCoWO_6$ where we did not observe any ferroelectric polarization. The change in ε with magnetic field near T_N is small compared to the lower temperature where rare-earth ordering can play a role. This result further indicates that the magnetodielectric coupling is largely induced by the earth magnetization. There is no significant feature in the loss data except the 8 T data which may arise from measurement noise.

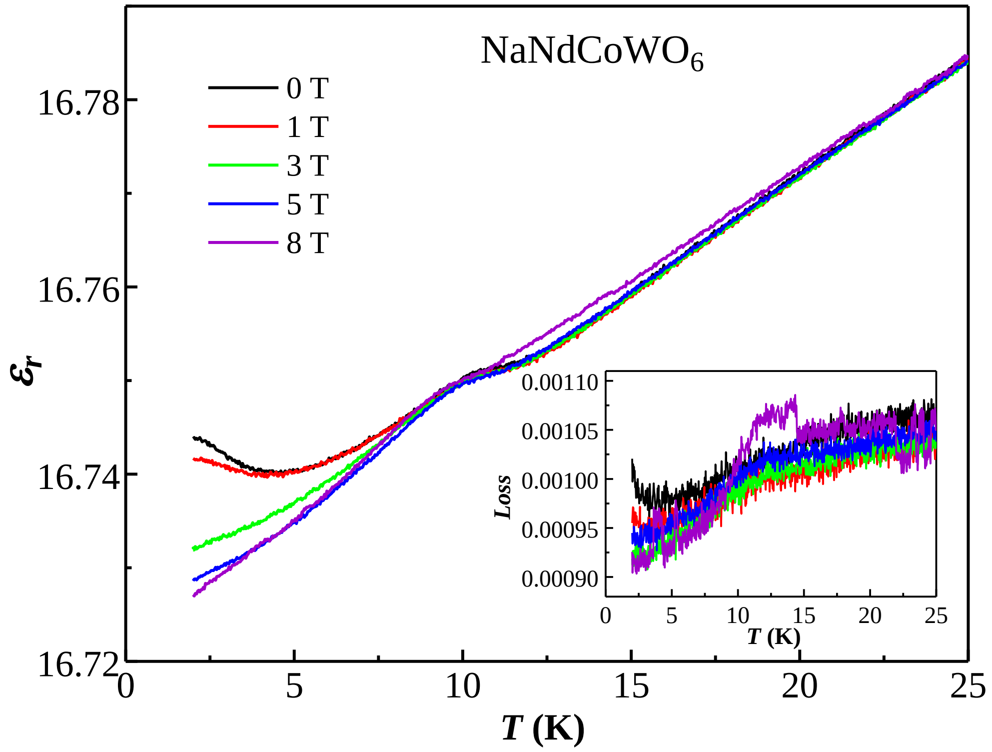

Figure 5.14 Low temperature dielectric and loss data measured at 100 kHz under various fields.

5.3.5 Dielectric property near room temperature

Dielectric permittivity and loss data of NaLnMnWO$_6$ (Ln = La, Nd and Tb) measured at various frequencies are shown in figure 5.15 (a, b and c) and 5.15 (d, e and f), respectively. The value of dielectric constant is low and is almost independent of frequency and temperature up to 250 K. Intriguingly, it shows a peak at ~ 270 K with a dispersion in frequency. Correspondingly, the loss data also exhibit peaks and similar frequency dispersion at the same temperature. Certainly, these dielectric anomalies cannot be attributed to ferroelectricity as we have not observed ferroelectric polarization over a wide range of temperatures above and below including dielectric anomaly temperature. The lower value of dielectric constant indicates that the space charge contributions from electrode material and grain boundaries are not significant. The dielectric anomaly temperature does not vary with the frequency irrespective of the electrode materials (silver or gold) used, which indicate that the dielectric anomaly is not associated with any relaxation mechanism.

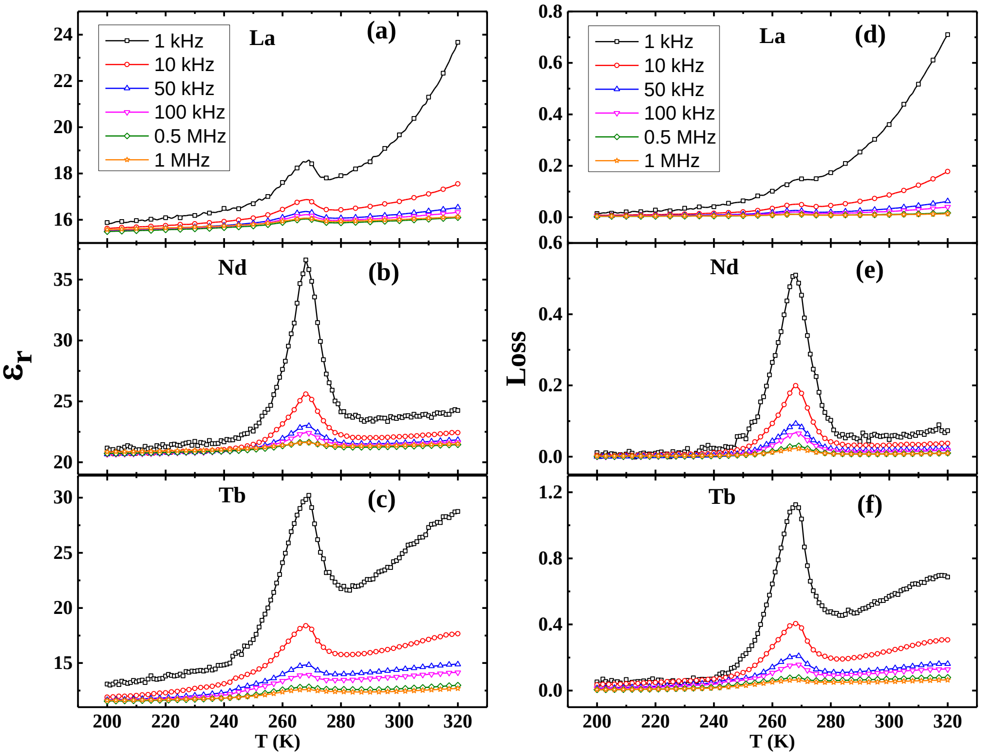

Figure 5.15 Variation of dielectric constant (a, b and c) and Loss (d, e and f) with temperature at various frequencies.

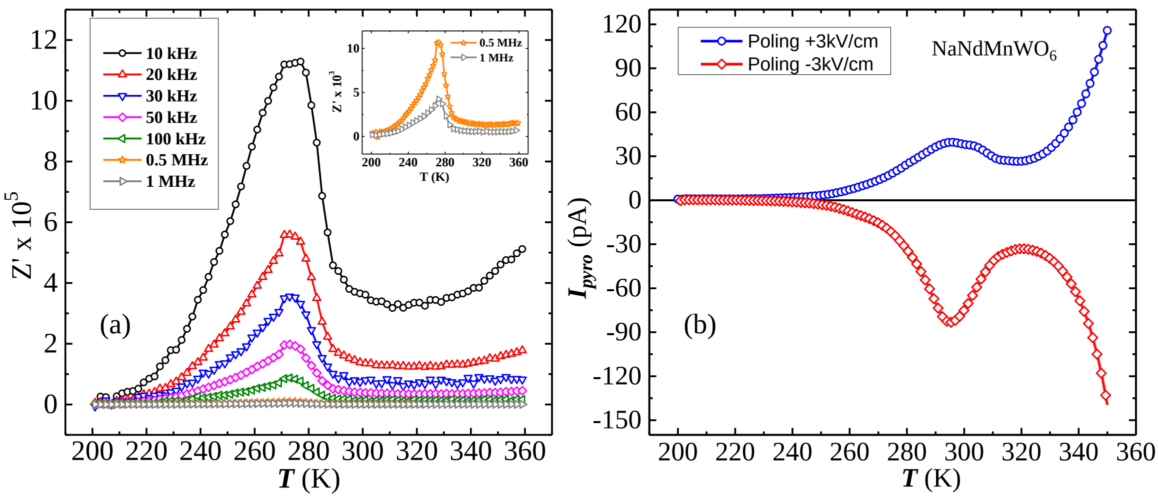

Figure 5.16 (a) ac resistivity *vs.* temperature plot of NaNdMnWO6 at various frequencies. (b) Pyroelectric current data of $NaNdMnWO_6$ for positive and negative poling field.

It should be mentioned here that the *dc* conductivity does not necessarily always leads to the change in dielectric constant, but *ac* conductivity is related to dielectric constant through Kramers-Kornig relation [56]. To further confirm the resistive origin of the dielectric anomaly, we performed *ac* resistivity *vs*. temperature measurement in $NaNdMnWO_6$ and the result is shown in figure 5.16(a). We see a broad anomaly in the vicinity of the dielectric anomaly temperature. Therefore, we suggest that the dielectric anomaly is due to change in conductivity which may arise from locally generated charge carrier [56, 57] because of some local structural distortion and therefore the dielectric anomaly is not related to ferroelectricity. We believe that this mechanism is applicable to the other two samples as well. [58] [58] [58] [58] [58] [58] We have also measured pyroelectric current as a function of temperature while warming at 4 K/min after an electric field poling across the dielectric anomaly temperature as shown in figure 5.16(b). A pyroelectric current peak is seen in the vicinity of dielectric anomaly. Further, unlike the ferroelectric materials, the pyroelectric current peaks for positive and negative poling fields are highly asymmetric as depicted in figure 5.16(b). The peak is also observed in the leakage current measurement even after many heating and cooling cycles. It should be noted that this kind of leakage current peaks are generally not observed at the ferroelectric transition. Similar behavior is observed for the other two samples as well. The origin of such pyroelectric peaks is also related to the anomalous behavior of the resistivity and does not represent ferroelectric polarization.

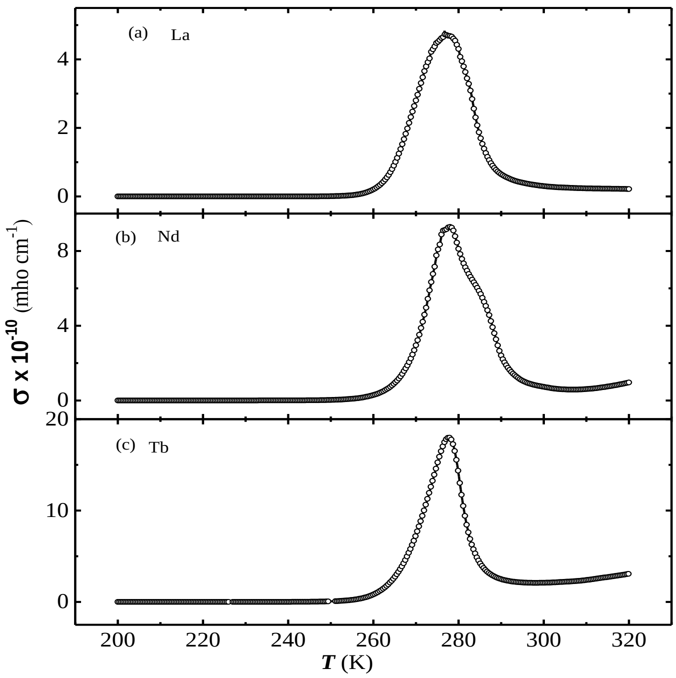

Figure 5.17 DC conductivity vs. Temperature data while warming at 2 K/min.

In order to understand the origin of the dielectric anomaly and pyrocurrent, we have recorded DC-bias current using two-probe method as described in chapter 3. The calculated *dc* conductivity data of all the samples are shown in the figure 5.17. From this data we do not see the representative double peak feature of positive and negative peak, thus we conclude that the presence of a pyroelectric current peak does not necessarily indicate ferroelectric polarization. Also by looking at the common peak around 280 K in the DC-bias current for all the samples we understand that the all the samples contain Na ions which is hygroscopic. Therefore it is possible that at the sample surface or particularly at the periphery of the sample i.e. the gap between the electrodes can slightly absorbs moisture and have more conductive nature at the particular temperature region near room temperature.

5.4 Results on high pressure synthesized $NaYMnWO_6$ and $NaHoCoWO_6$

5.4.1 Crystal Structure

Rietveld refinements of room temperature XRD data of both $NaYMnWO_6$ and $NaHoCoWO_6$ are consistent with the polar $P2_1$ symmetry as reported earlier for $NaHoCoWO_6$ [31]. Small amount (~2%) of Y_2WO_6 impurity was present in the former and therefore included in the refinement. The crystallites of both the samples were found to exhibit preferred orientation along [001] direction. In order to minimize the effect of preferred orientation, we have taken care in the preparation of sample for x-ray data collection and the preferred orientation parameter was varied in the refinement. The XRD patterns along with the final refinement for these two compounds are shown in figures 5.18(a) and (b), respectively. The structural parameters of $NaYMnWO_6$ and $NaHoCoWO_6$ are given in table 5.9 and 5.11. Selected bond lengths and bond angles are given in tables 5.10 and 5.12. The crystal structure showing the layered ordering of A-cations and rock-salt ordering of B-cations and the octahedral distortion of MnO_6 and WO_6 with various bond lengths obtained from the structural parameters are shown in figure 5.19.

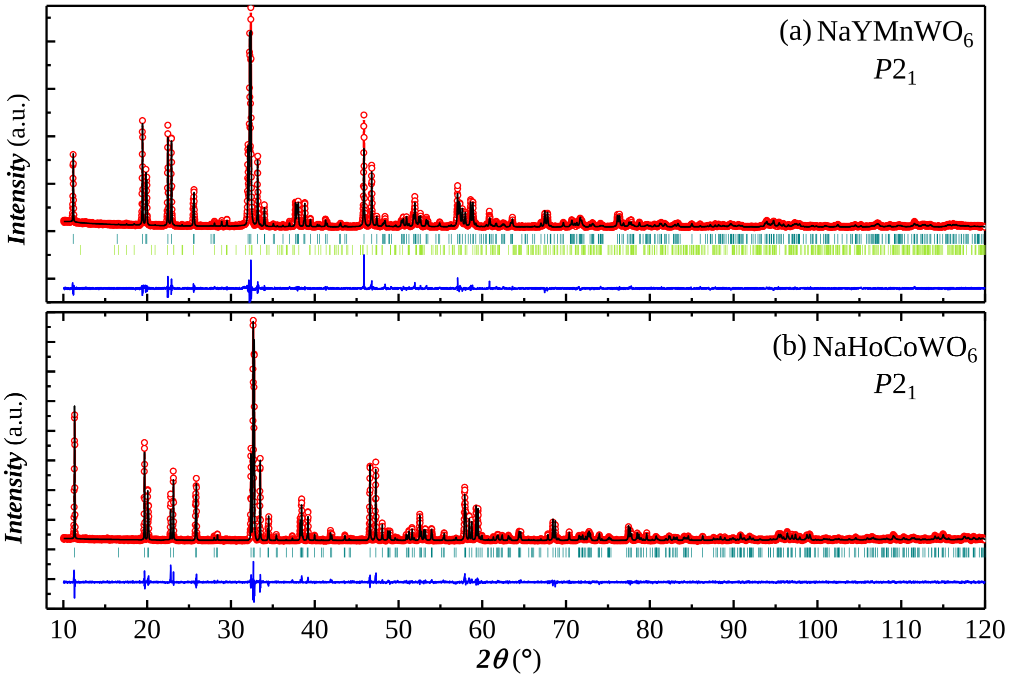

Figure 5.18 Powder X-ray diffraction pattern recorded at room temperature and the Rietveld refined pattern using $P2_1$ space group in (a) $NaYMnWO_6$ (b) $NaHoCoWO_6$. The second Bragg lines in $NaYMnWO_6$ correspond to the impurity phase Y_2WO_6.

Table 5.9 Structural parameters of NaYMnWO$_6$ obtained from Rietveld refinement of X-ray diffraction data at room temperature. *Space group*: $P2_1$; a = 5.39367(5) Å, b = 5.58174(3) Å, c = 7.90523(4) Å, β = 90.3355(3)°, Vol: 237.991(2)Å^3; χ^2 = 1.99; Bragg *R*-factor = 5.08 (%), R_f-factor = 4.00 (%)

Atom	Wyckoff position	*x*	*y*	*z*	B_{iso}	Occ.
Na	2a	0.260(4)	0.213(4)	0.002(2)	0.4(4)	1
Y	2a	0.269(2)	0.316(2)	0.5000(6)	0.7(1)	1
Mn	2a	0.755(2)	0.253(7)	0.237(9)	0.4(1)	1
W	2a	0.764(5)	0.2500	0.759(3)	0.2(3)	1
O1	2a	0.540(6)	0.523(6)	0.708(4)	1.0	1
O2	2a	0.545(6)	0.527(6)	0.275(4)	1.0	1
O3	2a	-0.072(5)	-0.094(5)	0.226(3)	1.0	1
O4	2a	-0.089(5)	-0.091(5)	0.780(3)	1.0	1
O5	2a	0.851(5)	0.208(7)	0.499(3)	1.0	1
O6	2a	0.667(4)	0.286(8)	-0.013(3)	1.0	1

Table 5.10 Selected bond lengths and bond angles from the X-ray Refinement of Na*R*MnWO$_6$ (*R*=Y, Nd and La).

Compound	Atom	O1	O2	O3	O4	O5	O6
NYMW	Mn	2.09(4)	1.93(5)	2.15(4)	2.02(3)	2.15(3)	2.04(3)
	W	1.98(3)	2.09(3)	1.88(3)	2.09(3)	2.13(2)	1.89(2)
	Mn-O-W	153(2)	157(2)	143(2)	135.2(2)	150.1(1)	148.3(2)
NNMW	Mn	2.16(7)	1.99(7)	2.28(5)	2.07(5)	2.21(4)	2.02(4)
	W	2.03(7)	1.97(6)	1.94(5)	1.94(5)	2.13(4)	1.94(4)
	Mn-O-W	150(3)	149(3)	146(2)	144(2)	151(2)	145(2)
NLMW	Mn	2.18(9)	2.04(10)	2.41(5)	2.11(8)	2.26(4)	2.09(4)
	W	1.89(9)	1.99(9)	1.82(5)	1.90(7)	2.07(4)	1.82(4)
	Mn-O-W	160(4)	148(4)	145(2)	155(3)	155(2)	154(2)

Table 5.11 Structural parameters of NaHoCoWO$_6$ obtained from Rietveld refinement
Space group: $P2_1$; a = 5.34673(2) Å, b = 5.52193(2) Å, c = 7.78959 (3) Å, β= 90.2823(2)°, Vol: 229.979(1) Å^3; χ^2 = 2.65; Bragg *R*-factor = 6.18 (%), R_f-factor = 5.07 (%).

Atom	Wyckoff position	*x*	*y*	*z*	B_{iso}	Occ.
Na	2a	0.257(4)	0.218(4)	0.004(2)	0.9(4)	1
Ho	2a	0.2677(9)	0.312(1)	0.5012(4)	1.7(1)	1
Co	2a	0.752(2)	0.238(4)	0.2457(9)	0.6(2)	1
W	2a	0.7625(5)	0.2500	0.7649(3)	0.10	1
O1	2a	0.491(7)	0.490(6)	0.704(5)	1.0	1
O2	2a	0.489(7)	0.522(6)	0.295(5)	1.0	1
O3	2a	-0.078(5)	-0.108(4)	0.210(3)	1.0	1
O4	2a	-0.095(5)	-0.070(4)	0.792(3)	1.0	1
O5	2a	0.850(5)	0.207(6)	0.491(3)	1.0	1
O6	2a	0.682(4)	0.281(1)	-0.006(3)	1.0	1

Table 5.12 Selected bond lengths and bond Angles from the X-ray Refinement of $NaHoCoWO_6$.

Atom	O1	O2	O3	O4	O5	O6
Co	1.93(4)	2.14(4)	2.13(3)	2.14(3)	1.99(2)	2.00(2)
W	2.02(4)	1.90(4)	1.87(3)	1.94(2)	2.20(2)	1.84(2)
Co-O-W	154.4(2)	155.0(2)	138.3(2)	140.8(2)	150.2(1)	155.0(2)

The highly distorted nature of MnO_6 and WO_6 octahedra is evident from six different bond lengths in each case. The short W-O(6) bond length or displacement of W-ion directed towards Na^+ layer indicates the presence of second order Jahn-Teller distortion. In contrast, the MnO_6 and CoO_6 octahedra remain almost symmetric which suggests that the Mn and Co-ions do not contribute polarization. The various Mn-O-W and Co-O-W bond angles are much smaller than the corresponding doubly ordered perovskites with bigger *R*-ions (table 5.10). This reveals a much larger rotation of octahedra in compounds with smaller *R*-ions [8, 59, 60].

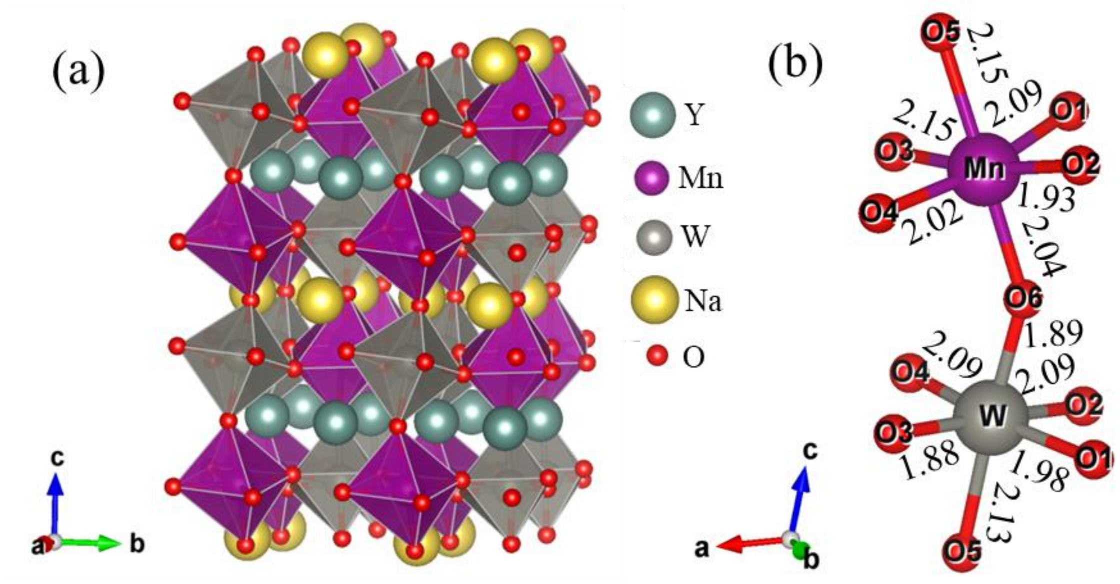

Figure 5.19 (a) Crystal structure of $NaYMnWO_6$ showing layered ordering of Na and Y and rock-salt ordering of Mn and W with rotated and tilted octahedra of the Mn and W atom. (b) Coordination of oxygen around Mn and W ions with different Mn-O and W-O bond lengths.

5.4.2 Magnetic properties

Temperature dependence of DC magnetization *M*(T) data of $NaYMnWO_6$ and $NaHoCoWO_6$, measured under zero-field cooled (ZFC) and field-cooled (FC) conditions with an applied field of 1000 Oe, in the temperature range 2 – 30 K are shown in figure 5.20(a) and (c), respectively. The heat capacity data measured under zero magnetic field are also given the respective figures. The magnetization and heat capacity data of NaYMnWO$_6$ confirm the antiferromagnetic ordering of Mn^{2+} ions at 8.7 K. In the case of NaHoCoWO$_6$, in addition to antiferromagnetic ordering of Co^{2+} ions at 8.9 K, the *M*(T) and *C*(T) data show a broad anomaly around 5.8 K which indicates a short range magnetic ordering of Ho^{3+} ions. However, it requires neutron diffraction study to understand the nature of magnetic ordering and spin structure of these compounds. The lower ordering temperatures of Mn^{2+} and Co^{2+} ions result from the long super-exchange path of Mn(Co)-O-W-O-Mn(Co) [28]. The low temperature broad hump near 4 K is suppressed with field as seen the field dependent heat capacity data (figure 5.22). The upturn at further low temperature below 3 K can be due to the ordering Ho^{3+}. The antiferromagnetic ordering of Co^{2+} reduces to 6 K under magnetic field of 7 T.

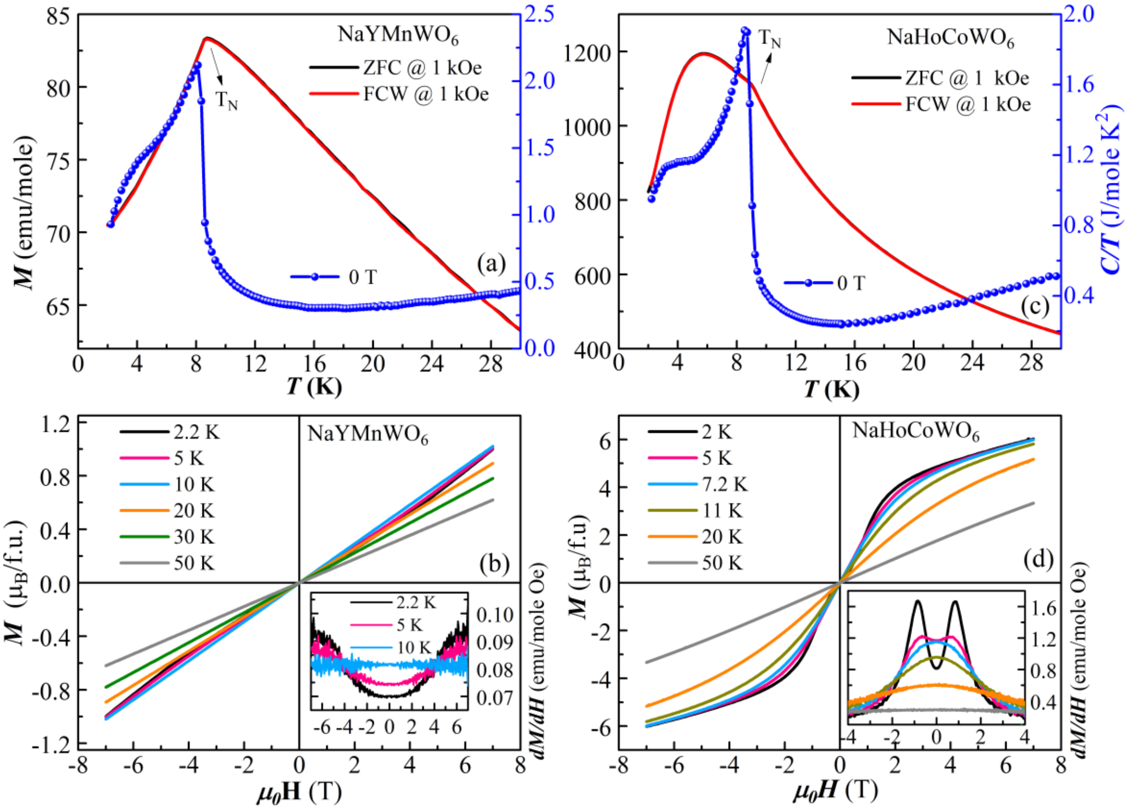

Figure 5.20 (a) and (c) DC magnetization on the left axis measured at zero field cooled and field cooled condition with 1 kOe and heat capacity divided by temperature on the right axis measured at 0 T for NaYMnWO$_6$ and NaHoCoWO$_6$. (b) and (d) are *M*(*H*) curves at various temperatures along with *dM/dH* in the inset, respectively.

The linear fit to the inverse molar susceptibility ($1/\chi_m$) *vs.* temperature curve as shown in the figure 5.21 gives the μ_{eff} as 6.01 μ_B/Mn, which is consistent with the spin only value of theoretical moment of Mn^{2+}- ions. In the case of cobalt compound, the obtained value of μ_{eff} is 12.12 μ_B/Co,Ho, which is in good agreement with the calculated vector sum of the Co^{2+} and Ho^{3+} moments (see table 5.8). The Curie-Weiss temperatures for Mn and Co compounds are $\theta_c = -36$ K and -11 K, respectively, which is consistent with the antiferromagnetic ordering. The isothermal *M*(H) loop measured below and above the Néel temperatures and the derived dM/dH curve for these two compounds are shown in figure 5.20(c) and (d), respectively. While the *M*(H) behavior of $NaYMnWO_6$ is consistent with a collinear magnetic ordering, we notice a non-linear behavior below 20 K in $NaHoCoWO_6$ with a distinct change in the slope below 7 K. This characteristic is prominent in the *dM/dH* curves where we see a clear peak near 1 T field at 2 K and a very broad peak at the same field at 5 K. This feature is suppressed above the short-range ordering of Ho^{3+} ions. This behavior indicates a metamagnetic transition related to the magnetic field induced phase transition associated with Ho^{3+} ions. The non-linear behavior persists above 7 K till 20 K suggesting possible magnetic interaction between the 4*f* moments of Ho^{3+} and 3d moments of Co^{2+} or due to the local ordering of Co^{2+} ions.

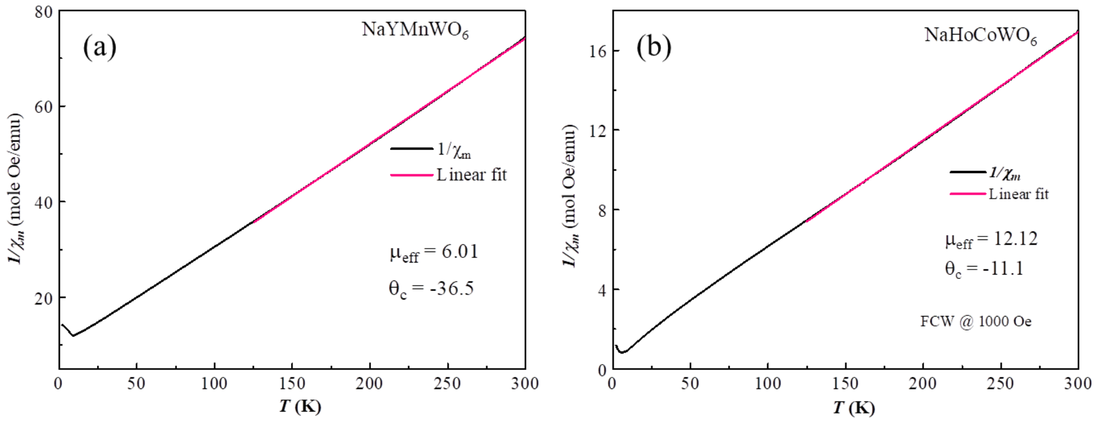

Figure 5.21 Linear fit of the inverse molar susceptibility of (a) $NaYMnWO_6$ and (b) $NaHoCoWO_6$

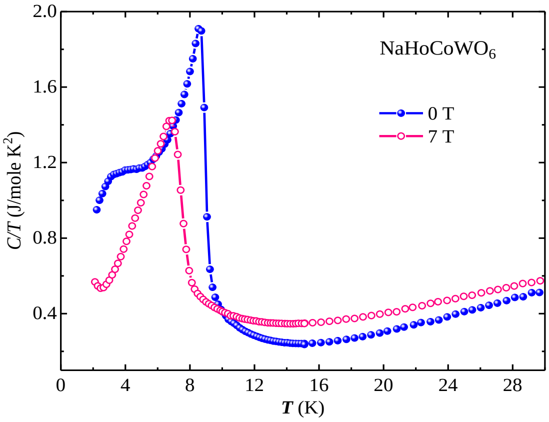

Figure 5.22 Heat capacity divided by temperature measured at 0 and 7 T magnetic field.

5.4.3 Dielectric properties

Earlier studies have shown the absence of ferroelectric polarization in the paramagnetic state of Na*Ln*MnWO$_6$ (*Ln* = La, Nd and Tb) [40] and Na*Ln*FeWO$_6$ (Ln = La and Nd) [41] with bigger Ln-ions. Since the compounds NaYMnWO$_6$ and NaHoCoWO$_6$ have polar crystal structure ($P2_1$) at room temperature, we have performed piezoelectric displacement and *P*(*E*) measurements to verify the ferroelectric nature of these compounds. For these measurements, thin disc shaped samples were made by polishing the wide area. Unfortunately, we could not apply sufficiently large enough electric field to obtain a proper piezoelectric or *P*(*E*) curves at room temperature because of significant conductivity of these materials. However, we have performed *P*(*E*) measurements at lower temperatures inside the PPMS sample chamber under high vacuum, which is a suitable condition for applying higher electric field.

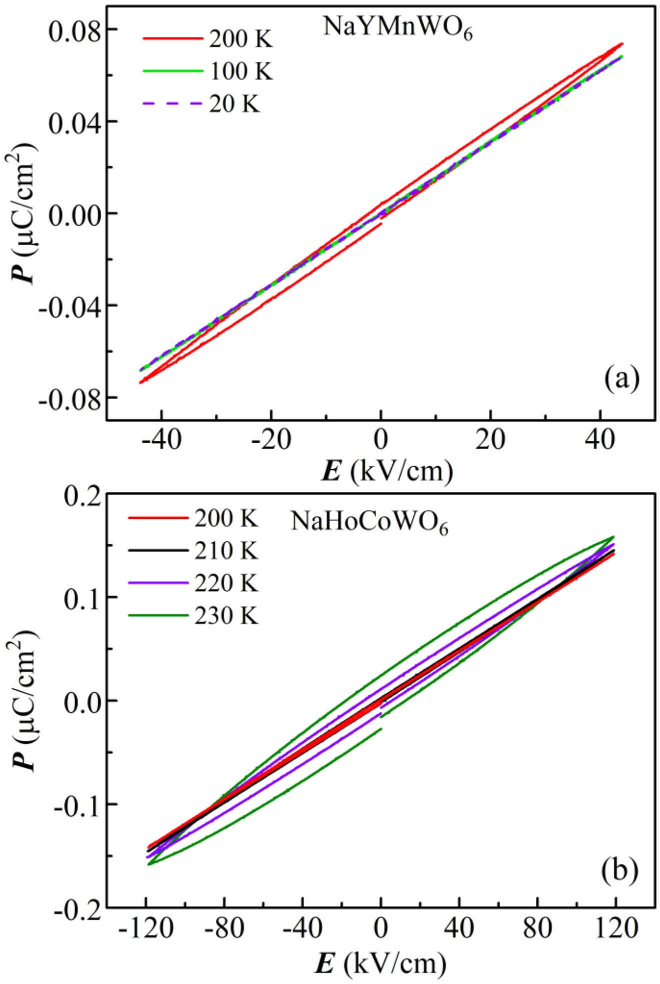

Figure 5.23 Polarization *vs.* electric field loop measured at different temperatures with $f = 1$ Hz pulse for (a) NaYMnWO$_6$ and (b) NaHoCoWO$_6$.

In the case of $NaYMnWO_6$, we could apply a maximum voltage of 40 kV/cm that gives a linear *P*(*E*) curve in the temperature range 20 - 200 K (figure 5.23(a)). On the other hand, for $NaHoCoWO_6$, the conductivity was sufficiently low at 200 K and it was possible to measure the *P*(*E*) loop with nearly 120 kV/cm field (figure 5.23(b)). Even at this temperature and electric field we see only a linear curve indicating either the coercive field is higher than 120 kV/cm or the non-switchability of these samples. It is important to note that 120 kV/cm is substantially high field and most of the classical ferroelectric materials, for example, $BaTiO_3$, $Pb_{0.5}Zr_{0.5}TiO_3$, $BiFeO_3$ are switchable below 120 kV/cm [61, 62]. Therefore, these results probably indicate that the doubly ordered perovskites are only pyroelectric because the octahedral rotation may involve large energy barrier particularly with smaller *Ln*-ions. A small opening in *P*(*E*) loop of $NaHoCoWO_6$ with increasing temperature above 200 K indicates lossy dielectric behavior and does not represent ferroelectricity [63, 64].

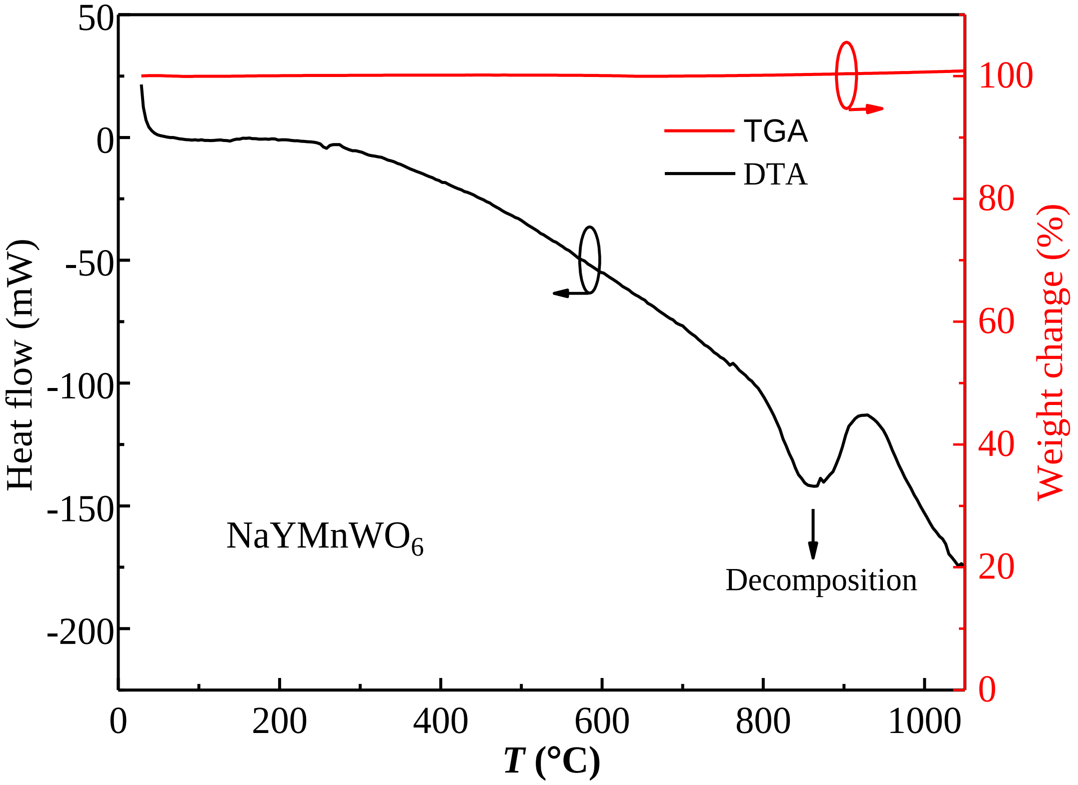

Figure 5.24 TGA and DTA curve obtained in NaYMnWO6 under N_2 atmosphere with 3°/min warming rate.

Since the polar to non-polar phase transition is not detected by differential thermal analysis up to its decomposition temperature of 850°C (figure 5.24), it is not possible to measure non-switchable spontaneous polarization by pyroelectric measurements. There is no significant weight change in the sample as observed in the TGA data. There is a broad endothermic anomaly around 850°C in the DTA curve which indicates a possible phase change occurring. However the sample color was changed from green to black as we saw after the measurement. An X-ray diffraction scan was performed to check whether the sample phase is present or not. We observed that there is no NaYMnWO$_6$ phase present in the residue sample. Therefore we conclude that the broad anomaly at 850°C is indicative of sample decomposition.

5.4.4 Low temperature dielectric and pyroelectric properties

In order to explore whether the electrical properties around the magnetic ordering temperature will be useful to understand the polar nature of these materials and possible magnetoelectric coupling, we have investigated the low temperature dielectric and pyroelectric properties. The low temperature frequency dependent dielectric data of both NaYMnWO$_6$ and NaHoCoWO$_6$ are presented in figure 5.25 (a-b) and (c-f), respectively. The dielectric constant of the former at 2 K is 15.7 that increase monotonously to 16.5 at 240 K with an anomaly at the antiferromagnetic ordering temperature (9 K) of Mn^{2+} ions as shown in the expanded scale in figure 5.25(b). It can be seen that there is a small magnetocapcitance effect at 7.6 K (see inset). In the later compound, a similar variation of dielectric constant is observed with broad maxima at 40 K (DR1) and 100 K (DR2), corresponding to two dipolar relaxations (DR), which exhibit frequency dispersion. A frequency independent anomaly at the magnetic ordering temperature and the corresponding loss can also be noticed in figure 5.25(c) and figure 5.25(d), respectively. More importantly, the dielectric anomaly at the magnetic ordering temperature shifts towards lower temperature with increasing magnetic field as shown in figure 5.25(e). This behavior is consistent with the decrease of T_N as revealed by the heat capacity data shown in figure 5.22. Thus, we measured the magnetodielectric properties around the magnetic ordering temperature. Indeed, we observe a magnetodielectric effect extending from 2 to 30 K with maximum amplitude at 8.6 K which is just below the magnetic ordering temperature (figure 5.25(f)) similar to the previous compounds. The presence of such a sharp anomaly in the dielectric constant along with the magnetocapcitance effect is an indication of either a simple magnetodielectric effect or electric polarization induced by the magnetic ordering as mentioned earlier. In order to understand the nature of dielectric anomaly, we have carefully measured the pyroelectric current across the magnetic ordering temperatures in both the samples with and without an electric field poling.

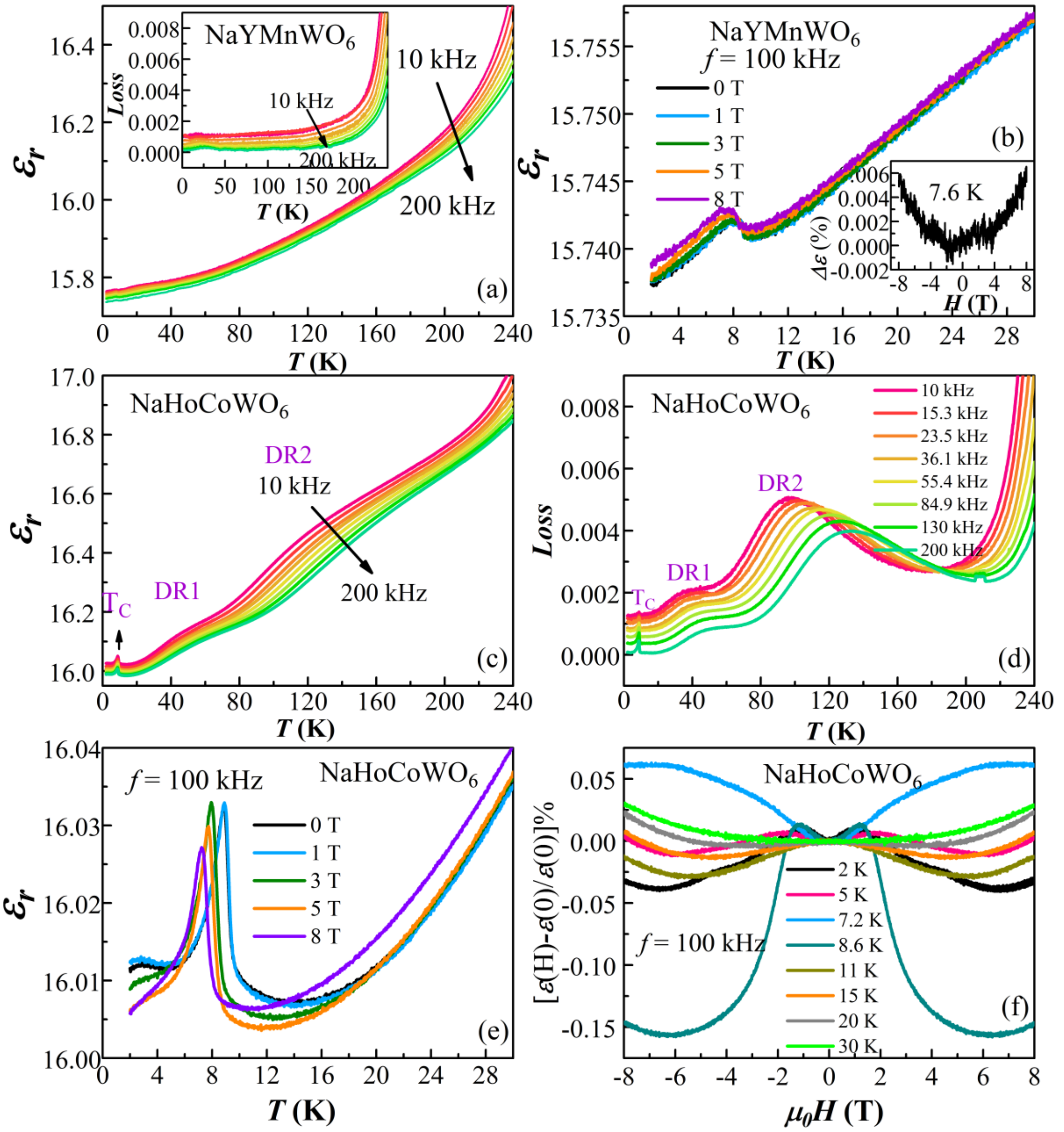

Figure 5.25 (a) Frequency dependent dielectric constant and loss (inset) in NaYMnWO$_6$ measured form 2 to 240 K at zero field. (b) Dielectric constant measured at various magnetic field from 2 to 30 K at 100 kHz. Inset shows the magnetodielectric effect at 7.6 K. (c) Frequency dependent dielectric constant (d) the corresponding loss data recorded from 2 to 240 K in NaHoCoWO$_6$. (e) Magnetic field dependent dielectric constant measured from 2 to 30 K at 100 kHz. (f) Magnetodielctric effect at various temperatures in NaHoCoWO$_6$.

The results of pyroelectric current measurements for both the compounds are presented as polarization versus temperature in figure 5.26(a) and (c). It is intriguing to note the emergence of electric polarization at the magnetic ordering temperature without an electric poling in $NaYMnWO_6$. Upon applying a poling field of ±6 kV/cm, the sign of the polarization remains in the same direction as that of zero electric field polarization. The recorded pyrocurrent data are shown in the inset of the respective figures. Similar features are observed for $NaHoCoWO_6$ as well and shown in figure 5.26(c) and (d). These results indicate that these doubly ordered perovskites have polar structure in the paramagnetic state and the magnetic ordering enhances the polarization (ΔP). The change in polarization could be due to coupling of magnetism and electric polarization through magnetoelastic effect or the magnetic ordering itself may induce independent polarization. If the magnetically ordered state has the same monoclinic symmetry of the paramagnetic state ($P2_1$), then the polarization direction should remain along the *b*-axis. If the symmetry reduces to triclinic, then the polarization direction can be different from that of the paramagnetic state. The non-switchable nature of the ΔP at the magnetic ordering temperature indicates that the magnetic ordering contributes to polarization in the same direction as that of the paramagnetic state. It should be noted that in multiferroics the polarization induced by magnetic ordering is switchable. However, a detailed neutron diffraction study is required to determine the magnetic structure and understand the mechanism of induced polarization.

The absence of switchable electric polarization upon reversing the sign of the poling electric field demonstrates that these doubly ordered perovskites with smaller *Ln*-ions are only pyroelectric, indicating a large energy barrier between the two polar states. Application of magnetic field does not influence the polarization significantly in $NaYMnWO_6$ whereas the polarization is suppressed completely in $NaHoCoWO_6$ under the magnetic field of 5 T applied parallel with respect to the electric field (figure 5.26(c)). The suppression of polarization in the later may be due to the exchange interaction between 4*f*-moments of Ho^{3+} ions and 3d-moments of Co^{2+} ions, which is enhanced by the applied magnetic field. Or there is a major role of rare-earth ion in inducing the polarization thus in presence of magnetic field when the rare-earth orders with the applied magnetic field it destroys the electric polarization. A similar behavior of suppression of electric polarization under magnetic field has recently been reported in $RFeWO_6$ (R=Dy, Tb) [65].

It is important to mention here that the polar compound with larger *Ln*-ion, $NaLaMnWO_6$ did not show dielectric anomaly or pyrocurrent at the magnetic ordering temperature which is probably in agreement with the theoretical calculation that the energy difference between high temperature paraelectric and the ground state polar phases increases with the decrease in size of the *Ln*-ion and thus the polarization increases. The relatively large energy barrier may also explain the absence of switchable polarization in $NaYMnWO_6$ and $NaHoCoWO_6$. However, a detailed study of magnetic structure as a function of the size of *Ln*-ions would be required to understand the switchability of polarization and coupling of magnetism to electric polarization that induces change in electric polarization at the magnetic ordering temperature.

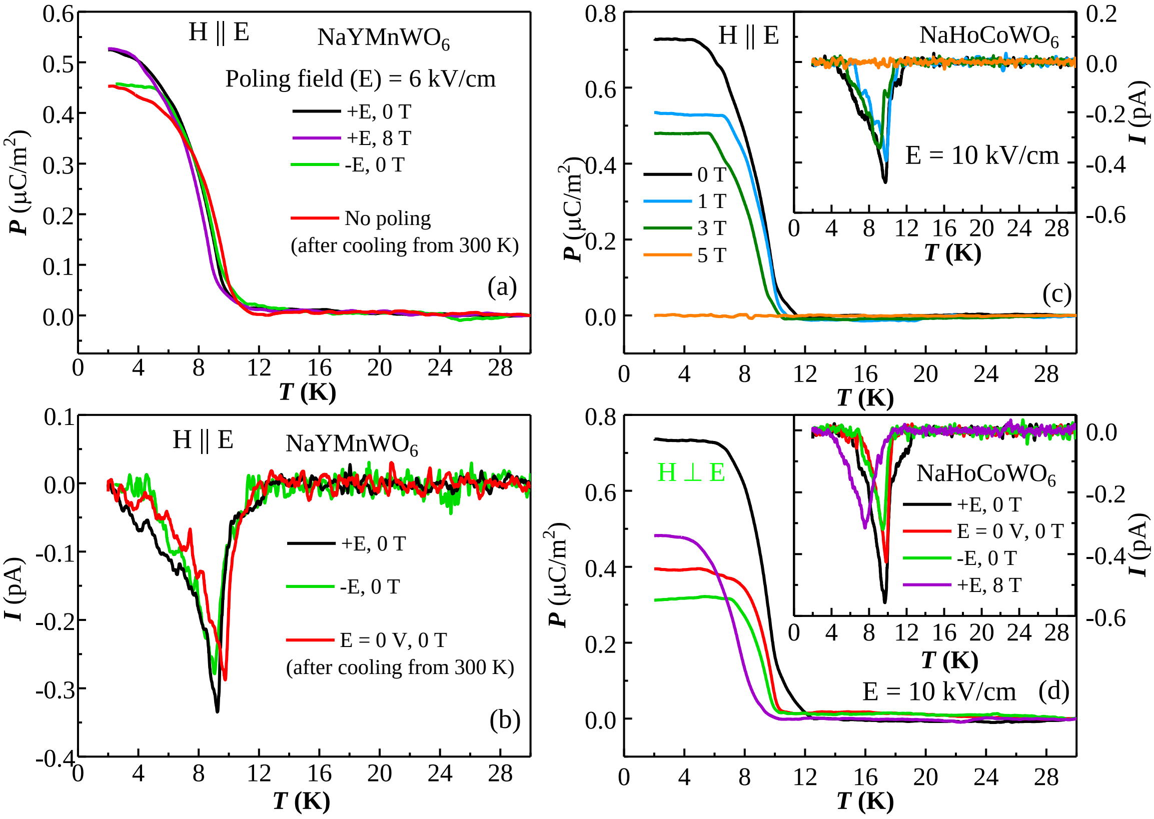

Figure 5.26 (a) Change in polarization with temperature across magnetic ordering obtained through pyrocurrent in $NaYMnWO_6$ under various poling process. (b) Pyrocurrent data recorded in different poling conditions for $NaYMnWO_6$. Effect of magnetic field on the change of polarization with constant electric field poling in $NaHoCoWO_6$ (c) when H ∥ E and (d) H ⊥ E. Insets show the respective pyrocurrent feature.

5.5 Conclusion

Based on conventional *P*(*E*) loop, PUND and piezoelectric measurements we conclude that the higher size rare-earth containing Na*R*MWO$_6$ (M = Mn, *R* = La, Nd and Tb; *M* = Co, *R* = La and Nd) materials are not ferroelectric at room temperature thus may not possess a non-centrosymmetric structure or the polarization may be non-switchable. The magnetic ordering in all the compounds induces intrinsic dielectric anomalies. A fare magnetodielectric coupling is also observed in magnetic rare-earth containing samples. However no electric polarization is observed corresponding to the dielectric anomalies. From the detailed analysis of magnetic field dependent dielectric constant and magnetization value we understand that the magnetodielectric effect occurs due to the net magnetization of both rare-earth and transition metal moment and the non-collinear spin structures of the transition metal ions. A large dielectric anomaly is found just below the room temperature for all the Mn containing sample due to the change in conductivity which does not contribute any ferroelectric polarization.

With the lower size rare-earth containing double perovskites, high pressure was necessary to stabilize the structure. Interestingly, the high pressure synthesized NaYMnWO$_6$ and NaHoCoWO$_6$ compound indeed crystallize in the polar (*P*2$_1$) structure. Magnetic measurements suggest that Mn^{2+} and Co^{2+} ions order antiferromagnetically at low temperatures similar to the ambient pressure phases below 15 K. In addition to the magnetodielectric coupling in these samples, a non-switchable polarization is observed concomitantly with the magnetic ordering. Particularly, in Ho-sample, a magnetoelectric coupling is also present along with the mangnetodielectric effect distinctly for both parallel and perpendicular direction of magnetic field with respect to the electric field. The non-switchability implies that the energy barrier between the two polar state in the hybrid improper ferroelectricity is quite high. A thin film measurement can be helpful in order to see the switching of polarization as well a typical ferroelectric loop in the *P*(*E*) measurements. A piezoforce microscopic measurement will be performed later in these samples. The absence of polarization at T_N for Mn sample with La, Nd and Tb, indicates that they might have centrosymmetric structure (*P*2$_1$/*m*) on the other hand Y sample has *P*2$_1$ structure so that the magnetic structure of Mn modifies the electric polarization with the help of magnetodielectric coupling thus absent for other large size rare-earth compounds.

References

[1] C. Giacovazzo, Fundamentals of crystallography (Oxford university press, USA, 2000).

[2] N. A. Benedek, A. T. Mulder, and C. J. Fennie, J. Solid State Chem. **195**, 11 (2012).

[3] S.-W. Cheong and M. Mostovoy, Nat. Mater. **6**, 13 (2007).

[4] J. M. Rondinelli and C. J. Fennie, Adv. Mater. **24**, 1961 (2012).

[5] H. J. Zhao, J. Íñiguez, W. Ren, X. M. Chen, and L. Bellaiche, Phys. Rev. B **89**, 174101 (2014).

[6] B. Xu, D. Wang, H. J. Zhao, J. Íñiguez, X. M. Chen, and L. Bellaiche, Adv. Funct. Mater. **25**, 3626 (2015).

[7] H. T. Stokes, E. H. Kisi, D. M. Hatch, and C. J. Howard, Acta Crystallographica Section B: Structural Science **58**, 934 (2002).

[8] N. A. Benedek and C. J. Fennie, Phys. Rev. Lett. **106**, 107204 (2011).

[9] E. Bousquet, M. Dawber, N. Stucki, C. Lichtensteiger, P. Hermet, S. Gariglio, J.-M. Triscone, and P. Ghosez, Nature **452**, 732 (2008).

[10] K. T. Delaney, M. Mostovoy, and N. A. Spaldin, Phys. Rev. Lett. **102**, 157203 (2009).

[11] Y. S. Oh, X. Luo, F.-T. Huang, Y. Wang, and S.-W. Cheong, Nat. Mater. **14**, 407 (2015).

[12] W. P. Mason and B. Matthias, Phys. Rev. **74** (1948).

[13] W. G. Cady., Dover.

[14] J. Bardeen, L. N. Cooper, and J. R. Schrieffer, Phys. Rev. B **108**, 1175 (1957).

[15] E. Dagotto, T. Hotta, and A. Moreo, Phys. Rep. **344**, 1 (2001).

[16] H. Hayashi, H. Inaba, M. Matsuyama, N. G. Lan, M. Dokiya, and H. Tagawa, Solid State Ionics **122**, 1 (1999).

[17] T. Mizokawa, D. I. Khomskii, and G. A. Sawatzky, Phys. Rev. B **61**, 11263 (2000).

[18] T. Zhao *et al.*, Nat Mater **5**, 823 (2006).

[19] T. Kimura, T. Goto, H. Shintani, K. Ishizaka, T. Arima, and Y. Tokura, Nature **426**, 55 (2003).

[20] E. V. Milov, A. M. Kadomtseva, G. P. Vorob’ev, Y. F. Popov, V. Y. Ivanov, A. A. Mukhin, and A. M. Balbashov, Jetp Lett. **85**, 503 (2007).

[21] G. King and P. M. Woodward, J. Mater. Chem. **20**, 5785 (2010).

[22] M. C. Knapp and P. M. Woodward, J. Solid State Chem. **179**, 1076 (2006).

[23] G. King, S. Thimmaiah, A. Dwivedi, and P. M. Woodward, Chem. Mater. **19**, 6451 (2007).

[24] P. K. Davies, Current Opinion in Solid State and Materials Science **4**, 467 (1999).

[25] V. Caignaert, F. Millange, B. Domengès, B. Raveau, and E. Suard, Chemistry of Materials **11**, 930 (1999).

[26] B. J. Kennedy, C. J. Howard, Y. Kubota, and K. Kato, Journal of Solid State Chemistry **177**, 4552 (2004).

[27] G. King, L. M. Wayman, and P. M. Woodward, J. Solid State Chem. **182**, 1319 (2009).

[28] G. King, A. S. Wills, and P. M. Woodward, Phys. Rev. B **79**, 224428 (2009).

[29] T. Fukushima, A. Stroppa, S. Picozzi, and J. M. Perez-Mato, Phys. Chem. Chem. Phys. **13**, 12186 (2011).

[30] A. Glazer, Acta Crystallographica Section B: Structural Crystallography and Crystal Chemistry **28**, 3384 (1972).

[31] P. Zuo, C. V. Colin, H. Klein, P. Bordet, E. Suard, E. Elkaim, and C. l. Darie, Inorg. chem. **56**, 8478 (2017).

[32] M. Fukunaga and Y. Noda, J. Phys. Soc. Jpn. **77** (2008).

[33] S. M. Feng, Y. S. Chai, J. L. Zhu, N. Manivannan, Y. S. Oh, L. J. Wang, Y. S. Yang, C. Q. Jin, and K. H. Kim, New Journal of Physics **12** (2010).

[34] Y. S. Chai, Y. S. Oh, L. J. Wang, N. Manivannan, S. M. Feng, Y. S. Yang, L. Q. Yan, C. Q. Jin, and K. H. Kim, Phys. Rev. B **85**, 184406 (2012).

[35] K. M. Ok, E. O. Chi, and P. S. Halasyamani, Chemical Society Reviews **35**, 710 (2006).

[36] J. Rodriguez-Carvajal, in *satellite meeting on powder diffraction of the XV congress of the IUCr* (Toulouse, France:[sn], 1990).

[37] S. García-Martín, E. Urones-Garrote, M. C. Knapp, G. King, and P. M. Woodward, J. Am. Chem. Soc. **130**, 15028 (2008).

[38] S. García-Martín, G. King, G. Nénert, C. Ritter, and P. M. Woodward, Inorg. chem. **51**, 4007 (2012).

[39] J. Young, A. Stroppa, S. Picozzi, and J. M. Rondinelli, Dalton Trans. **44**, 10644 (2015).

[40] C. De, T. H. Kim, K. H. Kim, and A. Sundaresan, Phys. Chem. Chem. Phys. **16**, 5407 (2014).

[41] M. Retuerto *et al.*, Inorg. chem. **52**, 12482 (2013).

[42] E. Stryjewski and N. Giordano, Adv. Phys. **26**, 487 (1977).

[43] P. Lunkenheimer *et al.*, Nat Mater **11**, 755 (2012).

[44] S. Horiuchi, Y. Tokunaga, G. Giovannetti, S. Picozzi, H. Itoh, R. Shimano, R. Kumai, and Y. Tokura, Nature **463**, 789 (2010).

[45] M. Fiebig, T. Lottermoser, D. Frohlich, A. V. Goltsev, and R. V. Pisarev, Nature **419**, 818 (2002).

[46] S. Ghara, K. Yoo, K. H. Kim, and A. Sundaresan, J. App. Phys. **118**, 164103 (2015).

[47] A. B. Harris, T. Yildirim, A. Aharony, and O. Entin-Wohlman, Phys. Rev. B **73**, 184433 (2006).

[48] T. Suzuki, K. Adachi, and T. Katsufuji, in *Journal of Physics: Conference Series* (IOP Publishing, 2006), p. 235.

[49] A. Pimenov, A. Mukhin, V. Y. Ivanov, V. Travkin, A. Balbashov, and A. Loidl, Nat. Phys. **2**, 97 (2006).

[50] T. D. Sparks, M. C. Kemei, P. T. Barton, R. Seshadri, E.-D. Mun, and V. S. Zapf, Phys. Rev. B **89**, 024405 (2014).

[51] C. G, Appl. Phys. Lett. **88** (2006).

[52] G. Lawes, B. Melot, K. Page, C. Ederer, M. Hayward, T. Proffen, and R. Seshadri, Phys. Rev. B **74**, 024413 (2006).

[53] R. Tackett, G. Lawes, B. C. Melot, M. Grossman, E. S. Toberer, and R. Seshadri, Phys. Rev. B **76**, 024409 (2007).

[54] T. D. Sparks, M. C. Kemei, P. T. Barton, R. Seshadri, E.-D. Mun, and V. S. Zapf, Phys. Rev. B **89**, 024405 (2014).

[55] G. Lawes, A. Ramirez, C. Varma, and M. Subramanian, Phys. Rev. Lett. **91**, 257208 (2003).

[56] S. Weber, P. Lunkenheimer, R. Fichtl, J. Hemberger, V. Tsurkan, and A. Loidl, Phys. Rev. Lett. **96**, 157202 (2006).

[57] A. Long, Adv. Phys. **31**, 553 (1982).

[58] Y. Kohara, Y. Yamasaki, Y. Onose, and Y. Tokura, Phys. Rev. B **82**, 104419 (2010).

[59] A. T. Mulder, N. A. Benedek, J. M. Rondinelli, and C. J. Fennie, Adv. Funct. Mater. **23**, 4810 (2013).

[60] N. A. Benedek, J. M. Rondinelli, H. Djani, P. Ghosez, and P. Lightfoot, Dalton Trans. **44**, 10543 (2015).

[61] P. H. Evert, D. N. Minh, D. Matthijn, and R. Guus, Sci. Technol. Adv. Mater **14**, 045006 (2013).

[62] Y. Zhang, Z. Chen, W. Cao, and Z. Zhang, Appl. Phys. Lett. **111**, 172902 (2017).

[63] J. Scott, J. Phys. Condens. Matter **20**, 021001 (2007).

[64] J. Scott and J. Gardner, Mater. Today, https://doi.org/10.1016/j.mattod.2017.12.003 (2018).

[65] S. Ghara, E. Suard, F. Fauth, T. T. Tran, P. S. Halasyamani, A. Iyo, J. Rodríguez-Carvajal, and A. Sundaresan, Phys. Rev. B **95**, 224416 (2017).

Chapter 6

Part-I

Multiferroicity in high-pressure synthesized isovalent cation ordered Bi_2FeAlO_6*

Summary

This chapter deals with two distinct new multiferroic materials. First part demonstrates a high pressure stabilized polar phase of Bi_2FeAlO_6. The interesting finding in this material is the ordered arrangement of isovalent Fe^{3+} and Al^{3+} ions which crystallizes in a lower symmetry of *R*3 instead of the *R*3*c* present in the end compounds. A typical butterfly piezoelectric loop and a PUND ferroelectric loop confirmed the ferroelectric nature in Bi_2FeAlO_6 where it undergoes an antiferromagnetic transition near room temperature.

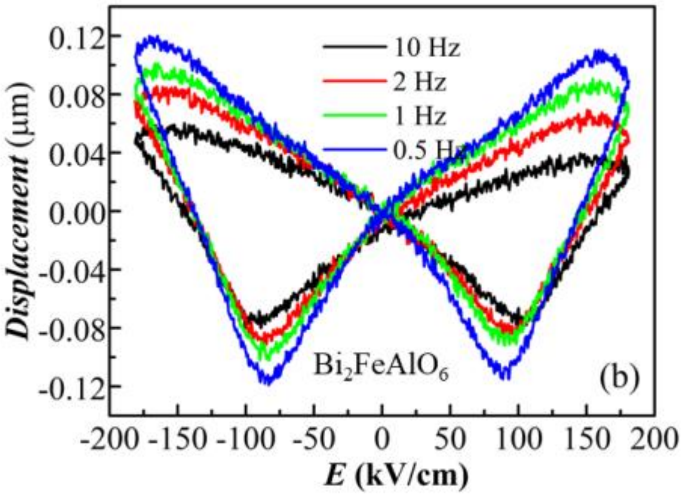

---

*Paper based on this work **C. De** and A. Sundaresan, to be communicated (2018).

6.1 Introduction

The study of multiferroic materials where more than one ferroic ordering coexists has attracted considerable attention due to their potential application in the memory devices, sensors, spintronics, etc. [1-3]. The major challenges for the practical applications of multiferroics is that most of the materials either have ordering temperature below the room temperature or a poor coupling between the ferroic properties. Although there is a continuous search of new magnetoelectric or multiferroic materials, $BiFeO_3$, since its discovery in 2003, is probably the most studied and suitable multiferroic material which meets the requirements for practical applications since both the magnetic and electric ordering occurs far above room temperature and also possible to synthesize under ambient pressure condition. The intrinsic ferroelectric polarization is as large as 90 $\mu C/cm^{2,}$ and the critical temperatures of the ferroelectric and antiferromagnetic (AFM) transitions are $T_C \approx 1100$ K and $T_N \approx 640$ K) respectively [4]. Further, Bi-based perovskite and non-perovskite compounds ($BiMO_3$ M=Co, Cr, and Mn) have been synthesized under high-pressure investigated vastly to produce lead-free piezoelectric as well as multiferroic materials [5-8]. Here, Bi-ions tend off-centering similar to Pb-based perovskites since Bi^{3+} and Pb^{2+} ions both have the stereochemically active $6s^2$ lone pairs [9]. However, the poor magnetoelectric coupling owing to the independent origins and the inherent leakage current for the half-filled 3*d* orbital transition metal ions need to be overcome for the device applications. On the other hand, $BiMO_3$ (M=Al, Sc, Ga, and In) with non-magnetic ions at the B-site may produce only ferroelectric properties [7]. In $BiFeO_3$, a magnetoelectric coupling was demonstrated due to the inverse DM interaction which also marginally contributes to the electric polarization based on type-II mechanism, [10, 11]. There have been numerous studies of the rare-earth element doping at the Bi-site and various transition metal ions at the Fe-site in $BiFeO_3$ to tune the magnetoelectric property as well as weak ferromagnetic behavior in bulk as well as in thin films [12-16].

Further, it is interesting to note that Al_2O_3 and Fe_2O_3 both have corundum structure at room temperature with space group $R\overline{3}C$, but $AlFeO_3$ possess an orthorhombic structure with space group $Pna2_1$. Under applying pressure, AlFeO3 adopts parent compound structure, i.e. $R\overline{3}C$. $BiAlO_3$ is isostructure ($R3C$) with the multiferroic $BiFeO_3$ but can be prepared under high pressure and high temperatures [17]. Theoretical study on $BiAlO_3$ predicted that it should be a high-performance piezoelectric and ferroelectric material [18]. The non-centrosymmetric structure of $BiAlO_3$ was established from the experimental study of ferroelectric loop, Raman spectra and second-harmonic generation (150 times that of quartz) [13,15]. From high-pressure study up to 10 GPa at room temperature revealed two phase transitions at about 4 and 7 GPa with *R3m* and *Amm2* space group [17, 19, 20]. On the other hand, the isostructural $BiFeO_3$ has different high pressure-room temperature structural behavior [21, 22]. In this contest, we wanted to look at the structure of $BiFeO_3$ with Al doping in the Fe site under high-pressure synthesis.

Here, we study the high-pressure synthesis and characterization of perovskite $BiFe_{1-x}Al_xO_3$ (x = 0.2, 0.3, 0.4 and 0.5) which reveals that the compound with 50% Al doping has an ordered arrangement of Fe and Al ions, thus Bi_2FeAlO_6 possessing *R*3 structure while the other substituted compounds possess the parent structure R3c. The investigation of dielectric, ferroelectric, and piezoelectric properties demonstrate that Bi_2FeAlO_6 has considerably lower dielectric loss and indeed showed a piezoelectric displacement and ferroelectric property at room temperature. On the other hand magnetization study shows an antiferromagnetic ordering near room temperature.

6.1.1 Experimental details

Polycrystalline samples of $BiFe_{1-x}Al_xO_3$ (x = 0.2-0.5) were prepared by high pressure and high temperature solid-state reaction. The stoichiometric amount of starting materials Bi_2O_3, Fe_2O_3 and Al_2O_3 (99.9% purity for all) were mixed and ground in an agate mortar for sufficient time in order to form a homogeneous mixture. The mixture was then sealed in a gold capsule and subjected to pressure 6 GPa using a Walker two-stage multi-anvil high pressure apparatus. At the stable high-pressure condition, the samples were heated to 1000 °C and held for 20 min at this temperature, and then quenched to room temperature, followed by release of the pressure. The products were dense sintered cylindrical pellet and were characterized by the powder XRD technique using Bruker D8 advanced powder diffractometer. Structure of 50% Al doping compound was further studied by time of flight neutron diffraction experiment using high-resolution powder diffractometer “WISH” at ISIS, UK. Rietveld refinements of both X-ray and the neutron data were carried out using FULLPROF software package. DC-magnetization measurements were performed in SQUID VSM. Dielectric property was measured using Agilent E4980A Precision LCR meter. Physical Property Measurement System (PPMS) was employed to access the temperature. *PE,* PUND loop and piezoelectric displacement loops were recorded using Radiant Precision Multiferroic tester equipped with piezoelectric displacement optical sensor. For the low temperature *PE* loop, PPMS sample chamber was used for the high vacuum sample environment and low temperature access which permitted to apply a high electric field to the sample.

6.1.2 Results and discussions

6.1.2.1 Structure

Room temperature X-ray diffraction data along with Rietveld refinement of $BiFe_{1-x}Al_xO_3$ samples are shown in figure. 6.1. Following the preparation conditions adapted in this work, a maximum solubility of Aluminum in $BiFe_{1-x}Al_xO_3$ is achieved for x=0.4. All the samples for up to x= 0.4 possess polar *R3c* crystal structure however we could not obtain a good fit for $BiFe_{0.5}Al_{0.5}O_3$ sample. Although the Bi_2O_3 precursor did not contain $Bi_2O_2CO_3$, we observed small amount of this phase in all the samples. We believe that this phase could have formed due to carbon heater and we included this phase in the refinement. For x=0.5, the refinements of the laboratory X-ray data resulted in a poor fit. Considering the unusual chemistry of the oxide $AlFeO_3$ as discussed in the introduction, we thought that the Fe^{3+} and Al^{3+} ions may have ordered arrangement at the 1:1 ratio in the perovskite oxide. A better agreement is found with *R*3 structure with the ordered arrangement of Fe^{3+} and Al^{3+} ions. In order to verify whether the cation ordering in this sample, we performed neutron diffraction at room temperature at ISIS using the instrument 'WISH'. Rietveld refinement indeed confirmed that the structure is *R*3 with 90% ordered arrangement of Fe^{3+} and Al^{3+}. This confirms the rock-salt ordering of Fe^{3+} and Al^{3+} ions along (111) direction and thus the chemical formula of this compound can be written as Bi_2FeAlO_6. The refined pattern is shown in figure 6.2. The structural details of Bi_2FeAlO_6 have been displayed in table 6.1. The crystal structure and the local coordination of oxygen ions around the Fe^{3+} and Al^{3+} ion sites are shown in figure 6.3. Importantly, neutron diffraction data did not show any magnetic impurity peak.

Table 6.1 Structural parameters of Bi_2FeAlO_6 obtained from Rietveld refinement of neutron diffraction data at room temperature. *Space group*: *R3*; a = 5.5052 (2) Å, b = 5.5052 (2) Å, c = 13.708 (1) Å, Vol: 359.80 (4) Å^3; χ^2 = 4.19; Bragg *R*-factor = 4.71(%), R_f-factor = 5.84 (%)

Atom	Wyckoff position	x	y	z	B_{iso}	Occ.
Al1	2a	0.000	0.000	0.723(2)	1.28(5)	0.288
Fe1	2a	0.000	0.000	0.723(6)	1.28(5)	0.045(2)

Bi	2a	0.000	0.000	0.510(0)	1.28(5)	0.333(0)
Bi	2a	0.667(0)	0.333	0.340(2)	1.28(5)	0.333(0)
Fe2	2a	0.000	0.000	0.234(2)	1.28(5)	0.309(1)
Al2	2a	0.000	0.000	0.234(2)	1.28(5)	0.024(1)
O1	2a	0.980(1)	0.530(5)	0.454(1)	1.28(5)	1.0
O2	2a	0.464(5)	0.013(1)	0.958(1)	1.28(5)	1.0

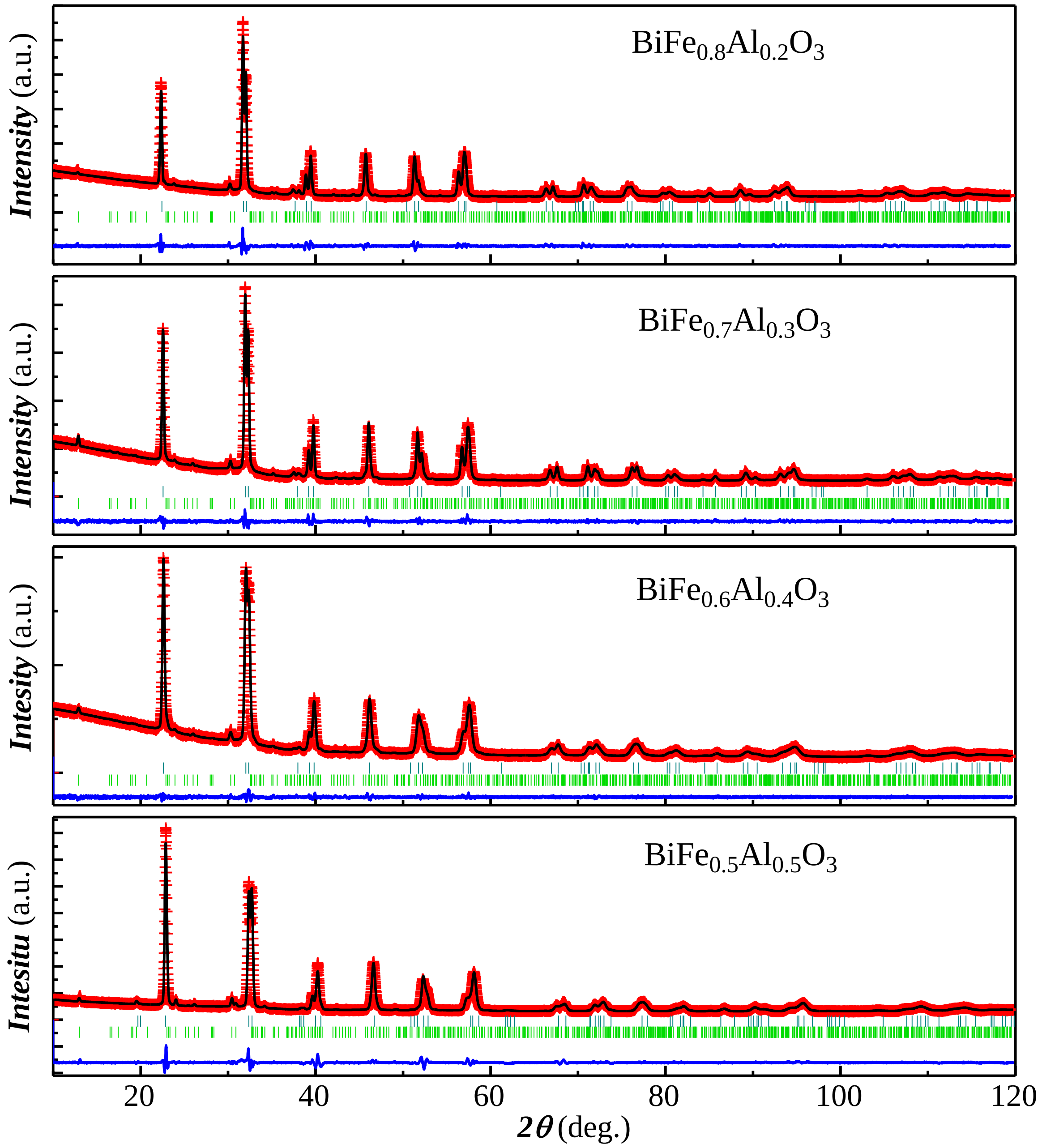

Figure 6.1 Room temperature powder X-ray pattern along with the fitted Rietveld refinement pattern in $BiFe_{1-x}Al_xO_3$ (x= 0.2, 0.3, 0.4 and 0.5). Green vertical lines indicating the Bragg planes corresponding to the impurity phase $Bi_2O_2CO_3$. All the patterns were fitted with $R3c$ space group except x=0.5 fitted with $R3$.

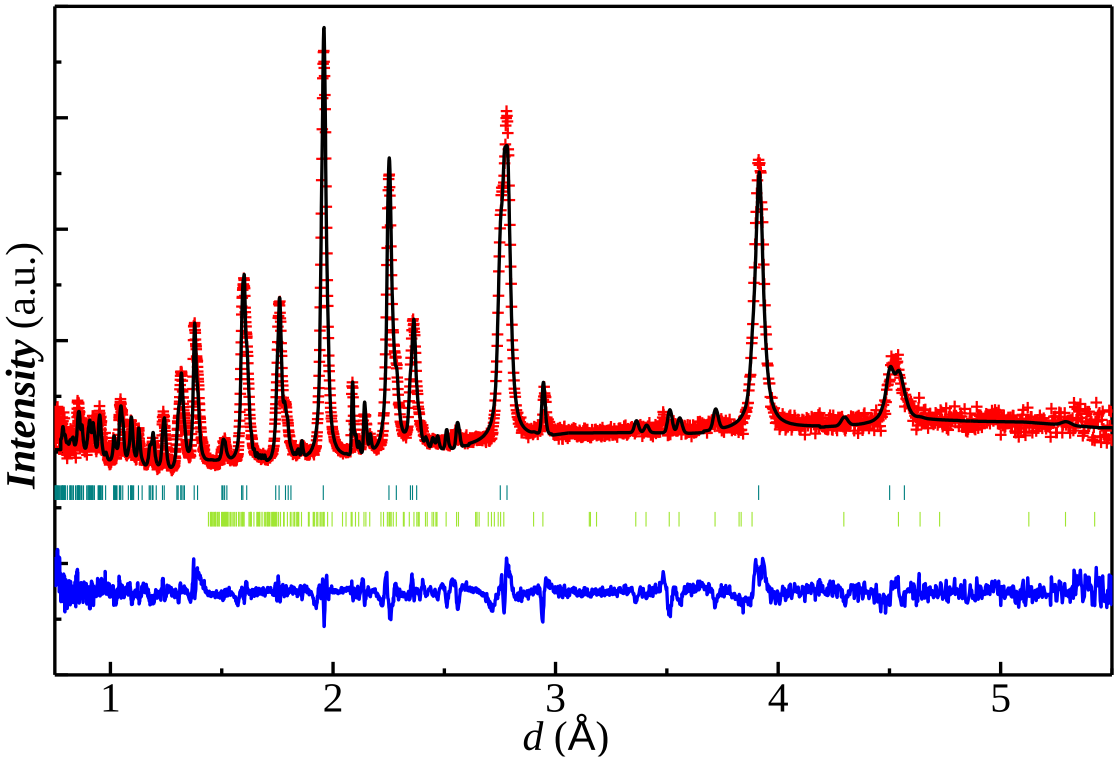

Figure 6.2 Rietveld refined pattern using *R*3 space group against time of flight neutron diffraction data recorded at room temperature. Green lines are indicating the Bragg planes for the impurity phase of $Bi_2O_2CO_3$. Refinement residuals are χ^2 = 4.19; Bragg *R*-factor = 4.71(%), R_f -factor = 5.84 (%).

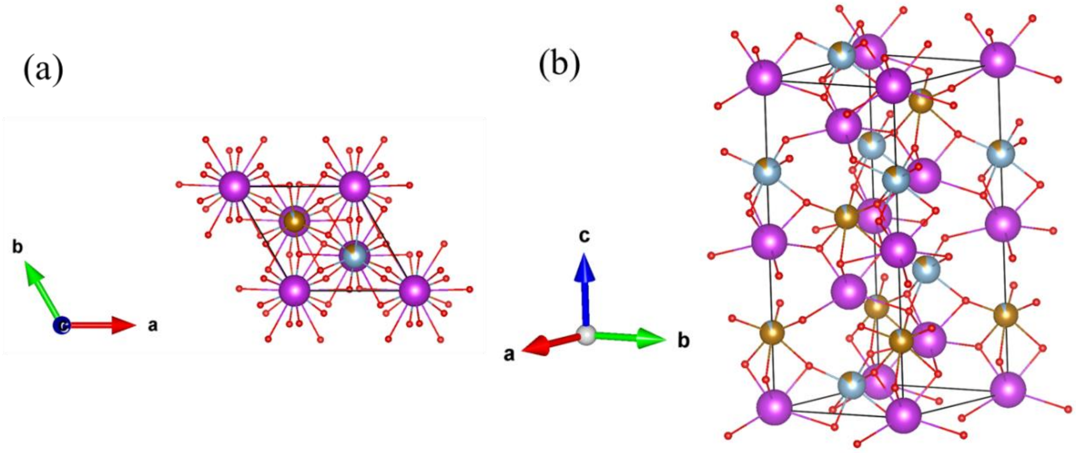

Figure 6.3 Crystal structure obtained from the refinement of the neutron diffraction data. (a) View along c-axis. (b) shows the layered arrangement of Fe and Al atoms.

6.1.2.2 Magnetic properties

Figure 6.4(a-d) shows the temperature dependent DC magnetization data for all the four samples measured under zero-field-cooled warming (ZFC), field-cooled-warming (FCW) and field-cooled-cooling (FCC) condition with 100 Oe field. Bi_2FeAlO_6 shows an antiferromagnetic transition near 280 K which can be attributed to the Fe^{3+} ion ordering. The 50% substitution of non-magnetic Al^{3+} ions into the Fe site with alternatively ordered arrangement is responsible for the decrease of antiferromagnetic ordering away from ~640 K (for pure $BiFeO_3$). The splitting of ZFC data from FCW or FCC data indicates that there are some Fe^{3+} concentrated regions which may have the higher antiferromagnetic ordering temperature. Since the sample is a metastable phase and prepared under high pressure, the magnetization measurement at high temperature was not possible.

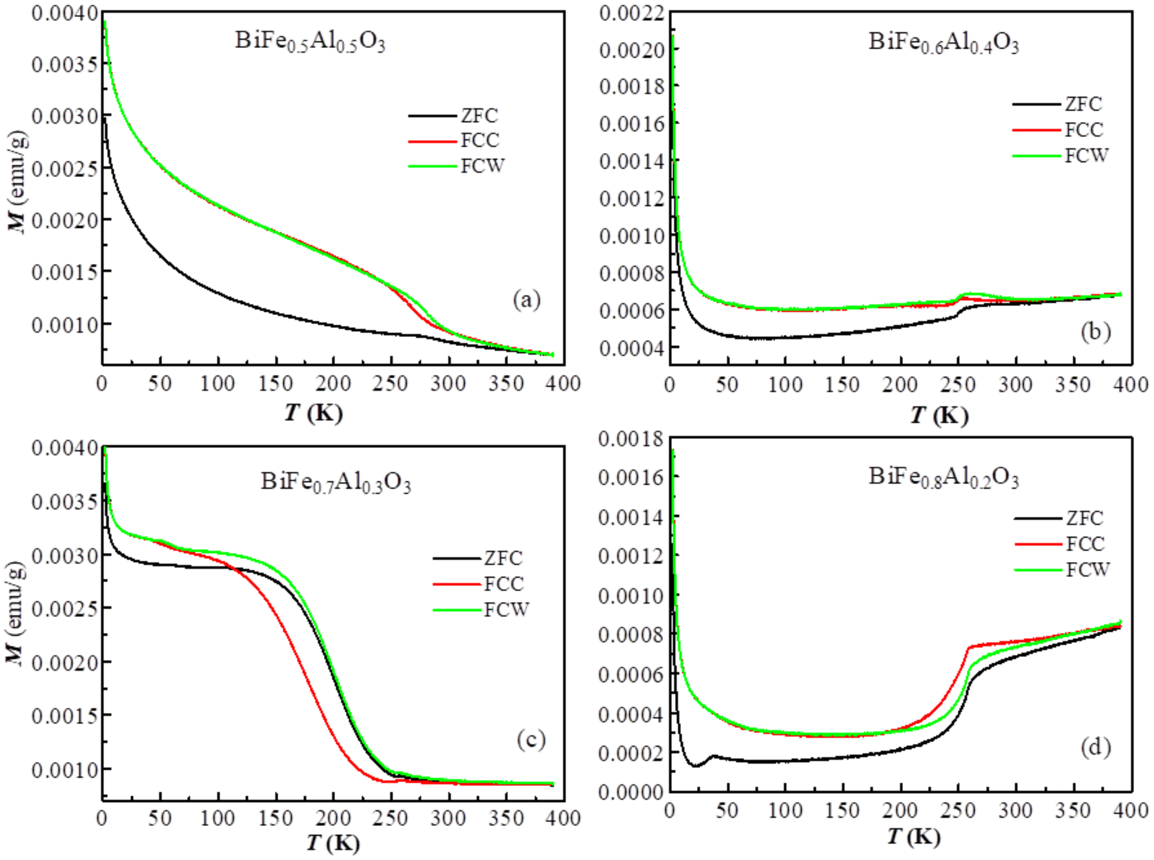

Figure 6.4(a-d) Magnetization versus temperature data measured under ZFC, FCC and FCW conditions with 100 Oe field for $BiFe_{1-x}Al_xO_3$ ($x = 0.2$, 0.3, 0.4 and 0.5).

The overall magnetic behavior measured below 390 K is comparable to the pure $BiFeO_3$ except for the lower ordering temperature [23]. The $M(T)$ data in other samples

$BiFe_{0.6}Al_{0.4}O_3$ and $BiFe_{0.8}Al_{0.2}O_3$ shows similar antiferromagnetic transition with a step-like a decrease in the magnetization which could be due to spin re-orientation as observed in many rare-earth orthoferrites and orthochromites [24]. $BiFe_{0.7}Al_{0.3}O_3$ shows a quite similar antiferromagnetic transition of Bi_2FeAlO_6, however, the large hysteresis in the FCC and FCW data suggests a possible spin-glass or cluster glass behavior [25]. From the $M(H)$ curve measured at various temperatures from 2 K to 390 K, we see a clear linear behavior corresponding to the antiferromagnetic ordering except at 2 K (figure 6.5(a-d)). The presence of non-linear behavior at 2 K is comparable to the parent $BiFeO_3$ compound [23]. The small opening in the $M(H)$ of the sample $BiFe_{0.8}Al_{0.2}O_3$ at higher temperature can be due to canted antiferromagnetic/weak ferromagnetic nature in the more iron-containing sample.

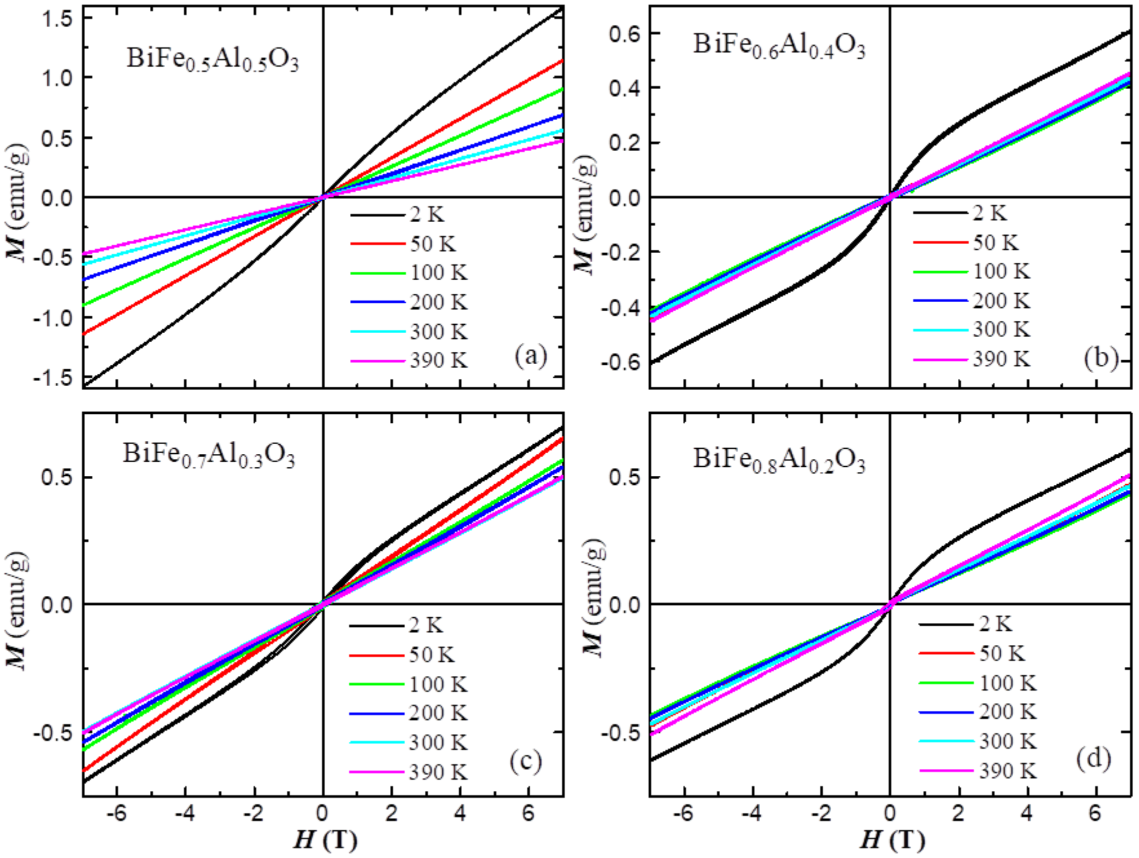

Figure 6.5(a-d) Isothermal magnetization versus field data recorded at various temperature for $BiFe_{1-x}Al_xO_3$ ($x = 0.2, 0.3, 0.4$ and 0.5).

6.1.2.3 Dielectric property

The temperature dependent dielectric constants and loss in Bi_2FeAlO_6 and $BiFe_{0.6}Al_{0.4}O_3$ measured below 300 K, frequency range 5 to 200 kHz, reveals no anomalies, indicating no phase transition (figure 6.6). The dielectric constant exhibits conventional temperature dependence, decreasing from approximately 100 at room temperature to 66 at 2 K. From both the dielectric constant as well as the loss data, it can be seen that the frequency dispersion starts above ~200 K. This frequency dispersion is indicative of the growing Maxwell-Wagner type relaxation above 200 K. The dielectric constant is intrinsic in nature below 200 K. It should be noted that a similar magnitude of dielectric constant was reported in $BiFeO_3$ compound [26].

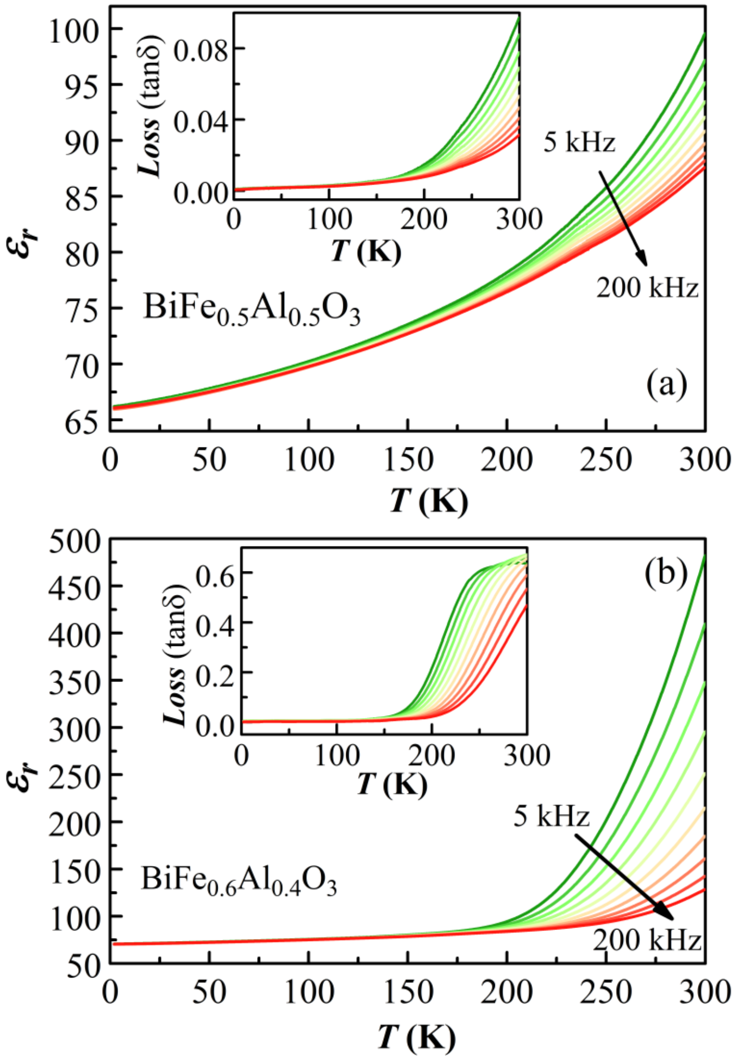

Figure 6.6 Frequency dependent dielectric constant and loss data recorded from 2 to 300 K in (a) Bi_2FeAlO_6 and (b) $BiFe_{0.6}Al_{0.4}O_3$.

With the comparison of dielectric and loss data of the sample $BiFe_{0.6}Al_{0.4}O_3$, it can be observed that the loss is smaller in Bi_2FeAlO_6 compared to the $BiFe_{0.6}Al_{0.4}O_3$ at 300 K which indicates lesser conductivity in Bi_2FeAlO_6 sample. The doping of some other elements as shown in earlier study, results decrease in conductivity and the shift of

Maxwell-Wagner relaxation towards higher temperature. Therefore we understand that in our study the Maxwell-Wagner relaxation in $BiFe_{0.6}Al_{0.4}O_3$ sample appears at somewhat lower temperature compared to the Bi_2FeAlO_6 depending on the concentration of Al^{3+} substitution. The conductivity is dominated by the hopping mechanism and expected to be high in more iron-containing sample. The low dielectric loss in Bi_2FeAlO_6 enables us to measure a $P(E)$ loop and piezoelectric loop which will be described in the following section.

6.1.2.4 Ferroelectric and piezoelectric properties

It is well known that the $BiFeO_3$ ceramic has an inherent leakage problem which did not allow to measure $P(E)$ loop at room temperature except Lebeugle *et al.* who grown a high quality single crystal and showed *PE* loop at room temperature through piezo-response force microscopy [27]. Therefore most of the electric polarization measurement was performed at lower temperature. It was first measured by Teague *et al.* at liquid Helium temperature where they found the polarization of 3.5 $\mu C/cm^2$ at 55 kV/cm field. A well-saturated *PE* loop was found in bulk single crystal of $BiFeO_3$ at 170 K and 90 K by Jun Lu *et al.* [23]. Therefore considering the dielectric loss above 200 K, we tried to measure *PE* loop at low temperatures using PPMS under high vacuum which could be a suitable condition for the application of higher voltage. The conventional *PE* loop at 300 K and 200 K shows a lossy unsaturated banana shape dielectric loop for Bi_2FeAlO_6 (not shown). By only looking at the banana type loop one cannot attribute it as a ferroelectric loop [28, 29]. Knowing the fact that the ferroelectric loop can be largely hindered by the sample conductivity, we have performed $P(E)$ loop measurement through Double-Wave-Method. In this experiment, after a pre-poling positive-negative pulse, two consecutive positive pulse (P and P') and two consecutive negative pulse (N and N') is applied to the sample in order to measure the polarization. Thus this method is also called as Positive-Up and Negative-Down (PUND). The polarization obtained in the first positive (P) or negative (N) pulse would contain all the contribution of polarization (intrinsic polarization as well as leakage) however in the second positive (P') or negative (N') pulses, there would be only leakage contribution.

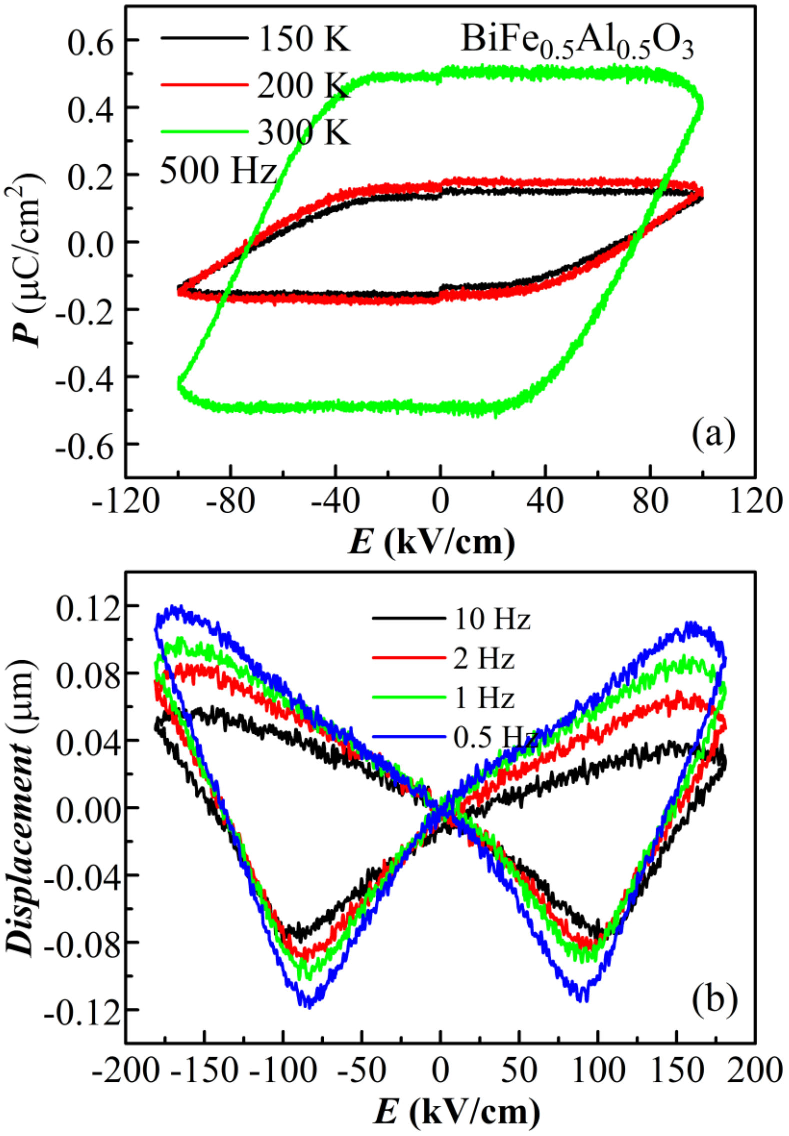

Figure 6.7 (a) PE loop extracted from the PUND measurement at various temperatures in Bi_2FeAlO_6. (b) Piezoelectric displacement loop obtained at room temperature with 180 kV/cm electric field at various excitation frequencies.

Thus after subtracting the polarization among (P and P') and (N and N'), we obtain the intrinsic ferroelectric polarization. This method is quite successful in determining the intrinsic ferroelectric polarization [30-32]. The resultant polarization versus electric field measured at 300 K, 200 K, and 150 K is shown in figure 6.7(a). Surprisingly we can see that there is a square type ferroelectric loop after the subtraction of leakage contributions. Although the loop is not completely saturated, we do not expect any loop in this measurement if there is no intrinsic ferroelectric contribution. Thus, this loop suggests a possible ferroelectric behavior which is expected in the polar structure of Bi_2FeAlO_6. Further, we have recorded the piezoelectric loop at room temperature in Bi_2FeAlO_6

sample. Silicon oil was used as a voltage applying media in the piezoelectric sample holder to apply higher electric field. The piezoelectric measurements have been performed with an excitation voltage of the applied electric field up to 4 kV at various excitation frequencies (0.5, 1, 2 and 10 Hz) on a sample approximately 1 mm^2 area and a thickness of 220 μm (figure 6.7(b)). The typical butterfly loop demonstrates that the sample is indeed piezo-active. The displacement is of the order of ~12 µm, and coercive field is ~150 kV/cm. The piezoelectric hysteresis loops exhibit weak frequency dependency. However, the overall feature remains almost same for more than one order of magnitude frequency range.

6.1.3 Conclusions

In conclusion, the solid solution of $BiFeO_3$ and $BiAlO_3$ is prepared under high pressure and high temperature in polar *R3c* structure. Specifically, 50% substitution of Al^{3+} resulted in an ordered arrangement of Fe^{3+} and Al^{3+} ions which possesses *R*3 structure. We have demonstrated a well saturated piezoelectric loop in the Bi_2FeAlO_6 compound at room temperature. An antiferromagnetic ordering is found near room temperature ~280 K in Bi_2FeAlO_6. The observed piezoelectric and polarization loop in this high-pressure metastable phase represent overcome of a crucial step towards developing a practical operational multiferroic material.

Part-II

Spin driven multiferroicity in ambient pressure and high-pressure phase of $MnSb_2S_4$*

Summary

The second part deals with the discovery of a new spin induced multiferroicity in ambient pressure monoclinic phase of $MnSb_2S_4$. The interesting point is that a magnetic field applied parallel to the electric field largely enhances the electric polarization. We attribute *p-d* hybridization as a possible route of the multiferroic behavior in this material.

Under high-pressure synthesis condition, $MnSb_2S_4$ forms an orthorhombic structure with *Pnam* space group. Among three sequential magnetic transitions, the lowest transition ~6.5 K provided a ferroelectric polarization. Apart from the multiferroic behavior, a pronounced dielectric anomaly (~48 K) above the highest magnetic transition temperature (~34 K) suggested a structural distortion.

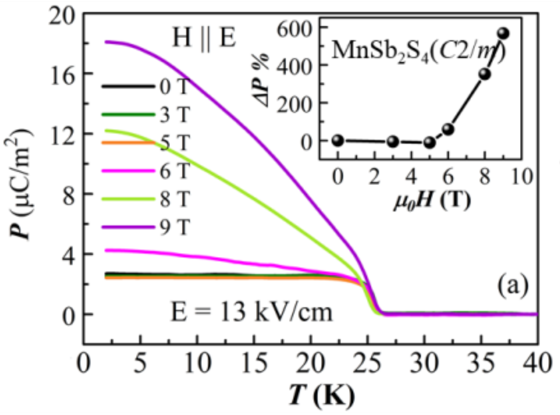

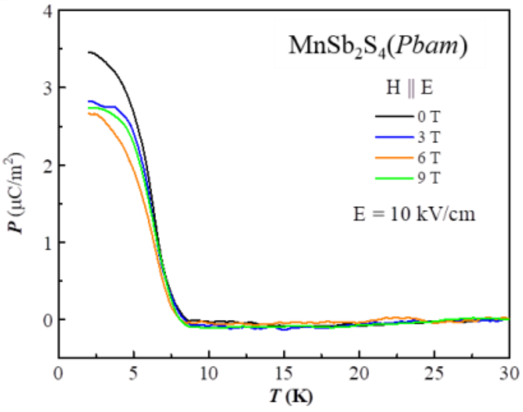

---

*Paper based on this work **C. De** and A. Sundaresan, communicated (2018).

6.2A Monoclinic $MnSb_2S_4$

As described in the introduction chapter, among the three types of spin-induced multiferroic materials, an intriguing frustrated spin induced multiferroicity was found in a triangular lattice antiferromagnet with a proper screw type magnetic structure with 120° spin rotation angle. This spin structure cannot induce polarization according to the spin-current model or exchange-striction model. However, an alternate model of spin-dependent *d*-*p* hybridization was proposed based on the covalence between transition metal *d* and ligand *p* orbitals which is modulated depending on the local spin moment direction via relativistic spin-orbit interaction [33, 34]. Induced polarization is proportional to $\cos 2\theta$, where θ is the angle between transition metal spins and the direction connecting transition metal and oxygen ions [34]. Although in most cases this term cancels out within the crystal, an appropriate combination of spin modulation and crystallographic lattice can allow a macroscopic electric polarization. For example, in delafossite $CuFeO_2$, a proper screw spin order in a triangular lattice with *R-3m* structure allows the P. According to the symmetry restriction, it was anticipated that the occurrence of *d-p* hybridization induced polarization may be observed in lower crystal symmetry e.g. triclinic, monoclinic and rhombohedral [34]. Such examples are delafossite (ABO_2) material with trigonal *R-3m* structure (e.g. $CuCrO_2$, $AgCrO_2$) [35], MI_2(M = Mn, Ni) [36] with CdI_2 structure and $RFe_3(BO_3)_4$ with *R32* structure [37]. While most of the spin induced multiferroics are oxide materials, only a few transition metal chalcogenides have been reported to exhibit multiferroic behavior [38-41].

The mineral clerite (named after Onisima Yegorovicha Klera) $MnSb_2S_4$ crystallizes in the monoclinic (*C2/m*) $HgBi_2S_4$ type structure consisting of chains of manganese ions in octahedral coordination which are connected by sharing their edges along the *b*-axis. These chains are interlinked along the *a*-axis through a distorted square pyramid of the Sb ions and form layers parallel to the *c*-axis [42]. From the electronic band structure calculations based on local spin density approximation, an antiferromagnetic ground state was found to be energetically favorable [43, 44]. Further, the magnetization measurements confirmed antiferromagnetic ordering below 25 K. Interestingly, neutron diffraction study had established an incommensurate helical spin structure where manganese magnetic moments lie in the *ac* plane. Along the chains of MnS_6 octahedra, the angle between adjacent spin is 133° while it is 66.85° along the a-axis and collinear along the *c*-axis [42]. Therefore this spin structure can be considered as a screw type where the propagation vector lies along the spin chain. This type of spin structure is quite similar to that of 120° spin rotation angle in a triangular lattice as observed in $CuCrO_2$ where the spin-dependent *d-p* hybridization induces ferroelectric polarization along the screw axis except that the angle of rotation in our case is ~133° [34, 35, 45, 46]. These features suggest that the material $MnSb_2S_4$ could be a potential candidate to show spin-induced multiferroicity.

In this section, we study the emergence of ferroelectric polarization below the helical spin ordering at 25 K. Remarkably, the polarization is enhanced by five times when the applied magnetic field is at 9 T, indicating a strong magnetoelectric coupling. We suggest that the spin-dependent *d-p* hybridization as a possible mechanism for the occurrence of multiferroicity. This study provides another prototype example of spin-induced multiferroic in a non-oxides material possessing centrosymmetric monoclinic crystal structure.

6.2A.1 Experimental details

$MnSb_2S_4$ was prepared by solid-state reaction of stoichiometric mixture of elemental Mn, Sb and S in an evacuated silica tube by heating at 500°C for five days. The heated mixture was pressed into pellets and sintered at 500°C for ten days. Powder X-ray diffraction showed a trace amount of Sb_2S_3 impurity. Magnetic measurements were carried out with an MPMS SQUID magnetometer (Quantum Design, USA) and heat capacity was measured in Physical Property Measurement System (PPMS). For the electrical measurements, the samples were cut into thin plates and silver paste was applied as electrodes onto the wide faces. The dielectric constant was measured with the LCR meter (E4980A). To determine the electric polarization, we measured the pyroelectric current using Keithley electrometer (6517A) with a constant rate of temperature sweep (10 K/min) and integrated it with time. In order to align the polar domains in the sample, a poling electric field was applied in the cooling process and removed at the lowest temperature and shorted for 30 min before the measurements of pyroelectric current. PPMS was used for the access of low temperatures and magnetic field.

6.2A.2 Results and discussions

6.2A.2.1 Structure

The crystal structure of $MnSb_2S_4$ is obtained from the refinement of X-ray data using FULLPROF package with the monoclinic space group *C2/m* which is in good agreement with the earlier reported structure [44]. The recorded x-ray diffraction data along with the refined data is shown in figure 6.8. The unmatched peaks marked with asterisks are due to minor impurity of elemental sulfur. The lattice parameters, atomic positions and overall refinement factors are displayed in table 6.2. The crystal structure obtained from the refined data is shown in figure 6.9(a) where we can see that the edge-shared MnS_6 octahedra are arranged in a chain along *b*-axis and distorted SbS_5 square pyramid are alternatively attached to the MnS_6 octahedra. The chains are interconnected along the *a*-axis and forms layer along the *c*-axis. The helicoidal spin structures of Mn^{2+} spins is drawn in figure 6.9(b) according to the reference [42].

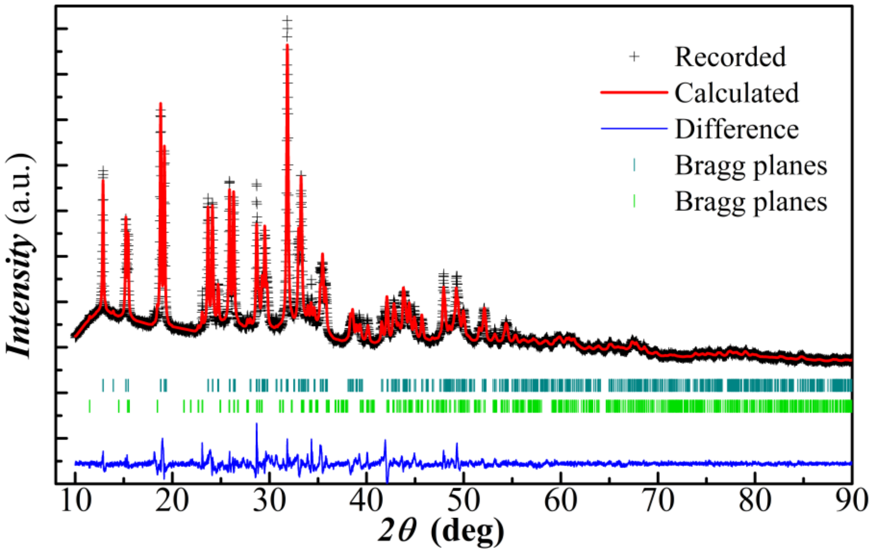

Figure 6.8 X-ray diffraction pattern recorded at room temperature along with the Rietveld refinement data using *C2/m* space group. The upper lines and lower lines indicate Bragg planes of sample and the impurity of S respectively. The bottom curve shows the difference between recorded and fitted pattern.

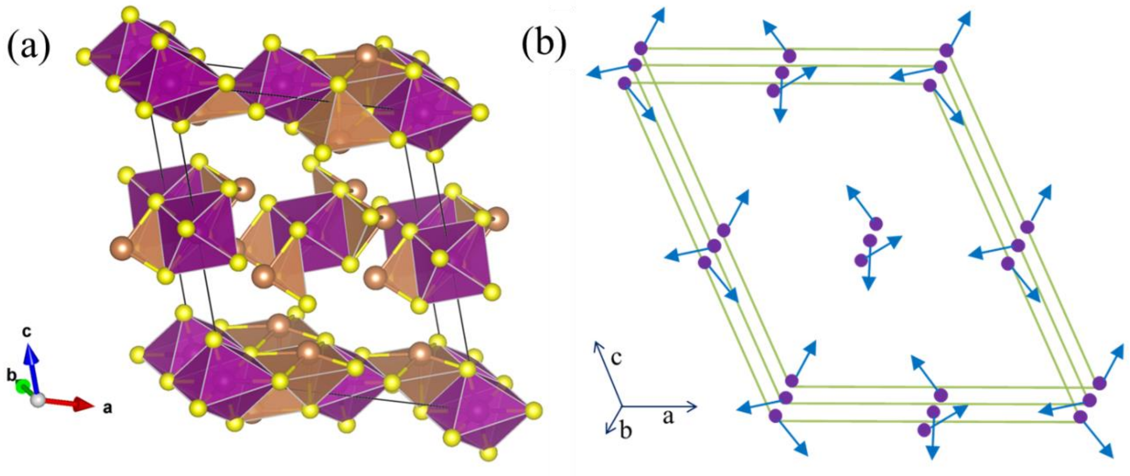

Figure 6.9 (a) Crystal structure of $MnSb_2S_4$ as obtained from the refinement. The yellow spheres represents sulfur. The purple and yellow color polyhedral are corresponding to the MnS_6 octahedra and SbS_5 square pyramid. The MnS_6 octahedra makes chain along *c*-axis and SbS_5 are interlinked to the chain making layers along *c*-axis. (b) Magnetic structure of Mn^{2+} ions drawn based on the reference.

Table 6.2 Structural parameters of $MnSb2S_4$ obtained from Rietveld refinement of X-ray diffraction data at room temperature. *Space group*: *C*2/m; *a* = 12.7329(6) Å, *b* = 3.79257(17) Å, *c* = 15.0483(7) Å, β = 113.867(2)°, Vol: 664.552(0.054)Å^3; χ^2 = 4.83; Bragg *R*-factor = 6.44 (%), R_f-factor = 9.87 (%).

Atom	Wyckoff position	*x*	*y*	*z*	B_{iso}(Å^2)	Occ.
Mn1	2a	0.00000	0.00000	0.00000	4.1(2)	0.5
Mn2	2a	0.00000	0.00000	0.50000	4.1(2)	0.5
Sb1	2a	0.3622(2)	0.00000	0.1325(2)	8.0(1)	1
Sb2	2a	0. 2359(3)	0.00000	0.3731(2)	8.0(1)	1
S1	2a	0. 3240(8)	0.00000	0. 9422(7)	5.4(2)	1
S2	2a	-0.0006(7)	0.00000	0.1580(6)	5.4(2)	1
S3	2a	0.3932(7)	0.00000	0.5487(7)	5.4(2)	1
S4	2a	0.8377(8)	0.00000	0.3279(6)	5.4(2)	1

6.2A.2.2 Magnetization and heat capacity

Figure 6.10 shows the temperature dependence of zero field cooled (ZFC) and field cooled (FC) magnetization at 100 Oe on the left axis and heat capacity divided by temperature on the right axis. The magnetization curve shows a maximum at 26 K indicating an antiferromagnetic transition. The magnetic behavior is similar to the earlier reported data, however, the monotonous decreasing trend of magnetization below the ordering temperature and the overlapping of ZFC and FC data compared to the earlier report suggest that there is no magnetic impurity present in our sample [42]. The linear fit of inverse molar susceptibility versus temperature data estimates the μ_{eff} value as 6.02 μ_B which is close to the theoretical value of Mn^{2+} ion moment (shown in the supplementary material). The obtained value of paramagnetic Curie temperature (θ_c) is -57 K and the calculated frustration parameter is $f = \left|\frac{\theta_c}{T_N}\right| \approx 2.5$ indicating the magnetism is moderately frustrated. The zero field heat capacity data (figure 6.10 right axis) shows two peaks ($T_{N1} = 25$ K and at $T_{N2} = 23.5$ K) that is in agreement with the previously reported data. At 7 T, the small peak at 25 K is suppressed and becomes a broad cusp. Considering the peak in dielectric constant and earlier report, the long range antiferromagnetic ordering occurs at 23.5 K. The magnetization *vs.* applied field recorded at various temperatures shows a nonlinear behavior below the ordering temperature such as 2 K, 10 K and 20 K and a linear behavior at 50 K (see inset of figure 6.10).

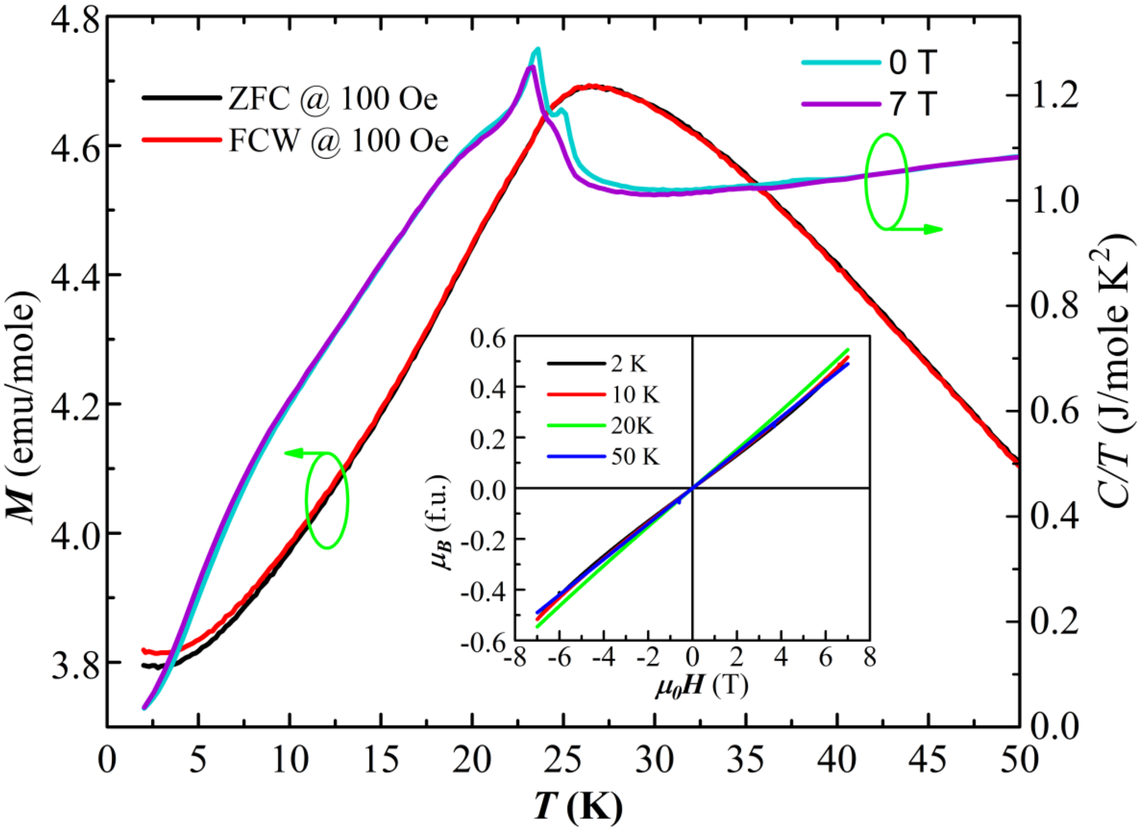

Figure 6.10 Left axis shows the temperature dependence of DC-magnetization measured under ZFC and FCW condition. Right axis shows the heat capacity divided by temperature data. Inset shows the *M*(*H*) curves measured at different temperatures.

6.2A.2.3 Dielectric property

The temperature dependence of the dielectric permittivity (ε) was measured in the absence and presence of magnetic field for both the parallel (H∥E) and perpendicular (H⊥E) configurations and shown in figure 6.11(a) and (b). A small kink type anomaly is evidenced near the magnetic ordering temperature 24 K in the absence of magnetic field. With the application of magnetic field, the anomaly becomes broad and diffusive suggesting a magnetodielectric effect. Moreover, the presence of dielectric anomaly at the magnetic ordering temperature indicates a possible ferroelectric transition concurrent with the magnetic ordering. The overall upturn feature of dielectric constant below 30 K may be related to evolution of magnetic moment of helical spin. A detailed temperature dependent magnetic structure determination is necessary to understand the dielectric behavior at low temperature.

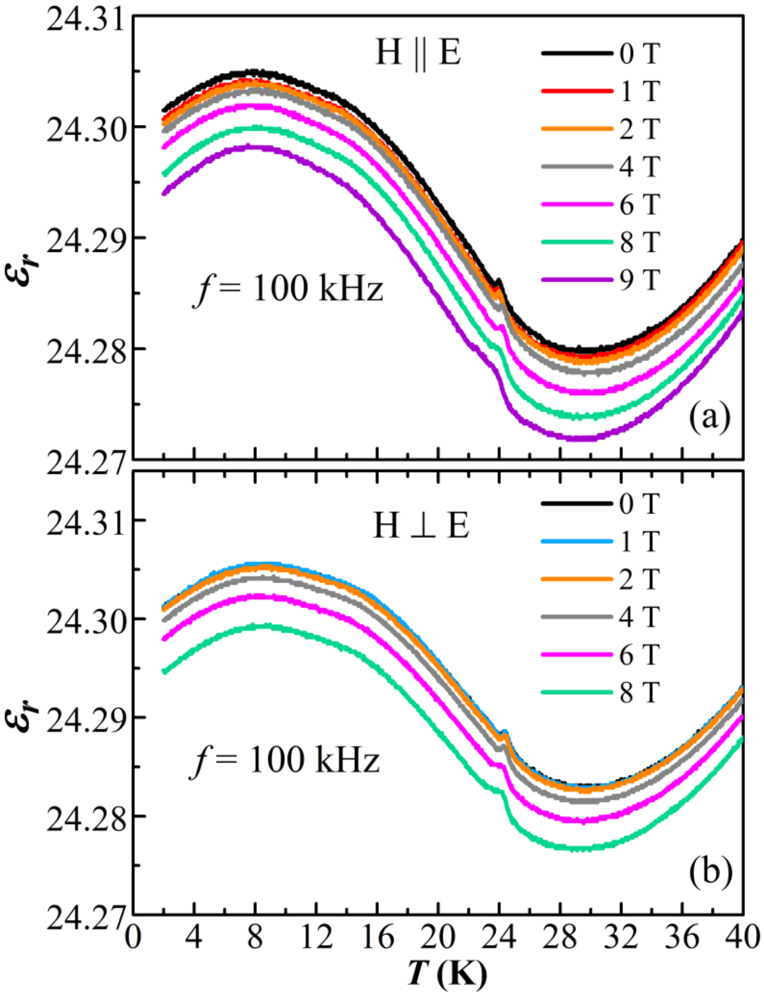

Figure 6.11 Temperature dependence of dielectric constant measured from 2 to 40 K at 100 kHz in presence of various magnetic field applied (a) parallel (b) perpendicular to the electric field.

6.2A.2.4 Ferroelectric polarization

The presence of a well-defined dielectric peak at the magnetic ordering temperature motivated us to perform the polarization measurements. In order to investigate the ferroelectric property we have poled the sample from 40 K to 2 K with E = 13 kV/cm and measured the pyroelectric current in the absence of electric field while warming the sample at 10 K/min rate. Like the dielectric measurement, the polarization is also measured in presence of magnetic field for both H||E and H⊥E configurations. A sharp asymmetric pyrocurrent peak was observed at the dielectric anomaly temperature in zero magnetic field. The polarization obtained from the pyrocurrent data for H||E and H⊥E are shown in figure 6.12(a) and (b), respectively.

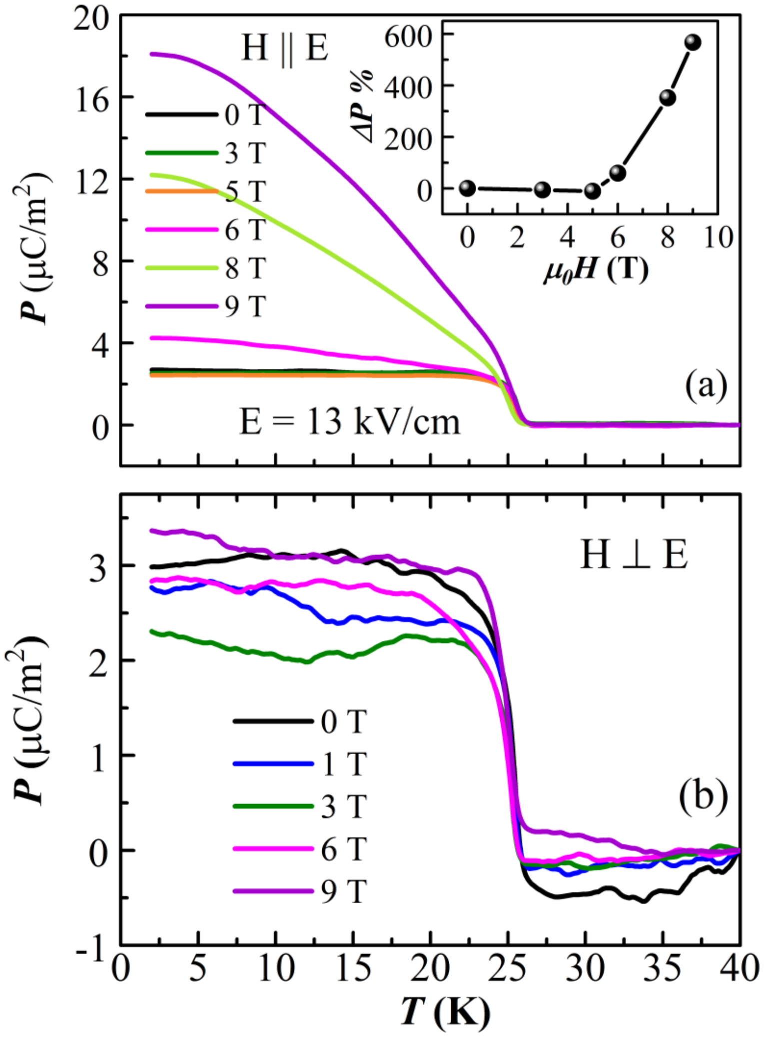

Figure 6.12 Temperature evolution of electric polarization after integrating the pyrocurrent recorded after poling the sample from 40 to 2 K under E = 13 kV/cm and various magnetic field (a) parallel and (b) perpendicular to the electric field. Inset shows the magnetic field variation of electric polarization under parallel configuration.

It should be mentioned that the polarization is switchable upon reversing the direction of electric field poling. Thus, the appearance of ferroelectric polarization at the magnetic ordering temperature indicates the spin induced ferroelectric polarization. The intrinsic nature of ferroelectric polarization is confirmed by the DC-biased current measurement where we see a consecutive polarization (positive) and depolarization (negative) peak at the ferroelectric ordering temperature while warming the sample in the presence of electric field as depicted in figure 6.13 [47].

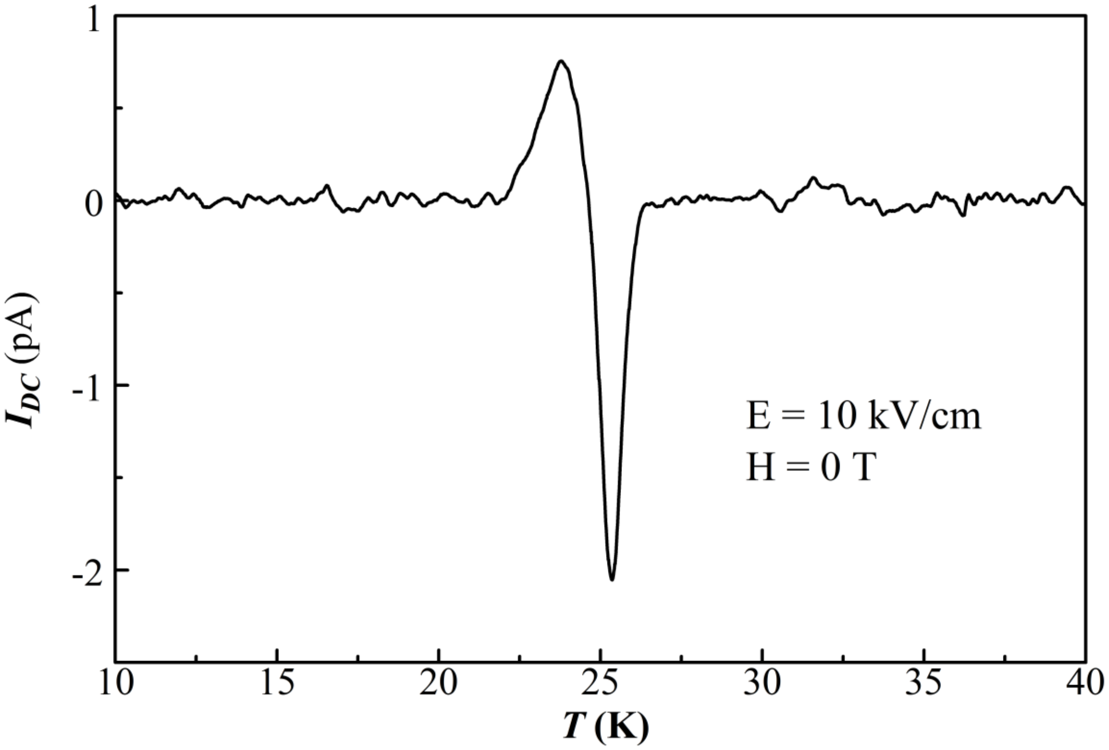

Figure 6.13 DC-bias current measured after cooling the sample to 2 K without applying any electric field and measured while heating the sample under an electric field of 10 kV/cm.

When magnetic field (H||E) is applied, a remarkable increase (~600%) of polarization is observed above a critical magnetic field of about 5 T. At $H < 5$ T field, the polarization remains almost constant. A similar increase in polarization was observed in $CuCrO_2$ multiferroic, but the enhancement of polarization is relatively low [35]. On the other hand, for H⊥E configuration the polarization slightly decreases for up to 3 T and revert to zero field value with further increasing field [35]. This large anisotropic behavior of polarization also confirms the spin-driven ferroelectricity in this material.

According to an earlier report, this compound shows an incommensurate magnetic structure with 1D propagation vector [0, 0.369, 0] which is unchanged down to lowest temperature (see figure 6.9(b)). The propagation vector was best fitted with a helicoidal model as mentioned in the introduction. In this spin texture, the polarization cannot be accounted by the spin-current model as well as exchange striction model. In 2007, T. Arima theoretically modeled a proper screw type spin structure towards the possibility of spin-driven ferroelectricity which was further extended by Jia *et al.* that the spin-orbit interaction contributes some modification on the d-p hybridization between ligand and 3d magnetic ions, which can cause the polarization along the bond direction and explained the ferroelectricity in the delafossite compounds $CuFe_{1-x}Al_xO_2$ [45, 46, 48], $ACrO_2$(A = Cu, Ag) with the proper screw and 120° rotation spin structure [35]. The spin-dependent d-p hybridization induced polarization can be written in a form of $P^{pd} \propto (S\,.\,e)^2 e$ with e being the vector from transition metal to ligand. In $MnSb_2S_4$, it has been shown theoretically, with an approximation of q = (0, 0.369, 0) incommensurate structure with the q = (0, 1/3, 0) commensurate, the magnetic frustration can produce the helical spin rotation along the b-axis [49]. Further, based on Berry phase calculation a ferroelectric polarization of 14 $\mu C/m^2$ has been predicted [49]. Therefore, we believe that the d-p hybridization may be responsible for the spin induced ferroelectricity in this material. A single crystal study would be beneficial to understand the origin of ferroelectricity and magnetoelectric effect. Also, a detailed neutron diffraction experiment in the ground state as well as under magnetic field is necessary to understand the magnetic field effect of polarization [39, 40, 50, 51]. A resonant soft x-ray measurement can also help to see the incommensurate orbital modulation at the Mn site which can confirm the validity of the magnetoelectric coupling in this material [52].

6.2B High pressure orthorhombic phase of $MnSb_2S_4$

We have also investigated $FeSb_2S_4$, which crystallize in $HgBi_2S_4$ type orthorhombic structure where the magnetic structure is very similar to the monoclinic $MnSb_2S_4$ type. Since distance between the adjacent FeS_6 octahedra layer is smaller compared to the $MnSb_2S_4$, the magnetic interaction strength is more in $FeSb_2S_4$ material. Because of this, the magnetic transition temperature is 50 K which almost double of the monoclinic $MnSb_2S_4$. Interestingly, $FeSb_2S_4$ also possesses similar proper screw type spin structure therefore we expect a multiferroic behavior in this compound as well. Hence we prepared $FeSb_2S_4$ and investigated the electrical properties. However, it is observed that this material is much more conductive compared to the $MnSb_2S_4$. In fact, at the lower temperature, the sample showed a Maxwell-Wagner type relaxation. Thus we could not see the intrinsic dielectric behavior at that temperature which might prevented to observe any magnetic spin induced dielectric anomaly. Further, the pyroelectric current showed a broad symmetric peak around 50 K corresponding to the thermally stimulated free charge carriers which is described in chapter 3 in details. Therefore we could not get any evidence of multiferroic behavior although it is expected.

Applying high-pressure, we could stabilize the orthorhombic polymorph of $MnSb_2S_4$. Interestingly, we see a magnetism induced multiferroic behavior in addition to the three successive magnetic transitions. Further, we observed a large dielectric anomaly above the magnetic ordering temperature which could be due to structural transition. In this section, we have presented the detailed results on orthorhombic polymorph of $MnSb_2S_4$.

6.2B.1 Experimental details

The as-synthesized monoclinic $MnSb_2S_4$ powder sample was sealed in gold capsule and pressed to 4.5 GPa using anvil type high-pressure apparatus. Once the pressure reached, the temperature was increased to 500 °C and kept for 1 h dwelling followed by quenching to room temperature and slowly reducing the pressure. The obtained sample was grey in color and well-sintered pellet. The sample was characterized by using powder x-ray diffraction pattern. The magnetic and electrical properties were measured similarly as performed in monoclinic $MnSb_2S_4$ in the previous section.

6.2B.2 Results and discussions

6.2B.2.1 Structure

The powder XRD pattern along with Rietveld refinement using orthorhombic *Pnam* space group is shown in figure 6.14. Except for Sb_2S_3, we did not find any other impurities in the sample. Therefore, we assume that the whole monoclinic phase has converted to the orthorhombic phase while Sb_2S_3 impurity remained as present before in the precursor sample. Importantly, Sb_2S_3 is a non-magnetic specimen and does not influence the properties of the main phase. The obtained structure is shown in figure 6.15.

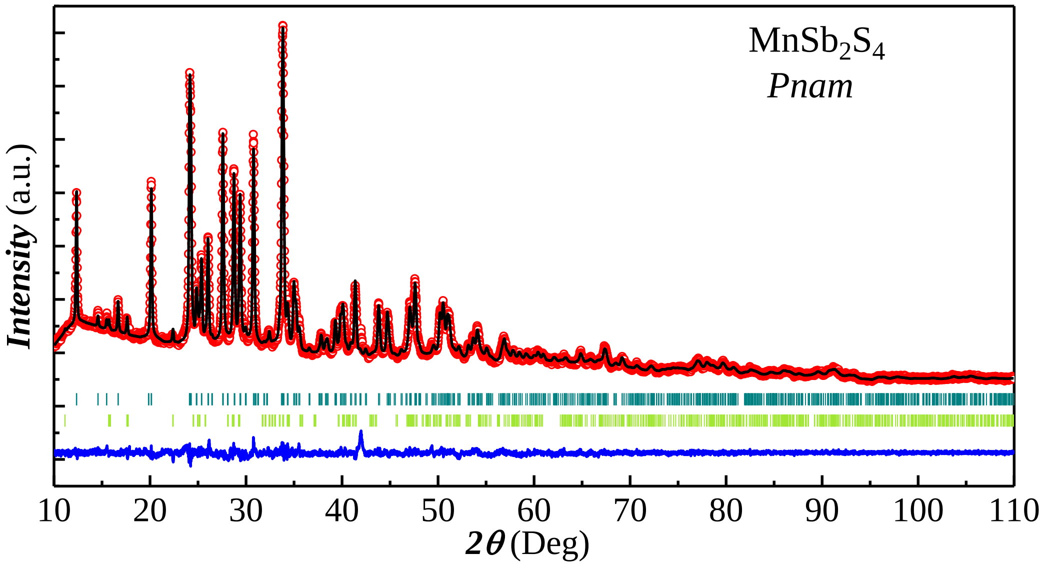

Figure 6.14 P-XRD pattern along with Rietveld refinement using *Pnam* space group in high-pressure phase of $MnSb_2S_4$.

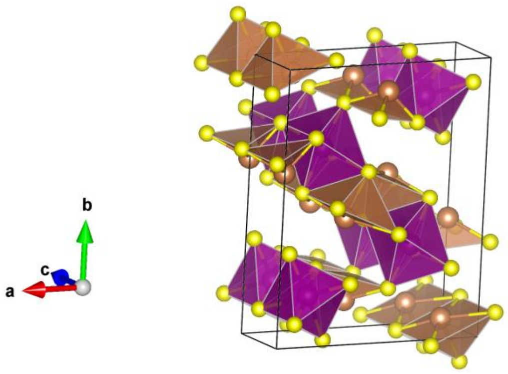

Figure 6.15 Crystal structure of high-pressure orthorhombic phase of $MnSb_2S_4$ as obtained from the refinement. The yellow spheres represent sulfur. The purple and yellow color polyhedra are corresponding to the MnS_6 octahedra and SbS_5 square pyramid. The MnS_6 octahedra make chain along *c*-axis.

6.2B.2.2 Magnetic properties

Figure 6.16(a) shown temperature dependent DC magnetization under ZFC, FCC and FCW conditions with 100 Oe field. The first magnetization anomaly is observed near 34 K which can be seen in the inset of magnified temperature region. Although this step like anomaly could be an indication of antiferromagnetic ordering, the splitting in the ZFC is suggesting a canted weak ferromagnetic behavior. The second large step-like anomaly in the FCC and FCW curve is observed below 15 K which could be an indication of weak ferromagnetic however the large bifurcation of ZFC curve below 13 K further suggesting a possible spin-glass or cluster glass ordering.

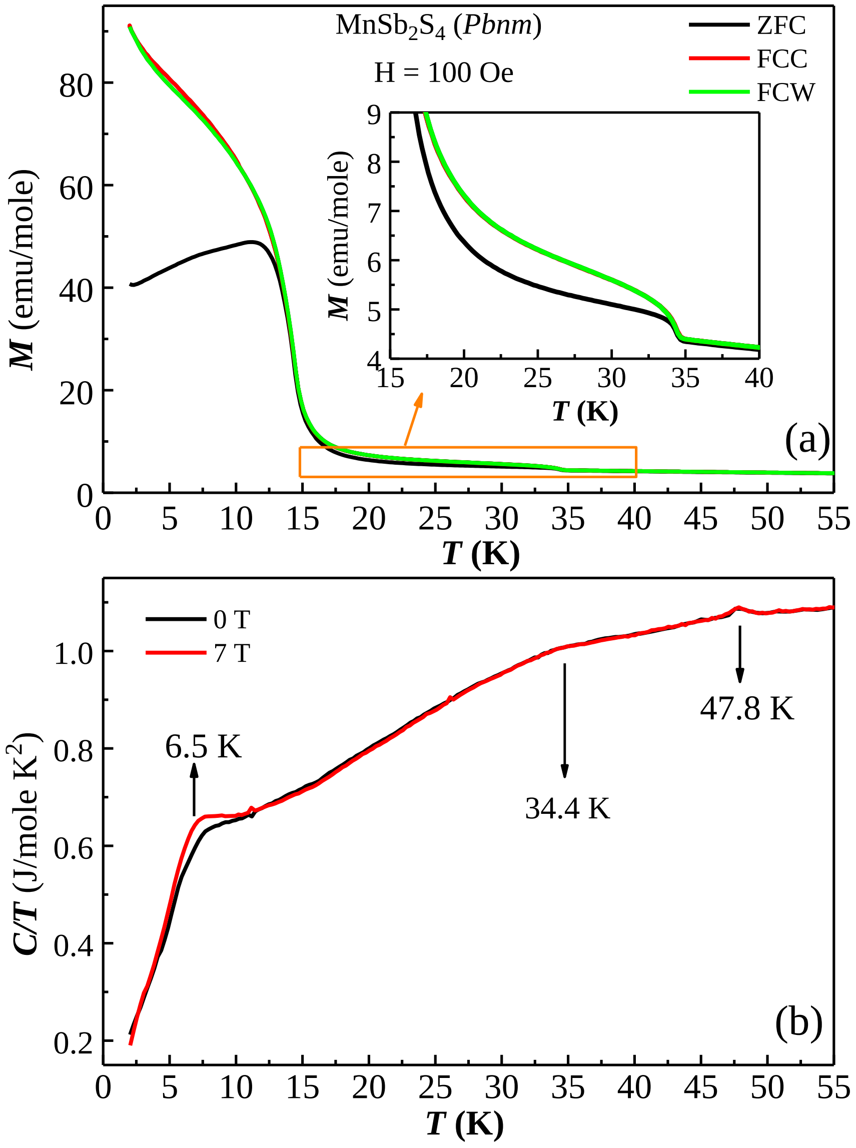

Figure 6.16 (a) DC magnetization *vs.* temperature data recorded from 2 to 300 K under ZFC, FCC and FCW conditions with 100 Oe field. (b) Heat capacity data measured under zero magnetic field as well as 7 T magnetic field in the temperature range of 2 to 55 K.

The thermal hysteresis of magnetization among ZFC and FCC/FCW in the range of 15 to 35 K can also be an indication of a short-range magnetic interaction. However, we could not see any indication of spin-glass feature in the memory experiment of the magnetization below that temperature. Further, in the heat capacity data, we do not observe any peak associated with the magnetization anomaly, except a broad hump near 34 K. (figure 6.16(b)). Most interestingly, a typical peak like anomaly is present in the heat capacity at around ~6.5 K which is an indication of long-range magnetic ordering which could not be noticed in the magnetization curves except a small change in the curvature at the same temperature in the ZFC curve. With the applied magnetic field (7 T) the peak becomes more pronounced indicating that magnetic field favors the long-range magnetic ordering. All these results suggest that this orthorhombic polymorph of $MnSb_2S_4$ has more rich magnetic phases as compared to the monoclinic one. Most strikingly, a tiny anomaly can be noticed at ~47.8 K in the heat capacity data (figure 6.16(b)) which is well above the magnetic ordering. Therefore this anomaly can be associated with some structural distortions which have been looked at further in the next section.

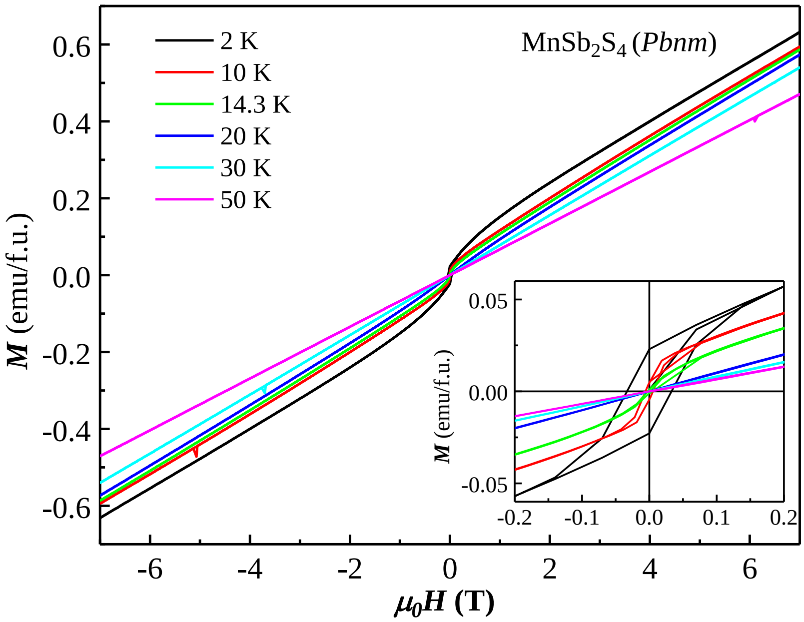

Figure 6.17 *MH* loop measured at 2, 10, 14.3, 20, 30 and 50 K. The inset shows the magnified region near the origin.

The Curie-Weiss fitting in the paramagnetic range 150 to 300 K gave the very close value of μ_{eff} to the monoclinic phase of $MnSb_2S_4$ which further indicates the absence of any magnetic impurity in the sample. Further, we have looked at isothermal magnetization at various temperatures in between the magnetic transitions as shown in figure 6.17. A linear *M*(*H*) curve is observed at 30 K and 20 K. The *M*(*H*) loop at 2 K and 10 K showed weak ferromagnetic type loop where the moment and coercive field is higher at 2 K. At 14.3 K; a bending can be noticed which is an indication of the appearance of the weak ferromagnetic component in the sample below the second magnetic transitions. At low temperature below 6 K, the spins order in long-range scale which can be either AFM or can be a similar helical spin ordering as observed in the monoclinic (*C*2/*m*) phase of $MnSb_2S_4$. All these results motivated us to perform the electrical measurements in this orthorhombic phase.

6.2B.2.3 Dielectric property

At first, we have recorded the dielectric constant from 2 K to 300 K at 1 K/min warming rate with various frequencies and shown the data only in the range of 2 to 80 K in figure 6.18. At a first glance we can see two distinct dielectric anomaly one at near 6.5 K where we observed a heat capacity anomaly and a broad magnetic anomaly. Another anomaly at ~48 K is concomitant with the heat capacity anomaly, well above the magnetic ordering.

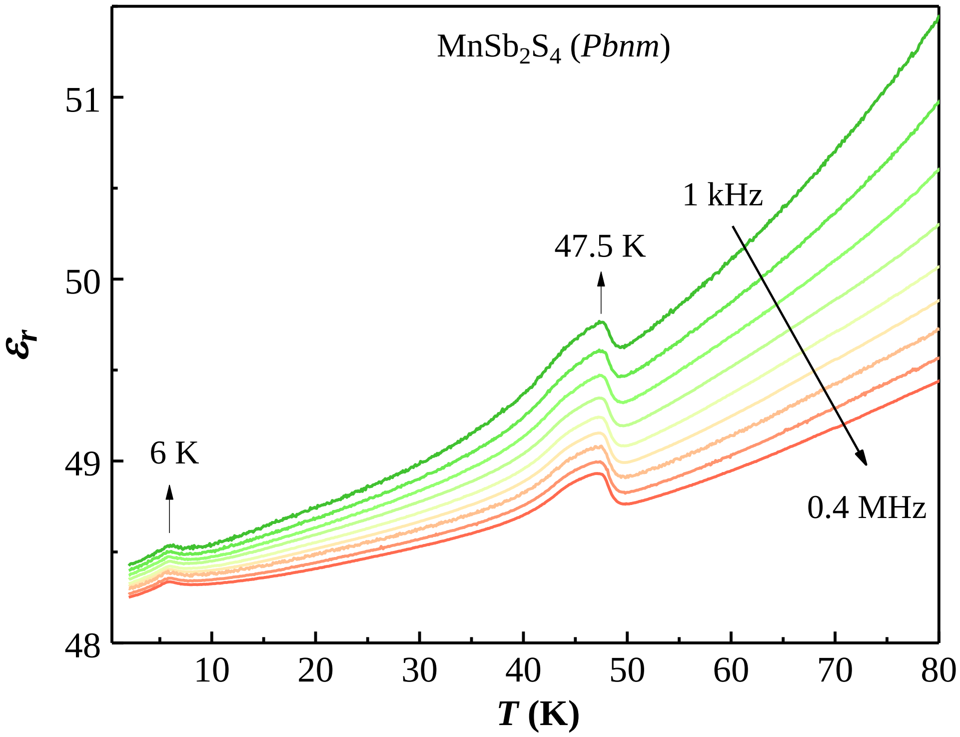

Figure 6.18 Dielectric constant recorded from 2 K to 80 K while warming with 1 K/min at various frequencies in orthorhombic $MnSb_2S_4$.

It is interesting to note that although frequency dispersion is present in the dielectric for the whole temperature range, indicating a relaxation behavior, none of the peak shifts with the frequencies. Therefore it is expected that both the anomaly has intrinsic origin to the sample where the first peak at 47.8 K indicates structural distortions and the second peak near 6.5 K has an origin in the magnetic spin ordering.

In order to get further insights to the anomalies, we have recorded the dielectric constant while warming and cooling the sample at different magnetic field and showed individually in two different graph in figure 6.19(a and b). We can see that the anomaly at 6 K has nominal changes with the applied magnetic field while there is no thermal hysteresis of cooling and warming data. This further confirms the magnetic origin of the dielectric anomaly. On the other hand, at 48 K, the dielectric anomaly showed a clear thermal hysteresis for cooling and warming the sample while no change with magnetic field. This further suggests a reversible structural distortion occurring above the magnetic ordering. Therefore, it is necessary to perform X-ray diffraction study below and above this transition temperature in order to know the structural details at low temperature. Since the dielectric anomaly is an indication of ferroelectric polarization we have looked at the pyroelectric current in the sample across both the dielectric anomalies.

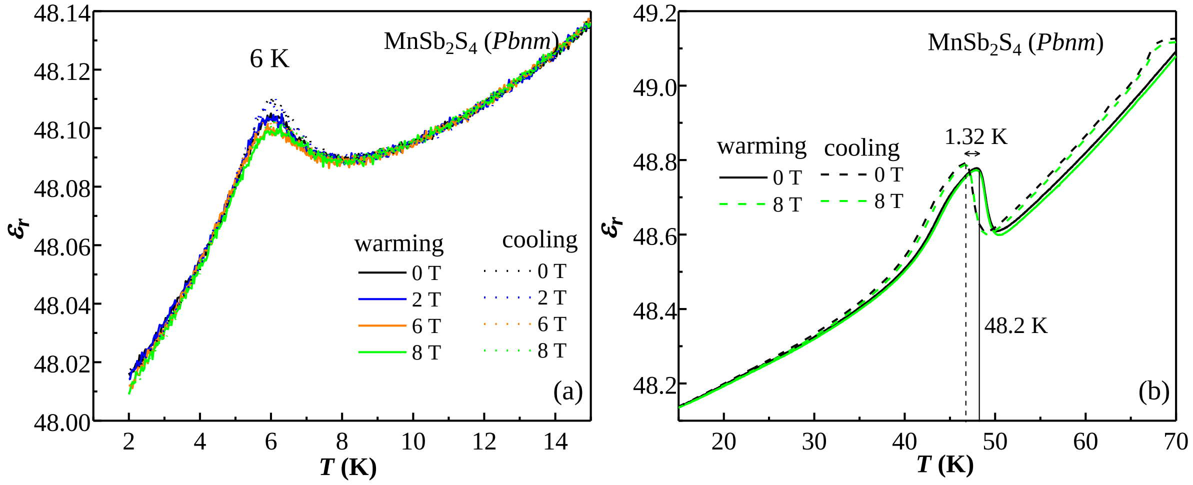

Figure 6.19 dielectric constant measured at 100 kHz while warming and cooling under various magnetic field in orthorhombic $MnSb_2S_4$ (a) 2 K to 15 K (b) 15 K to 70 K.

6.2B.2.4 Ferroelectric polarization

While performing the pyrocurrent measurements we found that this sample has considerable high electrical conductivity compared to the monoclinic phase. It is interesting to notice a higher conductivity in the different polymorph of $MnSb_2S_4$. It is a challenging issue to find any ferroelectric polarization in higher conducting sample as we had experienced in $FeSb_2S_4$. We attempted to record the pyrocurrent across both the dielectric anomaly temperature in high-pressure phase of $MnSb_2S_4$. However the conductivity near 48 K is considerable high which gives a very high leakage current therefore we could not be assured to argue the presence or absence of ferroelectric polarization at this temperature. Yet, at low temperature we indeed observed pyrocurrent peak around 6 K indicating a ferroelectric state below the magnetic transition. The integrated polarization is shown in figure 6.20 obtained for various magnetic field (H||E). The value of polarization is very close to the monoclinic phase except the dramatic increase of polarization under magnetic field. It should be mentioned here that the polarization under magnetic field perpendicular to the electric field was found to be almost same therefore we have not shown here. It is possible that the ferroelectric polarization in this orthorhombic phase at lower temperature magnetic transition has a different mechanism which cannot be understood without a detailed magnetic spin structure study.

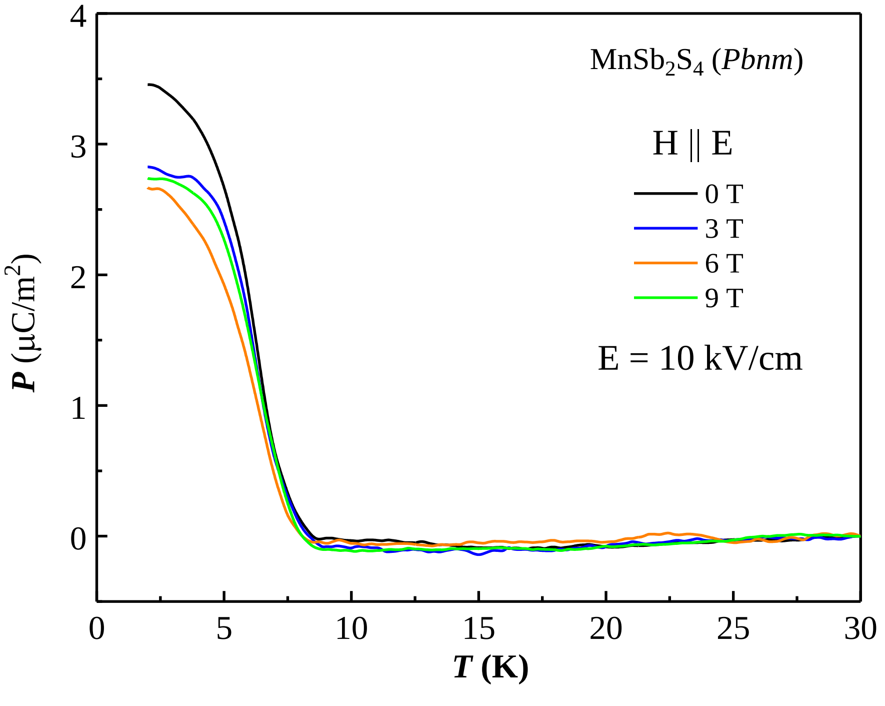

Figure 6.20 Ferroelectric polarization obtained from the pyrocurrent data measured across 6 K in orthorhombic $MnSb_2S_4$.

6.2B.3 Conclusions

In conclusion, a spin-driven ferroelectric polarization is observed in a centrosymmetric monoclinic $MnSb_2S_4$. Under magnetic field five-fold enhancement of polarization is observed demonstrating a large magnetoelectric coupling. Based on the unusual helical spin ordering, the *d-p* hybridization mechanism has been suggested to be responsible for the microscopic origin of ferroelectric polarization. The finding of spin-induced ferroelectricity in this non-oxide material indicates the importance of helicoidal spin structure for the discovery of new multiferroics.

On the other hand, three successive magnetic transitions are observed in orthorhombic polymorph of $MnSb_2S_4$ mineral. First, two anomalies, 34 K and 15 K does not produce any dielectric anomaly while the lowest magnetic ordering 6 K induces a ferroelectric polarization along with a concomitant dielectric anomaly. Besides, a comparatively large dielectric anomaly has been found near 48 K, corresponding to a possible reversible structural distortion. The detailed magnetic spin structure corresponding to the ferroelectric behavior and the detailed structural details for the possible distortions is necessary in order to elucidate the multiferroic character in this high-pressure polymorph of $MnSb_2S_4$.

References

[1] Y.-H. Chu *et al.*, Nat. Mater. **7**, 478 (2008).

[2] N. A. Spaldin and M. Fiebig, science **309**, 391 (2005).

[3] S. Wu, S. A. Cybart, P. Yu, M. Rossell, J. Zhang, R. Ramesh, and R. Dynes, Nat. Mater. **9**, 756 (2010).

[4] J. Wang *et al.*, science **299**, 1719 (2003).

[5] A. A. Belik, J. Solid State Chem. **195**, 32 (2012).

[6] S. Niitaka, M. Azuma, M. Takano, E. Nishibori, M. Takata, and M. Sakata, Solid State Ion. **172**, 557 (2004).

[7] J. Zylberberg, A. A. Belik, E. Takayama-Muromachi, and Z.-G. Ye, Chem. Mater. **19**, 6385 (2007).

[8] M. Gajek, M. Bibes, A. Barthélémy, K. Bouzehouane, S. Fusil, M. Varela, J. Fontcuberta, and A. Fert, Phys. Rev. B **72**, 020406 (2005).

[9] N. A. Hill, J. Phys. Chem. B **104**, 6694 (2000).

[10] C. Ederer and N. A. Spaldin, Phys. Rev. B **71**, 060401 (2005).

[11] I. Dzyaloshinsky, J. Phys. Chem. Solids **4**, 241 (1958).

[12] X. X. Shi, X. Q. Liu, and X. M. Chen, Adv. Funct. Mater. **27** (2017).

[13] S.-T. Zhang, Y. Zhang, M.-H. Lu, C.-L. Du, Y.-F. Chen, Z.-G. Liu, Y.-Y. Zhu, N.-B. Ming, and X. Pan, Appl. Phys. Lett. **88**, 162901 (2006).

[14] D. Wang, W. Goh, M. Ning, and C. Ong, Appl. Phys. Lett. **88**, 212907 (2006).

[15] Y. Wang and C.-W. Nan, Appl. Phys. Lett. **89**, 052903 (2006).

[16] D. Kan, L. Pálová, V. Anbusathaiah, C. J. Cheng, S. Fujino, V. Nagarajan, K. M. Rabe, and I. Takeuchi, Adv. Funct. Mater. **20**, 1108 (2010).

[17] A. A. Belik, T. Wuernisha, T. Kamiyama, K. Mori, M. Maie, T. Nagai, Y. Matsui, and E. Takayama-Muromachi, Chem. Mater. **18**, 133 (2006).

[18] P. Baettig, C. F. Schelle, R. LeSar, U. V. Waghmare, and N. A. Spaldin, Chem. Mater. **17**, 1376 (2005).

[19] H. Yusa, A. A. Belik, E. Takayama-Muromachi, N. Hirao, and Y. Ohishi, Phys. Rev. B **80**, 214103 (2009).

[20] R. Mangalam, S. Bhat, A. Iyo, Y. Tanaka, A. Sundaresan, and C. Rao, Solid State Commun. **146**, 435 (2008).

[21] M. Guennou, P. Bouvier, G. S. Chen, B. Dkhil, R. Haumont, G. Garbarino, and J. Kreisel, Phys. Rev. B **84**, 174107 (2011).

[22] Y. Wu, X. Han, and H. Huang, J. Phys. Chem. C (2018).

[23] J. Lu *et al.*, Eur. Phys. J. B **75**, 451 (2010).

[24] T. Yamaguchi, J. Phys. Chem. Solids **35**, 479 (1974).

[25] C. De, A. K. Nayak, M. Nicklas, and A. Sundaresan, Appl. Phys. Lett. **111**, 182403 (2017).

[26] S. Redfern, C. Wang, J. Hong, G. Catalan, and J. Scott, J. Phys. Condens. Matter **20**, 452205 (2008).

[27] D. Lebeugle, D. Colson, A. Forget, M. Viret, P. Bonville, J. F. Marucco, and S. Fusil, Phys. Rev. B **76**, 024116 (2007).

[28] J. Scott, J. Phys. Condens. Matter **20**, 021001 (2007).

[29] J. Scott and J. Gardner, Materials Today, https://doi.org/10.1016/j.mattod.2017.12.003 (2018).

[30] M. Fukunaga and Y. Noda, J. Phys. Soc. Jpn. **77** (2008).

[31] S. M. Feng, Y. S. Chai, J. L. Zhu, N. Manivannan, Y. S. Oh, L. J. Wang, Y. S. Yang, C. Q. Jin, and K. H. Kim, New J. Phys. **12** (2010).

[32] C. De, T. H. Kim, K. H. Kim, and A. Sundaresan, Phys. Chem. Chem. Phys. **16**, 5407 (2014).

[33] M. Collins and O. Petrenko, Can. J. Phys. **75**, 605 (1997).

[34] T.-h. Arima, J. Phys. Soc. Jpn. **76**, 073702 (2007).

[35] S. Seki, Y. Onose, and Y. Tokura, Phys. Rev. Lett. **101**, 067204 (2008).

[36] T. Kurumaji, S. Seki, S. Ishiwata, H. Murakawa, Y. Tokunaga, Y. Kaneko, and Y. Tokura, Phys. Rev. Lett. **106**, 167206 (2011).

[37] M. Kenzelmann *et al.*, Phys. Rev. Lett. **98**, 267205 (2007).

[38] H. Murakawa, Y. Onose, K. Ohgushi, S. Ishiwata, and Y. Tokura, J. Phys. Soc. Jpn. **77**, 043709 (2008).

[39] S. Seki, X. Yu, S. Ishiwata, and Y. Tokura, Science **336**, 198 (2012).

[40] E. Ruff, S. Widmann, P. Lunkenheimer, V. Tsurkan, S. Bordács, I. Kézsmárki, and A. Loidl, Sci. Adv. **1**, e1500916 (2015).

[41] K. Singh, A. Maignan, C. Martin, and C. Simon, Chem. Mater. **21**, 5007 (2009).

[42] P. Léone, C. Doussier-Brochard, G. André, and Y. Moëlo, Phys. Chem. Miner. **35**, 201 (2008).

[43] S. F. Matar, R. Weihrich, D. Kurowski, A. Pfitzner, and V. Eyert, Phys. Rev. B **71**, 235207 (2005).

[44] A. Pfitzner and D. Kurowski, Z. Kristallog. – Cryst. Mater. **215**, 373 (2000).

[45] T. Kimura, J. Lashley, and A. Ramirez, Phys. Rev. B **73**, 220401 (2006).

[46] S. Seki, Y. Yamasaki, Y. Shiomi, S. Iguchi, Y. Onose, and Y. Tokura, Phys. Rev. B **75**, 100403 (2007).

[47] C. De, S. Ghara, and A. Sundaresan, Solid State Commun. **205**, 61 (2015).

[48] T. Nakajima, S. Mitsuda, S. Kanetsuki, K. Tanaka, K. Fujii, N. Terada, M. Soda, M. Matsuura, and K. Hirota, Phys. Rev. B **77**, 052401 (2008).

[49] C. Tian, C. Lee, E. Kan, F. Wu, and M.-H. Whangbo, Inorg. chem. **49**, 10956 (2010).

[50] J.-W. G. Bos, C. V. Colin, and T. T. Palstra, Phys. Rev. B **78**, 094416 (2008).

[51] K. H. Miller, X. S. Xu, H. Berger, E. S. Knowles, D. J. Arenas, M. W. Meisel, and D. B. Tanner, Phys. Rev. B **82**, 144107 (2010).

[52] Y. Tanaka *et al.*, Phys. Rev. Lett. **109**, 127205 (2012).

Chapter 7

Magnetoelectric effect in frustrated spinel $CoAl_2O_4$*

Summary

The ground state of $CoAl_2O_4$ material has been a long time controversial issue due to the fact that the ratio of nearest neighbor interactions (J_1) among the inter FCC lattices and next nearest neighbor interaction in the intra FCC lattice (J_2) inhabits to the close boundary between spiral spin-liquid ground state and the long-range antiferromagnetic ordering. Here, we observe the magnetoelectric effect in $CoAl_2O_4$ single crystal which suggests that the magnetic ground state could be towards long-range antiferromagnetic ordering of Co^{2+} ions. From the value of polarization ratio P||(1-10) measured while magnetic field applied along H||(1-10) and H||(001), we propose that the magnetic easy-axis can be along (111). Single ion contribution of the magnetic ions located at the non-centrosymmetric environment is responsible for the magnetoelectric effect similar to that observed in other A-site magnetic spinel oxides Co_3O_4 and MnB_2O_4 (B = Al, Ga).

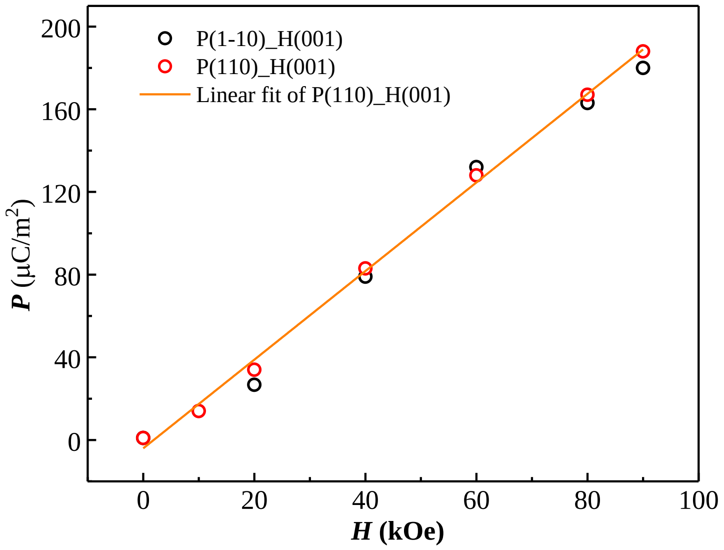

Paper based on this work **C. De** *et al.* manuscript under preparation (2018).

7.1 Introduction

The frustrated spin systems have come to the frontiers of the current research because of their exotic physical states such as spin-glass, spin-liquid, spin-ice, cluster of spins, heavy fermion like behavior of spins, *etc.* [1-5]. The spinel system having formula unit AB_2X_4 is one of the most conversant magnetic compounds where both A and B are metal cations with A and B having magnetic character and X is an anion [6, 7]. In this chemical unit cell, B-site forms corner-sharing octahedra with a pyrochlore structure which is subjected to have a strong geometrical frustration. On the other hand, A-site forms a diamond lattice which is bipartite consisting of two face-centered cubic lattice interpenetrated with each other [1] where the intriguing magnetic interactions and their consequences are remarkable. In 1964, there was a systematic study for spinel system with A = Co^{2+}, Mn^{2+} and Fe^{2+} and B = Al^{3+}, Co^{3+} in order to understand the kind of magnetic ordering depending on the A-site magnetic ions and B-site nonmagnetic ions [6]. It has been found that there is a magnetic frustration arises to the A-site depending on the magnetic ions present at the A-site as well as non-magnetic ions at the B-site. For example, Mn^{2+} shows a long-range antiferromagnetic ordering, Co^{2+} shows a very weak magnetic correlation at very low temperature below 4 K whereas for Fe, there is no long-range ordering even below mK temperature when the B-site is filled by Al^{3+} ions in all the compounds. On the other hand in Co_3O_4, for Co^{3+} ion at the B-site, Co^{2+} makes a long-range ordering above 30 K. This was explained based on the interaction path of A-X-B-X-A in the diamond lattice where two antiferromagnetic interactions are significant, namely, nearest neighbor J_1 (among the two FCC lattices) and next nearest neighbor J_2 (in one FCC lattice among the corner and face-centered lattice). This can be visualized in the model structure shown in figure 7.1 [8].

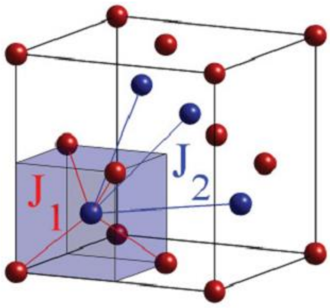

Figure 7.1 The cubic diamond lattice, where two fcc sublattices are interpenetrated with position (0 0 0) and (¼ ¼ ¼) along (111), with the two exchange interactions J_1 and J_2. (Adapted with permission from Ref. [8])

Considering this model, Bergman *et al.* have theoretically proposed a highly degenerate set of classical coplanar spirals-spin-liquid state whose propagation wave vectors form a continuous surface in momentum space for $J_2/J_1 > 1/8$ [1]. This model explains well for the long-range antiferromagnetic ordering in $MnAl_2O_4$ and Co_3O_4 where the J_2/J_1 is less than 1/8. On the other hand, a spiral-spin-liquid state were evidenced in $MnSc_2S_4$ with $J_2/J_1 \sim 0.85$. However, for $CoAl_2O_4$, J_2/J_1 is very close to 1/8 hence the ground state magnetism becomes ambiguous, whether it has a long range AFM ordering, spiral-spin-liquid state or a spin-glass state [8-12]. Apart from the frustrated magnetic interaction, another crucial factor in the $CoAl_2O_4$ material is the cation inversion ratio [8]. The cation inversion among the Co^{2+} and Al^{3+} ions seems to be unavoidable up to certain limit thus makes this system more complicated. The degree of inversion parameter is usually defined by x in the formula $[\mathrm{Co}_{1-x}\mathrm{Al}_x][\mathrm{Al}_{2-x}\mathrm{Co}_x]\mathrm{O}_4$. The x value mainly depends on the sample preparation conditions [10]. Considering a minimal inversion parameter, this A-site frustrated magnetic spinel $CoAl_2O_4$ were demonstrated to a realization of spiral-spin-liquid ground state [8]. An evidence came from a single crystal neutron scattering experiments which showed an unconventional magnetic state below a magnetic transition ~8 K. The magnetic Bragg peaks were broad and their line shapes were observed to have strong Lorentzian contributions. Thus, the observed short-range magnetic correlations were explained by the spiral-spin-liquid model [8]. Further, by the same authors, an unconventional magnetic state had been attributed in $CoAl_2O_4$ again using a single crystal study and raised an another intriguing fact that the microstructure, specifically [111] twin boundaries also could be responsible for the unusual magnetism in an addition to the next-nearest-neighbor interaction for the frustration [12]. The arguments became more intriguing when another group, based on single crystal neutron scattering, classified $CoAl_2O_4$ as a kinetically inhabited antiferromagnet where the long range correlation of magnetic ground states would be blocked by the freezing of domain-wall motion below an unusual magnetic phase transition at $T^*=6.5$ K [13]. This was further supported by another single crystal study which showed an unchanged spin correlations between $T = 2$ K and 250 mK and that was consistent with the frozen magnetic ground state. In fact with the comparable study on the spinel $MnAl_2O_4$ which had a clear antiferromagnetic phase transition below 39 K in spite of being prone to the cation inversion, the authors showed that $CoAl_2O_4$ is an unique case where the effect of next-nearest-neighbor exchange interaction has rather primary effect than the cation inversion [14]. The spiral-spin-liquid state was supported by another study varying the cation inversion with different heat treatment of the sample [10]. A spin-glass state was also derived in this compound for higher cation inversions $x \geq 0.101$ [10]. Concurrently, B. Roy *et al.* had reported a long range correlation at the low temperature for the minimum cation inversion sample studying through NMR and a neutron diffraction experiments which led them to propose magnetic easy axis to be along (100) direction. Very recently S. Ghara *et al*. has reported the magnetic ground state as long range antiferromagnetic ordering from a magnetoelectric study in polycrystalline materials with the minimum site inversion parameter of x~0.05 [15]. However a genuine magnetic ground state as well a magnetic easy axis determination still has to be derived from a single crystal study with a caution of site inversion parameter in the growth process which itself would be a challenging task.

Therefore, in order to elucidate the above scenario, here, we have grown the high-quality single crystal of $CoAl_2O_4$ using floating zone technique with a special attention to the cation disorder. By examining the dielectric and pyroelectric properties along various crystallographic directions, we confirm the existence of magnetoelectric effect in the high quality low disordered $CoAl_2O_4$ sample. From a comparison of polarization observed under magnetic field along certain directions and calculated symmetry allowed polarization ratio obtained under magnetic field along those directions, we propose the easy axis to be along (111).

7.2 Experiments

Powder sample of $CoAl_2O_4$, prepared via conventional solid-state route using Al_2O_3 and Co_3O_4 with 0, 5, 10 and 15% excess of Co_3O_4 were used for different single crystal growth varying the parameters in order to compensate the significant loss of the Co during the crystal growth using floating zone furnace. The powder synthesis was performed at 1000 °C for 12 h and 1100 °C for 24 h. Finally, the sample was heated at 1100 °C for 24h and cooled to room temperature with 0.5 °C/min. Nearly 8 cm rods were made from the synthesized powder using hydrostatic pressure for the different excess of Co_3O_4 and sintered at 1150 °C for 24 h and cooled to room temperature with 0.5 °C/min rate. The crystals were grown using a four-mirror type infrared image furnace (Crystal System FZ-T-10000-H-III-VPR) equipped with four 1 kW halogen lamp with the following growth conditions. For the individual excess Co_3O_4 containing sintered rod, the growth speed was varied from 1 mm/h to 6 mm/h to obtain the possible lowest disordered crystal. The feed and seed rods were kept at 20 rpm rotated in opposite directions for all the crystal growth. A mixture of Ar and O_2 flow with 95:5 ratios was used for all the crystal growth motivated by the previous crystal growth procedure in this sample [16]. Nearly 5 cm long crystals were obtained for each growth of different excess Co_3O_4 containing samples. Crystal homogeneity was confirmed by optical microscopy under polarized light and scanning electron microscopy (Zeiss Ultra Plus, Germany). The lowest disordered sample was found with the 10% excess of Co_3O_4. Further, the crystal was annealed at 1050 °C for 2 days and finally cooled to room temperature with 6 °C/h rate. The crystals were oriented and cut into a cubic shape with planes along the (001), (110) and (1-10) with a dimension of about 2 mm × 2 mm × 2 mm which was used for the magnetic measurements. For electrical measurement, the samples were further cut into thin square plates with the dimension of 2 mm × 2 mm × 0.5 mm for all the three (001), (110) and (1-10) directions while keeping the remaining orthogonal direction as the arms of the sample. Magnetic measurements were performed in Superconducting Quantum Interference Device magnetometer (Quantum Design MPMS-4). Electrical measurements were performed using Agilent E4980A Precision LCR meter and Keithley Electrometer (6517A) in PPMS. Electrical contacts were made using silver paste (PELCO High-Performance Silver Paste). Heat capacity was measured in PPMS.

7.3 Results and discussions

7.3.1 Structural data

The annealed crystal was crashed into powder and the powder X-ray diffraction pattern was recorded at room temperature which shows a single phase *Fd*-3*m* structure. From the refinement, the lattice parameter is obtained as 8.10 Å, which is very close to the previously reported value (figure 7.2). The as-grown crystal having metallic luster with ~5.5 mm diameter and over 2 cm in length is shown in figure 7.3(c). The Laue diffraction spots for (110) and (001) direction and a cubic geometry cut sample with the (110), (1-10) and (001) orthogonal direction is shown in figure 7.3(a, b and c) respectively. The cubic geometry sample was used for the magnetic measurements and the plate-shaped samples were used for the electrical measurements. The schematic 7.3(d) shows the various orthogonal directions in the cubic crystal.

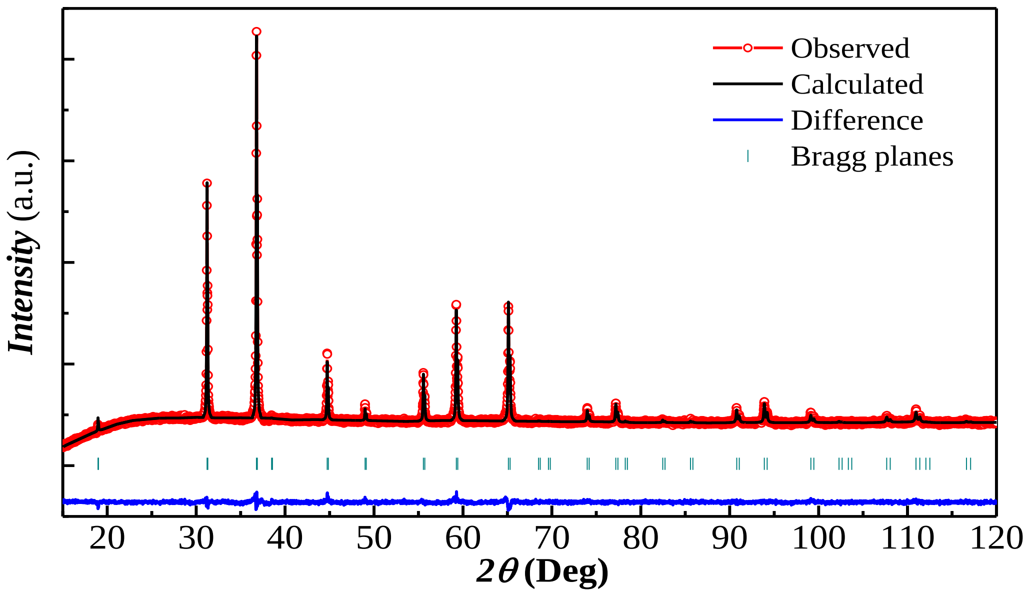

Figure 7.2 Powder X-ray diffraction pattern along with Rietveld refinement at room temperature in $CoAl_2O_4$ obtained from the crushed crystal.

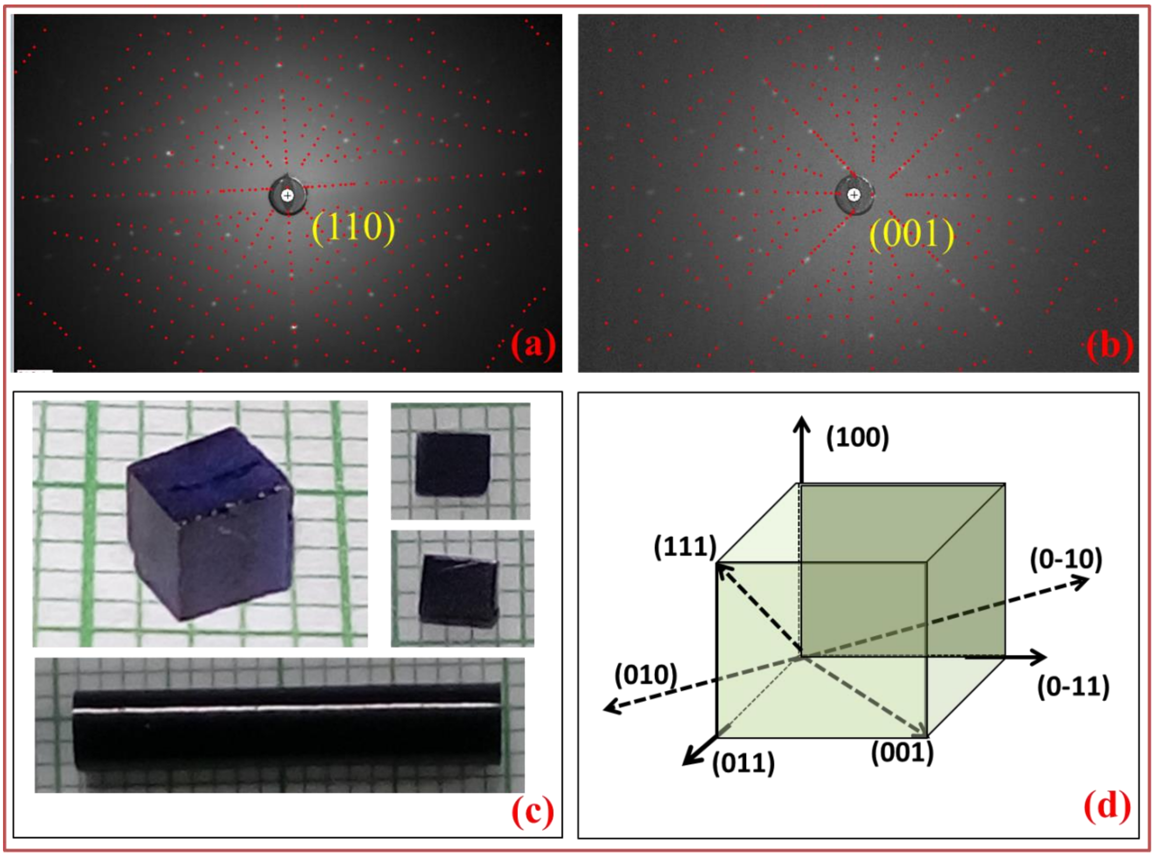

Figure 7.3 Laue diffracted spots overlapping with the simulated spots for (a) along (110) and and (b) along (001) direction. (c) As grown crystal image, cubic shape, thin plate square shape cut crystal pieces for magnetic and electrical measurements. (d) Schematic diagram to visualize the various orthogonal directions.

7.3.2 Magnetization and heat capacity

Figure 7.4 shows the magnetization data measured along various crystallographic directions of (110), (1-10), (001) and (111) under FCW condition with 100 Oe. We can see a broad peak centered on 17 K and a sharp decreasing trend below 10 K. This magnetization anomaly is quite similar to which was observed in earlier study where the sample has minimum site inversion parameter. This magnetization peak does not look like a typical antiferromagnetic behavior and it is not possible to distinguish the spiral-spin-liquid state or the long-range magnetic ordering state in this sample. We have taken the first derivative of magnetization with temperature which shows a quite sharp peak close to 10 K which is an indication of long-range ordering (figure 7.4 (d)). Further we have measured magnetization with ZFC and FCC condition in order to see if there is any splitting which would be an indication of spin-glass behavior. We can see that the ZFC, FCC and FCW magnetization curves overlap quite well almost down to low temperature. As discussed in the introduction, the magnetic property in $CoAl_2O_4$ is very sensitive to the amount of the cation inversion between A and B sites. Sample with inversion factor ($x \geq 0.08$) have been shown to have spin glass behavior whereas ($x \geq 0.05$) have been anticipated to have a spin liquid ground state [9, 10, 17]. However, from the absence of spiliting in the ZFC and FCW data we argue that the sample may have a long range ordering. The $1/\chi_m$vs T data measured under FCW condition under 100 Oe is shown in inset of figure 7.4(a). This data in the temperature range of 50 to 300 K has been fitted with Curie-Weiss law. The obtained effective moment is 4.87 which is somewhat higher than the theoretical spin only moment (3.87) which suggest a significant orbital moment present for the Co^{2+} ions and it is in quite well agreement with the literature value of the observed effective magnetic moment as we have already discussed in the chapter 5 where we see similar experimental value of effective moment of Co^{2+}. On the other hand, the obtained Curie-Weiss temperature (θ_{CW}) is close to -88 K. The value of θ_{CW} is much higher than the suggested long range ordering temperature (~10 K) thus the frustration parameter is ~9 which suggest the next nearest neighbor interaction (J_2) is significant thus a high magnetic frustration. Figure 7.4(c) shows the magnetic field dependence of magnetization measured along various directions at 2 K. The overall behavior of $M(H)$ curves are linear for all the directions except a small change in the curvature around 2 T. For further analysis of $M(H)$ data we have taken a first derivative of magnetization with respect to field and shown in figure 7.4(f). The slope change is clearly visible in this d*M*/d*H* curve.

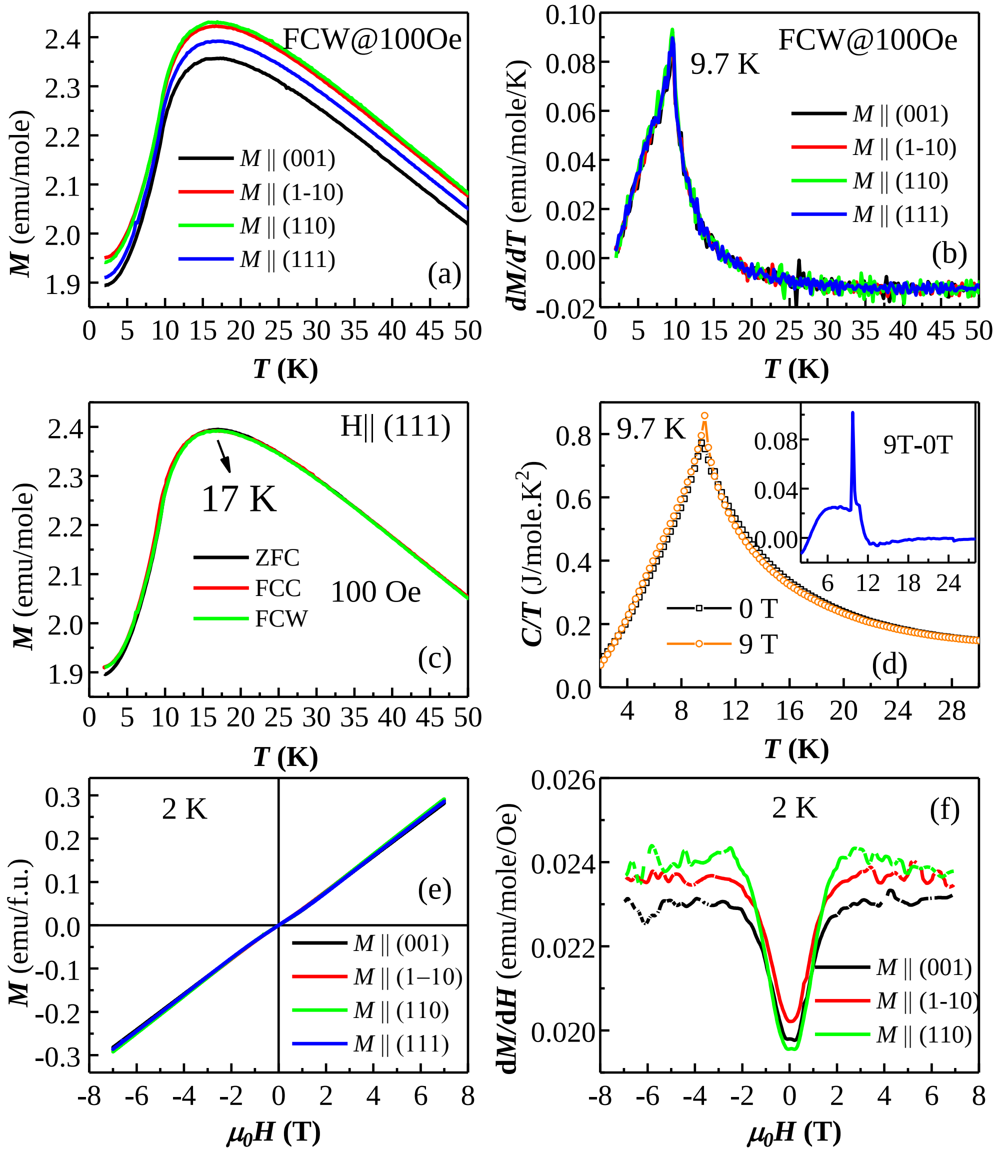

Figure 7.4 (a) DC magnetization measured along various directions in $CoAl_2O_4$ single crystal with cubic shape. (b) First derivative of magnetization with temperature. (c) DC magnetization measured under ZFC, FCC and FCW condition along (111) direction. (d) Heat capacity (*Cp*/*T*) vs. temperature under zero field and 9 T magnetic field. Inset shows the difference value of *Cp* (*H* = 9T) and *Cp* (*H* = 0T). (e) *M*(*H*) loop at 2 K along various directions. (f) First derivative of magnetization (d*M*/d*H*) with field along various directions.

Figure 7.4 (d) shows C_p/T versus temperature data measured at zero field and at 9 T magnetic field. The *Cp*/*T* curves show sharp peak centered at 9.8 K which further suggests a long-range magnetic ordering occurring below this temperature. Further, this heat capacity data can be compared with the previously reported by B. Roy *et al.* and S.

Ghara *et al.* where they suggested a long-range magnetic ordering of $CoAl_2O_4$ with inversion parameter x~0.05 [11, 15]. To estimate the magnetic contributions ($C_{Mag}(T)$) of the total heat capacity, the phonon contribution is calculated using a combine Debye-Einstein model as given by the following equation.

$$C_{ph} = C_{Debye} + C_{Einstein} = \frac{9Ra_1}{x_D^3}\int_0^{x_D} \frac{x^4 e^x}{(e^x-1)^2}\,dx + 3R\sum_{n=1}^{2} b_n \frac{x_{E,n}^2 e^{x_{E,n}}}{(e^{x_{E,n}}-1)^2}$$

where R is the universal gas constant, $x_{D,E} = {}^{\theta_{D,E}}\!/_{T}$, where $\theta_{D,E}$ are the Debye and Einstein temperature, respectively. The C_P data in the range of 50 to 100 K has been fitted with the above equation as shown in figure 7.5(a). One Debye and two Einstein terms have been used for the fit. In the Debye-Einstein model, the total number of modes is equal to the number of atoms in the formula unit, and the used coefficients of Debye and Einstein contributions are used as a_1, b_1 and b_2 as 1, 1, and 5 respectively [15].

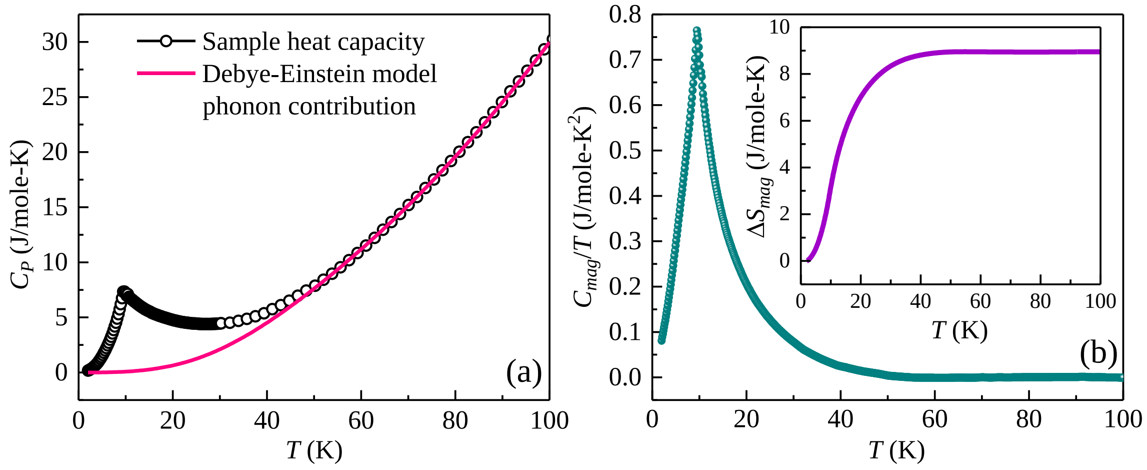

Figure 7.5(a) sample heat capacity and the phonon contributions from Debye-Einstein model versus temperature curve. (b) Calculated magnetic contribution of heat capacity (C_{mag}/T) with temperature. Inset shows the entropy change associated with the magnetic contribution of the heat capacity.

The fitting was quite satisfactory, and the fitted value was extrapolated down to the low temperature. The magnetic contribution was then calculated by subtracting the phonon contributions from the overall measured sample heat capacity and shown in figure 7.5(b). We can see a slightly higher value of magnetic contribution as compared to the previously reported value for $CoAl_2O_4$ compound with ~0.05 site inversion [15]. As we know that the magnetic contribution reduces with the increasing disorder, we infer that our single crystal sample has the disorder either very close to 0.05 or even less. The magnetic contribution associated entropy as calculated from the following equation is shown in the inset of figure 7.5(b) which is in good agreement with the lower value of inversion parameter ≤ 0.05 [15].

$$\Delta S_{Mag}(T) = \int_0^T \frac{C_{Mag}(T)}{T} dT$$

7.3.3 Magnetodielectric effect

Figure 7.6(a-i) shows the temperature dependence of dielectric constant (ε_r) along (1-10), (110) and (001) directions while applying various magnetic fields (0, 1, 2, 4, 6, 8 and 9 T) along (1-10), (110) and (001) measured at 100 kHz in the range of 2 to 30 K. At μ_0H = 0 T (where μ_0 is the magnetic permeability of vacuum), ε_r shows only a broad step near the magnetic ordering (figure 7.6(b)). By applying magnetic field, ε_r shows a λ - shaped peak near the magnetization peak around 10 K along all the measured directions. However, the nature of peaks intensity and broadness are quite different along the various directions of measurements as well as various direction of applied magnetic field. The peak has the highest intensity along (110) when the magnetic field was applied along (001) direction (figure 7.6(f)). On the other hand, the peak becomes less intense and becomes quite broad with applied field along (110) (figure 7.6(e)) whereas the peak is almost suppressed with the field along (1-10) (figure 7.6(d)). A similar magnetic field dependent behavior is observed along (1-10) where the highest peak intensity was observed with the field along both (1-10) and (001) (figure 7.6(a and c)). The magnetic field along (110) in the case of (1-10) direction dielectric constant has similar effect to the dielectric constant along (110) under magnetic field (1-10) where we observed a very small change in dielectric constant (figure 7.6(b and d)). Further the dielectric constant along (001) has comparatively less intensity for all the direction of applied magnetic field (figure 7.6(g-i)). All these results confirm an intrinsic magnetodielectric effect with a significant anisotropy. The fact that the dielectric peak appears only under magnetic fields inferring a magnetoelectric transition present in $CoAl_2O_4$ which in good agreement with the earlier report in polycrystalline $CoAl_2O_4$ [15]. With increasing H, the peak along (110) shifts to lower temperature when H was applied along (110). The magnetodielectric effect [$\Delta\varepsilon = [\varepsilon(H) - \varepsilon(0)]/\varepsilon(0)$] measured along (110) direction under magnetic field along (110) and (001) directions is shown in figure 7.7.

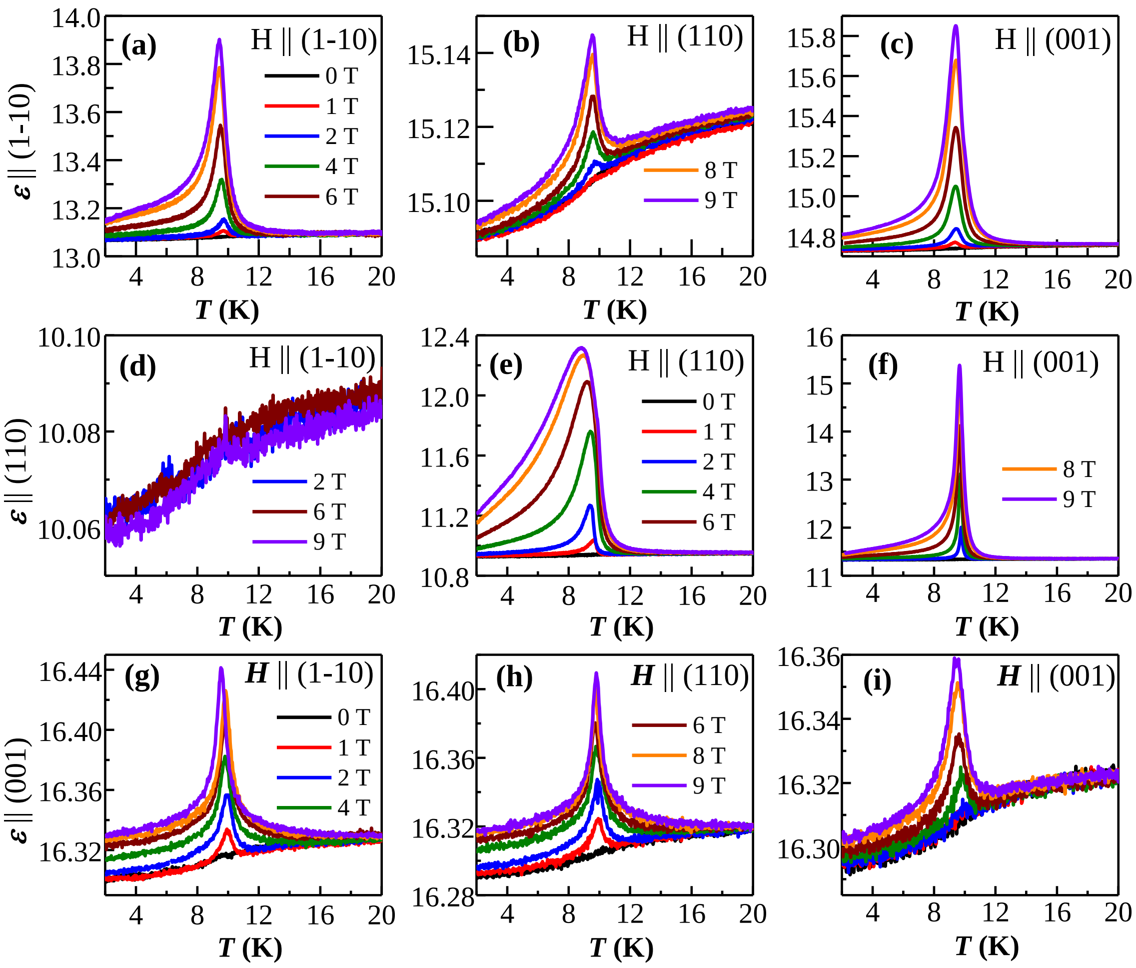

Figure 7.6 Dielectric constant measured along (1-10), (110) and (001) direction while magnetic field along (1-10), (110) and (001).

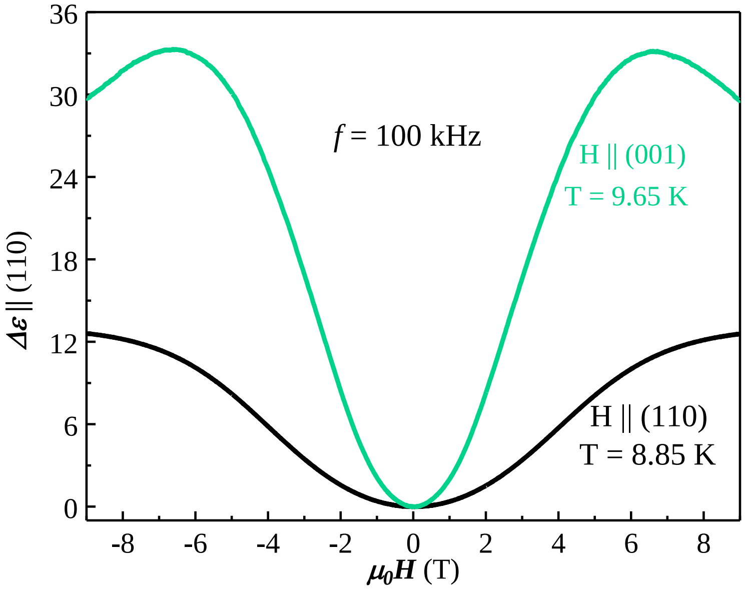

Figure 7.7 Magnetodielectric effect along (110) direction under magnetic field along (110) and (001).

A remarkable magnetodielectric effect can be noticed along (110) direction for both the magnetic field directions e.g. ~35% for (001) and ~12% for (110) direction at 9 T field near the transition temperatures. It is worth mentioning that this type of magnetic field induced peak in ε and magnetocapacitance was observed in Cr_2O_3 at the magnetoelectric transition temperature. Therefore these results indicate a possible magnetoelectric effect in this sample. The downturn of the $\Delta\varepsilon$ above ~6 T can be due to the decreasing of T_N under magnetic field.

7.3.4 Magnetoelectric effect

Pyrocurrent was recorded along all the direction under various applied magnetic field as performed in the dielectric measurements. In these measurements the sample was first poled with electric field from 30 to 2 K along with the various magnetic fields. Further the electric field was removed at 2 K, while the H was remained same and the current was recorded from 2 to 20 K in presence of H. Figure 7.8(a-i) shows T dependence of P along (110), (1-10) and (001) with H along (110), (1-10) and (001) directions. Although no polarization is observed along any direction at 0 T, the P arises below the dielectric anomaly temperature with applying H along all the directions. This confirms the magnetoelectric effect in the sample. It is to be noted that the electric polarization in our single crystalline $CoAl_2O_4$ is almost ten times higher than the observed polarization in polycrystalline $CoAl_2O_4$ with the disorder ~0.05 [15]. In general, a higher value of polarization is expected in single crystalline sample of the order of 4 to 5 times than the polycrystalline sample. Thus the ten times higher polarization can be due to the less disorder present in our single crystalline sample as suggested by our heat capacity data. It is important to notice that the polarization values are different along the various measured directions as well as magnetic field directions. The significant polarization is observed along (1-10) under H along (1-10), denoted as P_1 and H along (001), denoted as P_2. The polarization (1-10) under magnetic field (110) is very small compared to the maximum observed polarization thus can be regarded as due to a small misalignment of the crystal or magnetic field directions. Therefore, we consider it as zero polarization state. A similar anisotropic feature can be noticed along (110) where the maximum polarization was observed under magnetic field along (001) and very close to the polarization value along (1-10) which is denoted as P_2.

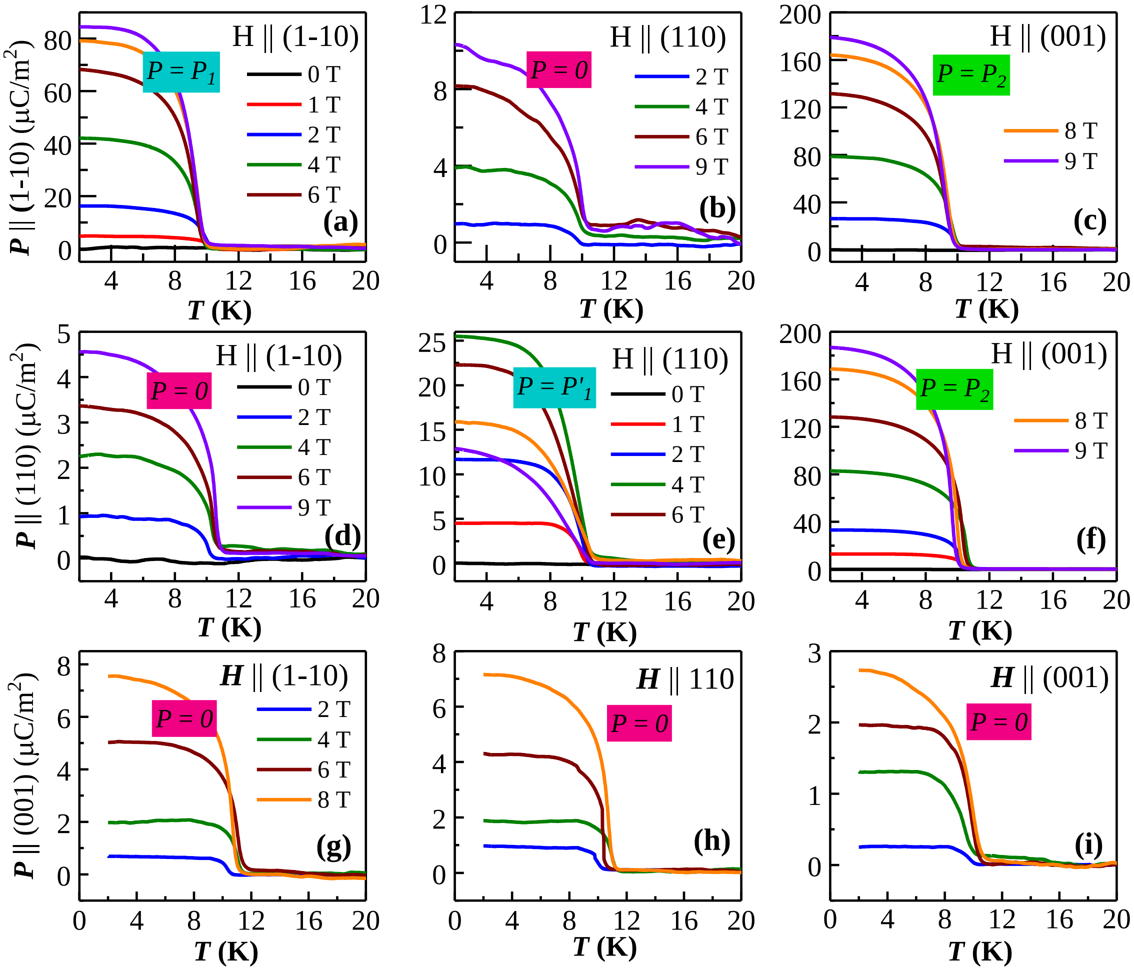

Figure 7.8 Polarization in $CoAl_2O_4$ single crystal obtained through measuring pyrocurrent along various directions and magnetic field along (1-10), (110) and (001) directions.

The lowest polarization was observed under magnetic field along (1-10) which we consider as zero polarization state (figure 7.8(d)). Interestingly, the polarization under magnetic field along (110) shows first an increasing trend below 4 T and a decreasing with further increasing of magnetic field (figure 7.8(e)). This anomalous polarization is denoted as P_3. On the other hand, the polarization along (001) was negligible for all the magnetic field directions (figure 7.8(g-i)). These results are in good agreement with the dielectric data where we observed the similar intensity of the dielectric peaks (figure 7.6(a-i)). The induced P is almost linear with the magnetic field for the all magnetic field direction, except (110), thus confirms the linear magnetoelectric effect in the material. The linear magnetoelectric coefficient was calculated from the slope of the linear fit of the P versus H data for P along (1-10) under H along (001) as shown in figure 7.9 which is found to be 27.3 ps/m, one order higher than that observed in polycrystalline $CoAl_2O_4$ [15]. Since the magnetoelectric effect requires a broken spatial as well as time reversal symmetry, we propose that the magnetic ground state as a long-range ordered state and there is no spiral spin liquid state. Although the magnetic properties are isotropic, the electrical polarization as well as dielectric constant is highly anisotropic which also further confirms the long-range magnetic ground state. However, it is also possible that the compound undergoes long-range ordered state with the application of magnetic field as in a previous neutron study evidenced that the magnetic peaks acquired more Gaussian line-shapes and increase in intensity under magnetic fields [8]. As reported in the case of Co_3O_4, the magnetic point group would be either $I4_1'/a'm'd$ or $R\bar{3}'m'$ where both of these allow magnetoelectric effect. Therefore, for a detailed microscopic view in this compound, a neutron diffraction experiment is necessary.

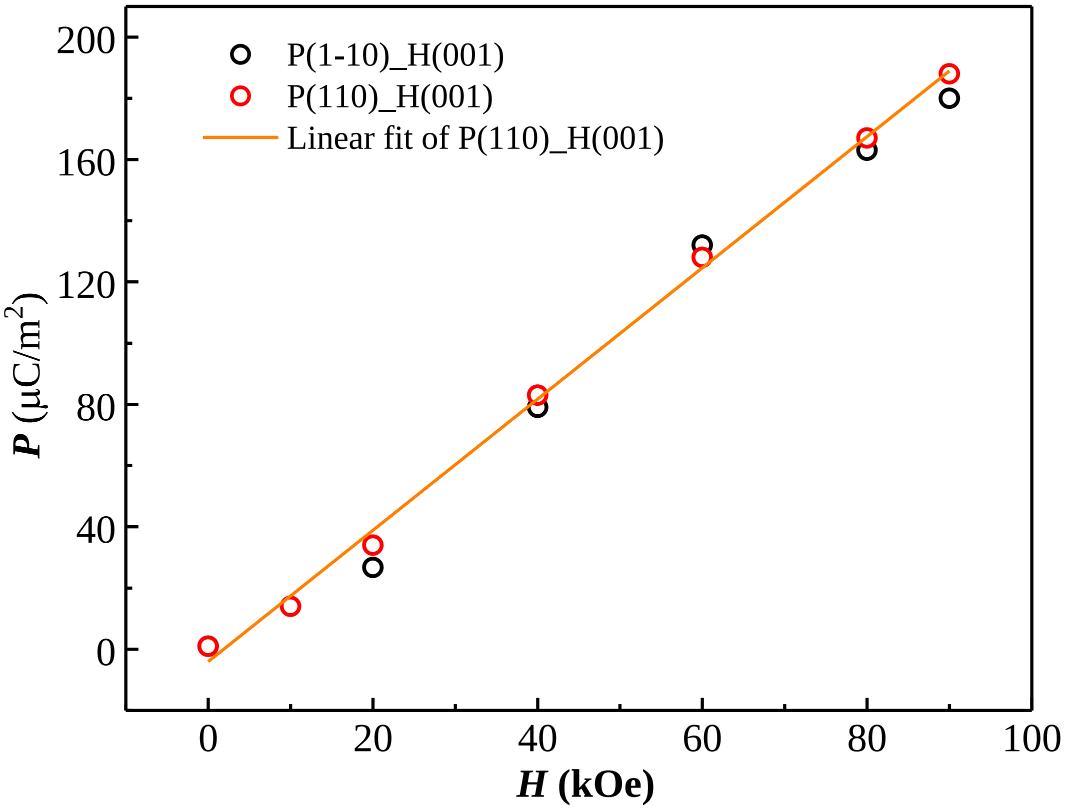

Figure 7.9 *P* versus *H* data at 2 K along (1-10) and (110) directions with the linear fit.

7.3.5 Neutron Laue Diffraction

We have looked at Laue diffraction pattern using neutron beam line 'CYCLOPS' at ILL to get more information about the magnetic ordering. A comparative Laue pattern of the 1.5 K (top) and 25 K (bottom) is shown in figure 7.10 where the (100) reflections have been highlighted with a white square. We see an increased intensity in this reflection below the magnetic ordering temperature. The temperature evolution of the selected reflection, correspond with the (100) is shown in figure 7.11. Based on the Laue diffraction, the propagation vector should be the k = (0, 0, 0), as no new reflections are observed between the paramagnetic (25 K) and the ordered phases (1.5 K). Moreover, the increase of intensity below the ordering temperature, suggests the occurrence of a long-range magnetic order.

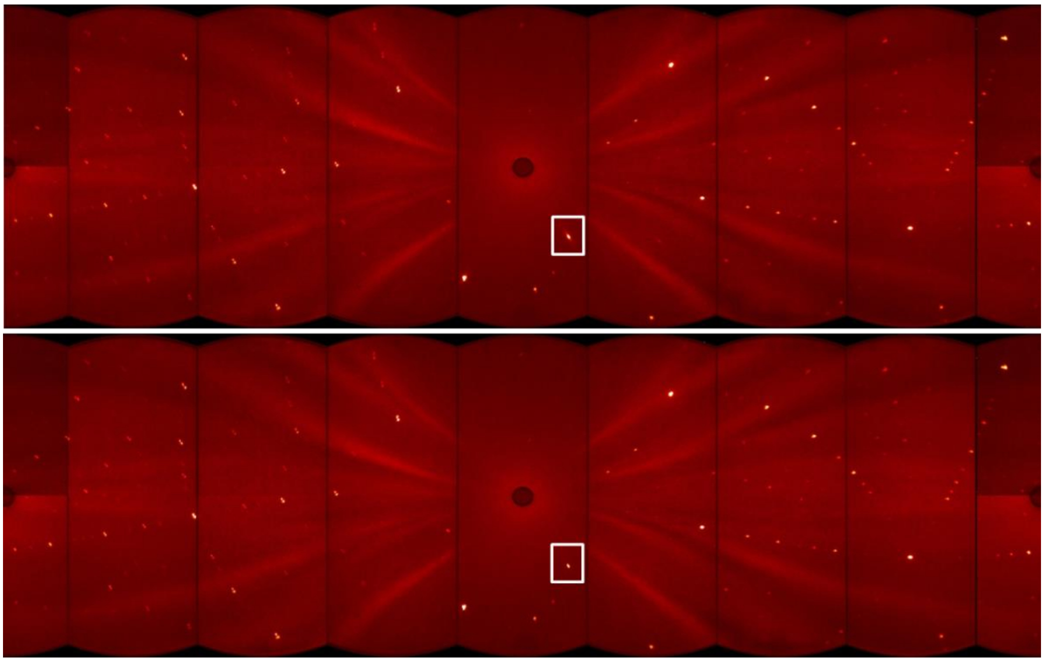

Figure 7.10 Comparative Laue diffraction pattern of 1.5 K (top) and 25 K (bottom).

We have also presented the intensity of the (100) reflection including the main reflection as well as the diffuse scattering (figure 7.12). The x-coordinates represents the position, i.e. basically pixels. The cyan and pink curves, 25 and 10 K respectively, correspond with the paramagnetic phase. Neither of these curves presents any signal of diffuse scattering. However, we can see the strong diffusive nature in the peaks below the magnetic ordering thus diffuse scattering have the magnetic origin. Furthermore, below 10 K the intensity of the (100) reflection is increasing with decreasing of the temperature, suggesting the k = 0 magnetic structure. It requires further investigations to understand the nature of magnetic ordering.

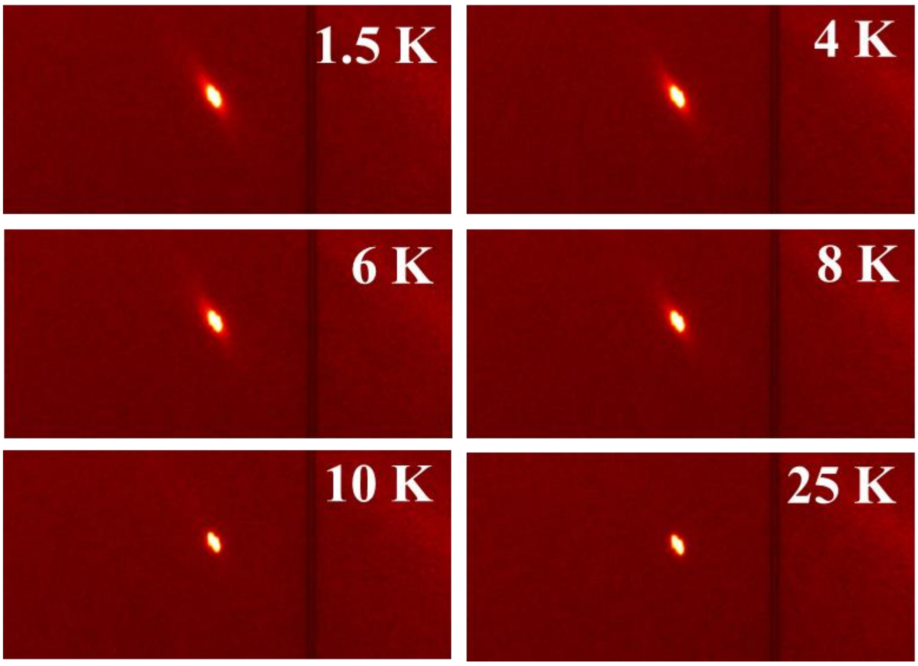

Figure 7.11 Temperature evolution of the (100) reflection.

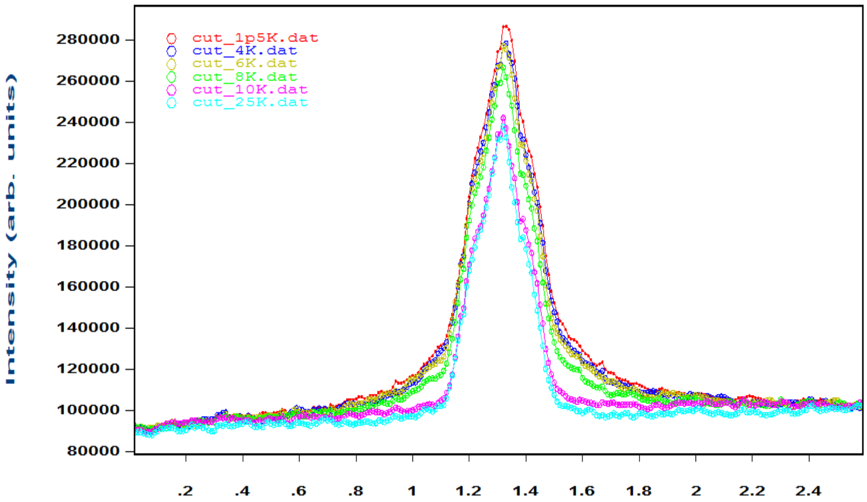

Figure 7.12 Temperature evolution of the integrated intensity of the (100) reflection.

7.3.6 Easy axis determination from electric polarization

In the cubic symmetry of this compound there are only two possibility of magnetic easy axis i.e. either along (001) or along (111). From the symmetry allowed polarization ratio along various direction we tried to find the magnetic easy axis. It can be noted that this symmetry analysis was able to determine the correct magnetic easy axis for a spinel compound MnAl$_2$O$_4$. P||(1-10) at H||(001) was considered as P_2 which is almost same as P||(110) at H||(001) as expected from the $Fd\bar{3}m$ symmetry. The anomalous behavior of

P||(110) at H||(110) for H ≥ 4 T can be due to a spin flop transition. P||(1-10) at H||(1-10) was considered as P_1 which should be same as P||(110) at H||(110), but there is a difference which might me due to the spin flop transition. For the case of P||(001), the polarization should vanish for all studied magnetic field directions in this $Fd\bar{3}m$ symmentry and we observe a very small polarization which can be due to slight misalignment of the crystal or the applied magnetic field directions. Assuming $P=P_1$ and P_2 for P||[1-10] at H||[1-10] and H||[001], respectively, we have calculated their ratio of P_1/P_2. According to the theoretical calculation, for easy axis along (111), P_1/P_2 should be equal to $1/\sqrt{2}$ when there is no spin flop transition and P_1/P_2 should be equal to $1/\sqrt{3}$ for a spin flop case [18]. On the other hand, if the easy axis is along (001), the P_1/P_2 ratio should be equal to $\sqrt{2}$. From our polarization as well as magnetization data we observed a spin flop transition and the P_1/P_2 ratio is close to $1/\sqrt{3}$. Since the magnetic anisotropy in $CoAl_2O_4$ is quite low and the antiferromagnetic vector can easily orient as to be perpendicular to the magnetic field, the value $1/\sqrt{3} \approx 0.58$ is quite close to what is observed for P||(1-10) therefore we suggest that the easy axis should be along (111) direction. If the easy axis was along (001) then P||(1-10) at H||(1-10) should be bigger than at H||(001), which is not the case. We would like to point out here that a previous neutron diffraction experiment in powder sample suggested collinear magnetic state with easy axis along (001) and magnetic space group $F\bar{4}3m$ similar to the Co_3O_4 magnetic structure [11]. In contrast we found the magnetic easy axis to be along (111) thus the magnetic point group would be $R\bar{3}'m'$similar to the case of $MnGa_2O_4$ which has the magnetic easy axis along (111) [18].

7.4 Conclusion

In conclusion, we have grown $CoAl_2O_4$ single crystal with minimum site disorder which indicated long-range antiferromagnetic behavior in the magnetization and heat capacity. An electric polarization is observed below the magnetic ordering under magnetic field depending on the crystallographic directions as well as applied magnetic field directions. An increasing intensity with significant diffusive character is observed in the Laue pattern of neutron beam below the magnetic ordering. Thus, this study provides a significant contribution towards understanding the magnetic ground state in the A-site magnetic spinel $CoAl_2O_4$.

References

[1] D. Bergman, J. Alicea, E. Gull, S. Trebst, and L. Balents, Nat. Phys. **3**, 487 (2007).

[2] J.-S. Bernier, M. J. Lawler, and Y. B. Kim, Phys. Rev. Lett **101**, 047201 (2008).

[3] A. P. Ramirez, A. Hayashi, R. a. Cava, R. Siddharthan, and B. Shastry, Nature **399**, 333 (1999).

[4] S. T. Bramwell and M. J. Gingras, Science **294**, 1495 (2001).

[5] S. Kondo *et al.*, Phys. Rev. Lett **78**, 3729 (1997).

[6] W. Roth, Journal de Physique **25**, 507 (1964).

[7] R. Fichtl, V. Tsurkan, P. Lunkenheimer, J. Hemberger, V. Fritsch, H.-A. K. von Nidda, E.-W. Scheidt, and A. Loidl, Phys. Rev. Lett **94**, 027601 (2005).

[8] O. Zaharko *et al.*, Phys. Rev. B **84**, 094403 (2011).

[9] T. Suzuki, H. Nagai, M. Nohara, and H. Takagi, J. Phys. Condens. Matter **19**, 145265 (2007).

[10] K. Hanashima, Y. Kodama, D. Akahoshi, C. Kanadani, and T. Saito, J. Phys. Soc. Jpn. **82**, 024702 (2013).

[11] B. Roy, A. Pandey, Q. Zhang, T. Heitmann, D. Vaknin, D. C. Johnston, and Y. Furukawa, Phys. Rev. B **88**, 174415 (2013).

[12] O. Zaharko, S. Tóth, O. Sendetskyi, A. Cervellino, A. Wolter-Giraud, T. Dey, A. Maljuk, and V. Tsurkan, Phys. Rev. B **90**, 134416 (2014).

[13] G. J. MacDougall, D. Gout, J. L. Zarestky, G. Ehlers, A. Podlesnyak, M. A. McGuire, D. Mandrus, and S. E. Nagler, Proc. Natl. Acad. Sci. U.S.A. **108**, 15693 (2011).

[14] G. J. MacDougall *et al.*, Phys. Rev. B **94**, 184422 (2016).

[15] S. Ghara, N. Ter-Oganessian, and A. Sundaresan, Phys. Rev. B **95**, 094404 (2017).

[16] A. Maljuk, V. Tsurkan, V. Zestrea, O. Zaharko, A. Cervellino, A. Loidl, and D. Argyriou, J Cryst Growth. **311**, 3997 (2009).

[17] N. Tristan, J. Hemberger, A. Krimmel, H. K. Von Nidda, V. Tsurkan, and A. Loidl, Phys. Rev. B **72**, 174404 (2005).

[18] R. Saha, S. Ghara, E. Suard, D. H. Jang, K. H. Kim, N. V. Ter-Oganessian, and A. Sundaresan, Phys. Rev. B **94**, 014428 (2016).

Summary of the thesis

It is essential to design new materials with more functionality or to modify known materials to improve them for developing new technological devices. Among various multifunctional materials, multiferroic and magnetoelectric materials were chosen for our study. In this context, discovering new magnetoelectric and multiferroic materials and understanding the mechanism of origin of the electric polarization is crucial to achieve room-temperature magnetoelectric multiferroic which can be used in future devices. In this thesis, we have started with the understanding of intrinsic ferroelectric signature in multiferroics and aimed to explore new magnetoelectric multiferroics materials. We have investigated five different systems in the thesis. Firstly, we have worked on a mixed rare-earth manganites $Gd_{0.5}Dy_{0.5}MnO_3$ by growing single crystal sample that has spin origin mechanism i.e., the cycloidal magnetic ordering of Mn^{3+}, which can induce ferroelectricity. We found that the mixed rare-earth manganites have ferroelectricity below the magnetic cycloidal ordering which is suppressed below a short-range ordering of rare-earth ions. Further, under magnetic field, the polarization recovers as the cycloidal ordering of Mn^{3+} is released along with the long-range ordering of rare-earth ions under magnetic field. We have extended our work by investigating the doubly ordered double perovskite oxides (Na*R*MWO6, *R* =La, Nd, Ho Y and *M* = Mn and Co) which was potential for the non-centrosymmetric structure thus a polar class of materials. We found no typical ferroelectric polarization versus electric field loop at room temperature in these materials however a non-switchable ferroelectric polarization is discovered with lower size of rare-earth ions which was possible to synthesize under high-pressure and high temperature condition. Subsequently, we found an unusual ordering of isovalent charges Fe^{3+} and Al^{3+} in Bi_2FeAlO_6 multiferroic synthesized under further high-pressure and high temperature condition. Typical butterfly piezoelectric loop has been observed at room temperature as expected with the polar structure in this material. We discovered a new spin-induced multiferroic material where we found an electric polarization due to *p*-*d* hybridization of Mn^{2+} spin and S ligand ions in $MnSb_2S_4$ compound. In fact, in the high pressure phase of $MnSb_2S_4$ compound (orthorhombic phase) as well, a spin induced multiferroic property is found. Finally, we have explored the magnetoelectric properties of a frustrated spinel $CoAl_2O_4$ after growing a good quality single crystal sample.

List of abbreviations

AFM: Antiferromagnetic
C: Curie Constant
Cp: Heat Capacity
CW: Curie-Weiss
DR: Dipolar-Relaxation
DM: Dzyaloshinskii-Moriya
ε: Dielectric Constant
FCC: Field Cooled Magnetization
FCW: Field Cooled Warming
FE: Ferroelectric
FOJT: First Order Jahn-Teller
LCR: Inductance Capacitance Resistance
$M(H)$: Magnetization versus Magnetic field loop
NPD: Neutron Powder Diffraction
$P(E)$: Polarization versus Electric field loop
PPMS: Physical Property Measurement System
PUND: Positive Up Negative Down
SHG: Second Harmonic Generation
SOC: Spin Orbit Coupling
SOJT: Second Order Jahn-Teller
SQUID: Superconducting Quantum Interference Device
T: Temperature
T_N: Néel Temperature
TSFC: Thermally Stimulated Free Charge Carriers
τ: Tolerance Factor
VSM: Vibrating Sample Magnetometer
χ_m: Magnetic molar Susceptibility
XRD: X-ray Diffraction
ZFC: Zero Field Cooled